Metal oxides-based systems for efficient visible light conversion

Supervisor:

Dr. Paola Luches

Co-supervisor: Prof. Sergio D'Addato

PhD Program Coordinator:
Prof. Marco Affronte

Submitted by:

Eleonora Spurio

Abstract

Nowadays, the research in the field of renewable energy sources is fundamental, to stem the climate crisis and to overcome the reducing availability of fossil fuels. The high magnitude of solar energy has driven a lot of research towards the investigation of efficient methods to convert it into other energy forms (e.g. electric or chemical). One of the most promising methods to convert solar into chemical energy is visible light photocatalysis. The main aim of this thesis is the investigations of systems at the nanoscale that are promising candidates for visible light photocatalysis, and in particular of thin films of cuprous oxide and of cerium oxide combined with plasmonic nanoparticles (NPs). In the latter, cerium oxide has been coupled with NPs because the band gap of the bare oxide is too wide for the absorption of visible radiation, but previous works demonstrated that the formation of heterojunctions by coupling plasmonic nanostructures with semiconductors can greatly enhance the activity of photocatalysts by plasmonic energy transfer from the metal nanostructure to the semiconductor. The first part of this thesis will describe the growth and characterization of these systems, to extract information on their optical properties, with a specific focus on the ultrafast dynamics of excited states. For this purpose, systems composed by Ag, Au and Cu NPs surrounded by CeO_2 have been investigated by means of both time-resolved and static absorbance and emission analysis. First, systems composed by Ag NPs with CeO_2 have been investigated with time-resolved photoemission spectroscopy and free electron laser based time-resolved X-ray absorption spectroscopy. Secondly, the ultrafast dynamics of excited states induced by ultra-violet and visible light excitation has been explored in Au NPs combined with cerium oxide, aimed at understanding the excitation pathways, using femtosecond transient absorption spectroscopy. Finally, the last part of the thesis is centred on Cu NPs, also embedded in CeO_2 films, or surrounded by oxides, with a particular focus on Cu_2O, that, thanks to its band gap in the visible region, is a promising candidate for solar light photocatalysis. Cu NPs have been investigated in terms of their morphology, optical properties and stability in air conditions, and a procedure for growing metallic core-Cu_2O shell has been developed and investigated. Finally, Cu_2O crystals and films of different thickness have been grown and analysed by means of low energy electron diffraction, scanning tunneling microscopy and photoluminescence spectroscopy in a wide temperature range to obtain information on the behaviour of excitons.

Sommario

Al giorno d'oggi, la ricerca nel campo delle fonti energetiche rinnovabili è fondamentale, per arginare la crisi climatica e per superare la sempre minore disponibilitá di combustibili fossili. Il flusso significativo di energia dal Sole sta spingendo le attivitá di ricerca verso lo studio di metodi efficienti per convertirla in altre forme di energia (ad esempio elettrica o chimica). Uno dei metodi più promettenti per convertire l'energia solare in energia chimica è la fotocatalisi della luce visibile. Lo scopo principale di questa tesi è lo studio di sistemi su nanoscala che sono promettenti per la fotocatalisi di luce visibile, e in particolare di film sottili di ossido di rame e di ossido di cerio combinati con nanoparticelle plasmoniche. In questi sistemi, l'ossido di cerio viene combinato con nanoparticelle, dal momento che il *band gap* dell'ossido è troppo ampio per l'assorbimento della radiazione visibile. Lavori precedenti hanno dimostrato che la formazione di eterogiunzioni combinando nanostrutture plasmoniche con semiconduttori puó migliorare notevolmente l'attività fotocatalitica della ceria mediante trasferimento di energia plasmonica dalla nanostruttura metallica al semiconduttore. La prima parte di questa tesi descriverá la crescita e la caratterizzazione di questi sistemi, per ottenere informazioni sulle loro proprietà ottiche, con un focus specifico sulla dinamica ultraveloce e sull'evoluzione temporale degli stati eccitati. A tale scopo, sono stati studiati sistemi composti da nanoparticelle di Ag, Au e Cu circondati da CeO_2 mediante analisi di assorbanza ed emissione sia risolte nel tempo che statiche. In primo luogo, i sistemi composti da nanoparticelle di Ag con CeO_2 sono stati studiati con spettroscopia di fotoemissione risolta in tempo e spettroscopia di assorbimento di raggi X risolta in tempo basata su laser a elettroni liberi. In secondo luogo, la dinamica ultraveloce degli stati eccitati indotti dall'eccitazione della luce ultravioletta e visibile è stata esplorata in nanoparticelle di oro combinate con ossido di cerio, allo scopo di comprendere i percorsi di eccitazione, utilizzando la spettroscopia di assorbimento transitorio a femtosecondi. Infine, l'ultima parte della tesi è incentrata sulle nanoparticelle di Cu, anch'esse inglobate in film di CeO_2, o circondate da ossidi, con un focus particolare su Cu_2O, che, grazie al suo band gap nella regione del visibile, è un candidato promettente per la fotocatalisi di luce solare. Le nanoparticelle di Cu sono state studiate in termini di morfologia, proprietà ottiche e stabilitá in condizioni atmosferiche, ed è stata sviluppata e studiata una procedura per la crescita di particelle core-shell con nucleo metallico e shell di Cu_2O. Infine, cristalli e film di Cu_2O di diverso spessore sono stati cresciuti e analizzati mediante diffrazione di elettroni a bassa energia, microscopia a effetto tunnel e spettroscopia di fotoluminescenza in un ampio intervallo di temperature per ottenere informazioni sul comportamento degli eccitoni.

Contents

Chapter 1

Introduction

1.1 Oxides for photocatalysis

In recent years, the climate crisis and global warming have become one of the most important problems to solve. Moreover, the increasing demand on energy and the reducing availability of fossil fuels strongly encourages the development and improve of renewable energy sources. Solar energy harvesting from sunlight provides a convenient way to meet the demands of clean energy, it is then fundamental to convert the energy harvested from the sun into chemical fuel. Solar energy can be converted and stored in fuels such as hydrogen by water splitting and hydrocarbon compounds by CO_2 reduction [1, 2, 3, 4]. Solar light photocatalysis requires semiconducting materials with a band gap in the ultraviolet-visible (UV-Vis) range (ideally, for water splitting, between 1.9 eV and 2.3 eV), high stability in ambient conditions, efficient charge separation and low charge recombination rates. However, the majority of narrow band-gap semiconductors are not stable, while wide band semiconductors are stable, but inefficient in visible light absorption [5]. The most convenient materials for photocatalysis and water splitting are metal oxides (MOs) semiconductors, such as CeO_2, TiO_2, Cu_2O, ZnO, since they are abundant and cheap, non-toxic, with tunable properties [6]. In this thesis, I will focus in particular on CeO_2 and Cu_2O. These two MOs present different bandgap and different properties, but they are both very promising materials for photocatalysis and water splitting reactions.

1.1.1 Energy-Driven Water Splitting

One of the most critical points in the use of solar light as primary energy source is the cost-effective storage and dispatch of the converted solar energy upon demand. The implementation of technologies to enable in a convenient and scalably manufacturable form the capture, conversion, and storage of sunlight is then fundamental to mitigate the intermittency of the solar resource and to maintain stability of energy distribution [7, 8, 9]. One of the most promising pathways to overcome this challenge is the hydrogen generation via solar water splitting, as H_2 can be stored, transported and consumed without generating harmful byproducts [2, 10, 11, 12].

The overall water splitting is an 'up-hill' reaction with a high positive change in Gibbs free energy ($\Delta G_0 = +237.2$ kJ/mol), which, according to the Nernst equation, corresponds to $\Delta E^0 = 1.23$ V per electron transferred [2, 13]. Photocatalytic water splitting has fundamental requirements for photocatalysts on their band gaps and band levels. Semiconductor-based solar water splitting requires the semiconductor to absorb photons with energies $h\nu \geq 1.23$ eV (i.e. $\lambda \leq 1008$ nm) [2]. In particular,
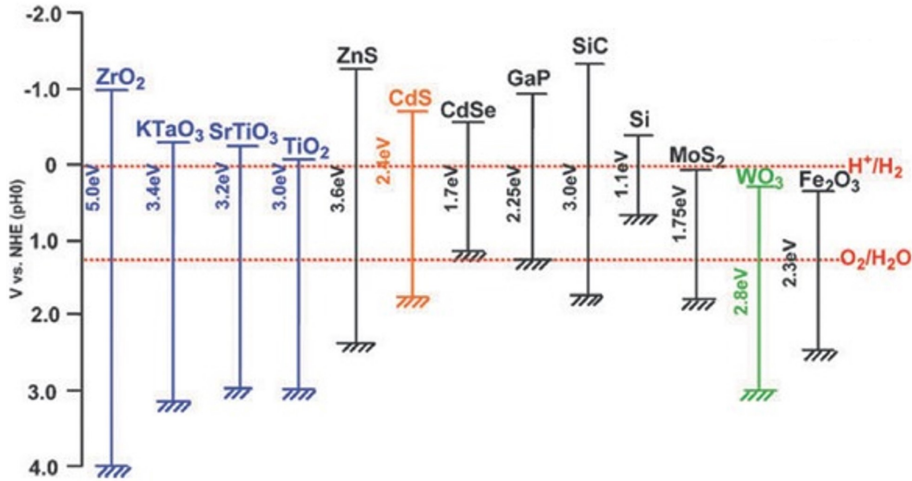
Figure 1.1: *Band structure of semiconductors and redox potentials necessary for light-driven water splitting [14].*

for water reduction reaction, the conduction band needs to be at a potential less than 0 V vs. NHE (H^+/H_2), while the valence band needs to be at a potential more than 1.23 V (see figure 1.1) [14].

Since ultraviolet photons are more energetic than visible photons, the photocatalysts that are sensitive to ultraviolet radiation have better performance per photon for hydrogen production via solar water splitting than visible light-based ones. On the other hand, ultraviolet radiation ($\lambda < 400$ nm) only composes $\sim 4\%$ of the total solar energy spectrum, that mainly includes visible (400 nm $< \lambda <$ 800 nm) and infrared ($\lambda >$ 800 nm) light, accounting respectively 53% and 43% of the total solar radiation. So far, the majority of the photocatalysts are only active in ultraviolet-light absorption [14], but it is crucial to fabricate photocatalysts that are able to harvest a larger fraction of the solar spectrum. Typical photocatalysts are semiconductor materials with a proper band gap (as schematized in figure 1.1), that can be combined with dopants and/or co-catalysts to optimize their performance. As already mentioned, a good photocatalyst must have a proper band gap for light harvesting and a suitable thermodynamic potential for water splitting, a high charge separation efficiency and low charge recombination rate. Moreover, it must also be stable in the operating conditions and low-cost. The reason for the first requirements are clear by looking at the steps that are necessary for light-driven solar splitting (figure 1.2a). When a semiconductor is irradiated with photons that have energy equal to or above its band gap, the incoming radiation may generate electrons in the conduction band and holes in the valence band. If they are transferred to water molecules on the semiconductor surface, the electrons can reduce water to form hydrogen while the holes can oxidize it to form oxygen [17]. Intuitively, this process requires high electron-hole pair generation rate and low recombination rate. A crystalline structure, with a low defect concentration, is beneficial for solar-driven water splitting, because defects can act as recombination sites [18].

Photoelectrocatalysis

Among all the solar-to-hydrogen conversion systems (such ad photovoltaic cells, solar thermochemical systems and concentrating solar thermal systems), one of the most promising ones are the photoelectrochemical (PEC) devices (a schematics is shown in figure 1.2b), because they allow the direct conversion of photon to chemical
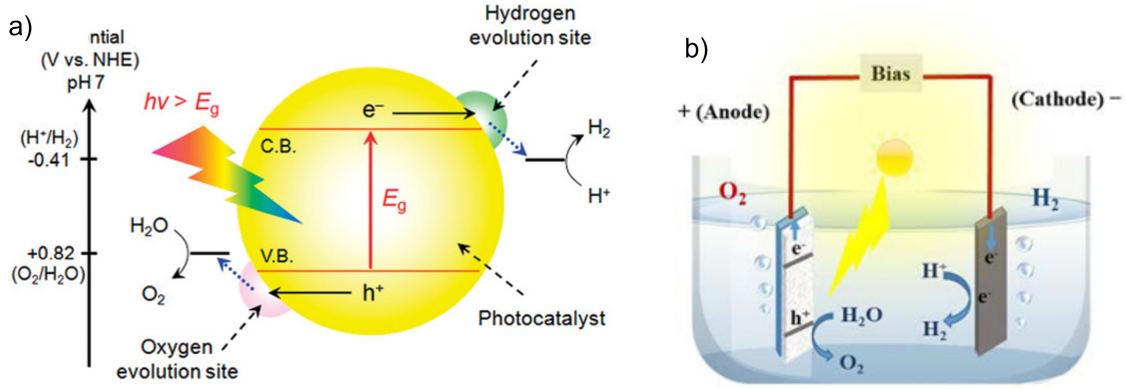
Figure 1.2: *a) Schematic of water splitting in a semiconductor photocatalyst [15] b) Mechanism of solar hydrogen production by PEC [16].*

energy, reducing the total cost of hydrogen production [16]. In PEC devices, oxygen and hydrogen are evolved at separate electrodes, which can be recombined in fuel cells to produce electricity. Typically, metal oxides are used as solar water-splitting photocatalysts, thanks to their reasonable stability and relatively low cost. However, as explained before, they need to fulfill the requirements on the band gap, on the band levels, on the electron-hole pair generation and recombination rates.

So far, there are not commercially available photocatalysts that are able to catalyze water-splitting reactions with the energy conversion efficiency larger than 10% under *one sun* radiation, which represents the threshold for commercialization of solar photocatalytic systems [19]. In fact, most narrow band gap semiconductors are unstable during photocatalytic reactions [19, 20]. One of the most common examples is cuprous oxide, that is cheap and easy to grow, with favorable energy band positions and a band gap of 2-2.2 eV that makes it a perfect candidate for visible light absorption. However, Cu_2O is unstable under illumination, and it can undergo photodegradation in aqueous solutions [21, 22].

Haematite ($\alpha - Fe_2O_3$) is an Earth-abundant semiconductor, that has a bandgap of 2 eV, in the optimal range for solar-light harvesting, and, contrary to Cu_2O, it is photostable, making it an ideal candidate as a photoanode for PEC devices [23, 24, 25]. However, its performance as a water-oxidizing photoanode are drastically limited by the low electron mobility and rapid trapping of the initial photoexcited state: the lifetime of photoexcited carriers in haematite is in the order of picoseconds, too short to drive water oxidation [25]. The discrepancy between the expected and the actual performance has recently been attributed to haematite's small polaron-limited, minority carrier conduction [26, 27].

Finally, wide band gap metal oxide semiconductors (such as CeO_2, TiO_2, ZnO) are stable, but can only absorb in the ultraviolet range, drastically reducing the solar-to-fuel energy conversion efficiency. Different techniques to extend metal oxides photosensitivity have been developed and studied in recent years. These techniques include nanostructuration [28], defect engineering (e.g. bandgap narrowing as proposed in [29]), doping (adding dopants such as Mn, Y, Fe and Sn [30, 31, 32]) and coupling with plasmonic nanoparticles (NPs).

In order to completely understand and then to optimize a photocatalytic material it is crucial to study not only its static properties, but also its dynamics, to properly describe the light-induced excitations. The use of time-resolved spectroscopy, probing time scales from femtoseconds to millisecond, with a spectral range in the UV and visible window, is a powerful tool to study the light-induced charge transfer

processes, to provide precious information for design of novel and optimized materials [33, 34]. The case of the small polaron formation in hematite is a clear example of the relevance of this kind of studies.

1.2 Cuprous oxide

Cuprous oxide (Cu_2O) is a semiconductor characterized by a direct, parity forbidden, band gap of 2.15 eV, that can be tuned by changing the oxidation state of Cu between 2.1 eV (for cuprous oxide) and 1.4 eV (for cupric oxide, CuO). Moreover, Cu_2O excitons, and in particular the 1S ortho- and para-excitons, have unique properties that make this material a perfect candidate for the understanding excitons properties. Moreover, the characteristics of excitons in cuprous oxide seems to make them perfect candidates for the study of Bose-Einstein condensates (BEC) [35, 36, 37, 38, 39]. However, the direct observation of the condensate have always been more difficult than expected. Various explanations have been suggested, such as a possible instability caused by the formation of bi-excitons at the corresponding BEC transition densities [40], or restrictions in the detection of a stable exciton condensate by luminescence spectroscopy [41], that is the conventional method used for the search of exciton BEC [42]. Only very recently, Morita et al. observed the BEC of 1s para-excitons in a bulk crystal of Cu_2O below 400 mK, by directly visualizing the exciton cloud in real space using mid-infrared induced absorption imaging, revealing that the para-exciton condensate is undetectable by conventional luminescence spectroscopy [43].

Excitons are electron-hole pairs bound by their Coulomb attraction and produced by optical excitation of the crystal. In Cu_2O, contrarily to the large part of other semiconductors, excitons have long lifetime due to a forbidden direct band gap, large binding energy due to relatively large electron and hole masses [44], and an electron-hole exchange interaction that inhibits the formation of molecules or electron-hole liquid [45]. Since excitons are a bound state of two fermions, they are expected to obey Bose statistics. The long life of para-excitons[1] in cuprous oxide, together with their relatively large radius and an high binding energy makes them perfect candidates for the study of Bose-Einstein condensate [43, 45, 47, 48]. Moreover, in 2014 the yellow exciton series in Cu_2O was observed by Kazimierczuk et al. up to a large principal quantum number of n = 25 [49]. This discovery has opened up the research field of giant Rydberg excitons and led to a variety of new experimental and theoretical investigations [36, 44, 50, 51, 52, 53, 54].

The interest in copper oxides as semiconducting materials for solar cells dates back to almost one century ago, when in 1926 L. O. Grondahl and P. H. Geiger first worked on a copper-Cu_2O-solar cell [55]. In the 1970s, the development of Cu_2O-based solar cells started, using mainly a metal-Cu_2O junction for the charge separation. However, these devices presented a limited conversion efficiency, lower than 3%, well below the one predicted by the Shockley–Queisser (SQ) limit estimated for Cu_2O (around 20%) [56]. The main problem of these devices, built by combining Cu_2O with a wide variety of metals, is related to the height of the Schottky barrier, in the range of 0.7-0.9 eV independently on the chosen metal. The most probable explanation for the high barrier is that most metals reduce Cu_2O, leading to the formation of a copper-rich region between the Cu_2O and adjacent metal

---

[1]1s excitons in cuprous oxide are distinguished in para- and ortho-excitons, depending on their spin and degeneracy. Para-excitons are the spin-triplet configuration of the 1S ground state exciton with lifetimes in the μs-range [35, 46]

layers, which renders all Schottky-type cuprous oxide solar cells [57]. One of the solutions proposed to solve this problem is the construction of heterojunction solar cells made by the combination of p-type Cu_2O with n-type semiconductors, such as ZnO or GaN [58, 59, 60, 61]. However, the conversion efficiency of these devices is still much lower than the predicted SQ limit. Recently a Cu_2O solar cell with 5.38% conversion efficiency was built using as n-type semiconductor Ga_2O_3 [62]: the improving in efficiency was related to the surface condition of the Cu_2O film before Ga_2O_3 deposition, causing a lower defect density at the interface. This suggests that a better knowledge of the Cu_2O thin films down to the atomic level is fundamental to improve the efficiency of Cu_2O-based solar cells. Other interesting applications of copper oxides can be found in the construction of electronic devices, for high temperature superconductivity [63], spintronics [28], and photocatalytic water splitting [64].

1.2.1 Crystal Structure

Cu_2O, also known as *cuprite*, represents the most stable among the three common copper oxide compounds (together with Cu_4O_3 and CuO). Cuprite crystallises in a cubic Bravais lattice, schematized in figure 1.3, with space group (Pn$\bar{3}$m). The lattice constant has been measured to be a = 4.27 Å, the Cu-O bond length is d_{Cu-O} = 1.85 Å, the O-O is d_{O-O} = 3.68 Å and the Cu-Cu is d_{Cu-Cu} = 3.02 Å [65]. The unit cell is formed by four copper atoms, positioned in a face-centred cubic lattice, and two oxygen atoms at the tetrahedral sites forming a body-centred cubic sub-lattice. The Cu ions are on the vertices of a tetrahedron centered on the oxygen sites and are twofold coordinated with the oxygen ions (D_3d site symmetry), whereas the oxygen ions are fourfold coordinated with Cu ones (T_d site symmetry). Choosing the origin of the coordinate system on an oxygen atom, the Cu ions are in the positions (1/4, 1/4, 1/4), (1/4, 3/4, 3/4), (3/4, 1/4, 3/4) and (3/4, 3/4, 1/4), in unit of lattice constant a.
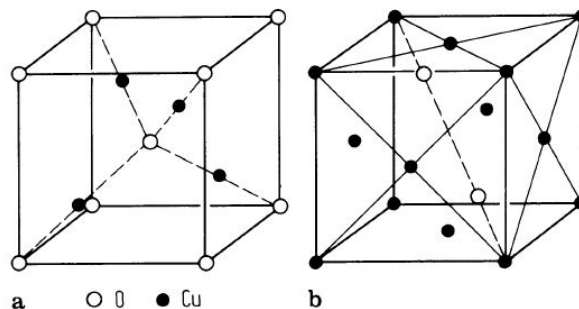
Figure 1.3: *Unit cell of cuprite with: a) origin on a oxygen site; b) origin on a copper site. Dashed lines represent the bonds. Taken from [35]*

1.2.2 Electronic Properties

The electronic Cu configuration is ($[Ar]3d^{10}4s^1$), then the configuration for Cu^+ ions in Cu_2O is ($[Ar]3d^{10}4s^0$), where the Cu $3d$ levels represent the valence band (VB) and the empty Cu $4s$ levels the conduction band (CB) [66], meaning that the CB and the VB have the same parity. As schematized in figure 1.4a, Cu_2O presents a direct, parity forbidden, band gap of 2.15 eV at room temperature (RT) [37] at
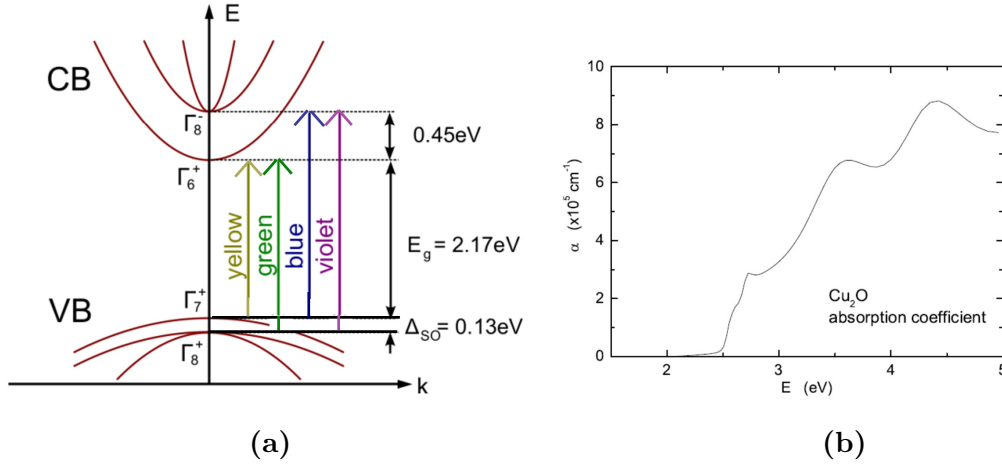
Figure 1.4: *(a) Band structure of Cu_2O near the Γ point [36]. The arrows represent the transitions giving rise to the four exciton series (yellow, green, blue and indigo). (b) Absorption coefficient at RT of Cu_2O [35].*

the center of the Brillouin zone (Γ point). The band gap at 4.2 K, i.e. the energy difference between the Γ_6^+ and the Γ_7^+, obtained as the limit of the yellow exciton series[2], has been measured to be $E_{gap} = 2.172$ eV [67, 68]. As expected, the band gap value decreases with increasing temperature [69].

1.2.3 Optical Properties

Cu_2O is a key material for the developing of excitons theory, providing the first experimental confirmation of the formation of excitons [70]. The absorption coefficient α of Cu_2O at RT is reported in figure 1.4b. A series of exciton-related peaks, particularly evident at low temperature, emerges close to the absorption edge. Cu_2O is characterized by a direct, yet forbidden, optical bandgap, and it starts to absorb light above 2.4 eV, corresponding to the dipole-allowed transition between the higher valence band and the second lower conduction band (see figure 1.4a). The refractive index at RT has been calculated in [71] and is $n \sim 2.7$ at low frequencies and $n \sim 2.6$ at high frequencies.

Excitons

When an electron in a semiconductor is excited in the conduction band, it leaves a hole in the valence band, and the two charged particles will be attracted to each other. This may result in the formation of a bonding between the electron and the hole, forming an *exciton*. The (attractive) exciton binding energy represents an energy state within the band states. Excitonic states have particular relevance at low temperature, at which the recombination probability is lower [72, 73, 74]. Excitons are typically divided into two limiting cases: **Frenkel** and **Wannier–Mott** excitons, depending on the ratio between the exciton radius r_{exc} and the lattice constant a. Frenkel excitons are composed of a tightly bound electron-hole pair and have a radius on the order of the lattice constant or smaller, whereas Mott-Wannier excitons have a much larger radius than the lattice constant, resulting in a weak

---

[2]i.e. the Γ^{6+}-Γ^{7+} transition. The theory of excitons in cuprous oxide will be better expanded in section 1.2.3

bound. In semiconductors, which are generally characterized by a large dielectric constant, electric field screening tends to reduce the Coulomb interaction between electrons and holes, and excitons are typically Mott-Wannier excitons [75]. Since this is also the case for Cu_2O, in this thesis I will focus on this type of excitons.

Wannier–Mott excitons can be described using a hydrogen-like model: being $r_{exc} >> a$, several atoms sit inside the exciton orbit, and the lattice can be approximated as a medium with permettivity ϵ_r, in which the electrons and the holes exist as free particles with effective masses m_e and m_h. According to this model, some relevant quantities to describe excitons are listed below (being $m_{r,H} \approx m_e$ the reduced mass of the hydrogen atom, $R_y \approx 13.6$ eV the Rydberg constant, $a_B \approx 0.53$ Å the Bohr radius, and n an integer number describing the various energetic levels) [35]:

$$m_x = m_e + m_h \text{ , Exciton mass} \tag{1.1a}$$

$$m_{r,x} = \Big(\frac{1}{m_e} + \frac{1}{m_h}\Big)^{-1} \text{ , Exciton reduced mass} \tag{1.1b}$$

$$R_{y,x} = \frac{m_{r,x}}{m_{r,H}} \cdot \frac{1}{(\epsilon_r)^2} \cdot R_y \text{ , Excitonic Rydberg constant} \tag{1.1c}$$

$$r_x = n^2 \cdot \epsilon_r \cdot \frac{m_{r,H}}{m_{r,x}} \cdot a_B \text{ , Exciton radius} \tag{1.1d}$$

$$E_{B,x} = \frac{R_{y,x}}{n^2} \text{ , Exciton binding energy} \tag{1.1e}$$

The peaks that appear in the absorption spectrum of cuprite shown in figure 1.5a are due to the resonant absorption of photons that form excitons inside the material (this is valid in general for all direct band-gap semiconductors). In Cu_2O, four hydrogenic excitonic series can be found: yellow, green, blue, indigo, in order of increasing energy (schematized also in figure 1.4b and highlited in figure 1.5a). The resonating energies follow the relation:

$$E(n) = E_{GAP} - \frac{R_{y,x}}{n^2} = E_{GAP} - E_{B,x} \tag{1.2}$$

where E_{GAP} corresponds to the energy difference between the bands occupied respectively by the electron and the hole forming the exciton. As is evident from the schematics in figure 1.4a, the yellow series is generated by the absorption of electron-hole pairs across Γ_7^+ and Γ_6^+, the green series in Γ_8^+ and Γ_6^+, the blue series in Γ_7^+ and Γ_8^- and the indigo series in Γ_8^+ and Γ_8^-.

In Cu_2O, a very large number of replicas are visible (figure 1.5b shows the yellow excitonic series). In the yellow and green excitonic series, the n = 1 lines do not follow the relation 1.2, because these excitons have a much smaller radius compared to the others, compatible with the Bohr radius, and therefore the plane wave approximation is no longer valid to describe the electron and hole wave function. Moreover, these lines, corresponding to the ground state $1s$ excitons, are splitted by the exchange interaction into a singlet and a triplet. The first one is called para-exciton, and it is characterized by a total angular momentum J = 0 and the second one is an ortho-exciton, with angular momentum J = 1. For the 1s exciton state the ortho-para-exciton energy splitting is 12 meV [39, 77]. Focusing on the yellow exciton series (electrons in the lowest conduction band Γ_6^+ and holes in the

(a)

(b)
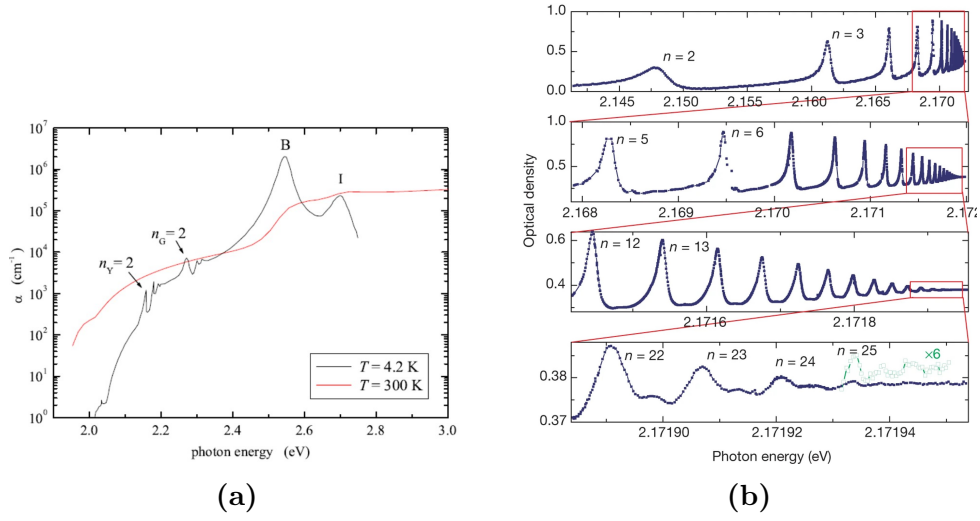
Figure 1.5: *(a) Absorption coefficient of Cu_2O at 4.2K (black line). For comparison, the absorption coefficient at 300K, the same as in figure 1.4b, is also reported (red line). The two curves can not be directly compared because of the shift of the energy gap with temperature [35, 76]. (b) Spectra measured at 1.2 K. The peaks correspond to resonances with different principal quantum number n. The panels below show close-ups of the areas marked by rectangles in each panel above [49].*
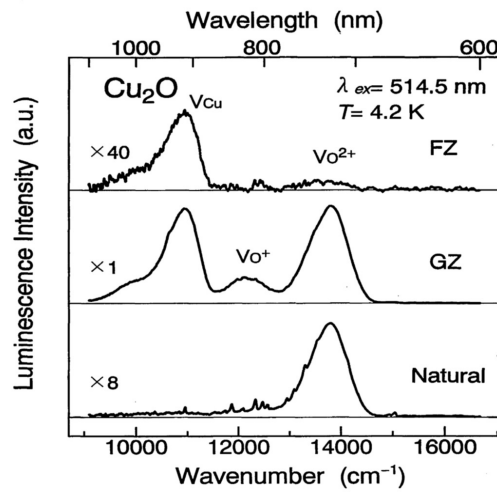
Figure 1.6: *PL spectra of Cu_2O due to vacancy recombination centers at 4.2 K [69].*

highest valence band Γ_7^+), the exchange interaction splits the $n = 1$ level into a Γ_{25}^+ triply degenerate ortho-exciton and a Γ_2^+ singly degenerate para-exciton. These two states yield several luminescence lines, related either to direct or phonon-assisted recombination luminescence [35]. Transitions between levels are only allowed when $\Delta J = \pm 1$ for one photon processes: this implies that the decay from any para-exciton state to the ground state is forbidden for all orders of perturbation and consequently that para-excitons are very long living: their lifetime is limited by the defects and impurities [35, 78]. For 1s ortho-excitons, the decay to the ground state is only quadrupole allowed. The lifetime of 1s ortho-excitons is mainly limited by transition to the lower lying para-exciton state [79]. Since radiative recombination is forbidden to all orders for the para-excitons and at first order for ortho-excitons, and since their binding energies are quite high, it is possible to observe Cu_2O excitons also at RT, for example in photoluminescence (PL) spectra [35, 36, 46]. At low temperatures, ortho-exciton lifetimes are limited by the conversion in para-exciton while the para-exciton lifetime is strongly dependent on the stoichiometry of the sample, in particular on the copper and oxygen vacancy concentration, ranging from tens of ns up to some ms [80]. The luminescence spectra of Cu_2O are expected to show a high spatial variability, depending on the stoichiometry of the examined spot. In particular, the luminescence bands in the infrared region are related to different activation centers, as shown in figure 1.6. In the PL spectrum, there are three particularly relevant bands: the band around 910 nm is related to exciton recombination caused by copper vacancies (V_{Cu}), and the bands around 720 and 820 nm are related to oxygen vacancies, respectively V_O^{2+} and V_O^+ [69]. In this thesis, I will describe the results obtained by Scanning Tunneling Microscopy (STM) and PL experiments to understand the excitons recombination behavior in thin and thick films of as-grown Cu_2O.

1.2.4   Oxidation of Cu thin films and NPs

The oxidation of Cu thin films has been extensively studied by N. Niklas and his group. From their previous studies on this material, we already knew the importance of the temperature and pressure conditions on the oxidation state and crystalline structure of cuprous oxide. In [81] and [82] they observed the temperature dependent oxidation of Cu thin films on Au(111) and Pt(111) substrates respectively. With increasing annealing temperature, in the first case they have observed the formation of a Cu_3O_2 monolayer with honeycomb structure, while in the second case they have observed the tendency of Cu to form Cu-Pt alloys. However, coherently with a large number of previous studies on the oxidation of Cu thin films which have shown that the low-pressure oxidation of Cu is inefficient to grow oxide films of more than monolayer thickness [83, 84, 85], they could never obtain bulk-like Cu_2O oxide layers. Finally, in [82] they have found the optimal a reliable pathway to produce bulk-like Cu_2O thin films, by exposing Cu layers to high oxygen pressures ($P_{O_2} = 50$ mbar) by using the procedure that will be described in the chapter 7.

Studies on the effects of oxygen on the optical properties of Cu NPs have demonstrated the strong impact of the formation of copper oxides on the position and shape of the plasmonic band of the NPs [86, 87, 88, 89, 90, 91]. In particular, the systematic study by Susman et al. [91] performed on *real-time* oxidation of Cu NPs, shown that the LSPR band red-shifts continuously with oxidation, while the absorption intensity increases until a maximum value at a characteristic time τ, after which the signal intensity continuously drops. They have observed that the oxidation mecha-
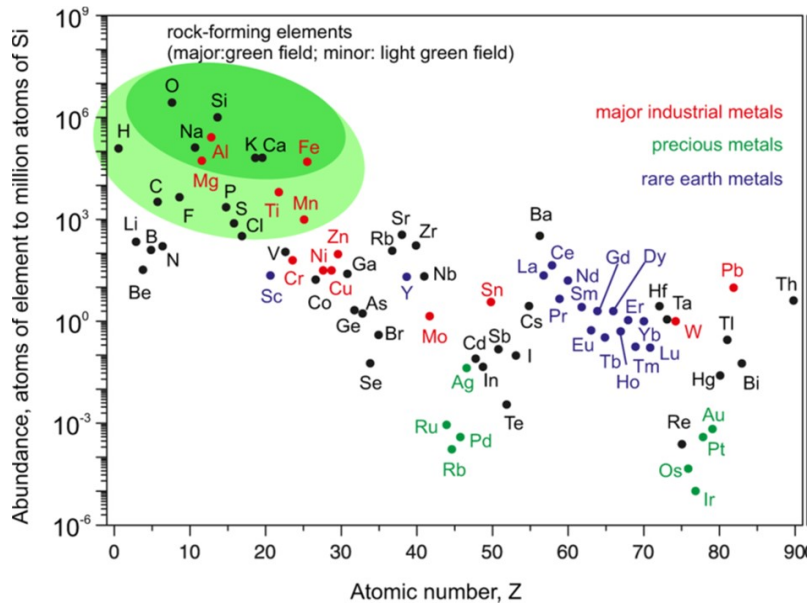
Figure 1.7: *Relative abundance of elements in Earth's upper continental crust in function of the atomic number. Rare earth elements are in blue [94].*

nism of Cu NPs depends on the metal-to-oxide conversion fraction, changing with the development of the oxide shell. They have confirmed the trend observed for the LSPR signal with theoretical calculations based upon Mie theory, and they have assigned the continuous red-shift of the LSPR band to the formation of internal voids at advanced stages of the oxidation, observed by TEM imaging.

1.3 Cerium Oxide

Cerium oxide is one of the most promising materials for catalytic applications, thanks to its unique ability of storing and releasing oxygen atoms. The reason behind this ability is the particular band structure of cerium, where only one electron occupies the localized $4f$ orbital. Cerium (Ce) is the second element in the lanthanide series, with atomic number 58. The lanthanide series is characterized by the filling of the 4f electron shell. In general, these elements are called rare earths, although their abundance is larger than other elements on Earth (figure 1.7). The interesting characteristic of these elements is the occupation of the $4f$ orbitals, shielded from the atom's environment by the $4d$ and $5p$ electrons, that gives to lanthanides unique catalytic, magnetic and electronic properties [92, 93]. Among all elements of the Earth, cerium is the 26th most abundant one, approximately 0.0046 wt % of the crust of the Earth [95]. Being the second element in the lanthanide series, Ce hosts only one electron in the $4f$ orbital, and the electronic configuration is ([Xe] $4f^15d^16s^2$). In the oxide, Ce^{4+} state is preferentially formed, but in nature a significant concentration of intrinsic defects is always present, with Ce in the Ce^{3+} valence state [96, 97]. In fact, because of the relatively low fourth ionization potential, Ce can form oxides in both the tetravalent (as Ce^{4+}) and trivalent (as Ce^{3+}) states. This gives cerium oxide the ability to store, release, and transport oxygen ions. Indeed, Ce^{4+} ions can release one oxygen atom in a reducing environment, turning into Ce^{3+} state. This process is easily reversible in oxidizing conditions. Cerium dioxide is a n-type semiconductor, characterized by a wide band gap in the UV range. Different values have been proposed for the precise optical gap of cerium

20
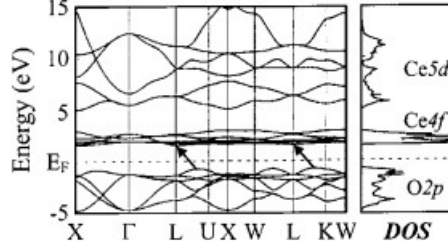
Figure 1.8: *Band structure and the density of states for pure CeO₂. Taken from [101].*

oxide depending on the defectivity of the material [98, 99], recently Pelli Cresi et al. have measured a value of 4 eV for highly stoichiometric films [100].

Figure 1.8 shows the calculated band structure and the density of states (DOS) for pure CeO_2. The arrows indicate the indirect transitions, which correspond to the fundamental gap of CeO_2 and the nanostructured CeO_x films. Note that the O2p→Ce4f transition ($\sim 4eV$), characteristic of CeO_2, should be forbidden because it violates the angular momentum selection rule ($\Delta l = 0, \pm 1$, where l is the angular momentum quantum number). However, this transition is manifested in all spectra of CeO_2 in the literature, because the highest occupied valence band (O2p band) is not exclusively due to O2p electrons, but it also contains a contribution from Ce4d electrons, providing a partial d character. Therefore, the electronic transition at 4 eV is only nominally a O2p→Ce4f transition, but it has actually a strong d →f, i.e. Ce4d→Ce4f character, which fulfills the selection rules [101].

1.3.1 Crystal structure

CeO_2, also known as *ceria* is characterized by a cubic fluorite-type structure (space group $Fm\overline{3}m$), with cerium and oxygen ions located at the $4a$ 0,0,0 and $8c$ 1/4,1/4,1/4 sites, respectively (1.9a). Ce cations are surrounded by 8 oxygen anions (coordination number, CN=8), while oxygen ions have CN=4 and the structure consists of OCe_4 tetrahedra (figure 1.9b). The crystal structure consists of CeO_8 cubes, as represented in figure 1.9c. The unit-cell parameter of ceria, a=5.41 Å at RT), together with both Ce and O displacement parameters (B(Ce) and B(O) respectively), increases with temperature. The increase of B(O) is larger compared to B(Ce), suggesting that O anions are more mobile than Ce cations in CeO_2 [102, 103].

| (a) *Crystal structure of the cubic fluorite-type ceria CeO_2* | (b) *Crystal structure of ceria with OCe_4 tetrahedra.* | (c) *Crystal structure of ceria with CeO_8 cubes.* |
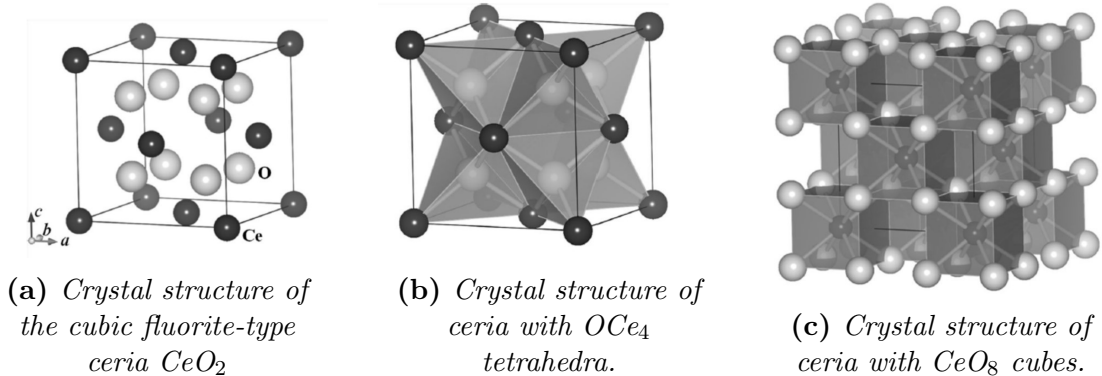
Figure 1.9: *Sketches of the CeO₂ structure in which different structural units are evidenced. Taken from [102]*
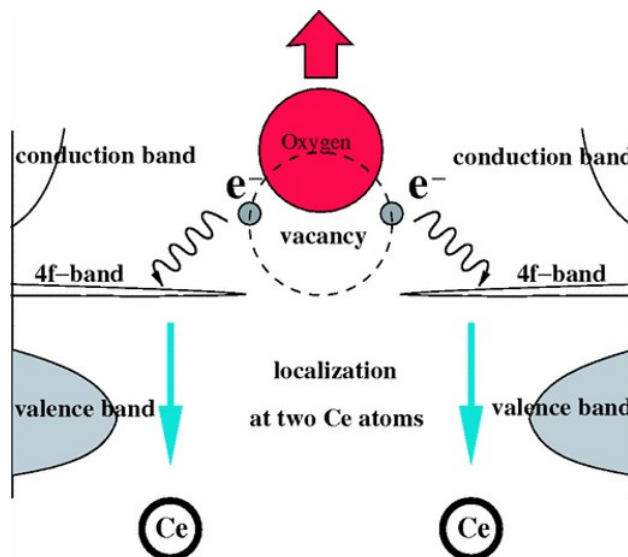
Figure 1.10: *The process of oxygen-vacancy formation in ceria [109].*

The thermodinamically most stable surface is the CeO_2(111)-oriented one, followed by (110) and (100). The (111) surface is characterized by a hexagonal symmetric atomic arrangement, with surface lattice parameter equal to 3.83 Å. It is non-polar, and terminates by three-fold coordinated O atoms and seven-fold coordinated cerium atoms [102]. The trilayer unit O-Ce-O is repeated along the direction normal to the (111) plane: a CeO_2(111) monolayer (ML), defined by the thickness of the trilayer unit, measures 3.12 Å [104, 105, 106, 107].

1.3.2 Electronic Structure

As already mentioned, the most interesting property of ceria for catalytic applications is its oxygen storage capacity (i.e. the ability to store, transport and release oxygen), related to the easy switch between the Ce^{3+} and Ce^{4+} states of Ce ions in cerium oxide. The two ionic configurations differ from the occupation of the 4f levels: they are empty in the Ce^{4+} [Xe] configuration and are occupied by one electron in the Ce^{3+} $[Xe]4f^1$ configuration. The process of oxygen-vacancy formation in ceria is schematized in figure 1.10. Starting from the stoichiometric CeO_2, where only Ce^{4+} ions are present, the removal of an oxygen atom from the lattice causes the reduction of two cerium ions, which turn from the Ce^{4+} to the Ce^{3+} state to neutralize the excess of charge caused by the O vacancy. The excess electrons occupy split-off states of the initially empty Ce 4f band, buried within the ceria band gap, between the O 2p and Ce 5d levels, highly localized in space. Recent studies which combine experimental evidences with *ab-initio* calculations demonstrated that at least one electron localizes in a Ce ion that is not adjacent to the O vacancy [108].

1.3.3 Applications

The high oxygen storage capacity of cerium oxide, together with its nontoxicity and relative abundance, makes it a unique material for catalytic applications, both as an active component and as a support for catalytically relevant metals. Ceria-based materials are attractive in a wide variety of fields, including energy, environmental protection, and healthcare applications. Moreover, the activity of cerium oxide increases when combined with other reducible oxides or with metallic structures

[102, 110, 111]. One of the most established and common applications of ceria is in the automotive field where it is used as a Three Way Catalyst (TWC), acting as oxygen buffer, to remove the pollutant produced by the combustion of gasoline. TWCs are used for the simultaneous oxidation of CO and unburnt hydrocarbons and the reduction of nitrogen oxides (NO_x), that are converted into harmless CO_2, H_2O and N_2 [94].

Another very promising application of ceria is in fuel cells, devices able to directly convert chemical energy into electricity by the inverse reaction of the electrolysis of water. One of the most promising systems is the so-called *proton exchange membrane fuel cells* (PEMFC). The major drawback of these devices is that they are based on very expensive Pt-containing materials as catalysts, making them problematic for large-scale commercialization. In order to increase the cost-efficiency in PEMFCs, it is possible to use as anode catalyst a thin films of ceria with low Pt loading, to decrease the overall cost of the devices [112]. In solid oxide fuel cells, ceria can also be used as anodes [113] or for coating cathodes [114].

Ceria can also be used, in combination with metals, for the water-gas shift reaction (WGS) ($CO + H_2O \rightarrow CO_2 + H_2$), fundamental to obtain clean hydrogen from CO and H_2O for industrial applications. Ceria, in combination with metals such as Au, Pt, Cu, induces higher catalytic activity and lower operating temperature in WGS reactions [115, 116, 117, 118].

Also dealing with clean energy applications, cerium oxide is a promising material in applications in the field on catalysis for solar fuels [119, 120, 121]. Furthermore, as will be better described in the next section, ceria, coupled with plasmonic nanostructures, can be sensitized to visible radiation for solar light harvesting.

Finally, it worth mentioning the recently developed applications of ceria in the field of healthcare, in particular for medical applications [122], or as support for stem cells cultures [123].

1.4 Plasmonic enhancement of metal oxide photocatalytic properties

The research in the field of photocatalytic materials that are capable of converting solar radiation into chemical energy by direct water splitting or by CO_2 reduction has tremendously increased in recent years [2]. As mentioned in section 1.1.1, one efficient way to extend the photocatalytic activity of wide band gap metal oxide semiconductors is the formation of heterojunctions by coupling plasmonic nanostructures with semiconductors [19]. One of the main topics of this thesis will be the coupling of CeO_2 thin films with NPs of different materials, in particular Au, Ag, and Cu NPs, mainly focusing on the ultrafast dynamics of these coupled systems.

Noble metal NPs are characterized by a very large cross section for the absorption and scattering of visible light. Plasmonic NPs have also been considered alone as candidates for photocatalysis, due to their surface catalytic properties and the strong and tunable light-matter interactions [126]. However, direct plasmonic photocatalysis is not convenient, because of the short lifetimes of charge carriers and the fast quenching of electronically excited adsorbates on metal surfaces [127, 128]. The combination of plasmonic NPs with wide band gap and stable metal oxides allows to overcome the intrinsic limitations in each material. The formation of a heterojunction between NPs and metal oxides facilitates light trapping and the excitation of charge carriers, and it may lead to a charge or energy transfer from the metal to the
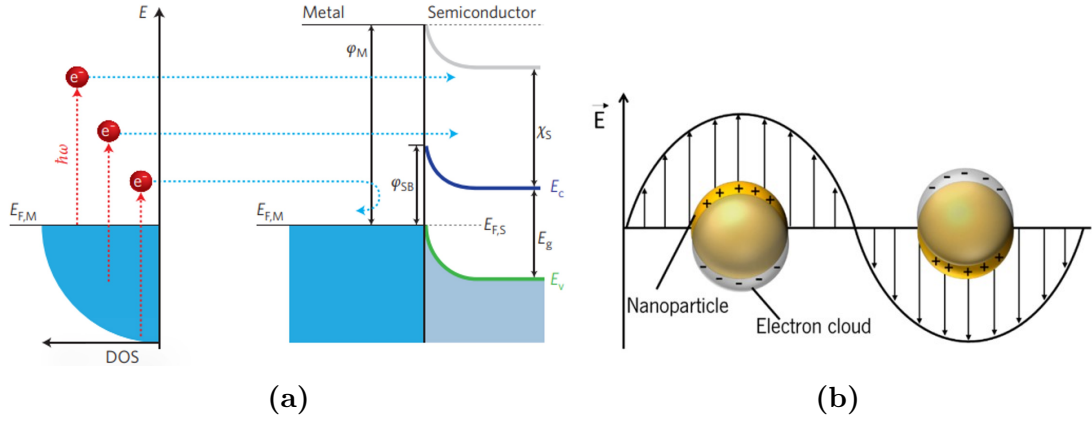
Figure 1.11: *(a) In the right scheme, electrons from occupied energy levels are excited above the Fermi energy ($E_{F,M}$) in the plasmonic NPs. The left panel shows the Schottky barrier ($\phi_{S,B} = \phi_M - \chi_S$) between the NP and the semiconductor. Hot electrons are injected into the conduction band (E_c) of the semiconductor (ϕ_M is the work function of the metal and χ_S is the electron affinity of the semiconductor [124]. (b) Schematic mechanism of LSPR: EM-field-induced coherent localized oscillation of the electron cloud [125].*

semiconductor. Moreover, the presence of a Schottky barrier prevents the electrons to travel back to the NPs, impeding fast charges recombination (as schematized in figure 1.11a). The main goal now is to find the most convenient systems that maximize the solar light photocatalytic activity with an optimized density of long-living excited states.

In systems composed of plasmonic NPs combined with metal oxides, the interaction of the metallic nanostructures with visible radiation triggers the so-called *Localized Surface Plasmon Resonances*, LSPRs. This is an optical phenomenon generated by the coupling between light waves and metallic NPs smaller than the wavelength of light. LSPR is basically the resonant collective oscillation of electrons, established when the frequency of photons matches the natural frequency of surface electrons oscillating against the restoring force of positive nuclei (schematized in figure 1.11b) [129].The resonant frequency of these oscillations is strongly influenced by different important factors, such as the material, size and geometry of the NPs, their dielectric environment and the distance between the NPs [130, 131] (an example of the dependence of the LSPR frequency on the NPs characteristic is reported in figure 1.12, taken from [131]). In general, in noble metal NPs as Au, Ag and Cu, LSPRs are triggered by visible photons, making these materials particularly appealing for solar light harvesting. At the LSPR frequency, the NPs exhibit a strong increase of light scattering and absorption. The lifetime of coherent electron oscillations due to plasmon excitation is below 100 fs, then the LSPR relaxes either by a radiative damping (dominant for structure larger than 50 nm), or non-radiatively by Landau damping, generating an electron-hole pair, or by interaction of excited surface plasmons with unpopulated adsorbate acceptor states [132, 133]. A large number of different studies have shown that the combination of plasmonic NPs with metal oxides leads to a charge transfer from the metal to the semiconductor, making these complex systems suitable for solar light absorption [19, 134, 135, 136, 137, 138]. In noble metal NPs, with LSPR in the ultraviolet-visible (UV-Vis) range, solar energy can be converted into a large amount of plasmonic energy. However, as already mentioned, the short lifetime of excited charge carriers makes plasmonic NPs alone bad candidates for photocatalytic applications. On the other hand, a well-designed plas-

24
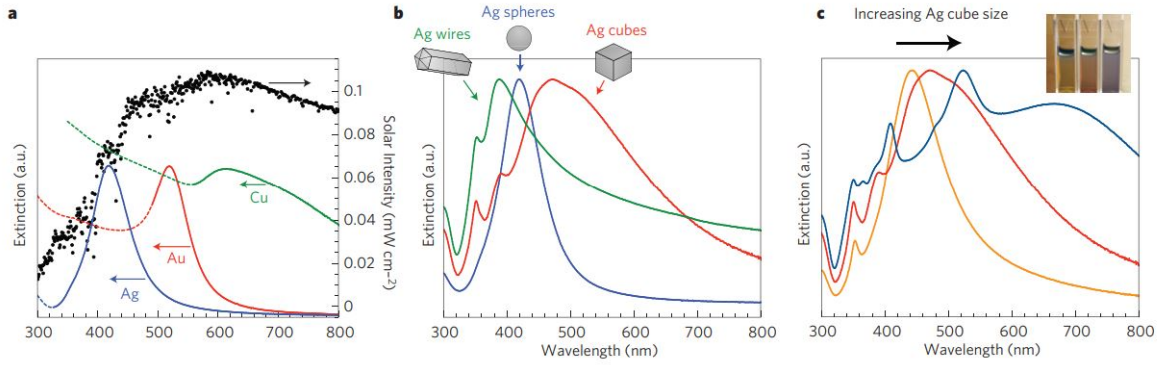
Figure 1.12: *Normalized extinction spectra of: (a) spherical Ag, Au and Cu NPs. The black line shows the intensity of solar radiation. The metal extinction is a consequence of the excitation of LSPR, while the dashed portions of the curves indicate interband transitions, (b) Ag NPs of different shapes, (c) Ag nanocubes of different sizes: the inset shows a photograph of the three samples suspended in ethanol [131].*

monic metal–semiconductor heterojunction can bring to a high energy-conversion efficiency. In these systems, the plasmonic material acts as a light antenna, transferring energy to the semiconductor and enhancing its photocatalytic activity both above and below the band gap [139].

Different mechanisms have been proposed for the photoactivity enhancement of the semiconductor when combined with plasmonic NPs. The dominant ones, schematized in figure 1.13, are light trapping, hot electron injection and direct electron transfer [19, 134, 135]:

- **light trapping**: Because of the large scattering cross section of the NPs, incident light can be scattered by the NPs increasing the photon flux in the semiconductor. This can lead to the enhancement of an optical transition within the semiconductor (above the band gap). This mechanism is dominant for NPs larger than 50 nm, and is relevant for semiconductors with a narrow bandgap;

- **hot electron injection**: electrons are generated in the NPs, either by interband transitions or by the relaxation of the LSPR by Landau damping. The hot electrons, i.e. the electrons that have an energy higher than the Schottky barrier at the metal–semiconductor interface (see figure 1.11a), can be injected into the conduction band of the semiconductor;

- **direct electron transfer**: after the interaction with visible radiation, the ultrafast relaxation of LSPR directly excites electrons into empty states in the conduction band of the semiconductor, leaving holes in the metal.

The weight and efficiency of the different mechanisms depend upon different factors related to the NPs (e.g. their size, shape, material, and distribution), the semiconductor (e.g. its composition, dielectric properties, and band structure), and the morphology of the interface (in particular, the height of the Schottky barrier).

To better understand the charge transfer mechanism, it is fundamental to study the dynamics of the system, especially in the first tens of fs after the interaction with visible radiation. Several works have already focused on the dynamics of the different processes that involve LSPR formation and relaxation and the consequent charge transfer to a surrounding semiconductor [19, 127, 134, 135, 137, 140, 141].
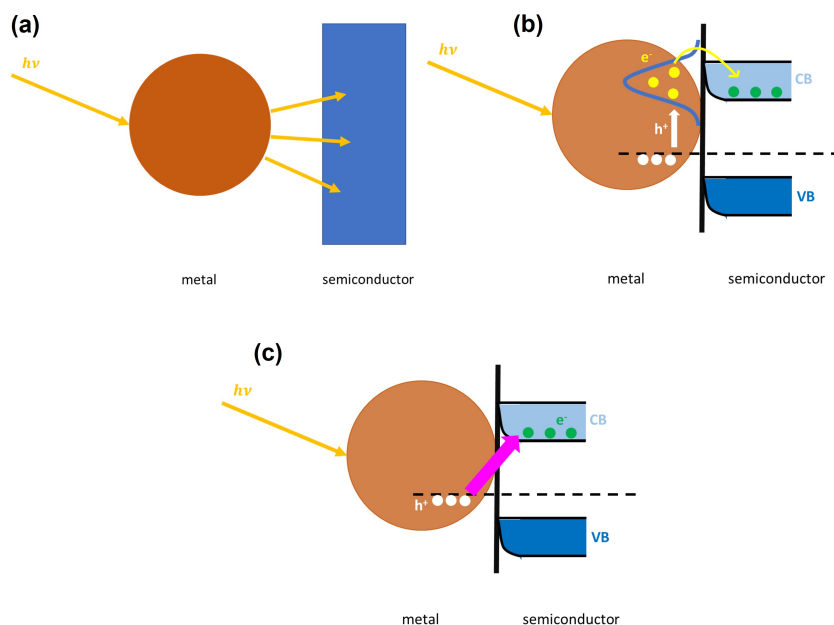
Figure 1.13: *The three main mechanisms of energy transfer from a metallic NP to a semiconductor after LSPR relaxation: (a) light trapping, (b) hot electron injection and (c) direct electron transfer.*

Figure 1.14 indicates the time-scales of the plasmon-induced hot carrier generation, hot electron transfer, and thermalization processes with/without a semiconductor surrounding the NPs (adapted from [142]). After the excitation of LSPR in clean metals, the coherent oscillation of electrons dephases non-radiatively, generating hot carriers in very short times after the interaction with light $(1 - 100$ fs). The hot electrons and holes generated are initially in a non-thermal distribution, and they thermalizes to a Fermi-Dirac distribution via electron-electron $(100$ fs -1 ps) and electron-phonon $(1 - 10$ ps) scattering, increasing the lattice temperature. Finally, this heat slowly dissipates to the environment $(100$ ps -10 ns) [143]. In the presence of a surrounding semiconductor with an electron-accepting orbital, electrons can be transferred from the NP to the semiconductor. As already mentioned, the two mechanism that dominate the charge transfer are the (indirect) hot electron transfer and the direct electron transfer. Direct transfer can be thought of as a single-step process and requires shorter times $(\sim 20 - 100$ fs) than indirect transfer, which requires the formation of hot electrons and the consequent injection.

As already mentioned, two of the main factors that strongly influences the charge generation and injection efficiency are the material and the geometry that characterize the NPs. Moreover, different materials have different properties, with advantages and disadvantages for large scale applications. In this thesis, I will focus on the combination between CeO_2 with Au, Ag, and Cu NPs and on the properties of Cu_2O and metallic Cu NPs. All the listed metals are noble metals with an LSPR frequency in the visible range: this makes them good candidates for combination with oxides for solar light photocatalysis. In the work by Liu et al. [144], they have tested different plasmonic materials from the point of view of the generation of hot electrons (HEs). Figure 1.15 schematizes their main results on the generation of HEs for different structures and materials. In their work, they have studied the HE generation efficiency of nanocubes of different plasmonic materials, either deposited on a glass substrate or forming a metastructure together with a continuous Au layer and an alumina spacer, proving this latter system to be more efficent in HE generation.

26
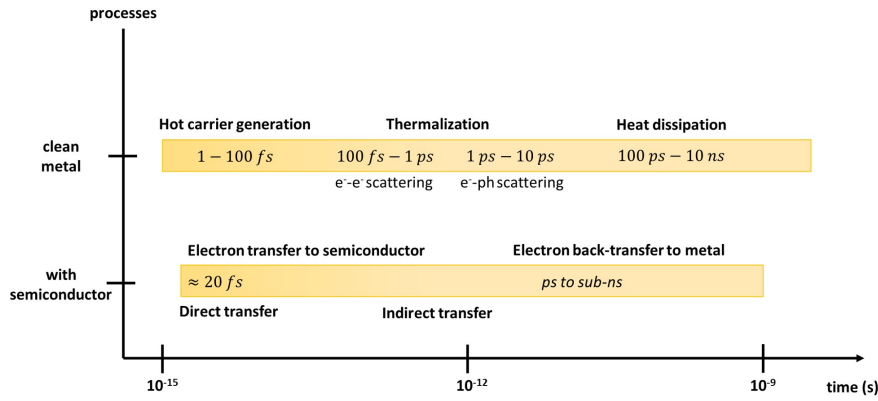
Figure 1.14: *Time scales of plasmon-induced hot carrier generation, hot electron transfer, and thermalization processes in a clean metal NP (top) and in a NP combined with a semiconductor support via a Schottky contact. Adapted from [142].*
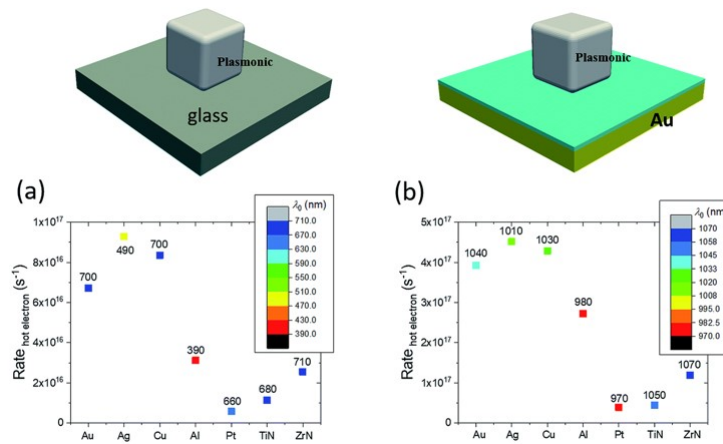
Figure 1.15: *Rates of HE generation at the peaks (the position λ_0 of the peaks of the different materials in the different geometries are indicated by the color-scale) for different structures and materials: (a) deposited on a glass substrate and (b) forming a metastructure together with a continuous Au layer and an alumina spacer [144].*

Ag is one of the most studied materials for NPs in combination with oxide structures such as TiO_2 and CeO_2. It presents the highest rate of hot electron generation among all the materials presented (see figure 1.15 and [144]), but it is a critical and expensive material. Moreover, it is unstable under atmosphere conditions because of its reactivity to oxygen, and it needs to be protected for applications in ambient conditions. On the other hand, Au is very stable in air, being inert to oxygen: this makes this noble metal suitable for in-air applications, even without a protecting capping. Moreover, also Au is very efficient in hot electrons generation [144]. The main drawback of using Au to extend the photocatalytic activity of oxides is that Au is one of the most critical and expensive materials, that makes its use problematic for large scale applications. Finally, Cu is cheaper than both Au and Ag. Moreover, as already mentioned, Cu oxides also present very interesting catalytic properties, and it is possible to create systems composed by a metallic core and an oxide shell for solar light photocatalysis. On the other hand, the strong reactivity of Cu to oxygen can also represent a problem for plasmonic applications: the oxidation of copper strongly alters the plasmonic properties of Cu.

Bibliography

[1] Aleksandra B. Djurišić, Yu Hang Leung, and Alan Man Ching Ng. Strategies for improving the efficiency of semiconductor metal oxide photocatalysis. *Materials Horizons*, 1(4):400, 2014.

[2] Michael G. Walter, Emily L. Warren, James R. McKone, Shannon W. Boettcher, Qixi Mi, Elizabeth A. Santori, and Nathan S. Lewis. Solar water splitting cells. *Chemical Reviews*, 110(11):6446–6473, 2010. PMID: 21062097.

[3] Akihiko Kudo and Yugo Miseki. Heterogeneous photocatalyst materials for water splitting. *Chem. Soc. Rev.*, 38:253–278, 2009.

[4] Takashi Hisatomi, Jun Kubota, and Kazunari Domen. Recent advances in semiconductors for photocatalytic and photoelectrochemical water splitting. *Chem. Soc. Rev.*, 43:7520–7535, 2014.

[5] Nianqiang Wu. Plasmonic metal–semiconductor photocatalysts and photo-electrochemical cells: a review. *Nanoscale*, 10:2679–2696, 2018.

[6] Babatunde A. Koiki, Benjamin O. Orimolade, Gbenga M. Peleyeju, and Omotayo A. Arotiba. Rapid and template-free synthesis of copper(I) oxide-graphitic carbon nitride heterojunction for photocatalytic degradation of orange II dye in water. *Solid State Sciences*, 97:105994, 2019.

[7] Martin I. Hoffert, Ken Caldeira, Gregory Benford, David R. Criswell, Christopher Green, Howard Herzog, Atul K. Jain, Haroon S. Kheshgi, Klaus S. Lackner, John S. Lewis, H. Douglas Lightfoot, Wallace Manheimer, John C. Mankins, Michael E. Mauel, L. John Perkins, Michael E. Schlesinger, Tyler Volk, and Tom M. L. Wigley. Advanced technology paths to global climate stability: Energy for a greenhouse planet. *Science*, 298(5595):981–987, November 2002.

[8] Jieyang Jia, Linsey C. Seitz, Jesse D. Benck, Yijie Huo, Yusi Chen, Jia Wei Desmond Ng, Taner Bilir, James S. Harris, and Thomas F. Jaramillo. Solar water splitting by photovoltaic-electrolysis with a solar-to-hydrogen efficiency over 30%. *Nature Communications*, 7(1), October 2016.

[9] Nathan S. Lewis. Toward cost-effective solar energy use. *Science*, 315(5813):798–801, February 2007.

[10] Tasneem Abbasi and S.A. Abbasi. 'renewable' hydrogen: Prospects and challenges. *Renewable and Sustainable Energy Reviews*, 15(6):3034–3040, August 2011.

[11] J NOWOTNY, C SORRELL, L SHEPPARD, and T BAK. Solar-hydrogen: Environmentally safe fuel for the future. *International Journal of Hydrogen Energy*, 30(5):521–544, April 2005.

[12] Mustafa Balat. Potential importance of hydrogen as a future solution to environmental and transportation problems. *International Journal of Hydrogen Energy*, 33(15):4013–4029, August 2008.

[13] Rishika Chakraborty, Mukul Pradhan, and Kishore Debnath. Band-gap engineering using metal-semiconductor interfaces for photocatalysis and supercapacitor application. In *Interfaces in Particle and Fibre Reinforced Composites*, pages 391–451. Elsevier, 2020.

[14] Si Yin Tee, Khin Yin Win, Wee Siang Teo, Leng-Duei Koh, Shuhua Liu, Choon Peng Teng, and Ming-Yong Han. Recent progress in energy-driven water splitting. *Advanced Science*, 4(5):1600337, January 2017.

[15] Kazuhiko Maeda and Kazunari Domen. Photocatalytic water splitting: Recent progress and future challenges. *The Journal of Physical Chemistry Letters*, 1(18):2655–2661, August 2010.

[16] Hanan H. Mohamed. Green processes and sustainable materials for renewable energy production via water splitting. In *Sustainable Materials and Green Processing for Energy Conversion*, pages 169–212. Elsevier, 2022.

[17] Akihiko Kudo. Photocatalysis and solar hydrogen production. *Pure and Applied Chemistry*, 79(11):1917–1927, January 2007.

[18] Ming Kong, Yuanzhi Li, Xiong Chen, Tingting Tian, Pengfei Fang, Feng Zheng, and Xiujian Zhao. Tuning the relative concentration ratio of bulk defects to surface defects in TiO_2 nanocrystals leads to high photocatalytic efficiency. *Journal of the American Chemical Society*, 133(41):16414–16417, September 2011.

[19] Nianqiang Wu. Plasmonic metal–semiconductor photocatalysts and photoelectrochemical cells: a review. *Nanoscale*, 10:2679–2696, 2018.

[20] Steven Y. Reece, Jonathan A. Hamel, Kimberly Sung, Thomas D. Jarvi, Arthur J. Esswein, Joep J. H. Pijpers, and Daniel G. Nocera. Wireless solar water splitting using silicon-based semiconductors and earth-abundant catalysts. *Science*, 334(6056):645–648, 2011.

[21] Michikazu Hara, Takeshi Kondo, Mutsuko Komoda, Sigeru Ikeda, Junko N. Kondo, Kazunari Domen, Michikazu Hara, Kiyoaki Shinohara, and Akira Tanaka. Cu_2O as a photocatalyst for overall water splitting under visible light irradiation. *Chemical Communications*, (3):357–358, 1998.

[22] Gang Wang, Roy van den Berg, Celso de Mello Donega, Krijn P. de Jong, and Petra E. de Jongh. Silica-supported Cu_2O nanoparticles with tunable size for sustainable hydrogen generation. *Applied Catalysis B: Environmental*, 192:199–207, September 2016.

[23] Andebet Gedamu Tamirat, John Rick, Amare Aregahegn Dubale, Wei-Nien Su, and Bing-Joe Hwang. Using hematite for photoelectrochemical water splitting: a review of current progress and challenges. *Nanoscale Horizons*, 1(4):243–267, 2016.

[24] Kevin Sivula, Florian Le Formal, and Michael Grätzel. Solar water splitting: Progress using hematite (α-fe2o3) photoelectrodes. *ChemSusChem*, 4(4):432–449, March 2011.

[25] Lucas M. Carneiro, Scott K. Cushing, Chong Liu, Yude Su, Peidong Yang, A. Paul Alivisatos, and Stephen R. Leone. Excitation-wavelength-dependent small polaron trapping of photoexcited carriers in α-fe2o3. *Nature Materials*, 16(8):819–825, July 2017.

[26] Alexander J. E. Rettie, William D. Chemelewski, David Emin, and C. Buddie Mullins. Unravelling small-polaron transport in metal oxide photoelectrodes. *The Journal of Physical Chemistry Letters*, 7(3):471–479, January 2016.

[27] Stephanie R Pendlebury, Xiuli Wang, Florian Le Formal, Maurin Cornuz, Andreas Kafizas, S. David Tilley, Michael Grätzel, and James R Durrant. Ultrafast charge carrier recombination and trapping in hematite photoanodes under applied bias. *Journal of the American Chemical Society*, 136(28):9854–9857, July 2014.

[28] Hao-Bo Li, Weichao Wang, Xinjian Xie, Yahui Cheng, Zhaofu Zhang, Hong Dong, Rongkun Zheng, Wei-Hua Wang, Feng Lu, and Hui Liu. Electronic structure and ferromagnetism modulation in Cu/Cu_2O interface: Impact of interfacial Cu vacancy and its diffusion. *Scientific Reports*, 5, 2015.

[29] Mohammad Mansoob Khan, Sajid Ali Ansari, Debabrata Pradhan, Do Hung Han, Jintae Lee, and Moo Hwan Cho. Defect-induced band gap narrowed CeO_2 nanostructures for visible light activities. *Industrial & Engineering Chemistry Research*, 53(23):9754–9763, 2014.

[30] Mahdi Kazazi, Banafsheh Moradi, and Mehdi Delshad Chermahini. Enhanced photocatalytic degradation of methyl orange using Ag/Sn-doped CeO_2 nanocomposite. *Journal of Materials Science: Materials in Electronics*, 30(6):6116–6126, 2019.

[31] R.M. Mohamed, D.L. McKinney, and W.M. Sigmund. Enhanced nanocatalysts. *Materials Science and Engineering: R: Reports*, 73(1):1–13, 2012.

[32] Sayyed Ehsan Hosseini Yeganeh, Mahdi Kazazi, Behzad Koozegar Kaleji, Sayed Habib Kazemi, and Batoul Hosseinzadeh. Electrophoretic deposition of sn-doped TiO_2 nanoparticles and its optical and photocatalytic properties. *Journal of Materials Science: Materials in Electronics*, 29(13):10841–10852, 2018.

[33] Hanan H. Mohamed and Detlef W. Bahnemann. The role of electron transfer in photocatalysis: Fact and fictions. *Applied Catalysis B: Environmental*, 128:91–104, November 2012.

[34] Jing-Yin Xu, Xin Tong, Peng Yu, Gideon Evans Wenya, Thomas McGrath, Matthew James Fong, Jiang Wu, and Zhiming M. Wang. Ultrafast dynamics of charge transfer and photochemical reactions in solar energy conversion. *Advanced Science*, 5(12):1800221, October 2018.

[35] F. Biccari. *Defects and doping in Cu_2O*. Lulu.com.

[36] Frank Schweiner, Jorg Main, Matthias Feldmaier, Günter Wunner, and Ch. Uihlein. Impact of the valence band structure of Cu_2O on excitonic spectra. *Physical Review B*, 93:195203, 2016.

[37] B. K. Meyer, A. Polity, D. Reppin, M. Becker, P. Hering, P. J. Klar, Th. Sander, C. Reindl, J. Benz, M. Eickhoff, C. Heiliger, M. Heinemann, J. Bläsing, A. Krost, S. Shokovets, C. Müller, and C. Ronning. Binary copper oxide semiconductors: From materials towards devices. *physica status solidi (b)*, 249(8):1487–1509, 2012.

[38] J. Thewes, J. Heckötter, T. Kazimierczuk, M. Aßmann, D. Fröhlich, M. Bayer, M. A. Semina, and M. M. Glazov. Observation of high angular momentum excitons in cuprous oxide. *Phys. Rev. Lett.*, 115:027402, 2015.

[39] J.S. Weiner, N. Caswell, P.Y. Yu, and A. Mysyrowicz. Ortho- to para-exciton conversion in Cu_2O: A subnanosecond time-resolved photoluminescence study. *Solid State Communications*, 46(2):105–108, 1983.

[40] James P Wolfe and Joon I Jang. The search for Bose-Einstein condensation of excitons in Cu_2O: exciton-Auger recombination versus bi-exciton formation. *New Journal of Physics*, 16(12):123048, December 2014.

[41] Kosuke Yoshioka and Makoto Kuwata-Gonokami. Absorption imaging of trapped $1s$ paraexcitons in bulk Cu_2O. *Phys. Rev. B*, 91:195207, May 2015.

[42] D. W. Snoke, J. P. Wolfe, and A. Mysyrowicz. Evidence for Bose-Einstein condensation of a two-component exciton gas. *Phys. Rev. Lett.*, 64:2543–2546, May 1990.

[43] Yusuke Morita, Kosuke Yoshioka, and Makoto Kuwata-Gonokami. Observation of bose-einstein condensates of excitons in a bulk semiconductor. *Nature Communications*, 13(1), September 2022.

[44] F. Schone, S.-O. Krüger, P. Grünwald, H. Stolz, S. Scheel, M. Aßmann, J. Heckötter, J. Thewes, D. Fröhlich, and M. Bayer. Deviations of the exciton level spectrum in Cu_2O from the hydrogen series. *Phys. Rev. B*, 93:075203, 2016.

[45] K. E. O'Hara, L. Ó Súilleabháin, and J. P. Wolfe. Strong nonradiative recombination of excitons in Cu_2O and its impact on Bose-Einstein statistics. *Phys. Rev. B*, 60:10565–10568, 1999.

[46] Stephan Steinhauer, Marijn A. M. Versteegh, Samuel Gyger, Ali W. Elshaari, Birgit Kunert, André Mysyrowicz, and Val Zwiller. Rydberg excitons in Cu_2O microcrystals grown on a silicon platform. *Communications Materials*, 1(1), 2020.

[47] David Snoke and G M Kavoulakis. Bose-Einstein condensation of excitons in Cu_2O: progress over 30 years. *Reports on Progress in Physics*, 77(11):116501, 2014.

[48] D. Snoke, J. P. Wolfe, and A. Mysyrowicz. Quantum saturation of a Bose gas: excitons in Cu_2O. *Phys. Rev. Lett.*, 59:827–830, 1987.

[49] Scheel S. et al. Kazimierczuk T., Fröhlich D. Giant Rydberg excitons in the copper oxide Cu_2O. *Nature*, 514:343–347, 2014.

[50] J. Heckotter, M. Freitag, D. Frohlich, M. Assmann, M. Bayer, M. A. Semina, and M. M. Glazov. High-resolution study of the yellow excitons in Cu_2O subject to an electric field. *Phys. Rev. B*, 95:035210, 2017.

[51] Frank Schweiner, Jorg Main, Gunter Wunner, Marcel Freitag, Julian Heckötter, Christoph Uihlein, Marc Assmann, Dietmar Fröhlich, and Manfred Bayer. Magnetoexcitons in cuprous oxide. *Phys. Rev. B*, 95:035202, 2017.

[52] D Semkat, S Sobkowiak, F Schöne, H Stolz, Th Koch, and H Fehske. Multicomponent exciton gas in cuprous oxide: cooling behaviour and the role of Auger decay. *Journal of Physics B: Atomic, Molecular and Optical Physics*, 50(20):204001, 2017.

[53] Matthias Feldmaier, Jörg Main, Frank Schweiner, Holger Cartarius, and Günter Wunner. Rydberg systems in parallel electric and magnetic fields: an improved method for finding exceptional points. *Journal of Physics B: Atomic, Molecular and Optical Physics*, 49(14):144002, 2016.

[54] Marcel Freitag, Julian Heckötter, Manfred Bayer, and Marc Aßmann. Role of phonons in the quantum chaos of Rydberg excitons. *Physical Review B*, 95, 2017.

[55] L. O. Grondahl and P. H. Geiger. A new electronic rectifier. *Journal of the A.I.E.E.*, 46(3):215–222, 1927.

[56] William Shockley and Hans J. Queisser. Detailed balance limit of efficiency of p-n junction solar cells. *Journal of Applied Physics*, 32(3):510–519, 1961.

[57] L. C. Olsen, R. C. Bohara, and M. W. Urie. Explanation for low-efficiency Cu_2O Schottky-barrier solar cells. *Applied Physics Letters*, 34(1):47–49, 1979.

[58] B.P. Rai. Cu_2O solar cells: A review. *Solar Cells*, 25(3):265–272, 1988.

[59] J. Herion, E.A. Niekisch, and G. Scharl. Investigation of metal oxide/cuprous oxide heterojunction solar cells. *Solar Energy Materials*, 4(1):101–112, 1980.

[60] B. Kramm, A. Laufer, D. Reppin, A. Kronenberger, P. Hering, A. Polity, and B. K. Meyer. The band alignment of Cu_2O/ZnO and Cu_2O/GaN heterostructures. *Applied Physics Letters*, 100(9):094102, 2012.

[61] Y. Ievskaya, R.L.Z. Hoye, A. Sadhanala, K.P. Musselman, and J.L. MacManus-Driscoll. Fabrication of ZnO/Cu_2O heterojunctions in atmospheric conditions: Improved interface quality and solar cell performance. *Solar Energy Materials and Solar Cells*, 135:43–48, 2015. EMRS 2014 Spring Meeting – Advanced materials and characterization techniques for solar cells II.

[62] Tadatsugu Minami, Yuki Nishi, and Toshihiro Miyata. High-efficiency Cu_2O-based heterojunction solar cells fabricated using a Ga_2O_3 thin film as n-type layer. *Applied Physics Express*, 6(4):044101, 2013.

[63] Hidekazu Mukuda, Sunao Shimizu, Akira Iyo, and Yoshio Kitaoka. High-T_c superconductivity and antiferromagnetism in multilayered copper oxides –a new paradigm of superconducting mechanism–. *Journal of the Physical Society of Japan*, 81(1):011008, 2012.

[64] Che-Chia Hu, Jun-Nan Nian, and Hsisheng Teng. Electrodeposited p-type cu_2o as photocatalyst for h_2 evolution from water reduction in the presence of wo_3. *Solar Energy Materials and Solar Cells*, 92(9):1071–1076, 2008.

[65] A. Werner and H. D. Hochheimer. High-pressure x-ray study of Cu_2O and Ag_2O. *Phys. Rev. B*, 25:5929–5934, 1982.

[66] R. J. Elliott. Symmetry of excitons in Cu_2O. *Phys. Rev.*, 124:340–345, 1961.

[67] Ch. Uihlein, D. Fröhlich, and R. Kenklies. Investigation of exciton fine structure in Cu_2O. *Phys. Rev. B*, 23:2731–2740, 1981.

[68] S. Nikitine, J.B. Grun, and M. Sieskind. Etude spectrophotometrique de la serie jaune de Cu_2O aux basses temperatures. *Journal of Physics and Chemistry of Solids*, 17(3):292–300, 1961.

[69] Takayuki Ito and Taizo Masumi. Detailed examination of relaxation processes of excitons in photoluminescence spectra of Cu_2O. *Journal of the Physical Society of Japan*, 66(7):2185–2193, 1997.

[70] E F Gross. Excitons and their motion in crystal lattices. *Soviet Physics Uspekhi*, 5(2):195–218, 1962.

[71] The dielectric and lattice vibrational spectrum of cuprous oxide. *Journal of Physics and Chemistry of Solids*, 34(12):2201–2208, 1973.

[72] M. Dresselhaus, G. Dresselhaus, S.B. Cronin, and A.G.S. Filho. *Solid State Properties: From Bulk to Nano*. Graduate Texts in Physics. Springer Berlin Heidelberg, 2018.

[73] P. YU and M. Cardona. *Fundamentals of Semiconductors: Physics and Materials Properties*. Graduate Texts in Physics. Springer Berlin Heidelberg, 2010.

[74] M.P. Marder. *Condensed Matter Physics*. Wiley, 2010.

[75] Gregory H. Wannier. The structure of electronic excitation levels in insulating crystals. *Phys. Rev.*, 52:191–197, 1937.

[76] J W Hodby, T E Jenkins, C Schwab, H Tamura, and D Trivich. Cyclotron resonance of electrons and of holes in cuprous oxide, Cu_2O. *Journal of Physics C: Solid State Physics*, 9(8):1429–1439, 1976.

[77] A. Mysyrowicz, D. Hulin, and A. Antonetti. Long exciton lifetime in Cu_2O. *Phys. Rev. Lett.*, 43:1123–1126, 1979.

[78] Dmitry Fishman. *Excitons in cuprous oxide*. PhD thesis, 2008.

[79] G. M. Kavoulakis and A. Mysyrowicz. Auger decay, spin exchange, and their connection to Bose-Einstein condensation of excitons in Cu_2O. *Phys. Rev. B*, 61:16619–16622, 2000.

[80] J. I. Jang, Y. Sun, B. Watkins, and J. B. Ketterson. Bound excitons in Cu_2O: Efficient internal free exciton detector. *Phys. Rev. B*, 74:235204, 2006.

[81] Christoph Möller, Hanna Fedderwitz, Claudine Noguera, Jacek Goniakowski, and Niklas Nilius. Temperature-dependent phase evolution of copper-oxide thin-films on Au(111). *Physical Chemistry Chemical Physics*, 20(8):5636–5643, 2018.

[82] Alexander Gloystein and Niklas Nilius. Copper oxidation on Pt(111)-more than a surface oxide? *The Journal of Physical Chemistry C*, 123(44):26939–26946, 2019.

[83] T. Matsumoto, R.A. Bennett, P. Stone, T. Yamada, K. Domen, and M. Bowker. Scanning tunneling microscopy studies of oxygen adsorption on Cu(111). *Surface Science*, 471(1-3):225–245, 2001.

[84] F Jensen, F Besenbacher, and I Stensgaard. Two new oxygen induced reconstructions on Cu(111). *Surf. Sci.*, 269-270:400–404.

[85] Fan Yang, YongMan Choi, Ping Liu, Dario Stacchiola, Jan Hrbek, and José A. Rodriguez. Identification of 5/7 defects in a copper oxide surface. *Journal of the American Chemical Society*, 133(30):11474–11477, 2011.

[86] Yibin Bu, J. W. Hans Niemantsverdriet, and Hans O. A. Fredriksson. Cu model catalyst dynamics and CO oxidation kinetics studied by simultaneous in situ UV/vis and mass spectroscopy. *ACS Catalysis*, 6(5):2867–2876, 2016.

[87] Katherine P. Rice, Edwin J. Walker, Mark P. Stoykovich, and Aaron E. Saunders. Solvent-dependent surface plasmon response and oxidation of copper nanocrystals. *The Journal of Physical Chemistry C*, 115(5):1793–1799, 2011.

[88] Katherine P. Rice, Andrew S. Paterson, and Mark P. Stoykovich. Nanoscale kirkendall effect and oxidation kinetics in copper nanocrystals characterized by real-time, in situ optical spectroscopy. *Particle and Particle Systems Characterization*, 32(3):373–380, 2014.

[89] David B. Pedersen, Shiliang Wang, and Septimus H. Liang. Charge-transfer-driven diffusion processes in Cu@Cu-Oxide core-shell nanoparticles: Oxidation of 3.0 ± 0.3 nm diameter copper nanoparticles. *The Journal of Physical Chemistry C*, 112(24):8819–8826, 2008.

[90] George H. Chan, Jing Zhao, Erin M. Hicks, George C. Schatz, and Richard P. Van Duyne. Plasmonic properties of copper nanoparticles fabricated by nanosphere lithography. *Nano Letters*, 7(7):1947–1952, 2007.

[91] Mariano D. Susman, Yishai Feldman, Tatyana A. Bendikov, Alexander Vaskevich, and Israel Rubinstein. Real-time plasmon spectroscopy study of the solid-state oxidation and Kirkendall void formation in copper nanoparticles. *Nanoscale*, 9:12573–12589, 2017.

[92] Zhengyi Hu, Silvia Haneklaus, Gerd Sparovek, and Ewald Schnug. Rare earth elements in soils. *Communications in Soil Science and Plant Analysis*, 37(9-10):1381–1420, 2006.

[93] Cedric Bouzigues, Thierry Gacoin, and Antigoni Alexandrou. Biological applications of rare-earth based nanoparticles. *ACS Nano*, 5(11):8488–8505, 2011. PMID: 21981700.

[94] Tiziano Montini, Michele Melchionna, Matteo Monai, and Paolo Fornasiero. Fundamentals and catalytic applications of CeO_2-based materials. *Chemical Reviews*, 116(10):5987–6041, 2016. PMID: 27120134.

[95] Gordon. Haxel. Rare earth elements: critical resources for high technology.

[96] JoséC. Conesa. Computer modeling of surfaces and defects on cerium dioxide. *Surface Science*, 339(3):337–352, 1995.

[97] Toshio Suzuki, Igor Kosacki, Harlan U. Anderson, and Philippe Colomban. Electrical conductivity and lattice defects in nanocrystalline cerium oxide thin films. *Journal of the American Ceramic Society*, 84(9):2007–2014, 2001.

[98] P. Patsalas, S. Logothetidis, L. Sygellou, and S. Kennou. Structure-dependent electronic properties of nanocrystalline cerium oxide films. *Phys. Rev. B*, 68:035104, 2003.

[99] S. Guo, H. Arwin, S. N. Jacobsen, K. Järrendahl, and U. Helmersson. A spectroscopic ellipsometry study of cerium dioxide thin films grown on sapphire by rf magnetron sputtering. *Journal of Applied Physics*, 77(10):5369–5376, 1995.

[100] Jacopo Stefano Pelli Cresi, Lorenzo Di Mario, Daniele Catone, Faustino Martelli, Alessandra Paladini, Stefano Turchini, Sergio D'Addato, Paola Luches, and Patrick O'Keeffe. Ultrafast formation of small polarons and the optical gap in CeO_2. *The Journal of Physical Chemistry Letters*, 11(14):5686–5691, 2020. PMID: 32580554.

[101] P. Patsalas, S. Logothetidis, L. Sygellou, and S. Kennou. Structure-dependent electronic properties of nanocrystalline cerium oxide films. *Physical Review B*, 68(3), July 2003.

[102] Alessandro Trovarelli and Paolo Fornasiero. *Catalysis by ceria and related materials*. IMPERIAL COLLEGE PRESS, 2nd edition, 2013.

[103] Masatomo Yashima and Daiju Ishimura. Crystal structure and disorder of the fast oxide-ion conductor cubic Bi_2O_3. *Chemical Physics Letters*, 378(3):395–399, 2003.

[104] N. V. Skorodumova, M. Baudin, and K. Hermansson. Surface properties of CeO_2 from first principles. *Phys. Rev. B*, 69:075401, 2004.

[105] JoséC. Conesa. Computer modeling of surfaces and defects on cerium dioxide. *Surface Science*, 339(3):337–352, 1995.

[106] Zongxian Yang, Tom K. Woo, Micael Baudin, and Kersti Hermansson. Atomic and electronic structure of unreduced and reduced CeO_2 surfaces: A first-principles study. *The Journal of Chemical Physics*, 120(16):7741–7749, 2004.

[107] Michael Nolan, Sonja Grigoleit, Dean C. Sayle, Stephen C. Parker, and Graeme W. Watson. Density functional theory studies of the structure and electronic structure of pure and defective low index surfaces of ceria. *Surface Science*, 576(1):217–229, 2005.

[108] Jan-Frederik Jerratsch, Xiang Shao, Niklas Nilius, Hans-Joachim Freund, Cristina Popa, M. Veronica Ganduglia-Pirovano, Asbjörn M. Burow, and Joachim Sauer. Electron localization in defective ceria films: A study with scanning-tunneling microscopy and density-functional theory. *Phys. Rev. Lett.*, 106:246801, 2011.

[109] N. V. Skorodumova, S. I. Simak, B. I. Lundqvist, I. A. Abrikosov, and B. Johansson. Quantum origin of the oxygen storage capability of ceria. *Phys. Rev. Lett.*, 89:166601, 2002.

[110] M. Verónica Ganduglia-Pirovano, Alexander Hofmann, and Joachim Sauer. Oxygen vacancies in transition metal and rare earth oxides: Current state of understanding and remaining challenges. *Surface Science Reports*, 62(6):219–270, 2007.

[111] Matteo Cargnello, Vicky V. T. Doan-Nguyen, Thomas R. Gordon, Rosa E. Diaz, Eric A. Stach, Raymond J. Gorte, Paolo Fornasiero, and Christopher B. Murray. Control of metal nanocrystal size reveals metal-support interface role for ceria catalysts. *Science*, 341(6147):771–773, 2013.

[112] Roman Fiala, Alberto Figueroba, Albert Bruix, Michal Vaclavu, Andrii Rednyk, Ivan Khalakhan, Mykhailo Vorokhta, Jaroslava Lavkova, Francesc Illas, Valerie Potin, Iva Matolinova, Konstantin M. Neyman, and Vladimir Matolin. High efficiency of Pt^{2+}- CeO_2 novel thin film catalyst as anode for proton exchange membrane fuel cells. *Applied Catalysis B: Environmental*, 197:262–270, 2016. Forty years of catalysis by ceria: a success story.

[113] Electrical properties of ceria-based oxides and their application to solid oxide fuel cells. *Solid State Ionics*, 52(1):165–172, 1992.

[114] Rajankumar L. Patel, Sai Abhishek Palaparty, and Xinhua Liang. Ultrathin conductive CeO_2 coating for significant improvement in electrochemical performance of $LiMn_1.5Ni_0.5O_4$ cathode materials. *Journal of The Electrochemical Society*, 164(1):A6236–A6243, 2016.

[115] J. A. Rodriguez, S. Ma, P. Liu, J. Hrbek, J. Evans, and M. Pérez. Activity of CeO_2 and TiO_2 nanoparticles grown on Au(111) in the water-gas shift reaction. *Science*, 318(5857):1757–1760, 2007.

[116] M. Melchionna and P. Fornasiero. The role of ceria-based nanostructured materials in energy applications. *Materials Today*, 17(7):349–357, 2014.

[117] Yusheng She, Qi Zheng, Lei Li, Yingying Zhan, Chongqi Chen, Yuanhui Zheng, and Xingyi Lin. Rare earth oxide modified CuO/CeO_2 catalysts for the water–gas shift reaction. *International Journal of Hydrogen Energy*, 34(21):8929–8936, 2009.

[118] Qi Fu, Howard Saltsburg, and Maria Flytzani-Stephanopoulos. Active non-metallic Au and Pt species on ceria-based water-gas shift catalysts. *Science*, 301(5635):935–938, 2003.

[119] Fangjian Lin, Matthäus Rothensteiner, Ivo Alxneit, Jeroen A. van Bokhoven, and Alexander Wokaun. First demonstration of direct hydrocarbon fuel production from water and carbon dioxide by solar-driven thermochemical cycles using rhodium–ceria. *Energy Environ. Sci.*, 9:2400–2409, 2016.

[120] Lucía Arribas, José González-Aguilar, and Manuel Romero. Solar-driven thermochemical water-splitting by cerium oxide: Determination of operational conditions in a directly irradiated fixed bed reactor. *Energies*, 11(9), 2018.

[121] Roberto Fiorenza, Stefano Andrea Balsamo, Marcello Condorelli, Luisa D'Urso, Giuseppe Compagnini, and Salvatore Scirè. Solar photocatalytic H_2 production over CeO_2-based catalysts: Influence of chemical and structural modifications. *Catalysis Today*, 380:187–198, 2021. SI:Photo(thermo)catalysis.

[122] Ivana Celardo, Jens Z. Pedersen, Enrico Traversa, and Lina Ghibelli. Pharmacological potential of cerium oxide nanoparticles. *Nanoscale*, 3:1411–1420, 2011.

[123] Corrado Mandoli, Francesca Pagliari, Stefania Pagliari, Giancarlo Forte, Paolo Di Nardo, Silvia Licoccia, and Enrico Traversa. Stem cell aligned growth induced by CeO_2 nanoparticles in PLGA scaffolds with improved bioactivity for regenerative medicine. *Advanced Functional Materials*, 20(10):1617–1624, 2010.

[124] César Clavero. Plasmon-induced hot-electron generation at nanoparticle/metal-oxide interfaces for photovoltaic and photocatalytic devices. *Nat. Photonics*, 8(2):95–103, 2014.

[125] Marco S. Rodrigues, Joel Borges, Cláudia Lopes, Rui M. S. Pereira, Mikhail I. Vasilevskiy, and Filipe Vaz. Gas sensors based on localized surface plasmon resonances: Synthesis of oxide films with embedded metal nanoparticles, theory and simulation, and sensitivity enhancement strategies. *Applied Sciences*, 11(12), 2021.

[126] Suljo Linic, Phillip Christopher, Hongliang Xin, and Andiappan Marimuthu. Catalytic and photocatalytic transformations on metal nanoparticles with targeted geometric and plasmonic properties. *Accounts of Chemical Research*, 46(8):1890–1899, 2013. PMID: 23750539.

[127] Matthew J. Kale, Talin Avanesian, and Phillip Christopher. Direct photocatalysis by plasmonic nanostructures. *ACS Catalysis*, 4(1):116–128, 2014.

[128] Abraham Nitzan and L. E. Brus. Theoretical model for enhanced photochemistry on rough surfaces. *The Journal of Chemical Physics*, 75(5):2205–2214, 1981.

[129] Katherine A. Willets and Richard P. Van Duyne. Localized surface plasmon resonance spectroscopy and sensing. *Annual Review of Physical Chemistry*, 58(1):267–297, 2007. PMID: 17067281.

[130] Eleonora Petryayeva and Ulrich J. Krull. Localized surface plasmon resonance: Nanostructures, bioassays and biosensing—a review. *Analytica Chimica Acta*, 706(1):8–24, 2011.

[131] Suljo Linic, Phillip Christopher, and David B. Ingram. Plasmonic-metal nanostructures for efficient conversion of solar to chemical energy. *Nature Materials*, 10(12):911–921, 2011.

[132] Phillip Christopher and Martin Moskovits. Hot charge carrier transmission from plasmonic nanostructures. *Annual Review of Physical Chemistry*, 68(1):379–398, 2017. PMID: 28301756.

[133] Martin Moskovits. The case for plasmon-derived hot carrier devices. *Nature Nanotechnology*, 10(1):6–8, 2015.

[134] K. Wu, J. Chen, J. R. McBride, and T. Lian. Efficient hot-electron transfer by a plasmon-induced interfacial charge-transfer transition. *Science*, 349(6248):632–635, 2015.

[135] Jacopo Stefano Pelli Cresi, Maria Chiara Spadaro, Sergio D'Addato, Sergio Valeri, Stefania Benedetti, Alessandro Di Bona, Daniele Catone, Lorenzo Di Mario, Patrick O'Keeffe, Alessandra Paladini, Giovanni Bertoni, and Paola Luches. Highly efficient plasmon-mediated electron injection into cerium oxide from embedded silver nanoparticles. *Nanoscale*, 11:10282–10291, 2019.

[136] Jacopo Stefano Pelli Cresi, Eleonora Spurio, Lorenzo Di Mario, Patrick O'Keeffe, Stefano Turchini, Stefania Benedetti, Gian Marco Pierantozzi, Alessandro De Vita, Riccardo Cucini, Daniele Catone, and Paola Luches. Lifetime of photogenerated positive charges in hybrid cerium oxide-based materials from space and mirror charge effects in time-resolved photoemission spectroscopy. *The Journal of Physical Chemistry C*, 126(27):11174–11181, 2022.

[137] Jacopo Stefano Pelli Cresi, Emiliano Principi, Eleonora Spurio, Daniele Catone, Patrick O'Keeffe, Stefano Turchini, Stefania Benedetti, Avinash Vikatakavi, Sergio D'Addato, Riccardo Mincigrucci, Laura Foglia, Gabor Kurdi, Ivaylo P. Nikolov, Giovanni De Ninno, Claudio Masciovecchio, Stefano Nannarone, Jagadesh Kopula Kesavan, Federico Boscherini, and Paola Luches. Ultrafast dynamics of plasmon-mediated charge transfer in Ag@CeO$_2$ studied by free electron laser time-resolved x-ray absorption spectroscopy. *Nano Letters*, 21(4):1729–1734, 2021. PMID: 33570965.

[138] Daniel C. Ratchford, Adam D. Dunkelberger, Igor Vurgaftman, Jeffrey C. Owrutsky, and Pehr E. Pehrsson. Quantification of efficient plasmonic hot-electron injection in gold nanoparticle–TiO$_2$ films. *Nano Letters*, 17(10):6047–6055, 2017. PMID: 28850243.

[139] Scott K. Cushing, Alan D. Bristow, and Nianqiang Wu. Theoretical maximum efficiency of solar energy conversion in plasmonic metal–semiconductor heterojunctions. *Phys. Chem. Chem. Phys.*, 17:30013–30022, 2015.

[140] Akihiro Furube, Luchao Du, Kohjiro Hara, Ryuzi Katoh, and Masanori Tachiya. Ultrafast plasmon-induced electron transfer from gold nanodots into TiO$_2$ nanoparticles. *Journal of the American Chemical Society*, 129(48):14852–14853, 2007. PMID: 17994750.

[141] Christophe Bauer, Jean-Pierre Abid, and Hubert H. Girault. Hot adsorbate-induced retardation of the internal thermalization of nonequilibrium electrons in adsorbate-covered metal nanoparticles. *The Journal of Physical Chemistry B*, 110(10):4519–4523, 2006. PMID: 16526676.

[142] Yuchao Zhang, Shuai He, Wenxiao Guo, Yue Hu, Jiawei Huang, Justin R. Mulcahy, and Wei David Wei. Surface-plasmon-driven hot electron photochemistry. *Chemical Reviews*, 118(6):2927–2954, 2018. PMID: 29190069.

[143] Younghyun Wy, Hayoon Jung, Jong Wook Hong, and Sang Woo Han. Exploiting plasmonic hot spots in au-based nanostructures for sensing and photocatalysis. *Accounts of Chemical Research*, 55(6):831–843, 2022. PMID: 35213153.

[144] Tianji Liu, Lucas V. Besteiro, Zhiming Wang, and Alexander O. Govorov. Generation of hot electrons in nanostructures incorporating conventional and unconventional plasmonic materials. *Faraday Discuss.*, 214:199–213, 2019.

Chapter 2

Experimental techniques

The main goal of this thesis is the growth and investigations of oxides, eventually coupled with plasmonic NPs, in particular cerium oxide and cuprous oxide, suitable for photocatalytic applications. In this chapter, I will describe the experimental techniques used for the growth, the static, and the dynamic characterization that have been employed for the systems presented in this thesis.

2.1 SESAMo Laboratories

Almost all samples described in this thesis (a part for the last chapter) have been grown in *Electronic Spectroscopies on Surfaces and Adsorbates laboratory in Modena* (SESAMo). The laboratory is split into two different apparatuses, respectively, called RAGNO-1 and RAGNO-2, both of them allowing to work in Ultra High Vacuum (UHV) conditions.

RAGNO-1, schematized in figure 2.1 is composed of three main chambers, all kept under UHV pressure conditions around 10^{-10} mbar: the MBE chamber, the main chamber, and the STM/AFM chamber.

The first chamber is dedicated to the synthesis of samples through Molecular Beam Epitaxy (MBE). In the chamber, different evaporators are mounted, including Ag, Ce, Au, and Cu evaporators. Moreover, the chamber is equipped with a quartz microbalance, to monitor the thickness of the growing samples, and with a gas line, that allows to modify the composition of the deposition atmosphere. A resistive heater is also mounted onto the sample holder, giving the possibility to vary the substrate temperature. The main chamber is dedicated to substrate preparation and sample chemical characterization, using X-Ray Photoelectron Spectroscopy (XPS), Ultraviolet Photoelectron Spectroscopy (UPS), and Low-Energy Electron Diffraction (LEED). For these purposes, the chamber is equipped with a sputtering stage (for substrate cleaning), a concentric hemispherical analyzer (OMICRON EA 125), a double-anode Leybold-Heraesus X-Ray source for XPS, and a Helium lamp for UPS. Finally, the third chamber is dedicated to morphological characterization, and it contains a room temperature (RT) scanning probe microscope for Scanning Tunneling Microscopy (STM) and Atomic Force Microscopy (AFM).

RAGNO-2 is shown in figure 2.2, and its structure is similar to RAGNO-1: it is also based upon connected UHV chambers, where it is possible to deposit thin films and NPs of different materials, and to perform in-situ XPS characterization after the growth. The chamber, schematized in figure 2.2 is composed by the fast entry (A), the NPs source (B), the deposition chamber (C), the chamber for XPS analysis (D) and the one for Auger analysis (E). Also RAGNO-2 is equipped with a
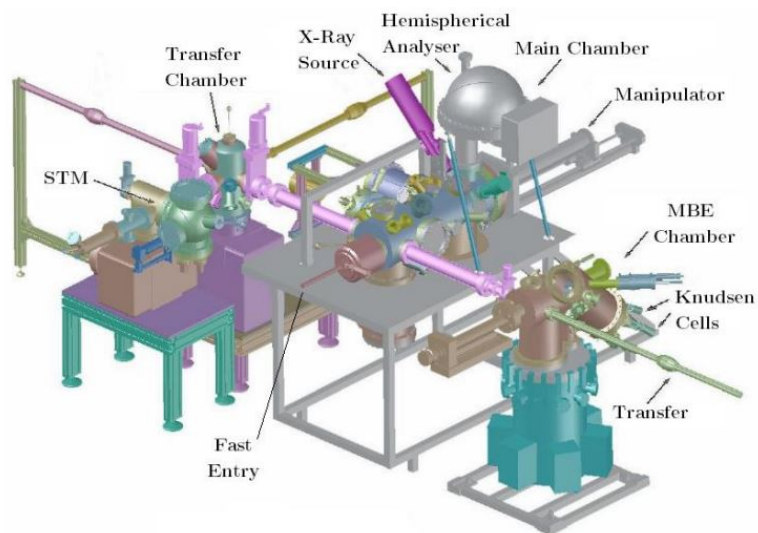
Figure 2.1: *Schematics of RAGNO-1 setup.*
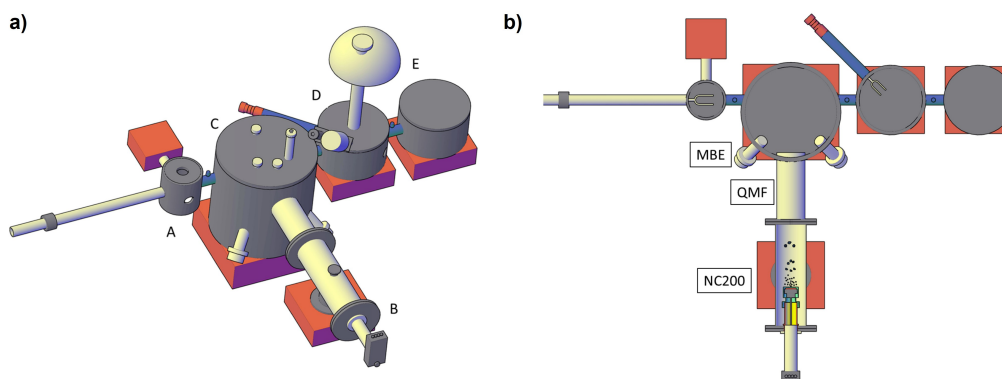
Figure 2.2: *Sketch of the experimental set-up of RAGNO-2: a) lateral perspective view, b) top view. In a: A is the fast entry, B is the aggregation chamber where the NPs are formed (better schematized in 2.3), C is the deposition chamber, D is the XPS chamber and E is the chamber to perform Auger analysis.*

Ce evaporator, that allows to deposit ceria films via MBE. Contrarily to RAGNO-1, however, in RAGNO-2 the NPs are synthesized using a DC Magnetron Sputtering (MS) cluster source NC-200 by Oxford Applied Research. The NPs of the desired metal are sputtered from a target, and they form NPs while travelling through the aggregation region, filled with an inert gas (Ar in this case). The MS and the aggregation region are shown in the schematics in figure 2.3. The NPs, formed in the aggregation region, pass through an orifice that generates a NPs beam. The NPs can be then mass-selected by a quadrupole mass filter (QMF200, Oxford Applied Research), and deposited over a substrate in the deposition chamber (base pressure $5 \sim 10^{-9}$ mbar). The geometry of the NPs and their composition strongly depend on the discharge power, the aggregation tube length and the pressure/type of inert gas. As already mentioned, the deposition chamber is connected with another chamber equipped with the apparatus for XPS measurements (XR50, Specs double anode X-Ray source and Phoibos 150, Specs hemispherical electron analyzer).
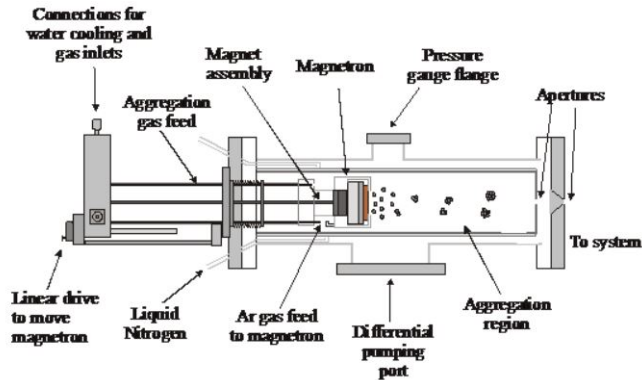
Figure 2.3: *Nanocluster Deposition Source-Model NC200U-B [1]*

2.2 Photoelectron Spectroscopy: XPS and UPS

Photoelectron spectroscopy techniques are based on the photoelectric effect: when an atom is irradiated by a photon beam, the photon energy is transferred to an electron, which can escape the material as a photoelectron. The excitation energy must be large enough for the electrons to overcome the work function of the solid. Depending on the energy of the incoming radiation, different properties of the investigated material can be extracted. In this section, I will focus on X-Ray photoelectron spectroscopy (XPS) and ultraviolet photoelectron spectroscopy (UPS), that give access respectively to the core levels and to the valence band of the investigated material.

XPS is a unique tool for surface investigation, used to obtain information on elemental composition of solid materials. It provides both quantitative and qualitative information on the sample surface. Its high sensitivity allows the detection of the presence of dopants even when very diluted and can provide precise information on the chemical state of the elements in the investigated sample. When a sample is irradiated with an X-Ray beam, the photon energy is transferred to core electrons that can escape from the material as photoelectrons. XPS is usually performed in UHV conditions, using mono-energetic soft X-Rays. The XPS spectrum is obtained as a plot of the number of photoelectrons detected per energy interval as a function of their kinetic energy (KE) measured at the analyzer. Each element has a unique spectrum, and the height of each XPS peak (or the area under the peak) provides quantitative information, and the precise measurement of the position and separation of the peaks, together with other spectral features, allows the precise identification of chemical states. The typical investigation depth of XPS is $\sim 10 - 20$ Å. Knowing the energy of the incoming X-Rays ($h\nu$) and the work function of the analyzer (ϕ_A), it is easy to extract the binding energy (BE) of the electrons using equation 2.1,

$$BE = h\nu - KE - \phi_A \qquad (2.1)$$

The number of collected photoelectrons depends on the inelastic mean free path λ, defined as the average distance that electrons can travel within a material without incurring in inelastic scattering events that modify their kinetic energy. The photoelectron mean free path strongly depends upon the photoelectron energy: since the binding energy of a specific core level only depends on the material, the investigation depth depends on the photon energy and on the material under investigation. In conventional X-Ray sources, the X-Ray beam is produced by electron bombardment of Al and Mg anodes. A fraction of the X-Rays derives from the bremsstrahlung,

but the majority of the intensity comes from characteristic X-Rays, specifically the K_α line. In all works described in this thesis, the XPS spectra were acquired using Al K_α photons from a double anode X-Ray source ($h\nu$=1486.6 eV). In the SESAMo laboratory, the electrons are detected with a Scienta Omicron concentric hemispherical analyzer, which can achieve an energy resolution of 0.1 eV. However, the effective limit of the resolution is due to the width of the fluorescence line (about 0.4 eV) [2].

UPS is based upon the same principle of XPS, but the ionizing radiation has much lower energy (in the range of tens of eV), making this technique suitable for the study of the valence band region. In the present work, the ultraviolet photons are produced by a He discharge lamp, using HeI radiation ($h\nu$=21.2 eV).

2.2.1   Ce 3d XPS spectra

As already mentioned, one of the most important information provided by XPS is the chemical state of a particular element within a material. In fact, variations in the chemical environment of a element involve a spatial redistribution of the valence charges, changing the potential felt by core electrons. This redistribution appears as a change in the binding energy. In this thesis, XPS has been largely employed to characterize the chemical state of Ce ions, by extracting the Ce^{3+}/Ce^{4+} ratio. The shape of Ce 3d core level spectra is not only influenced by the 4f electron configuration in the ground state but also by the coupling between the core hole that is left behind with valence electrons. In systems with incompletely filled f or d states, the coupling between the core hole and these levels is strong enough to bring information about characteristic spectral splittings. The complicated shape of Ce 3d XPS spectra have already been discussed in a large number of dedicated works, such like [3, 4, 5, 6]. Given the complexity of the spectrum, to obtain information about the oxidation state of Ce ions within the material, a fitting procedure is necessary to extract the ratio between Ce^{3+} and Ce^{4+} ions. The fitting procedure adopted for all CeO_2 samples described in this thesis is the one introduced by Romeo et al. [4] and improved by Skala et al. [7]. The Ce 3d XPS spectra were fitted with Voigt-shaped Ce^{3+}- and Ce^{4+}-related components, considering six doublets, the sixth used to model the asymmetry of the first peak. The additional doublet is shifted by 1.30 eV with respect to peak 1, with half intensity. The background is modeled as a Shirley background. The fit is performed by using only the area of the peaks as a free parameter, fixing all other parameters (i.e. the spin-orbit splitting, branching ratios and peak widths) to values close to the ones reported in [8], after a slight optimization. The percentage of Ce ions in the 3+ state is then calculated as the sum of the intensity of all peaks related to Ce^{3+}, divided by the total intensity of the Ce peaks. Given the complexity of the XPS spectrum, the absolute value extracted by the fit for the Ce^{3+} concentration can be affected by non negligible errors. However, if the fitting strategy is coherent for all samples under investigation, it is possible to reliably compare the Ce^{3+} concentration derived for the different samples. Figure 2.4 reports an example of XPS Ce 3d spectrum acquired for a film of 80 nm of cerium oxide grown by magnetron sputtering and the corresponding fit curve. Furthermore, the Shirley background (green line) and the components attributed to Ce^{4+} (pink) and Ce^{3+} (yellow), relative to the fit of the spectrum are shown.
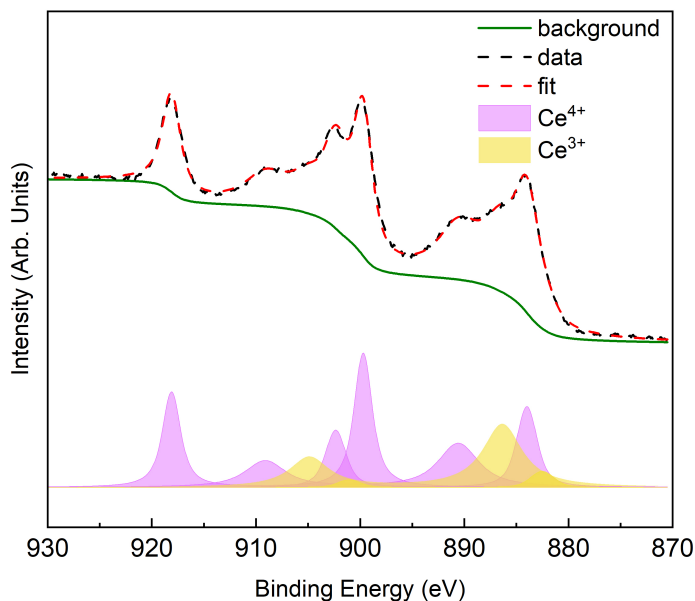
Figure 2.4: *XPS Ce 3d spectra of a 80 nm ceria film. The fit of the spectrum is shown as solid red line, while the experimental data as a black dashed line. An example of the different components and background used for the fitting is also shown.*

2.3 Optical characterization

As already mentioned, to optimize the complex systems formed by cerium oxide combined with plasmonic NPs, in terms of visible light harvesting efficiency and density of long-living excited states, it is fundamental to understand the optical properties of the investigated material, as well as the processes involved in the charge transfer, and the dynamics of the excited states formed within the oxide.

2.3.1 Spectrophotometry Characterization

The first, easy characterization that is convenient to perform, to understand if a system is suitable for visible light absorption, is the measurement of its static optical properties. These measurements have been performed on the samples grown in the SESAMo laboratories using a white photon beam generated by a Xe lamp, equipped with a ORIEL-MS257 monochromator and a Si detector. A polarizer placed after the monochromator allowed to obtain s- or p-polarized radiation. The surface normal of the samples under investigation were oriented to form an incident angle of 22° with the incident photon beam direction, which is the minimum angle that permits to measure not only the transmitted but also the reflected radiation. To account for the Xe lamp emission profile, the measured spectra were normalized by the incident light intensity obtained by removing the sample. The results of this normalization are the transmittance T and the reflectance R of the samples, from which it is possible to extract the absolute absorbance A as:

$$A = 1 - T - R \tag{2.2}$$

Polarizability simulations

The optical absorbance obtained with the procedure described above can be compared to theoretical expectations, by modelling the investigated system using the

45

Maxwell-Garnett model for optical absorption [9]. The model can be used to simulate the optical polarizability and to theoretically describe the LSPR excitation in the metal@oxide systems. The imaginary part of the optical polarizability α of the NPs immersed within a dielectric material have been calculated assuming an oblate ellipsoidal geometry, using the aspect ratio (AR, defined as the ratio between the *in-plane* and the *out-of-plane* dimensions of the NP) calculated on the basis of the NPs morphology. An oblate spheroid is an ellipsoid with its three axis a, b and c in the following relationship: $a = b > c$, being a and b the *in-plane* dimensions and c the *out-of-plane* axis. The polarizability of oblate spheroids can be calculated using the following relations:

$$e = \sqrt{\left(\frac{a}{c}\right)^2 - 1} \text{ , Eccentricity} \tag{2.3a}$$

$$L_z = \frac{1 + e^2}{e^3}[e - \arctan(e)] \text{ , } z \text{ depolarization factor} \tag{2.3b}$$

$$L_x = L_y = \frac{1 - L_z}{2} \text{ , } x \text{ and } y \text{ depolarization factor} \tag{2.3c}$$

$$\alpha_j \propto \frac{\epsilon_{NP} - \epsilon_M}{\epsilon_M + (\epsilon_{NP} - \epsilon_M) \cdot L_i}\epsilon_M \text{ , Polarizability along } j \tag{2.3d}$$

where $\frac{a}{c}$ is the NP AR, ϵ_{NP} is the bulk complex dielectric function of the metal composing the NPs and ϵ_M is the bulk complex dielectric function of the medium in which the nanoparticles are immersed. To obtain the light absorption maximum wavelength for the system of NPs embedded in the oxide, one needs to extract the imaginary part of the polarizability, Im_{α_j}. Since the quantity to be evaluated by simulations is the wavelength corresponding to the peak maximum, the term ϵ_M in 2.3d can be treated as a multiplicative term which has no effect on the peak position. For this reason, the imaginary part of the polarizability is reported in arbitrary units. The imaginary part of the polarizability can be written as:

$$Im_{\alpha_j} = \frac{\epsilon_{NP}^i \cdot \epsilon_M^R - \epsilon_{NP}^R \cdot \epsilon_M^i}{[L_j(\epsilon_{NP}^i - \epsilon_M^i) + \epsilon_M^i]^2 + [L_j(\epsilon_{NP}^R - \epsilon_M^R) + \epsilon_M^R]^2} \tag{2.4}$$

where ϵ_{NP}^R and ϵ_{NP}^i are respectively the real and imaginary part of the bulk dielectric function of the metal composing the nanoparticles, while ϵ_M^R and ϵ_M^i are respectively the real and imaginary part of the bulk dielectric function of the medium. The Maxwell–Garnett equation of the polarizability of an ellipsoid is:

$$\alpha_i = \frac{4}{3}\pi abc\epsilon_0 \frac{\epsilon - \epsilon_M}{\epsilon_M + [\epsilon - \epsilon_M] \cdot L_i} \tag{2.5}$$

In the case of a sphere (i.e. when the NPs AR = 1), the model yielded $L_i = 1/3$ for the three components, a = b = c = r (corresponding to the sphere radius), $\alpha_x = \alpha_y = \alpha_z = \alpha$ and equation 2.3d becomes:

$$\alpha_i = 12\pi r^3\epsilon_0 \frac{\epsilon - \epsilon_M}{2\epsilon_M + \epsilon} \tag{2.6}$$

2.3.2 Femtosecond Transient Absorption Spectroscopy

The most convenient techniques for studying the dynamics of excited states within a system are based upon *pump-probe* configuration. In particular, femtosecond transient absorption spectroscopy (FTAS) is a time-resolved pump-probe technique that can be used to study the ultrafast processes within materials [10, 11]. In the pump-probe configuration, two independent light pulses are sent to the investigated sample. First, a short light pulse is generated by a laser at a selected energy, exciting the sample. Then, after a variable delay time τ, a second light pulse is used to probe the absorbance response of the system (which, when $\tau > 0$, has been excited by the pump). This second pulse can have either a single wavelength or it can have a *supercontinuum* spectrum, i.e. a super-wide continuous optical spectrum. In general, the probe pulse is chosen to be less intense than the pump one, to avoid multistep and multiphoton processes, and with a narrower space distribution than the pump pulse, to be sure to investigate only the portion of sample hit by the pump. By measuring the difference in probe intensity after the sample with and without the pump pulse (I_{pump} and $I_{no-pump}$ respectively), it is possible to evaluate the variations in the response of the system after its first excitation. In fact, from these two values, it is possible to evaluate the absorbance A of the sample, in its ground state and after the interaction with the pump pulse, following the relation:

$$I = I_0 \cdot e^{-A} \tag{2.7}$$

The absorbance variation is thus given by

$$\Delta A = A_{pump} - A_{no-pump} = \ln\left(\frac{I_{no-pump}}{I_{pump}}\right) \tag{2.8}$$

The schematics in figure 2.5a reports an example of the electron energy bands before and after the interaction with a pump pulse with a energy resonating with the bandgap of the semiconductor, and in 2.5b the corresponding absorbance spectrum. Before the interaction with the pump (1), the system is in the ground state, and its absorbance is $A_{no-pump}$ and corresponds to the static absorbance spectrum. If the pump energy is enough to excite electrons from the valence (VB) to the conduction band (CB), the electronic configuration of the system is different after the interaction with the pump pulse (2). In this case, the absorbance of the system, A_{pump}, will be different with respect to the static absorbance. The transient spectrum reported in figure 2.5b represents a possible example of the absorbance difference ΔA as a function of the probe wavelength. In the spectrum, the first negative peak is related to the photobleaching (PB) of the ground state: because of the depletion of the VB after the interaction with the pump, the absorbance of the excited system is lower than the absorbance of the ground state $A_{pump} < A_{no-pump}$. The positive peak is related to the pump photoinduced absorbance (PIA): after the interaction between the pump pulse and the system, there are optically allowed transitions from the populated states in the CB to further excited states. At these probe wavelengths, $A_{pump} > A_{no-pump}$. Finally, the third negative peak is related to the stimulated emission (SE) from the excited states, which may eventually be triggered by the pump. The three signals may overlap with each other, or may be located at different wavelength positions as in the example reported in figure 2.5. To obtain the time evolution of the excited states, it is possible to vary the delay time of the probe with respect to the pump. By using a light supercontinuum as the probe stimulus, the transient signal in FTAS becomes a function of the wavelength of the probe and of
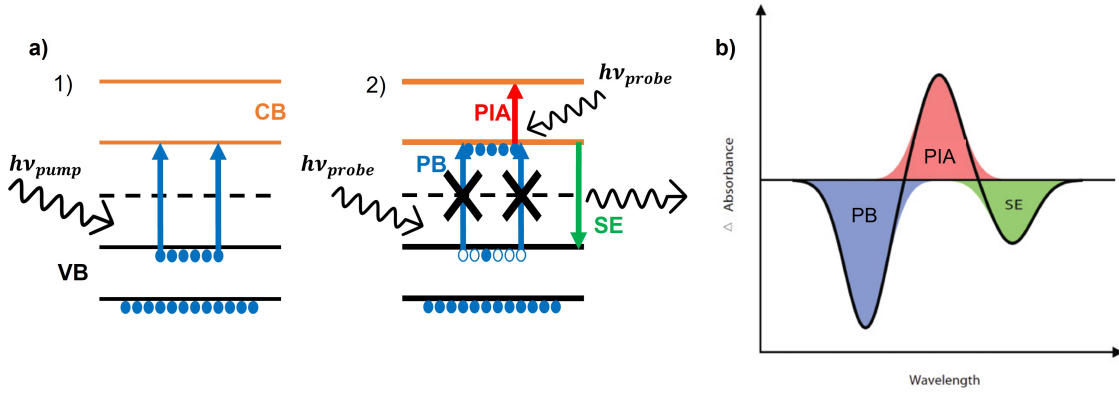
Figure 2.5: *(a) Example of electron energy levels (1) before and (2) after the interaction with a pump pulse with $h\nu \approx E_{GAP}$. Three possible signals may arise when the excited system interacts with the probe pulse, depending on its energy: PIA (photoinduced absorbance, in red), PB (photobleaching, in blue) and SE (stimulated emission, in green). (b) Possible types of signals obtained in a pump-probe transient absorption experiment as the difference in absorbance between the excited system and the system at the ground state [12].*

the delay time between the pump and the probe.

$$\Delta A = \Delta A(\lambda, t) \tag{2.9}$$

The results of the FTAS measurement are usually arranged in a matrix where one direction is related to the time delay and the other to the wavelength of the probe.

2.4 X-Ray absorption spectroscopy

X-Ray absorption spectroscopy (XAS) is a chemically sensitive technique that provides information on the fine structure of the X-Ray absorption coefficient near the absorption edge of a particular element. It allows to obtain information on the chemical state and on the local structure of one element within a compound. XAS is widely used to obtain element-specific information for the characterization of semiconductors, in solid or liquid, crystalline or amorphous, bulk or nanoscale form [13, 14]. With XAS, it is possible to study the behavior of the absorbance coefficient μ of a given atom as a function of the incident photon energy. The energy of the incoming X-Ray radiation is tuned over a range where core electrons can be excited (0.1-100 keV). The acquired spectrum consists of a continuous background interrupted by sharp features (called edges) at specific energies, in correspondence to transitions from core shells ($1s$, $2s$, $2p_{1/2}$, $2p_{3/2}$...) at the ionisation threshold. These edges are named after the core orbitals (K, L1, L2, L3... etc.) they originate from. By analyzing the spectral shape of the XAS measurement, it is possible to derive qualitative and quantitative information on the local structure of the excited element, including, for example, the geometry and the coordination number, the oxidation state.

X-Ray absorption Spectroscopy

X-Ray absorption spectroscopy (XAS) allows to determine the local geometric and electronic structure of atoms in samples in different phases, such like gas phase, solutions or solids [13]. Experiments are usually performed at synchrotron radiation

facilities, which provide intense and tunable X-Ray beams: usually, the element that will be probed by the incoming radiation is determined by the photon energy. When an incident X-Ray beam impinges onto a sample with intensity I_0, the extent of absorption depends on the photon energy E, on sample thickness t and material, according to Beer's law:

$$I_t = I_0 e^{-\mu(E)t} \tag{2.10}$$

where $\mu(E)$ is the X-Ray absorption coefficient of the element that depends on the incoming photon energy, and basically represents the probability for a photon to be absorbed by the material. $\mu(E)$ is a smooth function of the photon energy over a large energy region, decreasing with increasing energy approximately as:

$$\mu(E) \sim \frac{dZ^4}{mE^3} \tag{2.11}$$

where d is the target density, and Z and m are the atomic number and mass, respectively. However, when E equals the binding energy of a core electron, the X-Ray energy is enough to expel a photoelectron and to create a core-hole. This effect is observed as a sharp discontinuous rise in the cross-section, the so-called *absorption edge*. Above the absorption edge, $\mu(E)$ continues to fall as $1/E^3$. After a short time (of the order of 1 fs), the core-hole is filled by an electron from a higher energy state. The corresponding energy difference is released mainly by fluorescence X-Ray or Auger electron emission [14, 15, 16].

In correspondence of an edge, the absorption coefficient exhibits the X-Ray Absorption Fine Structure (XAFS), limited to a few eV around the edge for isolated atoms, while it can extend to and beyond one thousand eV above the edge for atoms in solids, because of the contributions of other atoms surrounding the absorber one. Different regions of XAFS can be distinguished (figure 2.6) [17, 18]:

- a pre-edge and edge region, limited to a few eV around the edge;

- the structure within 30-50 eV above the edge is called XANES (X-Ray Absorption Near Edge Structure) or NEXAFS (Near Edge X-Ray Absorption Fine Structure);

- the fine structure extending from the XANES region up to typically one thousand eV is called EXAFS (Extended X-Ray Absorption Fine Structure).

The pre-edge, edge and XANES regions contain information on the local electronic and geometric structure of the absorber atom. The EXAFS region provide information on the local geometric structure surrounding a given atomic species. An example of XAFS of the Ti K-edge in anatase is reported in figure 2.6.

2.5   Scanning Tunneling Microscopy

Scanning tunneling microscopy (STM) is a very powerful microscopy technique, capable to provide information on the distribution of single atoms on a conducting surface. Moreover, with STM it is possible to reach a lateral resolution of 0.1 nm and a vertical resolution of 0.01 nm, allowing imaging and manipulation of single atoms of the investigated material [19]. In contrast to classical optical spectroscopy methods, where the extracted information is averaged over macroscopic areas, STM allows a direct correlation between the optical characteristics and the structural properties of the studied material.
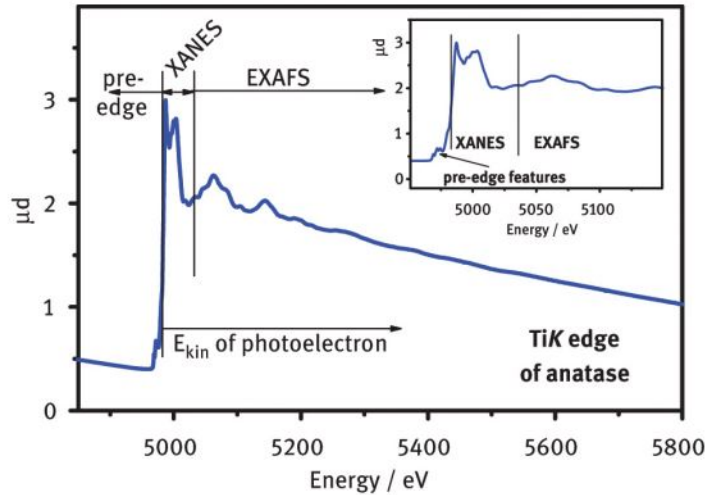
Figure 2.6: *Subdivision of the XAS spectrum in pre-edge, XANES and EXAFS regions. Taken from [18].*

2.5.1 Working principle

STM is based upon the exploitation of electron tunneling, and in particular on the exponential dependence of the transmission coefficient of electrons through a potential barrier (the tunnel current) on the thickness of the barrier. A sharp metallic tip is brought into close proximity (usually closer than 1 nm) with the surface to be studied: at these small distances, the electron wave functions of the tip and the surface overlap, leading to a finite probability of electron tunneling. The direction of tunneling (from the surface to the tip or vice versa) depends on the potential applied between the tip and the surface. The tunneling current is very sensitive to the position of the tip and will vary when the tip is on the top of a surface atom or in between two atoms. Thus, by scanning the surface with the tip and measuring the tunneling current, an atomically resolved picture of the sample surface, or a complete image of the surface topography, is produced. The current flowing I_t, typically in the range of nA or pA, drastically decreases with increasing tip-sample distance. Furthermore, I_t depends on the height of the tunnel barrier between the tip and the surface and the potential applied at the surface-tip junction. An STM is basically made up of the following parts (figure 2.7): (1) a sharp conductive tip, (2) a scan system that operates in three directions, (3) a power supply, (4) a current amplifier, (5) an electronic feedback loop, (6) a computer for data processing, and (7) a damping system to suppress external vibrations. In particular, the small tip-surface distances can be adjusted with piezo ceramics (z piezo), which are also used for the lateral displacement of the tip (x and y piezos).

STM can operate in two main scanning modes:

- Constant current mode: the tip-sample current I_t is kept constant by a feedback loop, controlling the z piezo (and then the tip-sample distance d), recording the motion of the z piezo. This is then translated into an image of the surface that contains topographic and electronic information.

- Constant height mode: the tip is kept at constant distance d over the sample during the scan process, and the current I_t is recorded. Operating in this mode allows to shorter the acquisition time, allowing the study of dynamic
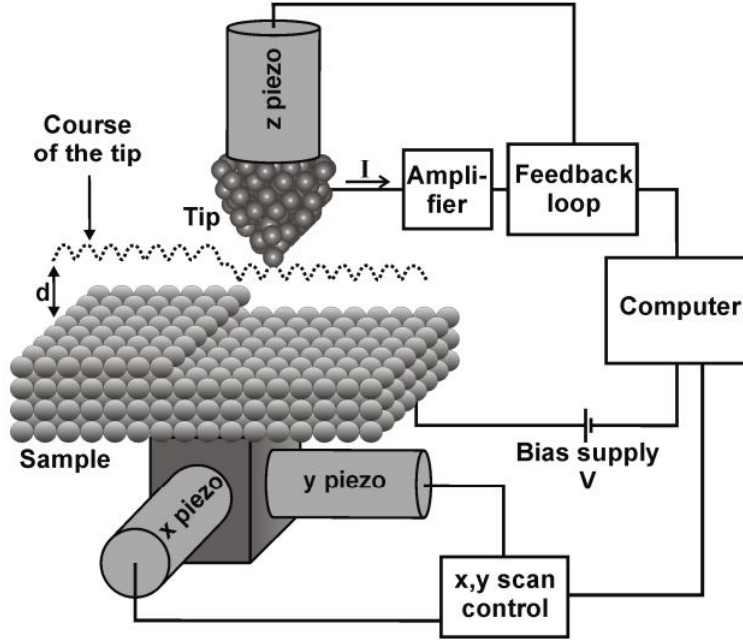
Figure 2.7: *Schematic representation of an STM setup [20]*

processes. However, its applicability is limited to flat samples, without large corrugations.

2.5.2 Theoretical approach

In order to translate the acquired images to the real atomic configuration of the probed surfaces it is necessary to model the tunneling processes in the STM junction. In fact, as already mentioned, both the contrast and the lateral resolution of the images depend on the tip-sample interaction, defined by the degree of overlap between electron wave functions and their symmetry on both sides of the tip-sample junction. These factors are determined by the applied bias, V_S, the tip material, and the tip-sample distance d. Not all these parameters are known, then, theoretical models underlay permanent refinement [21, 22].

Many approaches are based upon Bardeen's model that describes electron tunneling through a metal-insulator-metal junction by one-dimensional perturbation theory, considering both electrons as independent from each other with known eigenfunctions. [23]. In the Bardeen's model, the electron tunneling between the two electrodes can be regarded as a transition from an unperturbed initial to an unperturbed final state, with the transition probability determined by Fermi's golden rule. This model has been extended by Tersoff and Hamann to describe electron tunneling in STM junctions [24, 25]. In their model, the tip is assumed to have a s-character: under this assumption, it is possible to calculate transition matrix elements, and the tunneling current is proportional to the local density of states (LDOS) of the surface at the position of the tip. In a generalized form of the model proposed by Tersoff and Hamann, the tunneling current I_t can be derived from equation 2.12 [21, 26]:

$$I_t = \int_{-\infty}^{\infty} \rho_S(E)\rho_T(E - eV_S)T(d, E, eV_S)[f(E - eV_S, T) - f(E, T)]\, dE \qquad (2.12)$$

where ρ_S and ρ_T represent respectively the LDOS of the sample and of the tip,

this latter including the characteristics of the tip such as its shape and symmetry of the electronic states, $T(d, E, eV_S)$ is the transmission coefficient describing the tunneling probability and $f(E, T)$ is the Fermi distribution function describing the energy distribution at a temperature T. The transmission coefficient depends on the work functions of the tip and the sample (Φ_T and Φ_S respectively), on the tip-sample distance d, the energy E and the bias applied to the sample V_s according to the relation in equation 2.13:

$$T(d, E, eV_S) = exp(-\frac{2d\sqrt{2m}}{\hbar} \cdot \sqrt{\frac{\Phi_S + \Phi_T}{2} + \frac{eV_S}{2} - E}) \qquad (2.13)$$

In this thesis, the STM we used is operating a very low temperature. For temperatures close to 0K, i.e. when $k_B T << eV$, the Fermi distribution function can be approximated by a step function, and the equation 2.12 can be simplified as in equation 2.14:

$$I_T = \int_0^{eV_S} \rho_S(E)\rho_T(E - eV_S)T(d, E, eV_S) \, dE \qquad (2.14)$$

The description of electron tunneling by perturbation theory implies a weak tip-sample interaction. This assumption is valid when large tip-sample distances are considered, but it has also been demonstrated that this approximation can describe also the STM imaging properties even at small tip-sample separations for some oxide films [27].

Bibliography

[1] https://oaresearch.co.uk/cluster/.

[2] Leonard C Feldman. *Fundamentals of surface thin film analysis*. Prentice Hall.

[3] A. Bianconi, A. Marcelli, H. Dexpert, R. Karnatak, A. Kotani, T. Jo, and J. Petiau. Specific intermediate-valence state of insulating 4f compounds detected by x-ray absorption. *Physical Review B*, 35(2):806–812, 1987.

[4] M. Romeo, K. Bak, J. El Fallah, F. Le Normand, and L. Hilaire. XPS study of the reduction of cerium dioxide. *Surface and Interface Analysis*, 20(6):508–512.

[5] F. Le Normand, J. El Fallah, L. Hilaire, P. Légaré, A. Kotani, and J.C. Parlebas. Photoemission on 3d core levels of cerium: An experimental and theoretical investigation of the reduction of cerium dioxide. *Solid State Communications*, 71(11):885–889, 1989.

[6] Akio Kotani and Haruhiko Ogasawara. Theory of core-level spectroscopy in actinide systems. *Physica B: Condensed Matter*, 186-188:16–20, 1993.

[7] Tomáš Skála, František Šutara, Kevin C. Prince, and Vladimír Matolín. Cerium oxide stoichiometry alteration via Sn deposition: Influence of temperature. *Journal of Electron Spectroscopy and Related Phenomena*, 169(1):20–25, 2009.

[8] T Skála, F Šutara, M Škoda, K C Prince, and V Matolín. Palladium interaction with CeO_2, Sn-Ce-O and Ga-Ce-O layers. *Journal of Physics: Condensed Matter*, 21(5):055005, 2008.

[9] C. G. Granqvist and O. Hunderi. Optical properties of ultrafine gold particles. *Phys. Rev. B*, 16:3513–3534, 1977.

[10] Jacopo Stefano Pelli Cresi, Maria Chiara Spadaro, Sergio D'Addato, Sergio Valeri, Stefania Benedetti, Alessandro Di Bona, Daniele Catone, Lorenzo Di Mario, Patrick O'Keeffe, Alessandra Paladini, Giovanni Bertoni, and Paola Luches. Highly efficient plasmon-mediated electron injection into cerium oxide from embedded silver nanoparticles. *Nanoscale*, 11:10282–10291, 2019.

[11] C. Ruckebusch, M. Sliwa, P. Pernot, A. de Juan, and R. Tauler. Comprehensive data analysis of femtosecond transient absorption spectra: A review. *Journal of Photochemistry and Photobiology C: Photochemistry Reviews*, 13(1):1–27, 2012.

[12] Majed Chergui. Empirical rules of molecular photophysics in the light of ultrafast spectroscopy. *Pure and Applied Chemistry*, 87(6):525–536, 2015.

[13] Junko Yano and Vittal K. Yachandra. X-ray absorption spectroscopy. *Photosynthesis Research*, 102(2-3):241–254, 2009.

[14] Claudia S Schnohr and Mark C Ridgway, editors. *X-ray absorption spectroscopy of semiconductors*. Springer Series in Optical Sciences. Springer, 2015 edition.

[15] Jens Als-Nielsen and Des McMorrow. *Elements of modern X-ray physics*. Wiley-Blackwell, 2 edition.

[16] S. D. Kelly, D. Hesterberg, and B. Ravel. *Analysis of Soils and Minerals Using X-ray Absorption Spectroscopy*, chapter 14, pages 387–463. John Wiley and Sons, Ltd, 2008.

[17] Antonella Balerna and Settimio Mobilio. Introduction to synchrotron radiation. In *Synchrotron Radiation*, pages 3–28. Springer Berlin Heidelberg, Berlin, Heidelberg, 2015.

[18] Wolfgang Grünert and Konstantin Klementiev. X-ray absorption spectroscopy principles and practical use in materials analysis. *Physical Sciences Reviews*, 5(4), 2020.

[19] P.E.J. Flewitt and R.K. Wild. *Physical Methods for Materials Characterisation*. Graduate student series in materials science and engineering. Institute of Physics Pub., 1994.

[20] Hadj Mohamed Benia. *Spatially resolved optical measurements on supported metal particles and oxide surfaces with the STM*. PhD thesis, Humboldt-Universität zu Berlin, Mathematisch-Naturwissenschaftliche Fakultät I, 2008.

[21] C Julian Chen. Atomic force microscopy. In *Introduction to Scanning Tunneling Microscopy*, pages 379–400. Oxford University Press, 2021.

[22] D Drakova. Theoretical modelling of scanning tunnelling microscopy, scanning tunnelling spectroscopy and atomic force microscopy. *Reports on Progress in Physics*, 64(2):205–290, 2001.

[23] J. Bardeen. Tunnelling from a many-particle point of view. *Phys. Rev. Lett.*, 6:57–59, 1961.

[24] J. Tersoff and D. R. Hamann. Theory and application for the scanning tunneling microscope. *Phys. Rev. Lett.*, 50:1998–2001, 1983.

[25] J. Tersoff and D. R. Hamann. Theory of the scanning tunneling microscope. *Phys. Rev. B*, 31:805–813, 1985.

[26] Silvia Schintke and Wolf-Dieter Schneider. Insulators at the ultrathin limit: electronic structure studied by scanning tunnelling microscopy and scanning tunnelling spectroscopy. *Journal of Physics: Condensed Matter*, 16(4):R49–R81, 2004.

[27] W. Hebenstreit, J. Redinger, Z. Horozova, M. Schmid, R. Podloucky, and P. Varga. Atomic resolution by STM on ultra-thin films of alkali halides: experiment and local density calculations. *Surface Science*, 424(2):L321–L328, 1999.

Part I

Ultrafast dynamics of photoexcited states in CeO$_2$ films combined with plasmonic NPs

Chapter 3

Lifetime of Photogenerated Positive Charges in CeO$_2$ and Ag@CeO$_2$

As already mentioned in chapter 1, different methods have been developed and studied to extend the photocatalytic activity of ceria in the visible range, making it an efficient material for solar light harvesting. In this thesis, I will focus on the combination of cerium oxide with noble metal NPs, in particular with Ag and Au NPs (with the brief description of a preliminary work on ceria combined with Cu NPs). In the systems I will describe, plasmonic NPs are embedded within thin films of CeO$_2$. As described in chapter 1, when shined with visible light, the NPs strongly interact with incoming radiation, which triggers the localized surface plasmon resonance (LSPR). The relaxation of this excitation may lead to a charge transfer to CeO$_2$, and the presence of a Schottky barrier between the NPs and the oxide prevents a fast recombination of charge carriers. The study of the ultrafast dynamics of these systems is fundamental to construct systems with a high visible light harvesting efficiency and with an optimized density of long-living excited states, which can provide charge carriers to the environment. In this thesis, different time resolved techniques have been employed in order to characterize the dynamics of excited states and photoexcited holes on the oxide surface after the interaction with ultraviolet and visible radiation. In this chapter, I will describe the study of recombination dynamics of charge carriers onto a bare cerium oxide surface and in combination with Ag NPs, using photoemission spectroscopy.

3.1 Experimental methods

In this section, I will first report the experimental methods we used for the growth of CeO$_2$ thin films and for the deposition of Ag NPs within ceria layers, together with the spectroscopy technique for electronic characterization of these samples. Afterwards, I will describe the results obtained by Time-Resolved Photoemission Spectroscopy (trPES), that was used to study the re-neutralization characteristic time of positive charges generated by photoexcitation in ceria-based thin films.

3.1.1 Sample preparation

The samples used for the work described in this chapter are a CeO$_2$ thin film of 2 nm, used as reference sample, and a sample composed by Ag NPs embedded within

a CeO_2 matrix (from now on, I will refer to this last sample as $Ag@CeO_2$). The investigated samples have been grown in the RAGNO-1 chamber, in the SESAMo laboratory, described in 2.1. The CeO_2 sample was grown onto Cu(111) single-crystal, and the $Ag@CeO_2$ onto a Pt(111) single-crystal. Previous works revealed that the structure and morphology of CeO_2 films is compatible when the films are deposited on different single-crystal metal supports with a hexagonal surface symmetry (including Pt(111) and Cu(111) substrates) [1, 2, 3]. Before starting the deposition, it is necessary to obtain clean single-crystal substrates. The metallic substrates were prepared by repeated cycles of sputtering with Ar^+ ions and annealing in UHV until the concentration of the contaminant was below the detection limit of XPS. The repeated cycles consist in Ar^+ ($P_{Ar} \sim 10^{-6}$ Torr) sputtering (1 keV, 1 μA), followed by 5 minutes annealing (1040 K for Pt(111) and 620 K for the Cu(111)) with sputtering and finally 10 minutes annealing without sputtering. After the substrate preparation, the CeO_2 films were grown via molecular beam epitaxy (MBE), by evaporating Ce from an electron beam evaporator, in a controlled oxygen partial pressure of 10^{-7} mbar. During sample growth, the metallic substrates were kept at RT. The MBE chamber is equipped with a quartz microbalance that permits the control of the evaporation rate. The thickness of the reference CeO_2 film was chosen to be 2 nm, to have a full coverage of the substrate surface, as demonstrated in [4].

For the $Ag@CeO_2$ sample, Ag NPs were grown by evaporating Ag atoms from a Knudsen cell. Different works already demonstrated that this leads to the formation of self-assembled NPs on the CeO_2 surface [5, 6, 7]. On top of the ceria film grown on Pt(111), a nominal thickness [1] of 1.2 nm of Ag has been evaporated. Finally, in order to maximize the ceria-Ag interface, a top layer of 0.5 nm CeO_2 has been added, thinner than the bottom later to be sensitive to the interface between Ag NPs and CeO_2. After the deposition of each layer, in-situ XPS and UPS measurements were performed (figure 3.5). The samples investigated here are grown on highly reflective metal single crystals, which do not easily allow for optical characterization. A sample grown on a transparent MgO substrate with the same procedures and the same Ag nominal thickness shows a very broad LSPR-related absorption band in the visible [6].

SPRINT endstation

The investigation of recombination dynamics of charge carriers in the samples has been performed using time resolved photoemission spectroscopy (trPES) at the NFFA-SPRINT (Spin-Polarized Research Instrument in the Nanoscale and Time domain [8]) facility at Elettra, Trieste. To avoid exposure to air, an UHV suitcase ($P \sim 10^{-10}$ mbar) was used to transport the samples.

In general, PES is a powerful technique for the study of electronic properties in condensed matter systems. In trPES, ultrashort pulses in the pump-probe configuration are used, to access dynamics of the transient electronic structure of the investigated material on time scales typical of elementary electronic and lattice processes [9]. The most suitable sources of ultrashort radiation pulses, with photon energies ranging from extreme ultraviolet to hard X-Rays, are Free Electron Lasers (FELs, that will be described in the next chapter) and High Harmonic Generation (HHG) light sources.

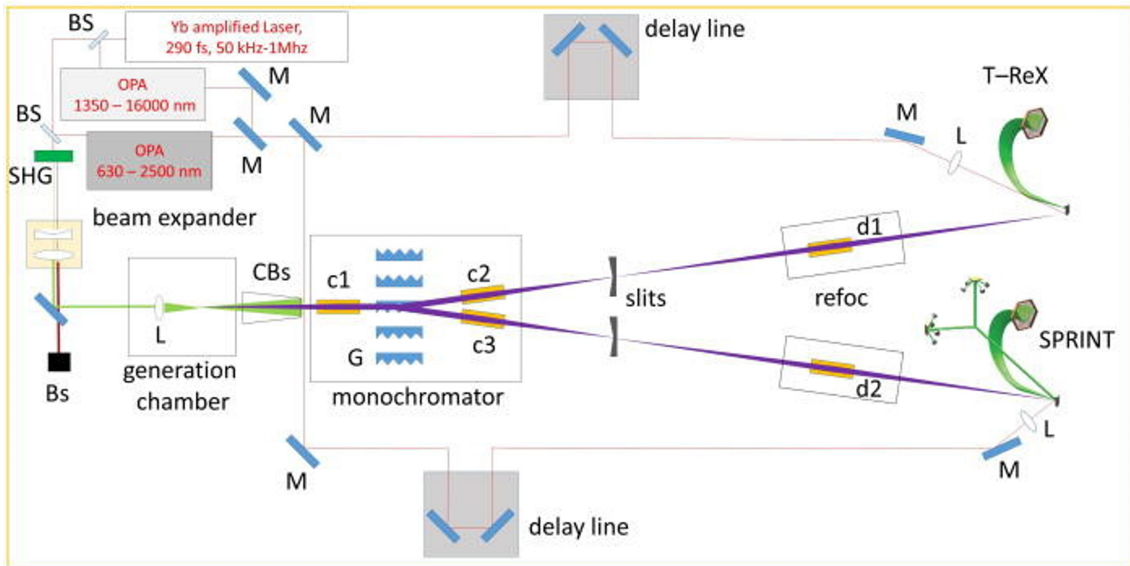[1]the nominal Ag thickness refers to the equivalent thickness of a uniform Ag film completely covering the ceria layer.

Figure 3.1: *Pump/probe setup, taken from [13]. M, mirror; BS, beam splitter; SHG, second-harmonic-generation crystal; Bs, beam stopper; CBs, cone beam stopper; L, lens; c1, c2, c3, d1, d2, toroidal focusing mirror; G, grating.*

The HHG process is a highly nonlinear optical effect, that takes place when an intense laser pulse illuminates a target (usually a gas). When the intensity of the electric field of the laser is comparable with the strength of atomic bonds in the medium [10], the light-matter interaction leads to the simultaneous generation of a number of odd harmonics of the seed photon energy. Remarkably, the intensity of the emission remains constant over a wide energy region (plateau), rather than showing a continuous exponential decrease typical for perturbative nonlinear processes [11]. The HHG process is usually described within the so-called three-step-model: tunnel ionization, free acceleration, and recombination (recollision) [12].

The full description of the NFFA-SPRINT endstation can be found in [13], and it is schematized in figure 3.1. The system is based on a Yb:KGW-based integrated femtosecond laser system (PHAROS, Light Conversion, 1030 nm, 300 fs) with two separate amplifiers pumped by the same oscillator. This configuration guarantees a high pulse-to-pulse stability. The first amplifier is used to pump an optical parametric amplifier whose output is used to provide pump pulses. The second amplifier is used to produce high harmonics of the laser fundamental constituting the probe signal. In the work presented in this chapter, we chose the 11th (26.5 eV) and the 13th harmonics (31.2 eV), with 5×10^6 and 10^7 photons per pulse. During the experiment, two pump energies have been used: 4.1 eV (i.e. approximately 300 nm) and 2.8 eV (i.e. around 440 nm), respectively, resonating with cerium oxide band gap and LSPR in Ag NPs. We used a repetition rate of 25 kHz, varying the energy-per-pulse between 0.3 and 1 μJ for the different pump-probe configurations, concentrated on a spot size of 300 μm. Electron detection is performed with a Scienta SES 2002 hemispherical electron analyzer equipped with a phosphor detector and a charge-coupled device (CCD) camera.

3.2 Space and Mirror Charges effect

As already mentioned in the previous section, PES can be used to study electronic properties in condensed matter systems. HHG light sources allows the production of

ultrashort radiation pulses with photon energies ranging from extreme ultraviolet to hard X-Rays. The use of ultrashort pulses in time-resolved PES (trPES) experiments in the pump-probe configuration provides access to the dynamics of the transient electronic structure of the investigated material on time scales typical of elementary electronic and lattice processes. However, the use of ultrashort and highly brilliant photon sources often gives rise to *space charge effects*, that cause a significant alteration of the PES spectrum and a consequent loss of the information contained in the intrinsic photoelectron energy distribution and its temporal dynamics. Since this phenomenon represents a severe limitation for trPES experiments, a great deal of research effort has been dedicated to model and minimize it. In the present work, we used the intensity variation of a specific PES feature generated by the space charge to study the dynamics of the surface pump-generated carriers in the two systems previously described (i.e., bare CeO_2 thin films and combined with Ag NPs). This study was carried out by modeling the dynamics of the space charge effect and its effect on PES spectra. In this way, trPES can provide complementary information to UV-Vis pump-probe absorption techniques, which are principally sensitive to the bulk properties of the sample and inefficient in separating the contributions of holes and electrons. Using the proposed procedure, we extracted information on the re-neutralization of positive carriers in the Ag@CeO_2 system by the pump, providing a physical interpretation of the results, which is fundamental in view of future applications in photocatalysis of the investigated materials [14, 15, 16, 17, 18].

Space charge effects are due to the mutual Coulomb interaction between the photoelectrons leaving the sample surface after excitation by an ultrashort light pulse of sufficient intensity. In pump-probe trPES experiments, the intense laser pump pulse generates numerous photoelectrons that leave the surface with a spatial distribution determined by their kinetic energy. The photoelectrons generated by the far less intense probe pulse, while traveling toward the detector, interact with the space charge, which introduces, in general terms, a broadening and a shift by up to several eV of the apparent energy distribution, decreasing the effective energy resolution of the experiment and preventing the detection of important information related to pump-induced photoexcited charge dynamics. Moreover, the effect of space charge is combined with the effect of holes left behind in the sample following the emission of photoelectrons, which is often referred to as the mirror charge effect [14, 15, 19]. Figure 3.3 schematizes the space and mirror charge effect in trPES. In the scheme, two different situations are presented, depending on the delay time t between the pump and the probe pulses. When $t > 0$, i.e. when the pump pulse shines on the sample before the probe pulse, a large number of photoelectrons is generated, leaving holes onto the sample surface. When a probe generated photoelectron exits the sample surface, it feels the effects of the electric fields generated by both the (negative) space and the (positive) mirror charges. On the other hand, when $t < 0$, the probe-generated photoelectron is emitted from the sample and it starts to travel towards the detector with a certain kinetic energy. When the pump pulse hits the surface, the photogenerated hole distribution is assumed to be completely screened by the pump-generated electron cloud (see figure 3.3).

Figure 3.2b reports an example of the PES valence band spectra of the CeO_2 sample at a positive ($+100$ ps) and a negative (-100 ps) delay time with the pump at 4.1 eV as well as a reference spectrum acquired without the pump. The spectra were acquired with a HHG probe at 31.2 eV (13th harmonics). The spectra show an intense and broad peak between 7 and 4 eV binding energy (BE) due to emissions from the valence band of the O 2p character and a less intense peak between 3 and 1
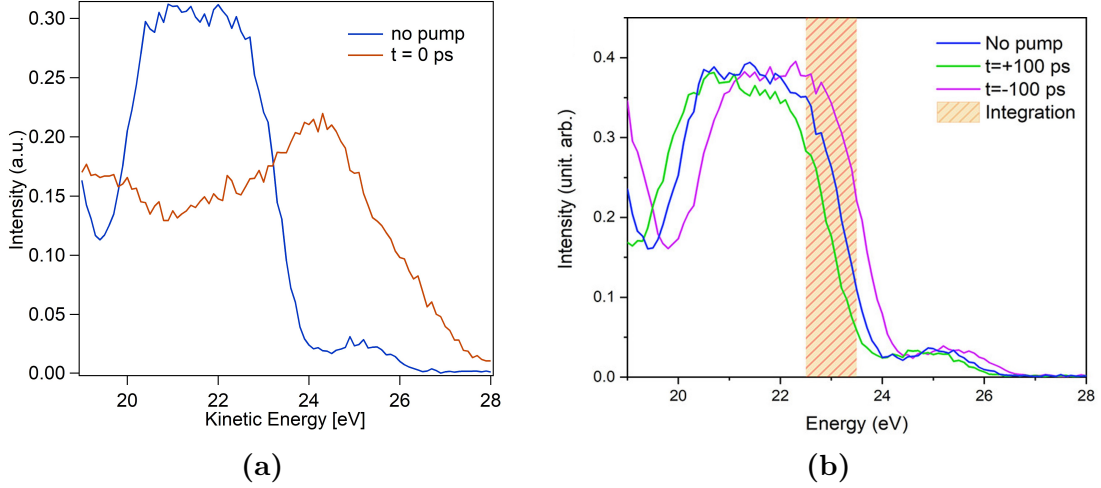
Figure 3.2: *PES spectrum (pump at 4.1 eV) of the valence band of the CeO$_2$ sample, obtained using the HHG 13th harmonic (31.2 eV): (a) without the pump (blue curve) and at t=0 ps (pump and probe simultaneously shining the sample). The spectral shape is lost for short pump-probe delays. (b) PES spectrum without the pump, at +100 ps (green curve) and -100 ps (purple curve) delay times. The red box represents the energy window to which the acquisition was restricted.*

eV due to emissions from occupied Ce 4f levels. At positive (negative) delay times, the spectrum appears rigidly shifted toward lower (higher) kinetic energies, with respect to the reference spectrum. The energy shift of the spectrum is the combination of the effects of space charge, which shifts the spectrum toward higher kinetic energies, and mirror charge, which shifts the spectrum in the opposite direction. The spectra, at the delay times that have been considered in the presented analysis (i.e., for $|t| \gtrsim 15ps$), only show a rigid shift in kinetic energy while their shape is unaltered, while for shorter delay times, as shown in 3.2a, the shape of the spectrum appears strongly altered.

3.3 Model and acquisition procedure

The aim of this work is to obtain information on the re-neutralization time of photogenerated holes that remain onto the surface after the interaction of the sample with a highly brillant and ultra-short light pulse. This information has been extracted exploiting the space and mirror charge effects caused by the interaction of the intense pump pulse with the investigated samples (CeO$_2$ and Ag@CeO$_2$), at two different energies: one resonating with ceria band gap, the other one with LSPR excitation in Ag NPs.

The data analysis is based upon the mean-field model described by Oloff et al. in the works [15] and [14]. This model is based on three main assumptions. The first one is that the cloud of electrons excited by the pump pulse has a Gaussian charge distribution in the surface plane (x and y directions) and moves along the direction normal to the surface (z direction, green arrow in figure 3.3), as schematized in figure 3.3. Moreover, the number of electrons generated by the pump pulse is assumed to be much higher than that of electrons generated by the probe. The validity of this assumption for the experiment here described was verified by measuring the drain current generated by the pump and the probe pulses: the current generated by the probe was ~ 2 pA, significantly lower than the pump-induced drain currents
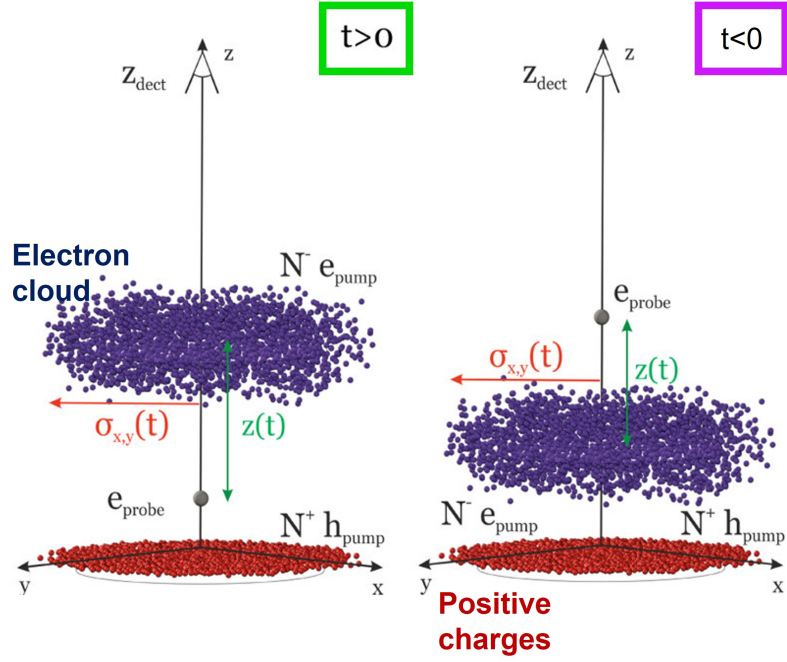
Figure 3.3: *Space charge generation (the electrons are denoted in blue and the holes are denoted in red) and its effects on the probe electron dynamics depending on z(t) (the distance between the electron cloud and the probe electron). The schematics on the left represent the situation when the pump pulse hits the sample before the probe (i.e. delay time t > 0), while the on the right is reported the case for t < 0.*

reported in table 3.2. Only for the CeO_2 sample pumped below the gap, the drain current is close to the limit conditions for the validity of the model, being just 1 order of magnitude higher than the probe-generated one. Finally, the spectral shape is assumed to be constant, and only the shift is considered: this is a good approximation for delay times $|t| \gtrsim 15$ ps.

The kinetic energy shift $\mu(t)$ experienced by a photoelectron generated by the probe pulse traveling toward the detector is due to the electric fields generated by the pump-induced electron cloud and by the positive carriers on the sample surface, as in equation 3.1.

$$\mu(t) = E_{k0} - E'_k = e(V^-(z(t)) - V^+(z(t))) \tag{3.1}$$

where E_{k0} is the unperturbed electron kinetic energy, E'_k is the perturbed one, e is the elementary charge, while V^- and V^+ are respectively the electrostatic potentials generated by the space charge (electrons) and by the mirror charge (positive charges) measured at a distance z_{det} (analyzer aperture distance from the sample, indicated by the detector in figure 3.3). The situation is schematized in figure 3.3: the effects of the space (blue cloud in figure 3.3) and mirror (red cloud in figure 3.3) charges depend on $z(t)$, that is a function of the delay time between the pump and the probe pulses.

The electrostatic potential generated by the pump-induced electron and hole clouds in the Gaussian shape approximation can be written as [20]:

$$V^\pm(z(t)) = \frac{N^\pm e}{4\pi^{3/2}\epsilon_0} \int_0^\infty \frac{exp(\frac{-z(t)^2}{2\sigma_z^2+q})}{\sqrt{(2\sigma_x^2+q)+(2\sigma_y^2+q)+(2\sigma_z^2+q)}}\, dq \tag{3.2}$$
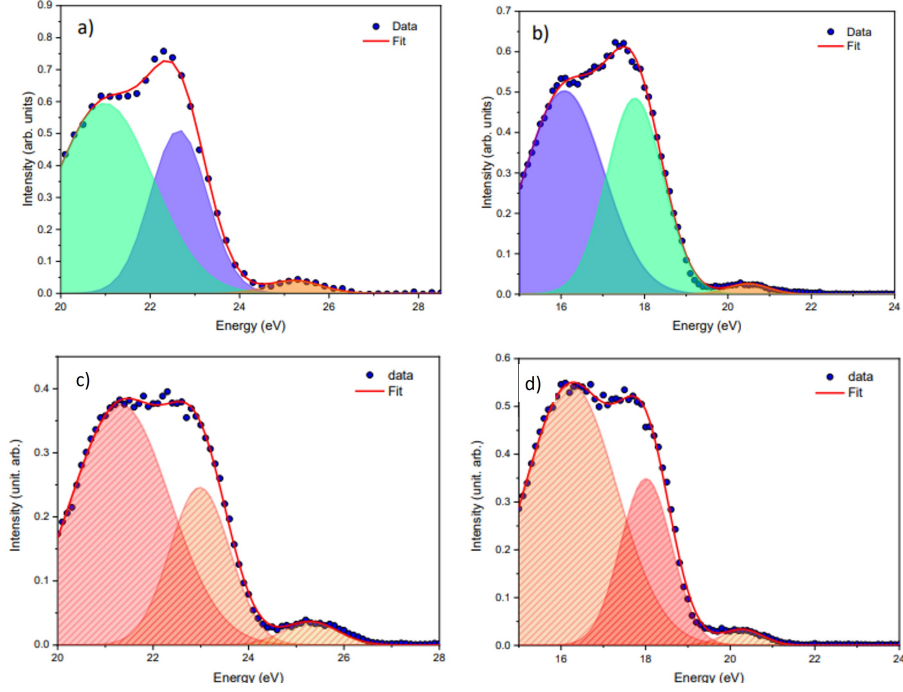
Figure 3.4: *PES spectra of (a) and (b) Ag@CeO$_2$ and (c) and (d) CeO$_2$ probed with HHG at (a) and (c) 31.2 eV and at (b) and (d) 26.5 eV.*

where N^- and N^+ are, respectively, the number of photoelectrons and holes generated by the pump, e is the elementary charge, ϵ_0 is the vacuum permittivity constant, $\sigma_{x,y,z}$ are the standard deviations of the Gaussian distribution in the three spatial directions (red arrows in figure 3.3), and $z(t)$ is the distance between the probe-generated electron and the space charge distribution. The independent variable q in equation 3.2 includes the time and spatial evolution of the Gaussian distribution, as explained in [20]. Following Oloff et al.'s works [14, 15] the electron cloud spatial expansion was taken into account using a correction linearly dependent on the cloud velocity. In equation 3.2, the number of holes on the surface (mirror charge) can be written as:

$$N^+ = N^- \cdot X \cdot e^{-\frac{t}{\tau}} \tag{3.3}$$

where X is the fraction of holes that survive rapid recombination such as Auger recombination and τ is the hole recombination time constant, characteristic of the material. For negative delay times (i.e., when the probe pulse reaches the sample before the pump pulse), the photogenerated hole distribution is assumed to be completely screened by the pump-electron cloud, so $V^+(z(t < 0)) = 0$ (see schematics in figure 3.3).

As mentioned in the previous section, we only considered times $|t| \gtrsim 15$ ps, where the spectral shape is unaltered and only the shift is relevant. Here, the PES intensity within a fixed kinetic energy window, centered where the spectrum intensity shows large variations, e.g., at the top of the valence band, can be directly correlated to the energy shift of the spectra (box in figure 3.2b). This gave us the possibility to restrict the acquisition to an energy window of 1 eV width, reducing the acquisition time, rapidly improving the statistics in relatively stable conditions.

The valence band spectra shown in figure 3.2b were modeled using three Gaussians, two to reproduce the O 2p and one for the Ce 4f peak, as reported in figure 3.4. The extracted Gaussian parameters are reported in table 3.1. For each Gaussian, the kinetic energy shift $\mu(t)$, due to the interaction between a probe generated

Sample	Energy (eV)	A1 (a. u.)	B1 (eV)	C1 (eV)	A2 (a.u.)	B2 (eV)	C2 (eV)	A3 (a.u.)	B3 (eV)	C3 (eV)
Ag@CeO$_2$	31.6	0.51	22.64	0.9	0.6	20.98	1.54	0.04	25.23	0.83
	26.5	0.50	16.08	1.34	0.49	17.77	0.96	0.026	20.49	0.69
CeO$_2$	31.6	0.38	21.32	1.47	0.25	22.98	0.89	0.04	25.3	0.80
	26.5	0.54	16.23	1.54	0.35	18.01	0.85	0.03	20.29	0.68

Table 3.1: *Parameters of the Gaussians used for fitting the PES.*

photoelectron and the space and mirror charges, calculated using 3.1, can be related to the integral of the measured PES intensity in the chosen energy interval by:

$$J^{(i)}(t) = I_0^{(i)} \int_{E_1}^{E_2} e^{-(E-\mu_0^{(i)}-\mu(t))^2/\sigma_0^{(i)}} \, dE \qquad (3.4)$$

where $\mu_0^{(i)}$, $I_0^{(i)}$ and $\sigma_0^{(i)}$ represent, respectively, the position of the centroid, the intensity, and the variance of the i-th Gaussian in the spectrum acquired without the pump (evaluated from the fit of the full PES spectra reported figure 3.4), with i ranging from 1 to 3, and E_1 and E_2 are the extremes of the chosen energy interval. The overall intensity integral variation, as a function of delay time between the pump and the probe pulses, is given by the sum:

$$J(t) = J^{(1)}(t) + J^{(2)}(t) + J^{(3)}(t) \qquad (3.5)$$

The intensity of the photoemission spectrum, measured within the chosen energy window, as a function of the delay time t was fit using equation 3.4. The free parameters of the fit were N^- (the number of photogenerated electrons), X (the fraction of holes in the sample that survive fast recombination), and τ (the hole recombination time constant). The x and y dimensions of the electron cloud for 3.2 at t = 0 were derived from the size of the spot on the sample (about 300 μm of FWHM [13]), while the z dimension was fixed to tens of nanometers. The number of pump-generated electrons N^- is compared with that of the drain current, as reported in table 3.2.

3.4 Results and discussion

3.4.1 XPS and UPS

In-situ XPS and UPS spectra have been acquired after sample growth to obtain information on the surface electronic structure of the samples. The Ce 3d XPS spectra of the two samples (figure 3.5a) show a line shape compatible with a dominant CeO$_2$ stoichiometry, confirmed by the good quality of the fit obtained using only Ce^{4+}-related components. The Ce^{3+} concentration is therefore below the sensitivity of the technique, as observed for ultrathin films grown in similar conditions [1]. The UPS spectra of the two samples, reported in figure 3.5, show a broad feature between 2 and 5 eV assigned to the valence band with the O 2p character. The minor differences in shape between the spectra acquired *in-situ* and the spectra shown in figure 3.2b, can be ascribed to the difference in photon energy between the HeI lamp, 21.2 eV, and the HHG at the SPRINT facility (26.5 and 31.2 eV). In the Ag@CeO$_2$ sample, the O 2p-related main feature around 3 eV is attenuated in intensity as compared to the bare ceria film and to Ag-related features around 5 eV and at the Fermi level [6]. The absence of valence band features related to the metallic substrates confirms the complete coverage of the substrate surface by the oxide films.
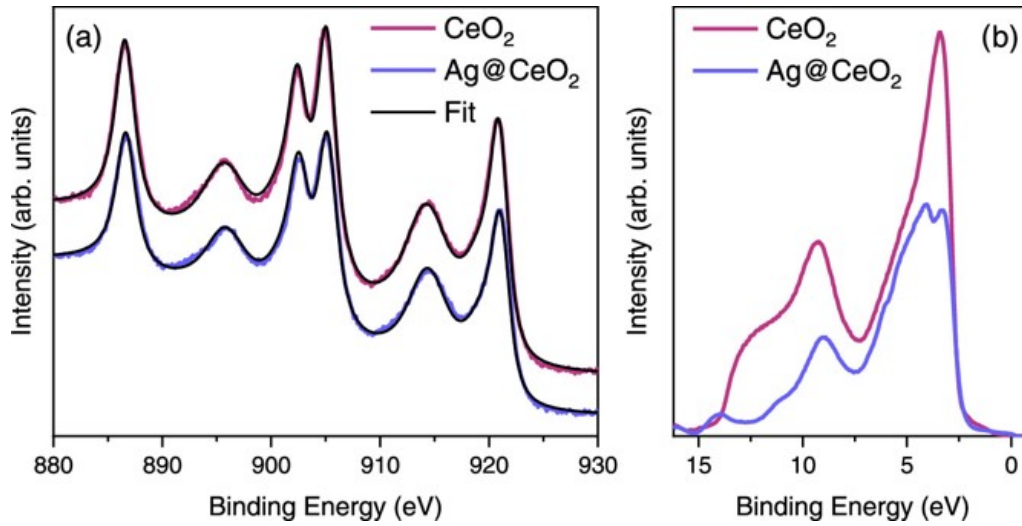
Figure 3.5: *(a) XPS Ce 3d spectra of CeO_2 (red) and $Ag@CeO_2$ (lilac) with Al K_α photons (1486 eV). The black lines are the fits of the spectra using Ce^{4+}- and Ce3+-related components. (b) UPS spectra of CeO_2 and $Ag@CeO_2$ at a photon energy of 21.2 eV.*

In analogy with previous experiments made on these systems [21, 22], the trPES measurements have been acquired on the CeO_2 and the $Ag@CeO_2$ samples using two different pump energies: one at 4.1 eV, resonating with ceria band gap, and one at 2.8 eV, at the Ag LSPR maximum and below the CeO_2 band gap. The trPES data for each pump and delay time have been acquired in the 1 eV energy window centered at the top of the valence band, as described in the previous section. Figure 3.6 shows the difference between intensity J of the photoemission spectrum in the selected window and that of the spectrum without the pump as a function of delay time (blue dots) for the two different samples and the two pump energies. The differences in the error bar intensities depend on the statistics (the number of acquisitions, determined by the acquisition time). The acquisition limited to $t \gtrsim 15$ ps prevented the detection of ultrafast dynamic decays, often observed in oxides after band-gap excitation [23, 24]. At negative delay times, J shows an increasing intensity as the delay time approaches zero for both samples and pump energies. The observed behavior agrees with a progressive shift of the spectra toward higher kinetic energies with decreasing Δt because of the pump-generated space charge (while the effect of the mirror charges is negligible). The two samples pumped above the band gap (figures 3.6a, c) show a marked asymmetry with respect to time 0. At positive delay times, both samples show a decrease in intensity (faster than the rise time at negative delays) and then, at delays longer than 100 ps, a slower increase of J, indicating that for positive delay times both space and mirror charge contributions are simultaneously at play. The rapid decrease of J(t) is due to the shift toward lower kinetic energies induced by the positive mirror charge, which dominates at short delay times [15, 19] while this is partially compensated by the presence of the space charge at longer delay times. At longer delay times, J(t) should tend to the same values; however, our temporal window was not wide enough to reach that condition. A similar behavior is observed at positive delays also for the $Ag@CeO_2$ sample with the pump at the LSPR of Ag (figure 3.6d), although in this case, the variation with respect to negative delays is less pronounced, in agreement with a lower density of holes generated in the sample in this case. Finally, the CeO_2 sample pumped below the band gap shows an almost symmetric behavior
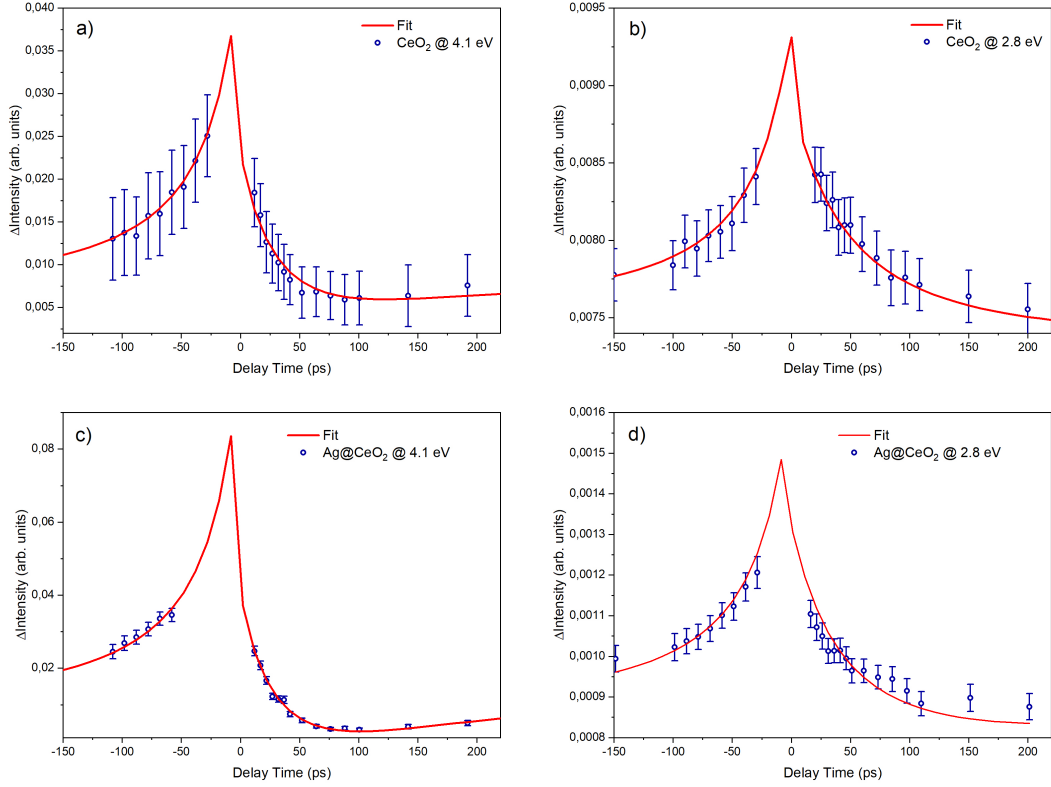
Figure 3.6: *PES area intensity within the chosen energy for the CeO_2 sample pumped (a) above (4.1 eV) and (b) below (2.8 eV) the band gap as a function of delay time (blue dots). The dynamics were obtained using a HHG probe of 31.2 eV for panels (a, d) and 26.5 eV for panels (b, c). Panels (c, d) show the intensity for $Ag@CeO_2$ pumped above (4.1 eV) and below (2.8 eV) the CeO_2 band gap. Panel (c) is obtained using a HHG probe of 26.5 eV, while panel (d) is obtained using a HHG probe of 31.2 eV.*

at positive and negative delay times (figure 3.6b). This is consistent with a fast recombination and with the expected very low density of holes formed in this sample, which has an extremely low absorbance at 2.8 eV [21]. The data presented in figure 3.6 were fitted using equation 3.4, reported as red lines in the figure. The free fitting parameters, reported for each sample and pump energy in table 3.2 are the fraction X of excited holes, their lifetime τ, and the number of photogenerated electrons N^-. The Gaussian functions used to describe the PES for each probe energy and the relative parameters for each sample, are reported in figures 3.4 and in table 3.1.

Then, it is possible to exploit space and mirror charge effects to obtain information on the dynamics of charge recombination in the material, in particular, on pump-induced holes, within the investigated time range. From the values extracted from the fit in table 3.2, the correlation between the space charge effect and the drain current is evident by comparing the values of current and the number of photogenerated holes N^-. Indeed, the ultrathin films used for the present experiment are grown on metallic substrates, and the Fermi level of the sample is at equilibrium with that of the experimental apparatus connected to the ground. The pump excitation leads to the formation of holes on the surface of the samples induced by different processes. The fitting procedure makes it possible to extract information on the compensation of such holes by the drain current from the ground and to infer important properties of the material based on the observed behavior. By comparing the values of N^- in the table 3.2, it is possible to notice an increase in electron yield in the presence of Ag NPs, that is partially ascribed to the direct emission of

Sample	Pump Energy (eV)/Fluence (μJ)	τ (ps)	X	N^-	I_{drain} (pA)
CeO$_2$	4.1/0.7	150	0.46	2700	104 (2.6 $\times 10^4$ carriers)
	2.8/0.9	87	0.29	140	27 (6.7 $\times 10^3$ carriers)
Ag@CeO$_2$	4.1/0.7	153	0.54	6500	600 (1.5 $\times 10^5$ carriers)
	2.8/1	300	0.35	1900	320 (8 $\times 10^4$ carriers)

Table 3.2: *Hole lifetime (τ), fraction of excited holes (X) and number of photogenerated electrons (N^-) extracted from the fit in figure 3.6, and measured drain current for the CeO$_2$ and Ag@CeO$_2$ samples at the two different pump energies (4.1 eV, i.e. above the CeO$_2$ band gap and 2.8 eV, below the gap). The values of the drain current are normalized to the laser frequency.*

electrons from the NPs into the vacuum through multiphoton processes at both 4.1 and 2.8 eV, although the latter energy is expected to be less efficient (considering that the intensity of the two pumps is low and similar). For this reason, the photoemission from defect levels should play a predominant role in the space charge formation. The introduction of Ag NPs within the CeO$_2$ films should increase the density of defects in the oxide matrix.

The band-gap excitation in ceria by the 4.1 eV pump leads to the formation of a large fraction of holes with a lifetime on the order of 100 ps on both samples. The fraction of estimated mirror charges and their lifetime does not show significant changes if Ag NPs are introduced into the oxide film since at this pump energy the holes are mainly formed within the oxide film. This is a further confirmation of the fact that the two films have comparable properties in spite of the different substrates used. This can be rationalized by considering that charge re-neutralization by electrons from the grounded substrate most likely takes place not only at ideal interface sites (film/substrate) overcoming the Schottky barrier but mainly along domain boundaries and defect sites. Although the pump wavelength of 4.1 eV is energetic enough to excite interband transitions in the Ag NPs, these are expected to have a lower cross section and to decay much more rapidly, compared to the above-band-gap excitation in the surrounding oxide [22], thus having a negligible effect on the photoelectrons at delay times longer than 15 ps. A lifetime for the holes above 100 ps, determined from trPES measurements, is consistent with the persistence of the ground-state bleaching feature for hundreds of picoseconds, observed in the same systems by femtosecond transient absorption spectroscopy after the above-band-gap excitation in [22]. Some other oxides, like TiO$_2$ in the form of single crystals with low defect concentrations, show comparatively long lifetimes of photoexcited states [25, 26]. On the other hand, hole lifetimes on the order of a few picoseconds have been reported for Fe$_2$O$_3$ thin films unless trapping states are involved [27].

In contrast with the similar behaviour of the ceria films with and without the NPs obtained by using a pump above CeO$_2$ band gap, the results obtained with a pump at 2.8 eV are quite different for the two samples. As reported in table 3.2, in the CeO$_2$ sample, a small fraction of holes is detected, with a lifetime of less than 100 ps. In this case, the holes are mainly generated by the excitation of low-density defect sites, or by multiphotonic absorption. The holes recombine in less than 100 ps, with electrons coming from the grounded metallic substrate, expected to propagate via hopping or through CeO$_2$ defects like domain boundaries. When Ag NPs are introduced, the efficiency of carrier generation increases by more than 1 order of magnitude (see drain currents and N$^-$ values reported in table 3.2). This can be related to the increased defect density generated at the interface between CeO$_2$
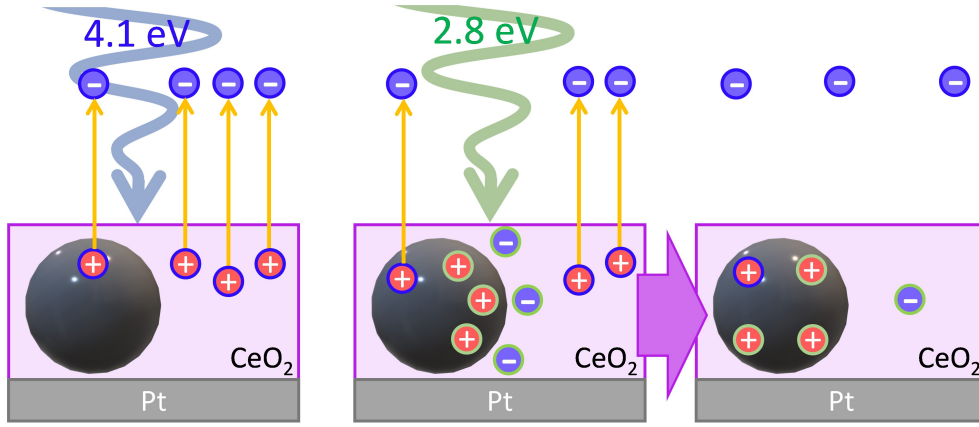
Figure 3.7: *Sketch of the processes that dominate at different pump energies for the Ag@CeO$_2$ sample. (a) The pump at 4.1 eV induces the formation of holes both in the NPs and in the oxide by defect states and multiphoton-induced photoemission; (b) the pump at 2.8 eV induces the formation of a few holes in the oxide and in the NPs by multiphoton-induced photoemission (blue contours) and of a relevant number of holes on the NPs via plasmon-mediated electron injection from the NP to the oxide (green contour); (c) the electrons and holes in the oxide recombine within short times (< 15 ps), leaving a relevant fraction of uncompensated positive charges on the NP surface.*

and the Ag NPs and to the excitation of LSPRs, which introduces a significant perturbation in the system. The fraction of excited holes is comparable to the one in the sample without the NPs, but they persist for significantly longer lifetimes of several hundreds of picoseconds, i.e., above the considered delay time. The longer lifetime of holes generated in the Ag@CeO$_2$ sample with the pump energy resonating with LSPR, can be qualitatively explained by considering that a high number of positive carriers are formed at this energy on the NP surface due to the injection of electrons, stemming from the LSPR decay, into CeO$_2$ [22, 28].

The sketch in figure 3.7 summarizes the processes that are expected to occur. At an excitation energy of 4.1 eV, the holes on the NPs are mainly generated by defects and multiphotonic photoemission (figure 3.7a), while using a 2.8 eV pulse, the holes are expected to be mainly generated by plasmon-mediated electron injection into CeO$_2$ (figure 3.7b). Most of the carriers formed in the Ag NPs after LSPR de-excitation survives for relatively long times due to the presence of a Schottky barrier between the NPs and the oxide, which prevents their recombination with electrons injected into the oxide. The corresponding injected electrons possibly compensate the holes directly formed on the oxide within shorter times, leading to a situation in which most of the unscreened positive charge is located on the NP surface within relatively short times (certainly well below 15 ps) from excitation (figure 3.7c). On the contrary, at 2.8 eV in the CeO$_2$ film, the holes due to defect state absorption are neutralized by means of fast nonradiative recombination with the electrons from the substrate. The mirror charge lifetimes resulting from the fit are related to the decay of the populations of the positive charges in the NPs and in CeO$_2$. Thus, the significantly different lifetimes extracted for the excitation at 2.8 eV for the CeO$_2$ sample (87 ps) and Ag@CeO$_2$ (300 ps) agree with the expected longer re-neutralization times of the positive carriers generated in the metal NPs as compared to the holes present in the ceria film. A further consideration that can be made based on the obtained results is that even the positive carriers generated after LSPR excitation in the Ag NPs recombine within a few hundreds

of picoseconds, preventing the accumulation of charges, which would hinder further electron injection to the oxide. This is a relevant aspect for an effective application of CeO_2 combined with plasmonic NPs as an efficient visible light photocatalyst. In previous works [22, 28] based on ultrafast optical UV-Vis and X-Ray ultraviolet spectroscopies, it was shown that either during or after the excitation of the LSPR in the Ag NPs there is significant efficiency of injection of electrons from the Ag into CeO_2. This process was shown to occur on a time scale of fewer than 200 fs, which is well below the temporal window available in the present experiment. However, the dynamics of the neutralization of the positive charges (holes) in the Ag NPs could not be easily studied using the techniques employed in the previous works. The approach here used allows us to isolate the effect of photogenerated holes, which play a relevant role in the functionality of the investigated system.

3.5 Conclusions

The work presented in this chapter exploits the space and mirror charge effect in trPES to infer information on the dynamics of photoexcited holes in a cerium oxide film, also in combination with plasmonic Ag NPs on time scales above 15 ps. We have applied a procedure that makes it possible to significantly reduce the acquisition times, allowing an increase in the number of samples and pump energies to be investigated in a single experiment. More importantly, the analysis of the time-resolved photoemission spectra allowed us to infer that the above-band-gap excitation in cerium oxide leads to the formation of holes with lifetimes exceeding 100 ps, independent of the presence of Ag NPs. The sub-band-gap excitation, on the other hand, results in the formation of holes with lifetimes on the order of a few tens of picoseconds in CeO_2, possibly induced by defect-related transitions or multiphoton absorption. Interestingly, when the oxide is coupled with Ag NPs, the excitation of the sub-band-gap localized surface plasmon resonance leads to the formation of positive charges in the metal with lifetimes exceeding 300 ps. This study represents an example of how to exploit the space charge effect in gaining access to the carrier dynamics in the CeO_2-based materials within the picosecond range of time, which is fundamental to describe the photocatalytic processes.

Bibliography

[1] P. Luches, F. Pagliuca, S. Valeri, and F. Boscherini. Structure of ultrathin CeO_2 films on Pt(111) by polarization-dependent x-ray absorption fine structure. *The Journal of Physical Chemistry C*, 117(2):1030–1036, 2013.

[2] Thorsten Staudt, Yaroslava Lykhach, Lutz Hammer, M. Alexander Schneider, Vladimir Matolín, and Jörg Libuda. A route to continuous ultra-thin cerium oxide films on Cu(111). *Surface Science*, 603(23):3382–3388, 2009.

[3] David C. Grinter, Roslinda Ithnin, Chi L. Pang, and Geoff Thornton. Defect structure of ultrathin ceria films on Pt(111): Atomic views from scanning tunnelling microscopy. *The Journal of Physical Chemistry C*, 114(40):17036–17041, 2010.

[4] P. Luches, F. Pagliuca, and S. Valeri. Morphology, stoichiometry, and interface structure of CeO_2 ultrathin films on Pt(111). *The Journal of Physical Chemistry C*, 115(21):10718–10726, 2011.

[5] Shanwei Hu, Yan Wang, Weijia Wang, Yong Han, Qitang Fan, Xuefei Feng, Qian Xu, and Junfa Zhu. Ag nanoparticles on reducible CeO_2(111) thin films: Effect of thickness and stoichiometry of ceria. *The Journal of Physical Chemistry C*, 119(7):3579–3588, 2015.

[6] Jacopo Stefano Pelli Cresi, Enrico Silvagni, Giovanni Bertoni, Maria Chiara Spadaro, Stefania Benedetti, Sergio Valeri, Sergio D'Addato, and Paola Luches. Optical and electronic properties of silver nanoparticles embedded in cerium oxide. *The Journal of Chemical Physics*, 152(11):114704, 2020.

[7] Francesco Benedetti, Paola Luches, Maria Chiara Spadaro, Gabriele Gasperi, Sergio D'Addato, Sergio Valeri, and Federico Boscherini. Structure and morphology of silver nanoparticles on the (111) surface of cerium oxide. *The Journal of Physical Chemistry C*, 119(11):6024–6032, 2015.

[8] https://www.trieste.nffa.eu/.

[9] Masaki Oura, Tatsuya Wagai, Ashish Chainani, Jun Miyawaki, Hiromi Sato, Masaharu Matsunami, Ritsuko Eguchi, Takayuki Kiss, Takashi Yamaguchi, Yasuhiro Nakatani, Tadashi Togashi, Tetsuo Katayama, Kanade Ogawa, Makina Yabashi, Yoshihito Tanaka, Yoshiki Kohmura, Kenji Tamasaku, Shik Shin, and Tetsuya Ishikawa. Development of a single-shot CCD-based data acquisition system for time-resolved X-ray photoelectron spectroscopy at an X-ray free-electron laser facility. *Journal of Synchrotron Radiation*, 21(1):183–192, 2014.

[10] M Ferray, A L'Huillier, X F Li, L A Lompre, G Mainfray, and C Manus. Multiple-harmonic conversion of 1064 nm radiation in rare gases. *Journal of Physics B: Atomic, Molecular and Optical Physics*, 21(3):L31–L35, 1988.

[11] M.C. Kohler, T. Pfeifer, K.Z. Hatsagortsyan, and C.H. Keitel. Chapter 4 - frontiers of atomic high-harmonic generation. In Paul Berman, Ennio Arimondo, and Chun Lin, editors, *Advances in Atomic, Molecular, and Optical Physics*, volume 61 of *Advances In Atomic, Molecular, and Optical Physics*, pages 159–208. Academic Press, 2012.

[12] Jeffrey L. Krause, Kenneth J. Schafer, and Kenneth C. Kulander. High-order harmonic generation from atoms and ions in the high intensity regime. *Phys. Rev. Lett.*, 68:3535–3538, 1992.

[13] Riccardo Cucini, Tommaso Pincelli, Giancarlo Panaccione, Damir Kopic, Fabio Frassetto, Paolo Miotti, Gian Marco Pierantozzi, Simone Peli, Andrea Fondacaro, Aleksander De Luisa, Alessandro De Vita, Pietro Carrara, Damjan Krizmancic, Daniel T. Payne, Federico Salvador, Andrea Sterzi, Luca Poletto, Fulvio Parmigiani, Giorgio Rossi, and Federico Cilento. Coherent narrowband light source for ultrafast photoelectron spectroscopy in the 17–31 eV photon energy range. *Structural Dynamics*, 7(1):014303, 2020.

[14] L.-P. Oloff, K. Hanff, A. Stange, G. Rohde, F. Diekmann, M. Bauer, and K. Rossnagel. Pump laser-induced space-charge effects in HHG-driven time- and angle-resolved photoelectron spectroscopy. *Journal of Applied Physics*, 119(22):225106, 2016.

[15] Lars-Philip Oloff, Ashish Chainani, Masaharu Matsunami, Kazutoshi Takahashi, Tadashi Togashi, Hitoshi Osawa, Kerstin Hanff, Arndt Quer, Ryuki Matsushita, Ryutaro Shiraishi, Maki Nagashima, Ayato Kimura, Kotaro Matsuishi, Makina Yabashi, Yoshihito Tanaka, Giorgio Rossi, Tetsuya Ishikawa, Kai Rossnagel, and Masaki Oura. Time-resolved HAXPES using a microfocused XFEL beam: From vacuum space-charge effects to intrinsic charge-carrier recombination dynamics. *Scientific Reports*, 6(1), 2016.

[16] S. Passlack, S. Mathias, O. Andreyev, D. Mittnacht, M. Aeschlimann, and M. Bauer. Space charge effects in photoemission with a low repetition, high intensity femtosecond laser source. *Journal of Applied Physics*, 100(2):024912, 2006.

[17] R Al-Obaidi, M Wilke, M Borgwardt, J Metje, A Moguilevski, N Engel, D Tolksdorf, A Raheem, T Kampen, S Mähl, I Yu Kiyan, and E F Aziz. Ultrafast photoelectron spectroscopy of solutions: space-charge effect. *New Journal of Physics*, 17(9):093016, 2015.

[18] S. Hellmann, K. Rossnagel, M. Marczynski-Bühlow, and L. Kipp. Vacuum space-charge effects in solid-state photoemission. *Phys. Rev. B*, 79:035402, 2009.

[19] X.J. Zhou, B. Wannberg, W.L. Yang, V. Brouet, Z. Sun, J.F. Douglas, D. Dessau, Z. Hussain, and Z.-X. Shen. Space charge effect and mirror charge effect in photoemission spectroscopy. *Journal of Electron Spectroscopy and Related Phenomena*, 142(1):27–38, 2005.

[20] S. Kheifets. Potential of a three-dimensional gaussian bunch. *3 pp.*, page (1976)., 1976.

[21] Jacopo Stefano Pelli Cresi, Lorenzo Di Mario, Daniele Catone, Faustino Martelli, Alessandra Paladini, Stefano Turchini, Sergio D'Addato, Paola Luches, and Patrick O'Keeffe. Ultrafast formation of small polarons and the optical gap in CeO_2. *The Journal of Physical Chemistry Letters*, 11(14):5686–5691, 2020. PMID: 32580554.

[22] Jacopo Stefano Pelli Cresi, Maria Chiara Spadaro, Sergio D'Addato, Sergio Valeri, Stefania Benedetti, Alessandro Di Bona, Daniele Catone, Lorenzo Di Mario, Patrick O'Keeffe, Alessandra Paladini, Giovanni Bertoni, and Paola Luches. Highly efficient plasmon-mediated electron injection into cerium oxide from embedded silver nanoparticles. *Nanoscale*, 11:10282–10291, 2019.

[23] Jacob M. Garcia, Lauren F. Heald, Ryan E. Shaffer, and Scott G. Sayres. Oscillation in excited state lifetimes with size of sub-nanometer neutral $(TiO_2)n$ clusters observed with ultrafast pump–probe spectroscopy. *The Journal of Physical Chemistry Letters*, 12(16):4098–4103, 2021. PMID: 33885304.

[24] Yu Zhang, Daniel T. Payne, Chi L. Pang, Cephise Cacho, Richard T. Chapman, Emma Springate, Helen H. Fielding, and Geoff Thornton. State-selective dynamics of TiO_2 charge-carrier trapping and recombination. *The Journal of Physical Chemistry Letters*, 10(17):5265–5270, 2019. PMID: 31434481.

[25] Yasuhiro Yamada and Yoshihiko Kanemitsu. Determination of electron and hole lifetimes of rutile and anatase TiO_2 single crystals. *Applied Physics Letters*, 101(13):133907, 2012.

[26] Mingchun Xu, Youkun Gao, Elias Martinez Moreno, Marinus Kunst, Martin Muhler, Yuemin Wang, Hicham Idriss, and Christof Wöll. Photocatalytic activity of bulk TiO_2 anatase and rutile single crystals using infrared absorption spectroscopy. *Phys. Rev. Lett.*, 106:138302, 2011.

[27] Alan G. Joly, Joshua R. Williams, Scott A. Chambers, Gang Xiong, Wayne P. Hess, and David M. Laman. Carrier dynamics in α-Fe_2O_3 (0001) thin films and single crystals probed by femtosecond transient absorption and reflectivity. *Journal of Applied Physics*, 99(5):053521, 2006.

[28] Jacopo Stefano Pelli Cresi, Emiliano Principi, Eleonora Spurio, Daniele Catone, Patrick O'Keeffe, Stefano Turchini, Stefania Benedetti, Avinash Vikatakavi, Sergio D'Addato, Riccardo Mincigrucci, Laura Foglia, Gabor Kurdi, Ivaylo P. Nikolov, Giovanni De Ninno, Claudio Masciovecchio, Stefano Nannarone, Jagadesh Kopula Kesavan, Federico Boscherini, and Paola Luches. Ultrafast dynamics of plasmon-mediated charge transfer in $Ag@CeO_2$ studied by free electron laser time-resolved x-ray absorption spectroscopy. *Nano Letters*, 21(4):1729–1734, 2021. PMID: 33570965.

Chapter 4

Ultrafast charge transfer in Ag@CeO$_2$ studied by time-resolved X-Ray absorption spectroscopy

In this chapter I will be focusing on the dynamics of plasmon-mediated charge transfer from Ag NPs to a surrounding layer CeO$_2$ (here referred to as Ag@CeO$_2$), similar to the one described in chapter 3, studied by time resolved X-Ray absorption spectroscopy (trXAS). To extract information on the charge transfer dynamics, we measured the ultrafast variations in absorbance of the Ce N$_{4,5}$ absorption edge in a laser pump-free electron probe configuration. trXAS represents a valuable tool to obtain element-specific information on light-triggered ultrafast processes, providing very high sensitivity to the fine details of the electronic structure of the individual elements present in the investigated materials. Free electron laser (FEL) sources are particularly suitable for ultrafast core-level spectroscopies, as they guarantee high pulse intensities in a rather large spectral range. In particular, the experiment described in this chapter has been performed at the EIS-TIMEX beamline at the FERMI FEL source in Trieste. This FEL offers the possibility of finely tuning the photon energy within the 20-300 eV photon energy range, guaranteeing remarkable spectral stability and nearly transform-limited pulses [1]. These features, accompanied by an almost jitter-free laser-FEL synchronization, are ideal for laser pump-X-Ray probe single-shot experiments [2]. The goal of our study is to obtain information on the plasmon mediated charge transfer mechanisms from Ag NPs to the surrounding CeO$_2$, using the FEL probe to investigate the ultrafast changes occurring in the electronic structure of Ce after the interaction between the laser pulse and the Ag@CeO$_2$ sample.

4.1 Sample growth and static characterization

For the present work, we have grown two different samples: a bare CeO$_2$ thin film of 10 nm, used as a reference, and a CeO$_2$ layer of about the same thickness (11.5 nm) with Ag NPs embedded in (Ag@CeO$_2$ sample). These two samples were grown in the RAGNO-2 chamber, at the SESAMo lab, described in 2.1, on ultrathin (100 nm) parylene-N self-standing foils (figure 4.1b), transparent substrates for soft X-Rays. The CeO$_2$ films were grown by molecular beam epitaxy (MBE), by evaporating Ce from an electron beam evaporator, in a controlled oxygen partial pressure of 10^{-7}
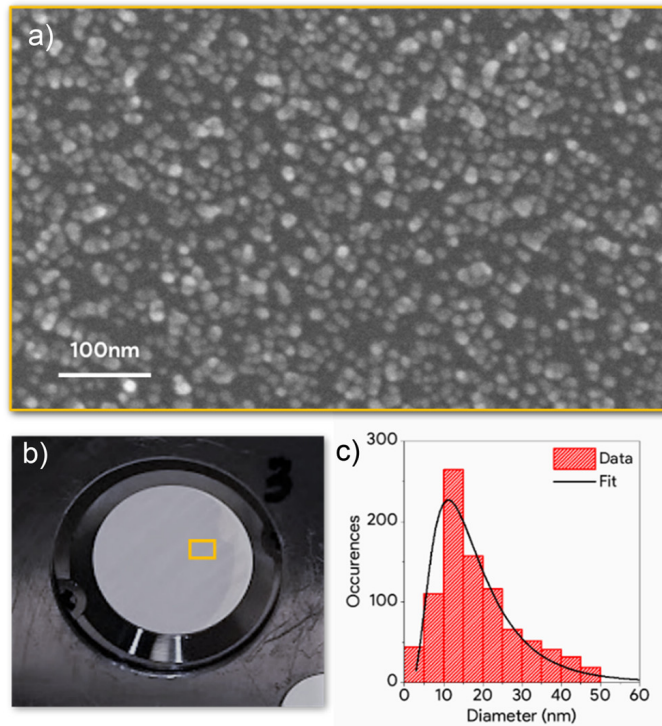
Figure 4.1: *(a) SEM image of a sample made of Ag NPs on top of a CeO$_2$ film grown on a Si substrate. (b) Picture of the Ag@CeO$_2$ sample on a parylene substrate. (c) Ag NPs size distribution extracted from (a).*

mbar. During sample growth, the parylene substrates were kept at room temperature. The MBE chamber is equipped with a quartz microbalance that permits the control of the evaporation rate: the thickness of the CeO$_2$ films was chosen to be 10 nm. As illustrated in 2.1, the mass-selected Ag NPs, were grown by an inert gas aggregation cluster source based on magnetron sputtering. For the present experiment, the NPs were co-evaporated with CeO$_2$ to form a film that embeds the NPs, maximizing the interface between the NPs and the oxide and protecting the NPs from contamination. Using the quartz microbalance, we could estimate a nominal thickness for the Ag NPs layer of 9.4 nm.

Figure 4.1a shows the SEM image of Ag NPs evaporated on a CeO$_2$ film (deposited on a Si substrate), under the same conditions as the Ag@CeO$_2$ investigated here. From the SEM image, we could extract the NP diameter distribution shown in figure 4.1c. The NPs have an average diameter $d \sim 20$ nm. After the growth, the two samples have been characterized by *in-situ* XPS, using Al K_α photons. The Ce 3d XPS spectra are shown in figure 4.2a, together with the fit (red lines). The fit of the spectra was obtained following the procedure illustrated in 2.2.1, and from the fit results it is possible to extract information on the Ce^{3+} concentration, with an uncertainty around 10% intrinsic to the procedure. The calculated concentration of Ce^{3+} in the bare CeO$_2$ is 18%, while for the Ag@CeO$_2$ sample is 14%. The Ce^{3+} concentration is comparable in the two samples within the errors, estimated to be approximately $\pm 3\%$ and it can be ascribed to defects on the film surface.

Figure 4.2b shows the static UV-Vis absorbance spectra of the bare ceria and of the Ag@CeO$_2$ sample, acquired as described in 1.2.3. The bare CeO$_2$ film exhibits a peak in the UV range at 300 nm, ascribed to the band gap excitation from the valence band to empty Ce4f levels, in agreement with literature [3, 4]. When the Ag NPs are introduced within the ceria film, the optical absorbance spectrum is
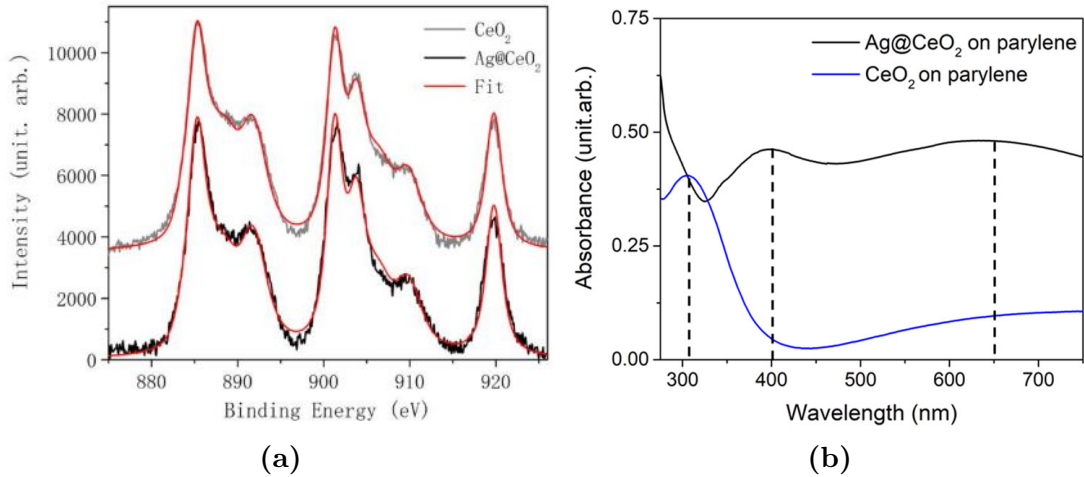
Figure 4.2: *(a) Ce 3d XPS spectra of CeO$_2$ (grey curve) and of Ag@CeO$_2$ (black curve) grown on parylene. The fitting obtained using Ce^{3+} and Ce^{4+} related components are also shown (red curve). (b) Absorbance spectra of the Ag@CeO$_2$ film (black) and of a ceria film (blue).*

strongly modified by the appearance of broad and intense peaks centered at 400 nm and 650 nm, related to the LSPR excitation of the NPs.

4.2 Boundary Element Method Simulations

The peaks in the spectrum in figure 4.2b can be ascribed to different specific configurations of the Ag NPs within the oxide and to the extended plasmon resonances introduced by the proximity of the NPs. These assumptions have been justified by simulating the absorbance of Ag NPs in a CeO$_2$ matrix, performed using the boundary element method [5], as implemented in the MNPBEM17 toolbox [6]. This simulation allows to calculate the scattering and the extinction coefficients of metallic NPs surrounded by a dielectric material. The dielectric constants were extracted from tabulated n and k values taken from the literature (Ag from [7], CeO$_2$ from [8] and parylene from [9]). Two situations have been taken into account for the simulations: a single Ag NP and a couple of Ag NPs with the same shape, in both cases surrounded by a CeO$_2$ matrix.

The first case is depicted in figure 4.3, where the Ag NPs are assumed to be spheroids with an *in-plane* dimension of 20 nm, 10 nm, and an *out-of-plane* size of 20 nm. This geometry is compatible with the possible agglomeration of the NPs during the deposition, and was previously observed by Pelli et al. [10] on similar systems. In figure 4.3a, the extinction cross section shows a strong peak below 350 nm, compatible with ceria band gap absorption, and two more polarization-dependent peaks. The two additional peaks are observed at 410 nm and 600 nm, if the light polarization is parallel or perpendicular to the shorter *in-plane* axis of the spheroid, respectively (see figure 4.3b). These two latter features are ascribed to the LSPR modes in the NPs, and are compatible with the experimental results.

Figure 4.4 simulates the situation of a couple of Ag NPs with the same shape (see figure 4.4b), to investigate the effect of extended plasmons. To compare the results, different distances have been taken into account. The two main plasmonic features in figure 4.4a are peaked at 400 nm and 585 nm, which are compatible with the experimental spectrum.

Figure 4.3: *Extinction spectra obtained for an Ag spheroid of $20 \times 10 \times 20$ nm (vertical section presented in the sketch) embedded in a layer of CeO_2 of 21 nm on parylene, considering two in-plane orientations of the light polarization, parallel (red line) and perpendicular (black line) to the short axis of the NP.*
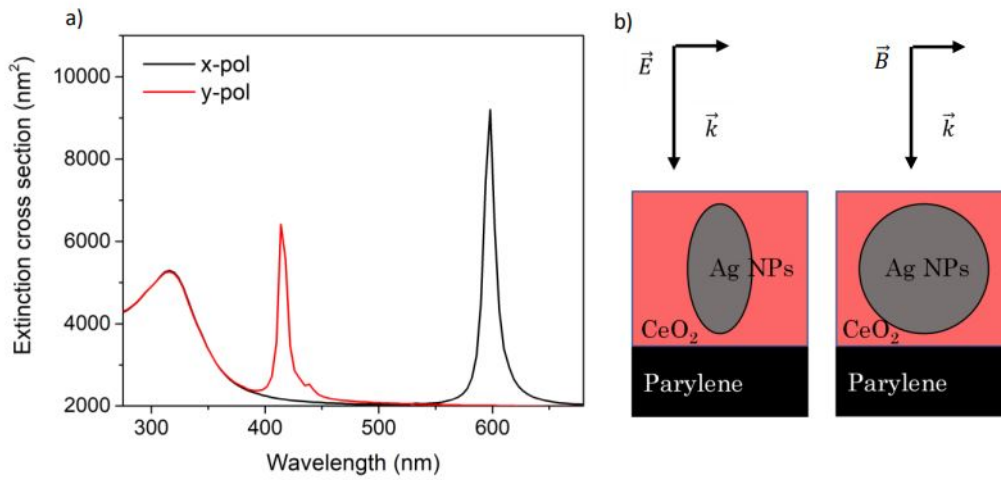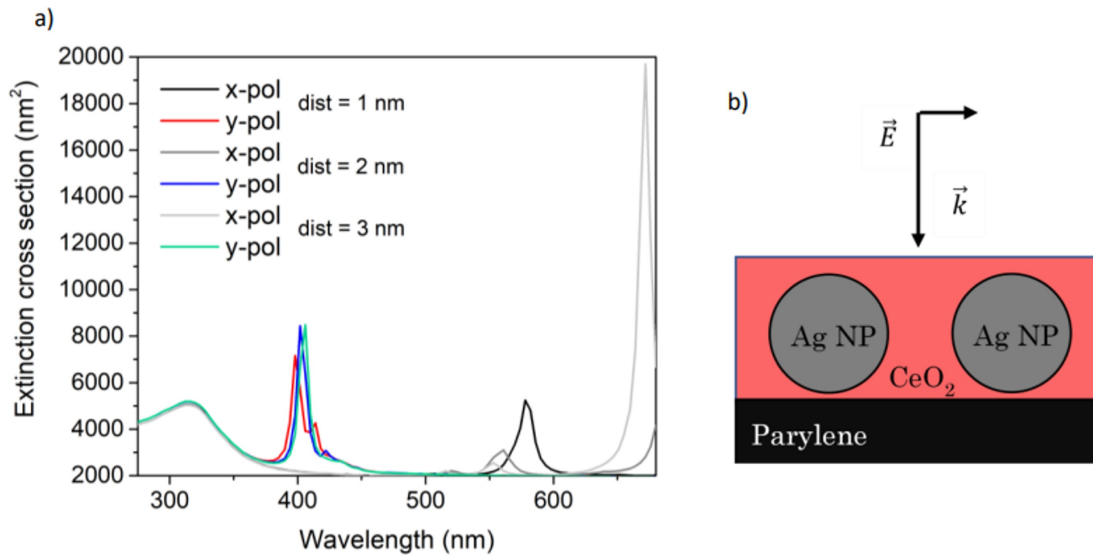

Figure 4.4: *Extinction spectra obtained for two Ag spheroids of $20 \times 20 \times 20$ nm (vertical section presented in the sketch) embedded in a layer of CeO_2 of 21 nm on parylene.*
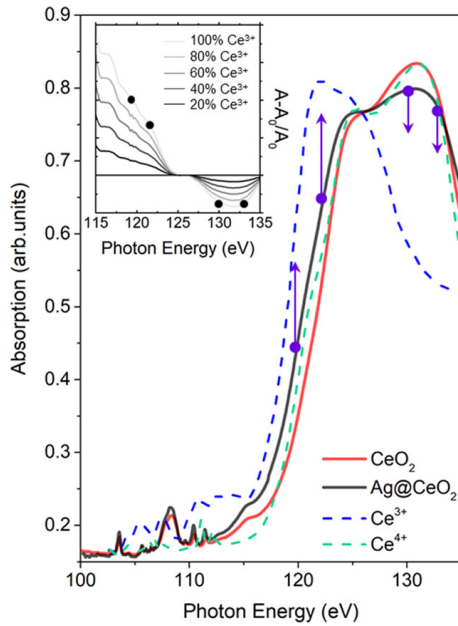
Figure 4.5: *Ce $N_{4,5}$ XAS absorption spectra measured in transmission mode for CeO_2 (red line) and $Ag@CeO_2$ (black line) samples, and reference spectra of Ce^{4+} (dashed green line) and Ce^{3+} (dashed blue line) samples [11], normalized to the maximum of the Ce^{4+} spectrum measured in our experiment. Inset: relative variation of absorption during the reduction of Ce ions estimated from the literature spectra. Purple points (black in the inset) indicate the selected FEL energies used to probe the variations of absorption.*

4.3 Stationary XAS

As already mentioned at the beginning of the chapter, in order to extract information on the charge transfer dynamics, we have studied the modifications of the Ce $N_{4,5}$ edge after the interaction of the system with visible radiation. Stationary XAS of the samples at the Ce $N_{4,5}$ edge have been measured at the BEAR IOM-CNR synchrotron radiation beamline at Elettra (Trieste, Italy) [12] as a reference. The results of the measurements (after pre-edge background subtraction), together with reference spectra of Ce^{3+} and Ce^{4+} taken from literature [11] are reported in figure 4.5. The Ce^{4+} and Ce^{3+} reference spectra were respectively acquired on CeO_2 and CeCl compounds, being CeCl more stable in air than Ce_2O_3, which can be easily oxidized to CeO_2. The spectrum of CeO_2 shown in figure 4.5 as a solid red line is compatible with the Ce^{4+} reference spectrum (dashed green line). The introduction of Ag NPs into the CeO_2 layer induces a red shift of about 1 eV of the Ce absorption edge and a decrease of the white line height. Both effects are compatible with a mild reduction of cerium oxide when combined with the Ag NPs. The edge absorption shape is modified by the introduction of NPs towards the Ce^{3+} reference spectrum (dashed blue line). The observed reduction derives from static electron transfer from Ag NPs to the oxide [13, 14] typical of metal NP/oxide systems and it should involve the ceria at the interface. The small changes in the Ce $N_{4,5}$ absorption edge are compatible with the Ce^{3+} concentration extracted from the XPS shown in figure 4.2a. The static reduction of Ce ions after the inclusion of Ag NPs is probably related to the morphology of the sample which induces the presence of defects on the ceria surface.

4.4 Time-resolved XAS

trXAS was performed using a single-shot laser pump-FEL probe configuration (figure 4.6) on the Ag@CeO$_2$ sample at selected energies (purple points in figure 4.5) across the Ce N$_{4,5}$-edge. The schematics of the setup is shown in figure 4.6: the measurements were performed in single-shot transmission mode, by rastering the sample in the plane perpendicular to the beam and illuminating a fresh spot of the sample at each pump shot. For each new spot, the transmission of the unperturbed sample was measured by exposing the sample to a sequence of probe pulses prior to pump exposure. The investigated time window is within a range of $\sim$ 1 ps from the pump-probe overlap (time zero), scanned with steps of 0.1 ps. In order to obtain good statistics for each photon energy, the single-shot measurements at each delay time were repeated in different positions. To account for possible nonuniformities of the sample, the uppermost and the lowermost 5% of the distribution of the measured changes in transmission for each energy and delay were excluded. Time zero was calibrated using Si$_3$N$_4$ as usually performed for FEL/Vis pump cross-correlation [15]. It is possible that slight variations in the zero delay from run to run (e.g., changing the photon energy of the FEL) can result in a variation of the delay by up to 100 fs. The diameters of the FEL and laser pump beam on the sample were 80 and 100 μm, respectively. The pump pulse duration was estimated to be about 200 fs, while the average FEL probe pulse duration was around 100 fs. The instrument response function (IRF) of the setup is thus dominated by the pump laser duration. The laser pump fluence was set to about 34 mJ cm^{-2}.

To measure the variations in absorbance caused by plasmon mediated charge transfer, we have used as a pump a ultrashort laser pulse at 430 nm, to selectively excite the Ag NPs LSPR. The pump energy we used is below the band gap of CeO$_2$, and the absorption of the ceria layer is negligible at 430 nm, as can bee seen in figure 4.2b. Moreover, the interband transitions in Ag are characterized by weak cross sections at this photon energy. To probe the excited states of the system, four FEL energies were used as a probe (119, 122, 130 and 133 eV), marked by the purple arrows in figure 4.5. These energies were chosen to maximize the sensitivity to possible changes in the electronic structure in Ce ions driven by ultrafast reduction of CeO$_2$.

4.5 Results and discussion

Figure 4.7 shows the relative variation of the absorption, as a function of the pump-probe delay time, at the selected FEL photon energies across the Ce N$_{4,5}$-edge highlighted in figure 4.5. After the interaction with the pump pulse, the X-Ray absorption coefficient exhibits a pronounced increase at 119 and 122 eV of about 10% (figure 4.7a,b) and a decrease at 130 and 133 eV of about 5% (figure 4.7c,d). The changes in absorption occur within the first few hundred femtoseconds, with a negligible decay in the considered time range. The measured absorption variations can be compared to the inset in figure 4.5, that reports the calculated relative absorption changes of Ce N$_{4,5}$ XAS spectra if the electronic configuration of Ce is progressively modified by adding electrons in the Ce 4f levels. With increasing concentration of Ce^{3+}, one can notice a pronounced increase of absorption below 125 eV and a moderate decrease above 125 eV, compatibly with the variations observed in figure 4.7. Therefore, the observed variations in absorbance after the interaction with the pump pulse can be ascribed to the ultrafast reduction of part of the Ce ions
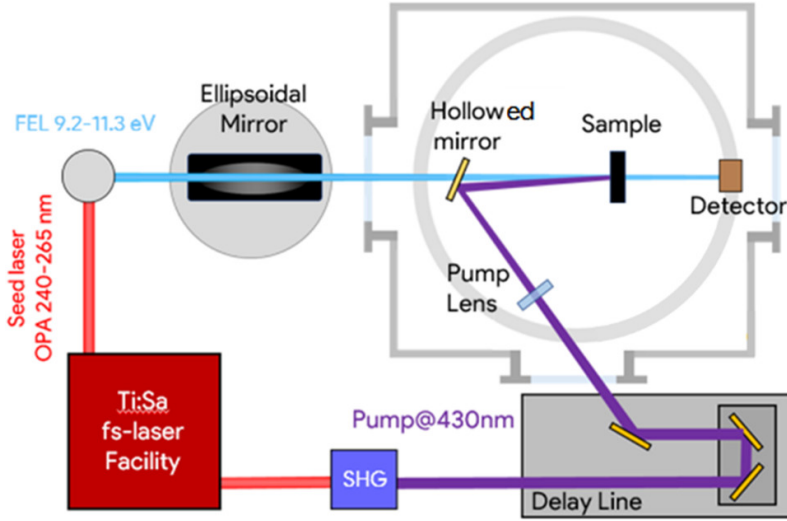
Figure 4.6: *EIS-TIMEX end-station setup for pump-probe XAS measurements in transmission geometry. Small angles between pump and FEL are achieved using a holey steering mirror positioned in the FEL beam path. Synchronization between the laser pump and FEL probe is nearly jitter-free being both the pulses generated by the same Ti:Sa oscillator.*

surrounding the Ag NPs driven by a LSPR-mediated electron injection in the Ce 4f localized states. In order to exclude possible contributions of multiphoton absorption processes directly in the CeO_2 matrix, the reference ceria layer was excited with a pump at the same energy and with a fluence similar to that used on the Ag@CeO_2 sample. The resulting variation in probe absorption (with a single FEL energy of 130 eV) is reported in figure 4.8, and it does not show any evident dynamics. This observation allows us to exclude any ceria-related contribution to the absorption variations observed in figure 4.7.

To extract information on the timescale involved in the charge transfer, we have fitted the data in figure 4.7 using a kinetic profile (obtained by the product of an exponential function and a step function) convoluted with an IRF of Gaussian shape with FWHM of 200 fs ($\sigma \sim 15$ ps) compatible with the width of the pump laser:

$$\Delta A(t) \int_{-\infty}^{\infty} \frac{1}{\sqrt{2\sigma\pi}} e^{-\frac{t}{\sqrt{2\sigma^2}}} \cdot A \cdot e^{-\frac{t-c}{\tau_1}} \cdot \Theta(t-c)\, dt \tag{4.1}$$

where Θ is the Heaviside function, A the intensity and τ_1 the characteristic rise time of the kinetic profile. From the fit, we extracted a rise time that is compatible with the time with of the laser pump (i.e. about 200 fs), confirming that the charge transfer process is faster than a typical thermal process. Indeed, thermalization through electron-phonon scattering, typically requires times of 1-10 ps, as shown in the schematics of figure 1.14 [16, 17]. The negligible decay of the transient XAS signal within the investigated time window is consistent with the long-lived excited state that was observed in previous experiments using a visible probe [10]. The amplitude of the observed absorption variations, estimated by the fit, can be related to the density of electrons transferred to ceria. Using the reference spectra of Ce^{3+} and Ce^{4+} samples [11], we related the measured variations in absorption at the different probe energies to the fraction of Ce ions affected by injected electrons. The extracted fraction, about 20%, indicates that charges are mainly transferred to the Ce atoms contained in the volume of the first interfacial cerium oxide monolayer (0.312 nm) that surrounds the Ag NPs. We could also provide an estimate for the
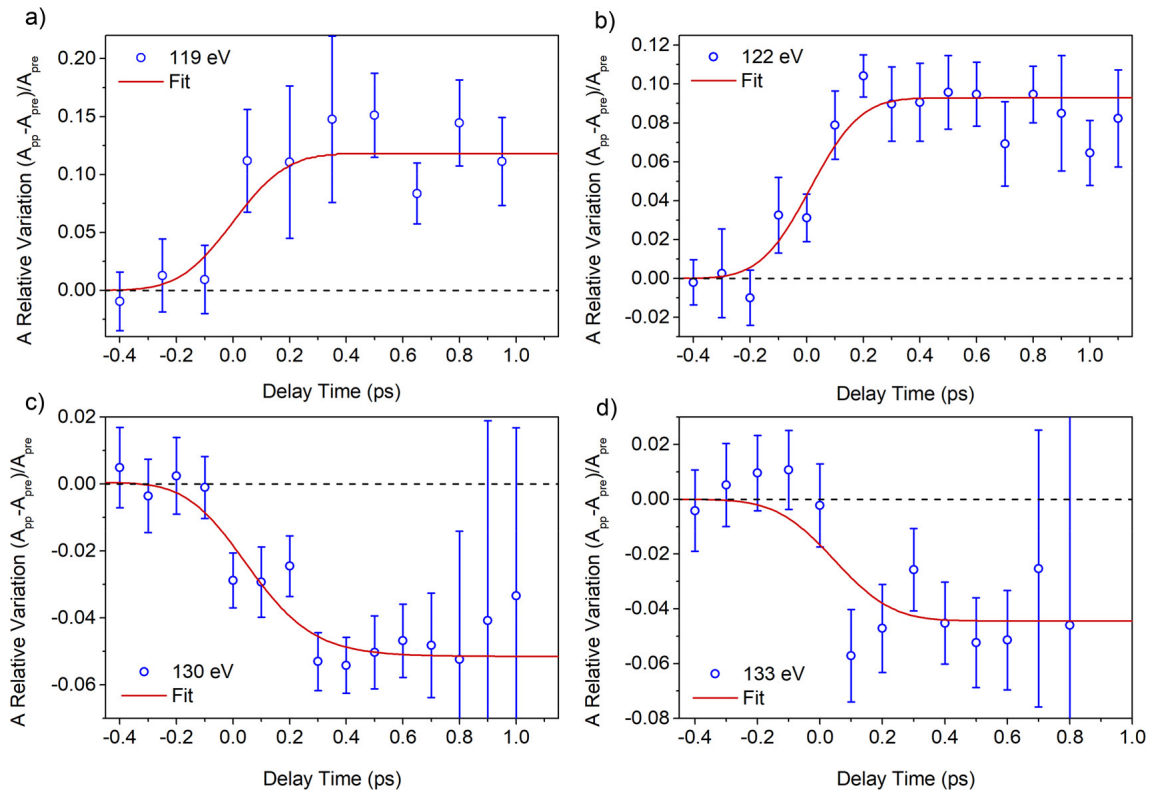
Figure 4.7: *Relative variation of absorption as a function of pump-probe delay time and corresponding fit (red curve) with pump at 430 nm and FEL at (a) 119 eV, (b) 122 eV, (c)130 eV, and (d) 133 eV.*
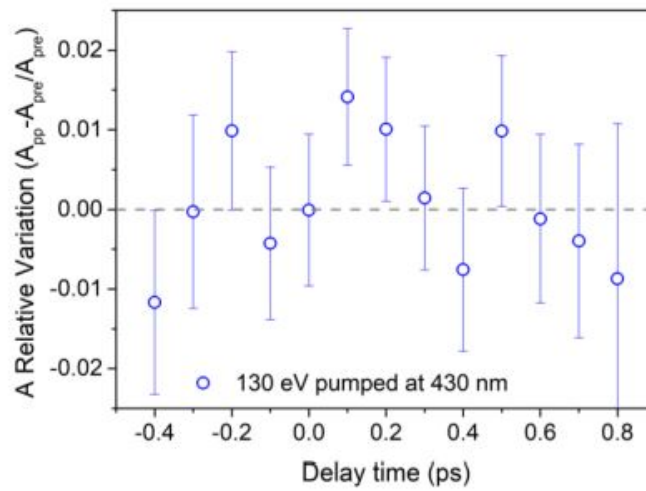

Figure 4.8: *Relative variation of absorption of CeO_2 as a function of pump-probe delay time. The probe energy was 130 eV while the pump wavelength was 430 nm*
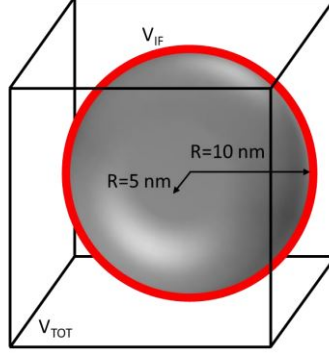
Figure 4.9: *Sketch of a NP with radius of $10 \times 5 \times 10$ nm. The red circle represents the volume of CeO_2 at the interface of the NP*

plasmon mediated charge injection efficiency as the ratio between the number of injected electrons and the number of absorbed photons, around 8%. The justifications for the last to statements are provided by the following calculations.

Estimation of electron injection efficiency

The Ag NPs are assumed to be uniformly distributed (as suggested by the SEM image in figure 4.1, with size $20 \times 10 \times 20$ nm (see figure 4.9) within the CeO_2 matrix. The NPs form a film with an equivalent thickness of $t_{Ag} = 9.4$ nm[1] and they are embedded in a film of CeO_2 with an equivalent thickness of $t_{Ce} = 11.5$ nm. In both cases, the nominal thickness has been estimated by means of a quartz microbalance. Considering 0.312 nm as the thickness of a monolayer of ceria (in the most stable 111 orientation), the volume of the interface ceria can be approximated to:

$$V_{IF} = \frac{4}{3}\pi \cdot [(10.312 \cdot 10.312 \cdot 5.312) - (10 \cdot 10 \cdot 5)] \sim 272 \text{ nm}^3 \qquad (4.2)$$

while the overall volume of the ceria film can be approximated to:

$$V_{TOT} = V_{Ag} \cdot \frac{t_{Ce}}{t_{Ag}} = \frac{4}{3}\pi \cdot (10 \cdot 10 \cdot 5) \cdot \frac{11.5}{9.4} \sim 2562 \text{ nm}^3 \qquad (4.3)$$

Combining 4.2 and 4.3, we can extract the ratio between the volume of interface ceria and the total volume:

$$\frac{V_{IF}}{V_{TOT}} \sim 10.6\% \qquad (4.4)$$

In figure 4.7, we measure a variation of the Ce^{3+} absorption edge of about 20%, meaning that more ceria than that present at the interface is reduced by the plasmon mediated mechanism in the first 200 fs after the excitation of the system.

To estimate the charge injection efficiency, we evaluated the number of injected electrons (n_{el}) as the number of Ce ions contained in 20% of CeO_2 film (i.e. the fraction involved in the charge transfer):

$$n_{el} = \frac{V_{exc}}{V_{Ce}} = \frac{2652 \text{ nm}^3 \cdot 0.2}{0.5413^3 \text{ nm}^3/4} = 12944 \text{ electrons} \qquad (4.5)$$

---

[1]as mentioned in the previous chapter, the nominal Ag thickness refers to the equivalent thickness of a uniform Ag film completely covering the ceria layer

where V_{Ce} is the volume occupied by a cerium atom in the cerium oxide unit cell (4 atoms per unit cell) and V_{exc} is the volume estimated to be excited by the pump laser (20% of the total volume of the ceria film V_{TOT}).

To calculate the number of absorbed photons, n_{ph}, we considered the absorbance $A(\lambda_{PUMP})$ of the material evaluated from figure 4.2b at an excitation wavelength of 430 nm, the pump fluence F, the *in-plane* surface of a NP (s = 10 nm × 5 nm × π = 157 nm), and the photon energy $\hbar\omega_{PUMP}$:

$$n_{ph} = \frac{A(\lambda_{PUMP}) \cdot F \cdot s}{\hbar\omega_{PUMP}} \sim 1.6 \times 10^5 \text{ photons} \tag{4.6}$$

Thus, the charge injection efficiency η will be:

$$\eta = \frac{n_{el}}{n_{ph}} \sim 8\% \tag{4.7}$$

The estimated injection efficiency supports the high efficiency for the plasmon-mediated electron transfers that was previously observed in a similar sample in a UV-Vis time-resolved experiment [10] and it suggests that by combining Ag NPs with ultrathin oxide shells the plasmon-induced oxide excitation can be maximized.

4.6 Conclusions

The experiment described in this chapter represents the first application of free electron laser-based time-resolved X-Ray absorption spectroscopy to a system composed by an oxide material combined with plasmonic nanoparticles. The trXAS measurements reveal that after the photoexcitation of LSPR in Ag NPs, part of the Ce atoms in the sample undergoes an ultrafast reduction, caused by the transient occupation of the Ce 4f levels that are empty for the unexcited system. The sign and entity of the variations in absorption after the excitation at the different probe energies and their ultrafast nature demonstrate that the decay of the LSPR in the Ag NPs involves electron transfer processes, which is the dominant process below 1 ps (see figure 1.14).

Bibliography

[1] E. Allaria, D. Castronovo, P. Cinquegrana, P. Craievich, M. Dal Forno, M. B. Danailov, G. D'Auria, A. Demidovich, G. De Ninno, S. Di Mitri, B. Diviacco, W. M. Fawley, M. Ferianis, E. Ferrari, L. Froehlich, G. Gaio, D. Gauthier, L. Giannessi, R. Ivanov, B. Mahieu, N. Mahne, I. Nikolov, F. Parmigiani, G. Penco, L. Raimondi, C. Scafuri, C. Serpico, P. Sigalotti, S. Spampinati, C. Spezzani, M. Svandrlik, C. Svetina, M. Trovo, M. Veronese, D. Zangrando, and M. Zangrando. Two-stage seeded soft-x-ray free-electron laser. *Nature Photonics*, 7(11):913–918, 2013.

[2] Miltcho B. Danailov, Filippo Bencivenga, Flavio Capotondi, Francesco Casolari, Paolo Cinquegrana, Alexander Demidovich, Erika Giangrisostomi, Maya P. Kiskinova, Gabor Kurdi, Michele Manfredda, Claudio Masciovecchio, Riccardo Mincigrucci, Ivaylo P. Nikolov, Emanuele Pedersoli, Emiliano Principi, and Paolo Sigalotti. Towards jitter-free pump-probe measurements at seeded free electron laser facilities. *Opt. Express*, 22(11):12869–12879, 2014.

[3] P. Patsalas, S. Logothetidis, L. Sygellou, and S. Kennou. Structure-dependent electronic properties of nanocrystalline cerium oxide films. *Phys. Rev. B*, 68:035104, 2003.

[4] Jacopo Stefano Pelli Cresi, Lorenzo Di Mario, Daniele Catone, Faustino Martelli, Alessandra Paladini, Stefano Turchini, Sergio D'Addato, Paola Luches, and Patrick O'Keeffe. Ultrafast formation of small polarons and the optical gap in CeO_2. *The Journal of Physical Chemistry Letters*, 11(14):5686–5691, 2020. PMID: 32580554.

[5] F. J. García de Abajo and A. Howie. Retarded field calculation of electron energy loss in inhomogeneous dielectrics. *Phys. Rev. B*, 65:115418, 2002.

[6] Ulrich Hohenester and Andreas Trügler. MNPBEM – a Matlab toolbox for the simulation of plasmonic nanoparticles. *Computer Physics Communications*, 183(2):370–381, 2012.

[7] R T Holm. Convention confusions. In *Handbook of Optical Constants of Solids*, pages 21–55. Elsevier, 1998.

[8] Woo-Hee Kim, W. J. Maeng, Min-Kyu Kim, Julien Gatineau, and Hyungjun Kim. Electronic structure of Cerium oxide gate dielectric grown by plasma-enhanced atomic layer deposition. *Journal of The Electrochemical Society*, 158(10):G217, 2011.

[9] T. E. F. M. Standaert, P. J. Matsuo, X. Li, G. S. Oehrlein, T.-M. Lu, R. Gutmann, C. T. Rosenmayer, J. W. Bartz, J. G. Langan, and W. R. Entley. High-density plasma patterning of low dielectric constant polymers: A comparison

between polytetrafluoroethylene, parylene-N, and poly(arylene ether). *Journal of Vacuum Science & Technology A*, 19(2):435–446, 2001.

[10] Jacopo Stefano Pelli Cresi, Maria Chiara Spadaro, Sergio D'Addato, Sergio Valeri, Stefania Benedetti, Alessandro Di Bona, Daniele Catone, Lorenzo Di Mario, Patrick O'Keeffe, Alessandra Paladini, Giovanni Bertoni, and Paola Luches. Highly efficient plasmon-mediated electron injection into cerium oxide from embedded silver nanoparticles. *Nanoscale*, 11:10282–10291, 2019.

[11] S. O. Kucheyev, B. J. Clapsaddle, Y. M. Wang, T. van Buuren, and A. V. Hamza. Electronic structure of nanoporous ceria from x-ray absorption spectroscopy and atomic multiplet calculations. *Phys. Rev. B*, 76:235420, 2007.

[12] L. Pasquali, A. De Luisa, and S. Nannarone. The UHV experimental chamber for optical measurements (reflectivity and absorption) and angle resolved photoemission of the bear beamline at ELETTRA. *AIP Conference Proceedings*, 705(1):1142–1145, 2004.

[13] Francesco Benedetti, Paola Luches, Maria Chiara Spadaro, Gabriele Gasperi, Sergio D'Addato, Sergio Valeri, and Federico Boscherini. Structure and morphology of silver nanoparticles on the (111) surface of cerium oxide. *The Journal of Physical Chemistry C*, 119(11):6024–6032, 2015.

[14] Paola Luches, Federico Pagliuca, Sergio Valeri, Francesc Illas, Gloria Preda, and Gianfranco Pacchioni. Nature of Ag islands and nanoparticles on the $CeO_2(111)$ surface. *The Journal of Physical Chemistry C*, 116(1):1122–1132, 2012.

[15] Riccardo Mincigrucci, Filippo Bencivenga, Emiliano Principi, Flavio Capotondi, Laura Foglia, Denys Naumenko, Alberto Simoncig, Simone Dal Zilio, Alessandro Gessini, Gabor Kurdi, Nicola Mahne, Michele Manfredda, Alessia Matruglio, Ivaylo Nikolov, Emanuele Pedersoli, Lorenzo Raimondi, Rudi Sergo, Marco Zangrando, and Claudio Masciovecchio. Timing methodologies and studies at the FERMI free-electron laser. *Journal of Synchrotron Radiation*, 25(1):44–51, 2018.

[16] Akihiro Furube, Luchao Du, Kohjiro Hara, Ryuzi Katoh, and Masanori Tachiya. Ultrafast plasmon-induced electron transfer from gold nanodots into TiO_2 nanoparticles. *Journal of the American Chemical Society*, 129(48):14852–14853, 2007. PMID: 17994750.

[17] Stephan Link and Mostafa A. El-Sayed. Spectral properties and relaxation dynamics of surface plasmon electronic oscillations in gold and silver nanodots and nanorods. *The Journal of Physical Chemistry B*, 103(40):8410–8426, 1999.

Chapter 5

Au NPs combined with CeO$_2$

In this chapter, I will focus on systems composed by Au NPs embedded in CeO$_2$ thin films. I will first describe the electronic, optical and morphological properties of bare Au NPs self-assembled on quartz substrates and of Au NPs grown within ceria matrices of different thicknesses. The presented results derive from the combination of experiments and numerical simulations. Afterwards, I will focus on the study of the ultrafast dynamics of charge excitation in a system composed by Au NPs surrounded by CeO$_2$.

5.1 Optical properties of Au NPs coupled with CeO$_2$

As already mentioned in the first chapter of this thesis, the plasmonic properties of NPs strongly depend on the characteristics of the NPs (size, shape, aspect ratio) [1] and on the dielectric properties of the environment. In the first part of this chapter, I will focus on the study of static optical properties of bare Au NPs and of NPs of the same size immersed within ceria films of different thicknesses, to investigate how the dielectric environment influences the optical absorbance of the NPs.

5.1.1 Experimental

The samples investigated in this chapter were all grown in RAGNO-1, described in 2.1. The samples used for the optical characterization were grown onto a quartz substrate, which ensures a good optical transparency in the visible range, and consist of a layer of Au NPs of 2 nm nominal thickness, either alone or embedded between CeO$_2$ thin films of different thicknesses: 1.6 nm, 4 nm and 8 nm. A bare CeO$_2$ film was also grown as a reference. The sample used for the morphological characterization by scanning electron microscopy (SEM) was grown on a Si substrate with thermal oxide and was composed of a CeO$_2$ film of 2 nm thickness with a layer of Au NPs on top. Finally, to have a complete picture of the properties of the system, we have also characterized the electronic properties by acquiring *in-situ* XPS and UPS spectra. The samples for UPS is equivalent to the one used for SEM analysis, but it has been grown on a metallic Pt(111) substrate, to avoid charging effects. Both the quartz and Si substrates were cleaned by a 5-minute bath in acetone at 423 K and by two subsequent ultrasonic baths in acetone and in isopropanol at 353 K for 3 minutes each. The Pt(111) substrate was prepared by cycles of sputtering (1 keV, 1 μA) and annealing (1040 K), until the surface contamination was below
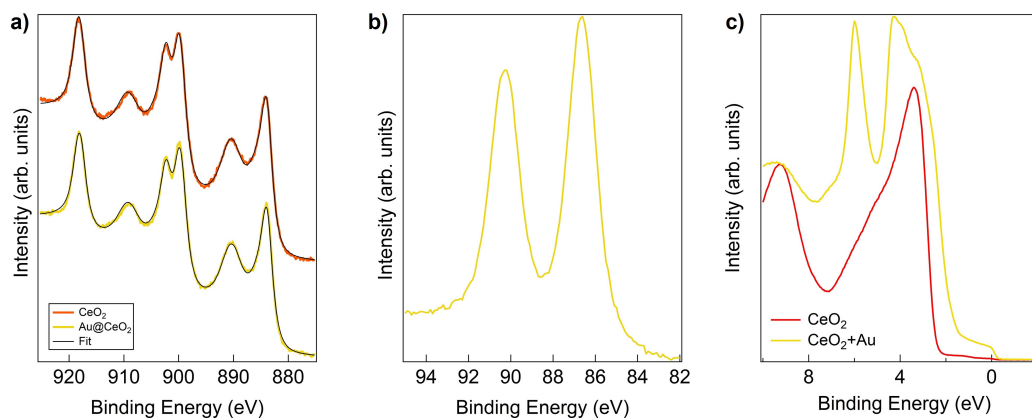
Figure 5.1: *a) Ce 3d XPS spectra of the CeO$_2$ and Au@CeO$_2$ samples and corresponding fit; b) Au 4f XPS spectrum of the Au@CeO$_2$ sample; c) UPS spectrum of the CeO$_2$ thin film (red line) and of the Au@CeO$_2$ sample (yellow line).*

the XPS detection limit. The ceria films were grown by reactive evaporation of Ce, using an e-beam evaporator, in an oxygen partial pressure of 10^{-7} mbar. Au was evaporated from a Knudsen cell and spontaneously self-assembled into NPs, as already explained for Ag NPs in chapter 3.

After the growth, all samples were characterized by *in-situ* XPS using Al K_α photons from a double anode X-Ray source, to obtain quantitative information on the deposited quantity of CeO$_2$ and Au and on possible variations of the chemical state of cerium oxide and of the metal. UPS using a He lamp was also performed on the sample grown on Pt(111) at different stages of the growth. Information on NP morphology was obtained using a SEM (FEI Nova NanoSEM 450) on the sample grown on the Si substrate. The sample morphology, and in particular the size, shape, and density of Au NPs, is not expected to be different on the different substrates used, since the surface of CeO$_2$ films grown at room temperature has a rough morphology even on flat single crystal metal surfaces [2]. The samples grown on the transparent quartz substrates have been analyzed through optical absorption spectrophotometry, using the apparatus described in 2.3.1. To obtain a theoretical model for the static absorbance, we performed polarizability simulations, based upon the Maxwell-Garnett model for optical absorption [3], as described in 2.3.1, evaluating the NPs AR by the SEM images.

5.1.2   Results and discussion

XPS and UPS results

The CeO$_2$ and Au@CeO$_2$ samples were characterized after the growth by *in-situ* XPS, acquired at normal emission using Al Kα photons. The Ce 3d spectra were used to estimate the Ce^{3+} concentration in the two samples, by fitting the spectra with Ce^{3+}- and Ce^{4+}-related components, following the procedure explained in chapter 2.2.1. The spectra and their fit are reported in figure 5.1a, in both cases the Ce^{3+} concentration evaluated by the fit is below the detection limit, indicating that the films have a good CeO$_2$ stoichiometry and that the Au NPs do not relevantly alter the Ce oxidation state. The Au 4f spectrum of the Au@CeO$_2$ sample, shown in figure 5.1b, is compatible with bulk Au.

Figure 5.1c shows the UPS spectra of a CeO$_2$ film before and after Au NP deposition. The spectrum of the CeO$_2$ thin film (red line) presents a dominant
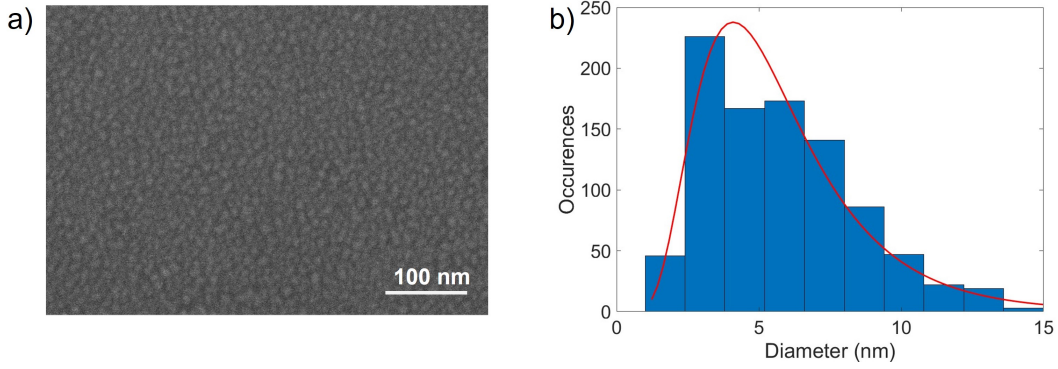
Figure 5.2: *a) SEM image of a 2 nm CeO₂+ 2 nm Au sample and b) the size distribution extracted from the SEM images.*

feature between 2 and 7 eV due to the valence band with O 2p character. The deposition of Au NPs modifies the UPS spectrum, introducing a peak at ~ 6 eV binding energy and a double peak between 2 and 5 eV binding energy, related to the Au 5d band, and a non-negligible intensity up to the Fermi edge, due to the 6s band, in analogy with bulk Au [4].

Morphology

To analyze the NP morphology, SEM images were acquired from a sample composed of 2 nm CeO₂ + 2 nm Au. In figure 5.2a, which reports a representative SEM image, it is possible to distinguish small Au NPs, with irregular shapes, partially interconnected. The Au NP size distribution, evaluated from the SEM images using the GMS3 GATAN software by DigitalMicrograph, is reported in figure 5.2b, together with the data fitting obtained using a lognormal distribution. From the fit, we could extract an average diameter of the NPs of $< d > \sim 5$ nm and a FWHM of ~ 4 nm, although the NPs exhibit a wide diameter distribution. The aspect ratio of the Au NPs, defined as the ratio between the *in-plane* average dimension and the *out-of-plane* average dimension, was estimated from the SEM image shown in figure 5.2a. The average *out-of-plane* dimension was calculated as $< h >= \frac{t_{nom}}{C}$, where t_{nom} is the nominal deposited Au thickness and the C is the fractional surface coverage. For the sample here investigated $t_{nom} = 2$ nm and $C = 0.5$, so $< h >= 5.7$. Considering the lateral size distribution of the NPs shown in figure 5.2b, the average NP *in-plane* dimension was calculated as 5.7 nm, which gives an average aspect ratio of $< AR >= 1.4$. Being the width of the distribution approximately 4 nm, and because of its asymmetric shape towards large *in-plane* NP sizes, the aspect ratio of the Au NPs in the sample ranges between approximately 1 and more than 2.

Optical properties

We performed stationary UV-Vis absorbance spectrophotometry on Au NPs in different dielectric environments, in all cases using transparent quartz substrates. Four different samples were investigated: a sample composed of a nominal thickness of 2 nm of bare Au NPs directly assembled on the quartz substrate and three samples of 2 nm Au NPs embedded between layers of 1.6, 4 or 8 nm of CeO₂. The static optical absorbance in the UV-Vis was measured using the setup described in 1.2.3, based upon a Xenon lamp and a polarizer, which enables to select either p or s polarization, i.e. parallel or perpendicular to the optical plane. The incident
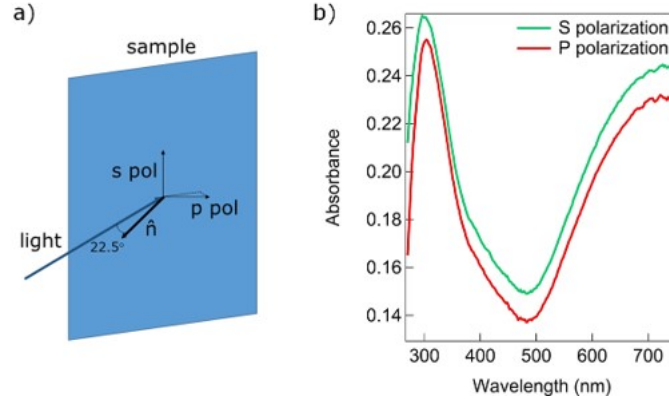
Figure 5.3: *Sketch of the scattering geometry, showing the direction of the incoming light (22° from sample normal) and the light polarization in the case of s and p polarization; for p polarization the in-plane and out-of-plane components are also shown; b) UV-Vis absorbance spectra of the $Au@CeO_2$ sample in s and p polarization.*

angle of the light was 22° from sample normal. The experimental configuration is shown in figure 5.3a: the s polarization is entirely in the surface plane, while in the case of p polarization a small *out-of-plane* component is also present. Figure 5.3b shows the optical spectra of the sample with Au NPs in 8 nm of ceria in the two polarizations. The shape of the spectra is the same, indicating that the samples are optically isotropic in the surface plane, as can be deduced from the geometry shown in figure 5.3a. This behaviour has been observed for all samples, independently on the presence of the surrounding medium. Because of the slightly higher signal over noise ratio, the spectra shown in this chapter were all acquired with s polarization.

Figure 5.4a shows the static UV-Vis optical absorbance spectra of bare Au NPs and of Au NPs surrounded by ceria layers of different thicknesses, while figure 5.4b reports the imaginary part of the *in-plane* component of the optical polarizability of Au NPs with different ARs immersed in different dielectric environments. The spectra are the results of numerical simulations, performed using the Maxwell-Garnett model [3], to calculate the polarizability of Au NPs embedded in a CeO_2/SiO_2 matrix (see section 2.3.1). Following the procedure in reference [5], we assumed the NPs as oblate spheroids, i.e. ellipsoids with the three axis a, b and c following the relationship: $a = b > c$, where a and b are the *in-plane* dimensions of the nanoparticles and c is the *out-of-plane* axis, with AR = 1.5, as suggested by the SEM investigations. For AR = 1.5, in equation 2.3d, $L_x = L_y = 0.272$, $L_z = 0.455$, so the polarizability components are different, $\alpha_x = \alpha_y \neq \alpha_z$. [6, 7, 8]. To simulate the optical properties of bare Au NPs on the quartz substrate, the NPs have been assumed to be completely immersed in a quartz matrix. This is clearly a strong approximation, but the simulations are not supposed to precisely describe the real systems (which, moreover, are composed by NPs with different dimensions and AR), but they should give an idea of the average behavior of the NPs in the different dielectric environments.

For simulations, we have used the dielectric functions found in reference [9] for bulk CeO_2, in [10] for Au, while we calculated the real part of the complex refractive index for quartz from the Sellmeier equation [11] applied to fused SiO_2 at room temperature [12]. To account for possible deviations of the AR from the average value, we also considered the case of Au NPs with AR = 2 and of spherical NPs (dashed and dotted lines in figure 5.4b respectively). Furthermore, to account for the finite thickness of the ceria layer [5, 8, 13], we have also simulated polarizability for a ceria layer with a smaller dielectric function (i.e. $\epsilon_{CeO_2} - 1$).
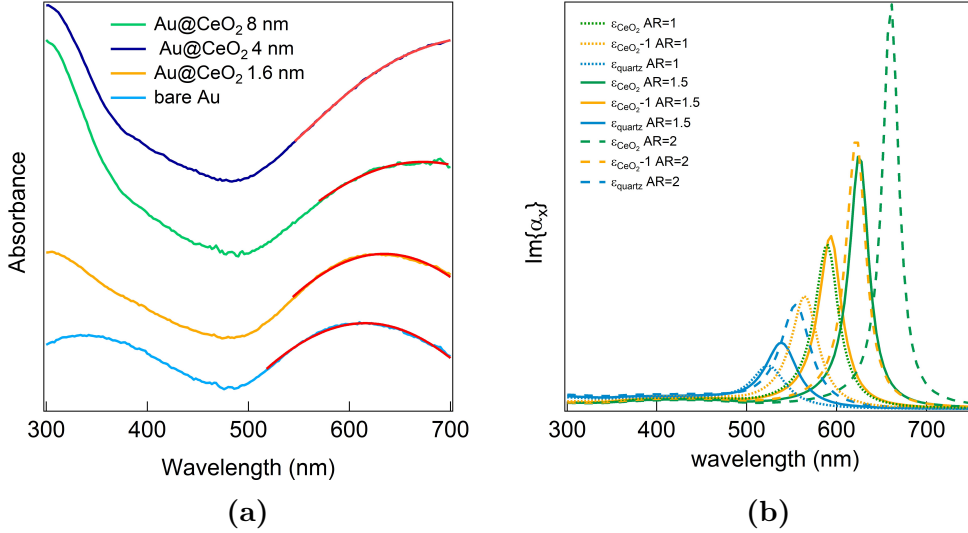
Figure 5.4: *(a) UV-Vis absorbance spectra of Au NPs embedded within CeO$_2$ films of different thickness. (b) Imaginary part of simulated in-of-plane polarizability of spherical (dotted lines) or ellipsoidal Au NPs with AR=1.5 (continuous lines) and AR=2 (dashed lines) embedded within media of different dielectric function.*

When we look at the absorbance spectrum of the bare Au NPs in figure 5.4a, we can distinguish two absorbance bands. The first, in the UV range, peaked around 350 nm, is ascribed to interband transitions from d-valence band to the empty states in the s and p bands above the Fermi level [14, 15, 16], while the second broad band, peaked around 600 nm, corresponds to the LSPR excitation of Au NPs [17, 18]. When we introduce the ceria layer around the NPs, the absorbance band related to the interband transition in Au is partially hidden by the more intense signal related to the band gap excitation of CeO$_2$ [19, 20], which shows a peak around 300 nm and becomes more intense as we increase the thickness of the ceria layer. As already demonstrated in chapter 4 (see figure 4.2b) and in many other works, such as [19, 20], the bare CeO$_2$ films do not absorb in the visible region. Thus, we can only ascribe the broad absorbance band in figure 5.4a to LSPR excitation of Au NPs.

The LSPR absorbance band broadens and red-shifts as the amount of ceria increases. We have deduced the LSPR band peak position λ_{peak} using a Gaussian fit, obtaining the values presented in table 5.1. A similar behavior (red-shift with increasing dielectric thickness until reaching a plateau) has been observed in similar systems, composed of Au NPs surrounded by TiO$_2$ or Al$_2$O$_3$ [21]. The experimental observations have been compared to the polarizability simulations shown in figure 5.4b. The peak position of the *in-plane* component of polarizability blue-shifts when the NPs AR decreases, while the increase in the value of the dielectric function causes a red-shift of the LSPR absorbance, coherently with previous observations on Ag NPs [8]. This is compatible with the fact that a higher AR means an increase of the *in-plane* NPs size and a decrease of the *out-of-plane* one. In the experimental observations reported in figure 5.4a, the LSPR peak is much broader with respect to the simulations, because the acquired spectrum includes the contributions of all NPs, characterized by a wide distribution of *in-plane* and *out-of-plane* dimensions, and then by different ARs. Indeed, the range of the absorbance band obtained experimentally for the different samples is compatible with the sum of contributions of NPs with AR ranging between 1 and 2 and immersed in different dielectric envi-

CeO$_2$ thickness (nm)	λ_{peak} (nm)
0 (bare Au)	613
1.6	635
4	723
8	715

Table 5.1: *Wavelength positions of the peak of LSPR for the different CeO$_2$ layer thicknesses combined with Au NPs.*
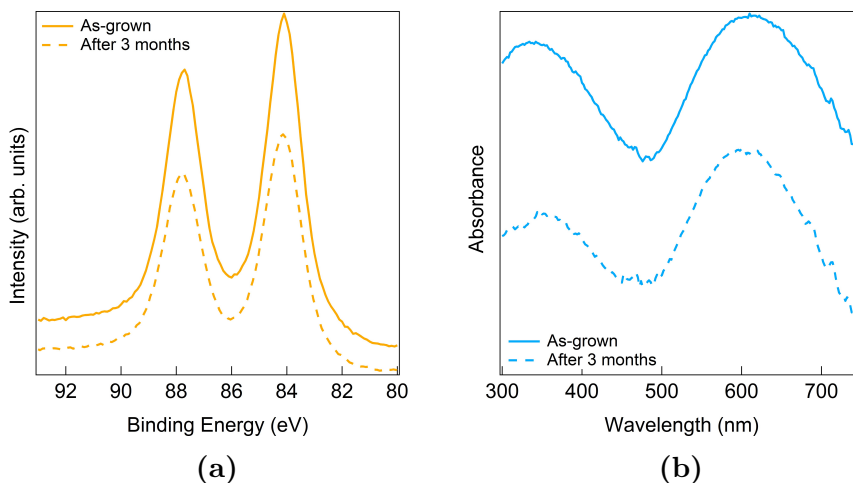

Figure 5.5: *Measurement of (a) Au 4f XPS lines and (b) optical absorbance of bare Au NPs on quartz after the growth and after 3 months in controlled N atmosphere.*

ronments. In detail, the LSPR band of the bare Au NPs (assumed to be immersed in quartz) is peaked at 613 nm, its wavelength position increases to 635 nm when the NPs are immersed in a thin layer of 1.6 nm of ceria, and it further increases as the ceria layer is thickened to 4 nm. The only variation in this behavior is observed when the ceria film thickens from 4 nm to 8 nm. In this case, we observe a very slight blue-shift of the LSPR peak position, contrarily with our expectations. If the dielectric functions of the two samples were strongly different with each other, one would have noticed a red-shift in the 8 nm film with respect to the 4 nm one. Since this shift is not observed, moreover, the signal from the thinnest ceria sample is slightly blue-shifted, it is possible to conclude that the two films have a similar dielectric function, that can be approximated with the bulk ceria one ϵ_{CeO_2}. Since the plasmonic peak position is strongly affected also by the NP ARs, the blue-shift of the 4 nm absorbance signal can be justified by a possible slightly different average ARs in the two samples.

Stability over time

In order to evaluate the effects of exposure to air on bare Au NPs, we have studied the stability of the plasmonic properties of Au NPs on the quartz substrate by repeating the optical measurements after 3 months from the deposition of the system, as shown in figure 5.5b. We have also analyzed the modifications of the surface of NPs by measuring the XPS spectra of the Au 4f region after growth and after 3 months in controlled N$_2$ atmosphere: the results are shown in figure 5.5a. Because of the stability of Au in air conditions, both the optical spectrum and the Au 4f line appear

almost unmodified after long time from the sample deposition. The XPS Au 4f line appears unmodified also for the Au@CeO$_2$ samples.

5.2 Ultrafast dynamics of excited charges in Au NPs coupled to CeO$_2$

As already mentioned in the first chapter of this thesis, the coupling of plasmonic NPs with cerium oxide can sensitize the system to visible radiation, taking advantage of the large absorption and scattering cross section in the visible range, typical of plasmonic NPs. The light-NP interaction can trigger LSPR in the NPs, which can relax by transferring charges or energy to the surrounding semiconductor. Different competing mechanisms are involved in the de-excitation of LSPRs and in the activation of the nearby semiconducting oxide. In general, LSPRs decay via the generation of charges with a broad energy distribution, some of which can be injected over the Schottky barrier towards the surrounding oxide. The process competes with a second mechanism in which the LSPR energy directly excites charge carriers into empty conduction band states in the oxide across the interface, leaving positive charges in the metal valence band [22, 23, 24]. These two mechanism are expected to involve different time scales, with the direct injection occurring within the first tens of fs after LSPR excitation, and hot electron indirect injection requiring a few hundreds of fs (see figure 1.14) [25]. On the picosecond timescale electron-phonon scattering, leading to local thermal activation of the catalyst, prevails [25]. The processes and their efficiency strongly depend on different variables, including the energy alignment of filled and empty bands of the two materials, the height and width of the Schottky barrier between them, and the NP size, shape and density. A large number of previous studies, included the one presented in the fourth chapter of this thesis, have revealed an enhanced activity in photocatalysts incorporating plasmonic NPs [25, 26, 27, 28, 29, 30] but only a limited number have tried to isolate the different activation mechanisms based on the dynamics of excited states [24, 27, 31].

In a previous study on CeO$_2$ coupled with Ag NPs using FTAS, Pelli Cresi et al. have identified an efficient and persistent plasmon-mediated electron injection from the Ag NPs to cerium oxide [20]. However, in the case of Ag NPs the investigation of the electron injection dynamics at ultrashort time scales was hindered by the superposition between a photo-induced absorption (PIA) signal, characteristic of CeO$_2$ excitation, and the plasmon-related transient absorption signal. The work described in chapter 4, i.e. an element-specific analysis of the process using FEL based pump-probe X-Ray absorption spectroscopy, allowed us to unambiguously identify a reduction of CeO$_2$ compatible with a plasmon-mediated transfer of electrons into Ce 4f levels and to estimate an upper limit of 200 fs for the injection time, a value short enough to exclude thermal effects.

The present section is focused on Au NPs combined with CeO$_2$, grown as described above. Since the LSPR-related absorption band in Au NPs is centered at a lower energy as compared to Ag NPs, the transient absorption signal related to electron injection could be clearly separated from the plasmon-related signal by FTAS. In the present section, we studied the ultrafast dynamics of excited states induced by UV and Vis-light excitation in Au NPs combined with cerium oxide, aimed at understanding the excitation pathways. The FTAS data show that the excitation of LSPRs in the Au NPs leads to an ultrafast injection of electrons into the empty
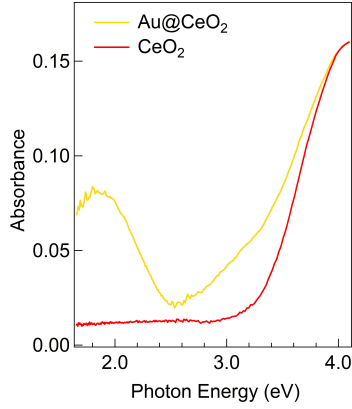
Figure 5.6: *Optical absorbance of the CeO$_2$ film (red line) and of the Au@CeO$_2$ sample (yellow line), acquired with s-polarized light as a function of the photon energy.*

4f states of the surrounding cerium oxide. Within the first few ps the injected electrons couple with the lattice distortion forming a polaronic excited state, with similar properties to the one which is formed after direct band gap excitation in the oxide. At sub-ps delay times we observed relevant differences in the energetics and the time dynamics as compared to the case of band gap excitation. Using different pump energies across the LSPR-related absorption band, the efficiency of the electron injection from the NPs into the oxide was found to be rather high, with a maximum above 30%. The injection efficiency has a different trend in energy as compared to the LSPR-related static optical absorbance, showing a significant decrease at low energies. This behavior is explained considering different de-excitation pathways with variable weight at the different excitation energies across the LSPR band. The result obtained suggests that improving the matching of the plasmonic response to the low energy part of the solar spectrum would not improve the overall solar catalytic efficiency of the material.

5.2.1 Experimental

In this section, we investigated the dynamics of charge transfer in the 8 nm film of CeO$_2$ coupled with Au NPs, deposited on a quartz substrate and described the first section of this chapter 5.1.1, using femtosecond transient absorption spectroscopy (FTAS), as described in chapter 2.3.2. The electronic properties of the sample, investigated by means of UPS and XPS and the morphology of the sample are reported respectively in figures 5.1 and 5.2. The optical absorbance of the Au@CeO$_2$ sample compared with the reference CeO$_2$ absorbance, measured with the impinging photon beam forming an angle of 22° with the sample surface normal with s polarization, is reported in figure 5.6.

To investigate the ultrafast dynamics of excited states, FTAS measurements have been performed using a pump-probe femtosecond laser system described in detail in [20, 32]. The transient absorption, measured as a function of the probe energy (E) and of the delay time between the pump and the probe (τ), is given by $\Delta A(E, \tau) = A_{pump}(E, \tau) - A_{no-pump}(E)$, where A_{pump} represents the absorbance of the sample at a delay time τ from the pump and $A_{no-pump}$ is the absorbance without the pump. The absorbance maps are shown in figure 5.7.

As an optical pump, we used a laser pulse generated by the optical parametric amplifier that was tuned either to an energy above the bandgap of ceria or to energies

in the visible range corresponding to different plasmonic resonances of the embedded Au NPs. For the probe, a small portion of the fundamental ($\sim 3\mu$J) was passed through a BBO crystal to generate the second harmonic (400 nm) that was focused into a rotating CaF_2 crystal to generate a supercontinuum in the UV energy range (3.50-4.35 eV). The temporal delay of the probe pulse was tuned by varying the length of the optical path of the beam used to generate the white light. In the transient absorbance maps presented in this work, the chirp of the probe pulse has been corrected. The instrument response function (IRF) has been evaluated in separate experiments to be Gaussian with a FHWM of 70 fs. The pump fluences were 0.7 mJ/cm^2 for the 4.5 eV and 3.3 eV energies and 1 mJ/cm^2 for the other pump energies, which is sufficiently low not to induce melting of the nanoparticles [33]. The pump-probe delay was scanned between -1 ps and 300 ps.

5.2.2 Results and discussion

Figure 5.6 shows the UV-Vis optical absorbance of the Au@CeO$_2$ sample compared with the reference CeO$_2$ sample. The absorbance of pure cerium oxide exhibits a strong increase in the ultraviolet region, peaked around 4.1 eV, and a very small intensity in the visible range, in agreement with previous measurements of CeO$_2$ films grown in the same conditions [19, 20]. The incorporation of Au NPs into the oxide significantly modifies the optical absorbance of the material, with a broad band, peaked at ~ 1.9 eV, appearing in the visible region due to the excitation of LSPR in Au NPs, as expected from the simulation of Au NPs in ceria reported in figure 5.4b [17, 18]. The width of the observed LSPR-related band is consistent with the irregular shapes of the self-assembled NPs as measured by SEM (figure 5.2) [34]. Moreover, the absorbance also shows an increase between 2.5 and 3.2 eV, due to the excitation of interband transitions in the Au NPs [25]. The excitation of sub-band gap defect states in the oxide, possibly present in the topmost CeO$_2$ film above the Au NP, can also contribute to absorbance in this region.

Figure 5.7 shows the false-color maps of transient absorption (TA) spectra of the Au@CeO$_2$ sample, excited with a pump at 4.5 eV, above the CeO$_2$ band gap (figure 5.7a), and below the band gap at the LSPR of Au NPs (1.9 eV, figure 5.7c), with a probe in the UV range and a delay time range limited to 0-10 ps. The energy position and the intensity of the transient features observed and their temporal evolution provide information on the dynamics of the photo-excited states in the investigated material. For both pump energies it is possible to clearly identify two main features in the map, one with a positive and one with a negative intensity. The positive features, labelled as PIA1 and PIA2 for the two pump wavelengths in Figure 2, appear at a photon energy of ~ 3.5 eV, while the negative features, labelled as PB1 and PB2, appear at a higher energy of ~ 4.1 eV. To explain the origin of PIA1 and PB1, we refer to figure 5.8, which reports a sketch of the filled and empty levels at the interface between CeO$_2$ and Au NPs based on literature DFT results [35], as well as on the UPS spectra of the sample shown in figure 5.1c. CeO$_2$ is an n-type semiconductor with a valence band (VB) with a predominantly O 2p character and a conduction band (CB) with a predominantly Ce 5d character. The energy distance between the top of the VB and the bottom of the CB is approximately 6 eV. The material is characterized by the presence of localized, empty Ce 4f states between the VB and the CB and the optical band gap in ceria is given by the energy difference between the top of the VB and the bottom of the empty Ce 4f states (~ 4 eV) [19]. Based on previous studies on pure CeO$_2$ [19] and on the same system
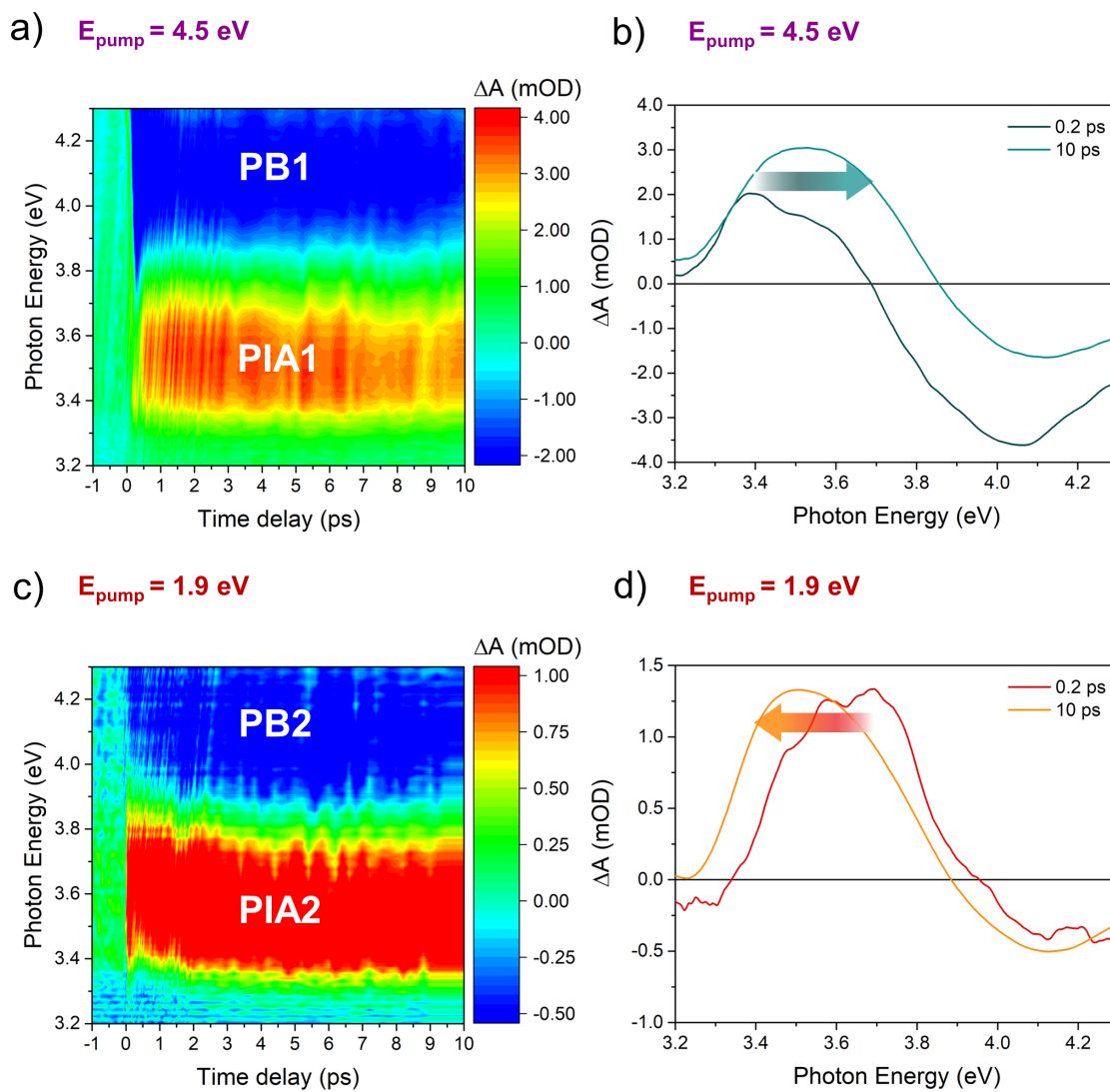
Figure 5.7: *False-color map of the TA spectra of the Au@CeO$_2$ sample excited with a pump at a) 4.5 eV (above the CeO$_2$ band gap) and b) 1.9 eV (below the band gap). The PIA signals at ~ 3.5 eV and the PB signals at ~ 4.1 eV are indicated. (b) and (d) show the TA spectra at selected delay times of 0.2 and 2 ps for the two pumps.*
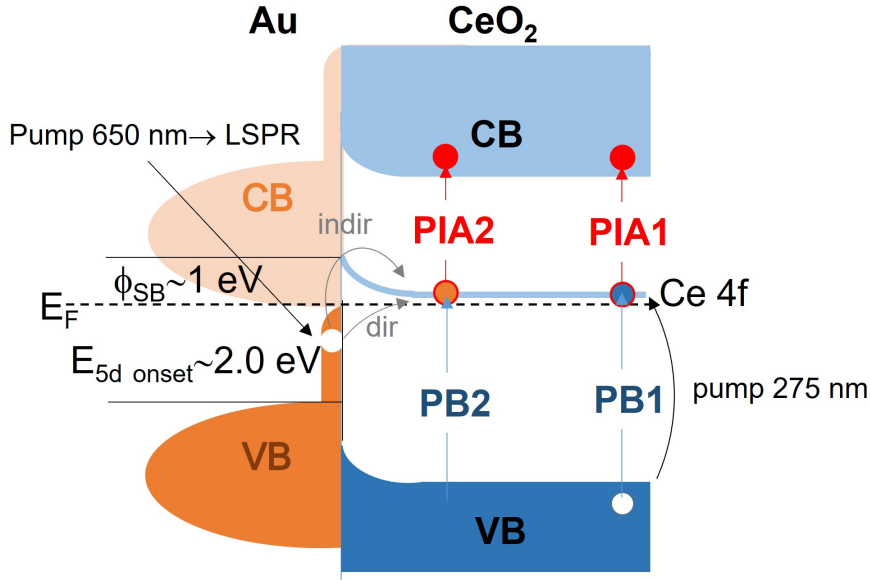
Figure 5.8: *Sketch of the bands at the Au/CeO$_2$ interface. The processes induced by band gap excitation (pump 4.5 eV) and LSPR excitation (pump 1.9 eV) and the corresponding PIA and PB signals are schematically shown.*

coupled with Ag NPs [20], the PIA1 feature at 3.5 eV is ascribed to photoinduced absorption (PIA) of valence band electrons excited by the pump into empty Ce 4f levels and subsequently re-excited by the probe into the conduction band of Ce 5d character (figure 5.8). In analogy, the PB1 feature at 4.1 eV, corresponding to the maximum of the CeO$_2$ optical absorbance, as shown in figure 5.6, is ascribed to photoinduced bleaching (PB) of the valence band, due to a decrease in the density of unoccupied 4f final states for the VB to 4f excitation, and to a decrease in the initial density of occupied states in the VB, as compared to the ground state. The PB2 and PIA2 features in figure 5.7, obtained with an excitation energy below the band gap at the Au NPs LSPR (1.9 eV), appear at approximately the same energy as PB1 and PIA1. To understand the origin of such features, the electronic band structure of Au at the interface with CeO$_2$ has to be considered (see the sketch in figure 5.8).

The density of states of the Au NPs investigated here - as shown by the UPS measurements reported in figure 5.1c - is not very different from the one of bulk Au, having a relatively low intensity 6s band extending within the first 2 eV below the Fermi level and a more intense 5d band with an onset at $\sim$ 2 eV binding energy. The alignment between metal and oxide energy levels at the interface critically depends on the interface properties and on possible charge transfers between the two materials. In the literature Au NPs grown on CeO$_2$ have shown a negligible steady state charge transfer [36], a result that has also been confirmed by DFT calculations [37], differently from the case of Ag [38] or Pt NPs [37], in which electrons are transferred from the metal to the cerium oxide support when they come into contact. The empty Ce 4f levels are very close to the Fermi level, so an upward band bending of the oxide CB and VB is expected at the interface with Au [39]. The Schottky barrier, Φ_{SB} in figure 5.8, between the metal and the oxide is approximately 0.9 eV [40]. The LSPR, excited in the Au NPs by the pump at 1.9 eV, can decay via the generation of hot electrons with an energy distribution that extends up to the value used for LSPR excitation (1.9 eV). The most energetic electrons have enough energy to be transferred over the approximately 0.9 eV high Schottky barrier by
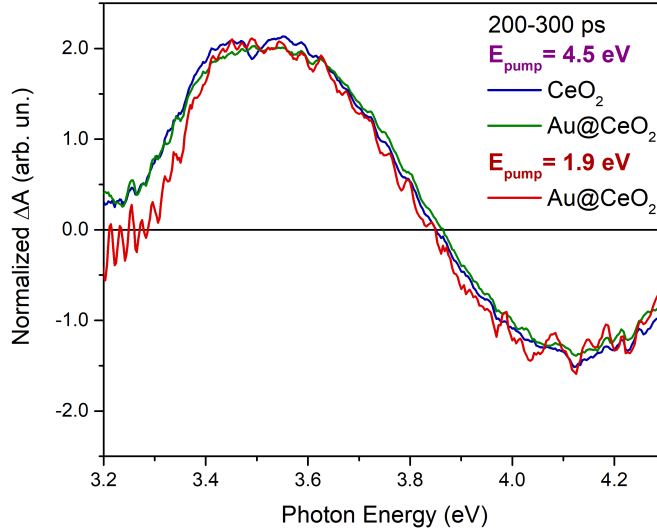
Figure 5.9: *Normalized TA spectra averaged over 200-300 ps of Au@CeO$_2$ (green line) and CeO$_2$ (blue line) samples excited with a pump at 4.5 eV (above the CeO$_2$ band gap) and of the Au@CeO$_2$ sample excited with a pump at 1.9 eV (red line).*

indirect transfer (path indicated as indir in figure 5.8). Alternatively, the LSPR can decay by direct charge transfer of electrons from the Au VB to the Ce 4f levels (path indicated as *dir* in figure 5.8). Both the PIA2 and the PB2 signals can be assigned to the transient occupation of Ce 4f levels caused by LSPR-mediated electron injection from the NPs to the semiconductor. While the PIA2 results from the excitation of the electrons injected into the 4f states to the CB, the PB2 signal is generated by the lower density of empty final states available for the VB to 4f transition, as compared to the unperturbed state (figure 5.8). We note that, as we expected, the intensity of the TA features observed after LSPR excitation is lower than in the case of band gap excitation due to the lower efficiency of the LSPR-mediated charge transfer process as compared to direct band gap excitation.

Before discussing the details of the time dependence of the transient signals, we focus on their spectral shapes at long time delays, when the systems have relaxed for hundreds of picoseconds after photoexcitation. In figure 5.9 the comparison of the normalized transient signals averaged over 200-300 ps time delays are shown, following excitation of i) CeO$_2$ at 4.5 eV (blue line), ii) Au@CeO$_2$ at 4.5 eV (green line) and iii) Au@CeO$_2$ at 1.9 eV (red line), revealing the same spectral responses in the three cases. This suggests that the final states are indeed the same. Based on the analysis presented in reference [19], which shows that above band gap photoexcitation in a pure cerium oxide results in the formation of a small polaron in the excited state, we conclude that both above gap and LSPR excitation in the Au@CeO$_2$ system result in the formation of a small polaron in analogy with pure CeO$_2$. This hypothesis is also consistent with the kinetic behavior of the PIA1, PIA2, PB1 and PB2 signals, which show a non-negligible intensity at all delay times investigated, in close analogy with CeO$_2$ [32] and Ag@CeO$_2$ [20], because of the relatively long recombination times of photoexcited carriers in the oxide. Therefore, Au NPs do not introduce different recombination channels within the investigated delay time range.

To analyze in detail the kinetics of the TA signals, we used a global analysis
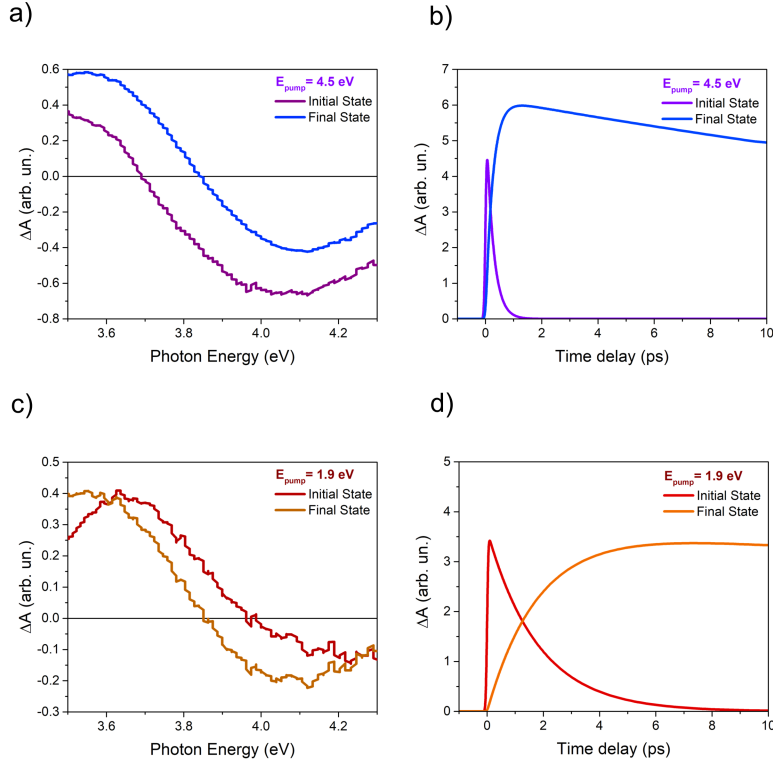
Figure 5.10: *a) Spectral components obtained from the global analysis for the pump at 4.5 eV (blue and violet lines) and c) 1.9 eV (red and orange lines); b) Weight dynamics of the two spectral components for the pump at b) 4.5 eV and d) 1.9 eV*

approach that allowed us to extract the transient photoexcited components from the TA spectra with their temporal evolution. As shown in figure 5.7b and d, the TA spectra show non-negligible modifications in energy and intensity within the first few ps after excitation for both pump energies. Following the approach used in reference [19] by Pelli Cresi et al., the temporal evolution of the spectra was modelled using two components, an initially photoexcited state, and a long living final state. The shape and the exponential decay/rise constants of the two components are left as free fitting parameters. The components obtained using this approach and the sequential exponential dynamics of their intensity for the two pump energies are shown in figure 5.10. In analogy with the case of pure ceria [19] for the pump at 4.5 eV the two components are interpreted as being due to the initially populated excited 4f states that relaxes into a polaronic state at lower energy, resulting in a higher energy PIA (see the arrow in figure 5.7b and figure 5.10a). In this model the PB remains at the same energy, although it may appear to shift due to the overlap with the PIA. As shown in figure 5.10b for the pump above the band gap the initial state decays into the final state within the first picosecond. Overall, the dynamics of the excited states of the Au@CeO$_2$ system pumped above the band gap shows the same trend as that of bare ceria observed in reference [19], consistent with the expected negligible modifications induced by the presence of Au NPs on electronic structure of the ceria matrix. The situation is significantly different in the case of plasmonic excitation of the Au@CeO$_2$ system shown in figure 5.10c, in which the PIA is initially at a higher energy than in the final state, contrary to what was observed in the case of excitation above the ceria gap (see the arrow in figure 5.7d). As shown in figure 5.7, in this case the time required to evolve from the initial to the final final state is longer (more than 4 ps) than for the above band

gap excitation (~ 1 ps). Both of the LSPR-mediated injection processes (*dir* and *indir*) occur on a much faster timescale, for example the Ag@CeO$_2$ system showed a time constant shorter than 200 fs [41]. Furthermore, the polaron state is also known to form with a time constant of approximately 300 fs after photoexcitation above the bandgap [19]. Therefore, the energetic and temporal dynamics observed here cannot be assigned to any of these processes. A possible explanation may lie in the fact that the electrons are injected into interface states, the energy of which may lead to a different energy position of the PIA maximum with respect to the energy position related to the bulk states. The hypothesis that the intermediate occupied 4f states decrease in energy more slowly than the final 5d conduction band states as the excited state propagates from the interface (see also sketch in figure 5.8) is consistent with the observed overall reduction of the transition energy of the PIA at ultrashort decay times and with the longer time required to evolve into the bulk-like polaronic state which dominates the TA spectra at long delay times.

Charge injection efficiency

Since the PIA signal intensity at sub-bandgap energies is proportional to the density of electrons in the Ce 4f levels after the excitation, the injection efficiency can be quantified by comparing the intensity of the PIA signal of the Au@CeO$_2$ sample pumped at different pump energies with the intensity of same signal of the CeO$_2$ sample pumped at 4.5 eV. Following the procedure reported in reference [17, 20], under the assumption that each absorbed photon with energy higher than CeO$_2$ band gap excites an electron from the valence band to Ce 4f levels, the absorbed photon density is:

$$n_{ph} = \frac{A(\omega_{pump}) \cdot \Phi}{E_{pump} \cdot D} \tag{5.1}$$

where $A(\omega_{pump})$ is the absorbance of the sample at the pump photon energy evaluated from figure 5.6, Φ is the pump fluence, E_{pump} is the pump energy and D is the total sample thickness. The absorbed photon density n_{ph} can be correlated to the density of electrons excited in the Ce 4f levels, estimated by the intensity of the PIA signal between 50 ps and 250 ps (see figure 5.11). The short delay time range was not considered, because the shape of the signals is affected by different shifts in energy at the different pump energies. The proportionality constant κ between the integral intensity of the PIA signal and n_{ph} was obtained as the ratio between these two quantities:

$$\kappa = \frac{\Delta A(t) \cdot t}{n_{ph}} \tag{5.2}$$

The ratio between the κ values of the Au@CeO$_2$ pumped at the different energies with the reference κ obtained by Au@CeO$_2$ pumped at 4.5 eV corresponds to the charge injection efficiency from the Au NPs to CeO$_2$. The values of κ and n_{ph} for the different pump energies are reported in table 5.2.

Figure 5.12 presents the electron injection efficiencies, estimated following the method exposed above, together with the optical absorbance of Au@CeO$_2$ in the same energy region (yellow curve). At a pump energy of 3.3 eV, the electron injection efficiency of $18 \pm 2\%$ is assigned to interband excitation in the Au NPs followed by an *indir* injection of the resulting hot electrons over the Schottky barrier between Au and CeO$_2$ (approximately 0.9 eV [40]), into the CeO$_2$ CB (figure 5.1c and figure 5.8). The electron injection efficiency drastically increases above $35 \pm 1\%$ at 2.25 eV, an energy which excites the high energy wing of the LSPR of the Au NPs,
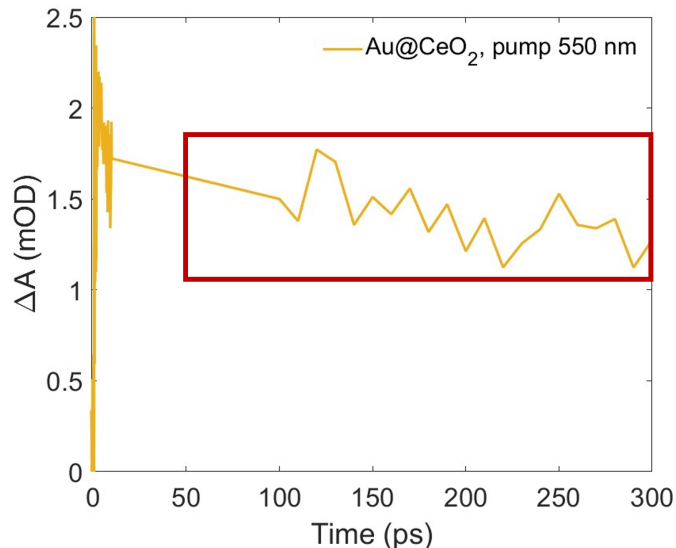
Figure 5.11: *Time window used to calculate $\Delta A(t)$ for the $Au@CeO_2$ sample pumped at 550 nm. A similar procedure has been repeted for several pump energies*

Pump energy (eV)	ΔA (mOD)	n_{ph}
4.5	2.3 ± 0.1	3.4×10^{20}
3.3	0.6 ± 0.2	5.2×10^{20}
2.5	0.49 ± 0.05	5.9×10^{20}
2.25	1.39 ± 0.02	5.2×10^{20}
2.1	1.33 ± 0.03	6.4×10^{20}
1.9	0.98 ± 0.04	7.5×10^{20}
1.77	0.65 ± 0.05	8.6×10^{20}
1.65	0.37 ± 0.05	9.2×10^{20}

Table 5.2: *Average of the PIA signal in the 50-250 ps time range for the $Au@CeO_2$ sample at the different pump energies and absorbed photon density, used to evaluate the LSPR-mediated electron injection efficiency.*

and it gradually decreases at lower pump energies, reaching a value below 10% at 1.6 eV, showing a trend that does not follow the intensity of the LSPR absorbance. Indeed, the *indir* injection is expected to decrease its efficiency as the photon energy is decreased. The observed non-monotonic trend of the injection efficiency with energy may be due to the additional action of LSPR–mediated *dir* mechanism (see also figure 5.8) that enhances the electron injection in the 1.90-2.25 eV energy range, while at lower pump energies the reduced efficiency is due to the lower probability to inject excited electrons into the semiconductor.

We note that a mismatch between the injection efficiency and the intensity of the LSPR resonance was observed also in the case of Au NPs coupled with TiO_2 [17, 42] and for Ag NPs coupled with cerium oxide [20]. As CeO_2 is a reducible oxide, the efficient charge transfer induced by visible light absorption is expected to have a relevant effect on the oxide catalytic properties. The presence of extra charge in the 4f states is in fact predicted to decrease the oxygen vacancy formation energy, and in turn to increase the redox activity. The low recombination rate of the excited charge within times of the order of hundreds of picoseconds is in agreement with the holes lifetimes observed on the similar system made of Ag NPs on CeO_2 [43]. We emphasize that this aspect is very promising in the view of obtaining an efficient photocatalytic material, in which the plasmon-induced thermal
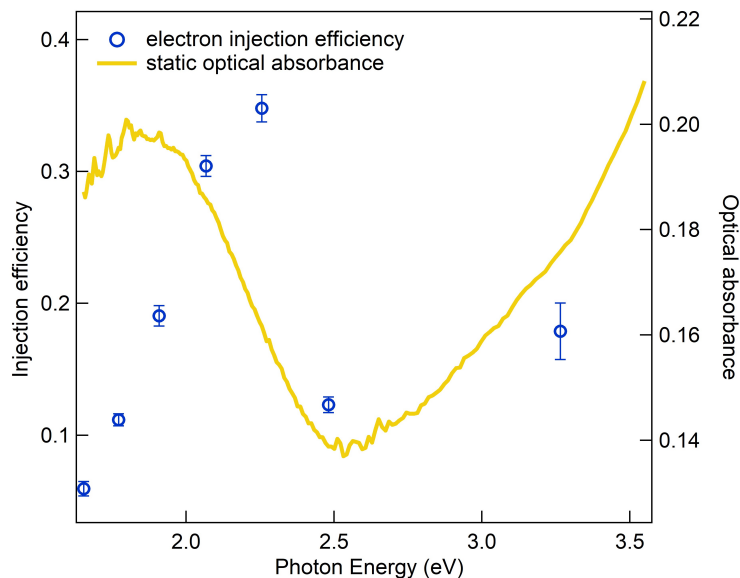
Figure 5.12: *Electron (blue circles) injection efficiencies as a function of the pump wavelength. The static optical absorbance (yellow curve) is also reported for comparison.*

activation, expected to take place in a nanosecond time regime, can be enhanced by favorable persistent electronic modifications. Further conclusions of this work are that interband transitions in gold are less efficient at transferring charge to the ceria than LSPR-mediated excitations and that increasing the overlap of the LSPR with the solar spectrum at lower energies will not increase the overall solar efficiency, giving fundamental insights in the design of devices based on metallic nanostructures embedded in wide band gap semiconductors.

5.2.3 Conclusions

We investigated the dynamics of photoexcited states in a composite system made of Au NPs embedded within a thin film of cerium oxide. The optical absorbance of the sample presents a broad band in the visible range that is assigned to the LSPR excitation in the NPs. FTAS measurements showed that LSPR excitations in the Au NPs relax by transferring electrons to the surrounding semiconductor. At ultrashort delay times, below a few ps, a markedly different energetic and temporal dynamics is observed in the case of LSPR-mediated injection as compared to direct band gap excitation. The observed differences are compatible with the expected modifications of the electronic properties at the interface between the metal NP and the oxide. Interestingly, after a few ps both band gap and LSPR excitation lead to the same bulk-like polaronic state. By comparing the injection efficiencies following interband and LSPR excitations we suggest that the interband injection is dominated by the *indir* mechanism while the LSPR-mediated injection takes place by both *dir* and *indir* mechanisms. The electron injection efficiency following LSPR excitation shows a maximum over 30% at 2.25 eV, an energy which does not correspond to the maximum of LSPR-related optical absorbance, suggesting that the injection efficiency does not simply follow the intensity of the plasmonic excitation.

Bibliography

[1] Ingve Simonsen, Rémi Lazzari, Jacques Jupille, and Stéphane Roux. Numerical modeling of the optical response of supported metallic particles. *Phys. Rev. B*, 61:7722–7733, 2000.

[2] P. Luches, F. Pagliuca, and S. Valeri. Morphology, stoichiometry, and interface structure of Ceo_2 ultrathin films on Pt(111). *The Journal of Physical Chemistry C*, 115(21):10718–10726, 2011.

[3] C. G. Granqvist and O. Hunderi. Optical properties of ultrafine gold particles. *Phys. Rev. B*, 16:3513–3534, 1977.

[4] D.R. Baer, R.L. Gordon, and C.W. Hubbard. Work function and UPS study of au and o on re. *Applied Surface Science*, 45(1):71–83, 1990.

[5] Leandro Pascua, Fernando Stavale, Niklas Nilius, and Hans-Joachim Freund. Ag/ZnO hybrid systems studied with scanning tunnelling microscopy-based luminescence spectroscopy. *Journal of Applied Physics*, 119(9):095310, 2016.

[6] Uwe Kreibig and Michael Vollmer. *Optical properties of metal clusters*. Springer Series in Materials Science. Springer, Berlin, Germany, 1995 edition, 1995.

[7] C. G. Granqvist and O. Hunderi. Optical properties of ultrafine gold particles. *Physical Review B*, 16(8):3513–3534, 1977.

[8] Jacopo Stefano Pelli Cresi, Enrico Silvagni, Giovanni Bertoni, Maria Chiara Spadaro, Stefania Benedetti, Sergio Valeri, Sergio D'Addato, and Paola Luches. Optical and electronic properties of silver nanoparticles embedded in cerium oxide. *The Journal of Chemical Physics*, 152(11):114704, 2020.

[9] Fu-Chien Chiu and Chih-Ming Lai. Optical and electrical characterizations of cerium oxide thin films. *Journal of Physics D: Applied Physics*, 43(7):075104, 2010.

[10] Kevin M. McPeak, Sriharsha V. Jayanti, Stephan J. P. Kress, Stefan Meyer, Stelio Iotti, Aurelio Rossinelli, and David J. Norris. Plasmonic films can easily be better: Rules and recipes. *ACS Photonics*, 2(3):326–333, 2015. PMID: 25950012.

[11] Gorachand Ghosh. Sellmeier coefficients and dispersion of thermo-optic coefficients for some optical glasses. *Appl. Opt.*, 36(7):1540–1546, 1997.

[12] G. Ghosh, M. Endo, and T. Iwasaki. Temperature-dependent sellmeier coefficients and chromatic dispersions for some optical fiber glasses. *Journal of Lightwave Technology*, 12(8):1338–1342, 1994.

[13] Xiaotong Liu, Dabing Li, Xiaojuan Sun, Zhiming Li, Hang Song, Hong Jiang, and Yiren Chen. Tunable dipole surface plasmon resonances of silver nanoparticles by cladding dielectric layers. *Scientific Reports*, 5(1), 2015.

[14] R. Lässer and N.V. Smith. Interband optical transitions in gold in the photon energy range 2–25 eV. *Solid State Communications*, 37(6):507–509, 1981.

[15] X. D. Li, T. P. Chen, Y. Liu, and K. C. Leong. Influence of localized surface plasmon resonance and free electrons on the optical properties of ultrathin Au films: a study of the aggregation effect. *Opt. Express*, 22(5):5124–5132, 2014.

[16] P. Romaniello and P. L. de Boeij. The role of relativity in the optical response of gold within the time-dependent current-density-functional theory. *The Journal of Chemical Physics*, 122(16):164303, 2005.

[17] Daniel C. Ratchford, Adam D. Dunkelberger, Igor Vurgaftman, Jeffrey C. Owrutsky, and Pehr E. Pehrsson. Quantification of efficient plasmonic hot-electron injection in gold nanoparticle–Tio2 films. *Nano Letters*, 17(10):6047–6055, 2017. PMID: 28850243.

[18] Akihiro Furube, Luchao Du, Kohjiro Hara, Ryuzi Katoh, and Masanori Tachiya. Ultrafast plasmon-induced electron transfer from gold nanodots into Tio2 nanoparticles. *Journal of the American Chemical Society*, 129(48):14852–14853, 2007. PMID: 17994750.

[19] Jacopo Stefano Pelli Cresi, Lorenzo Di Mario, Daniele Catone, Faustino Martelli, Alessandra Paladini, Stefano Turchini, Sergio D'Addato, Paola Luches, and Patrick O'Keeffe. Ultrafast formation of small polarons and the optical gap in Ceo$_2$. *The Journal of Physical Chemistry Letters*, 11(14):5686–5691, 2020. PMID: 32580554.

[20] Jacopo Stefano Pelli Cresi, Maria Chiara Spadaro, Sergio D'Addato, Sergio Valeri, Stefania Benedetti, Alessandro Di Bona, Daniele Catone, Lorenzo Di Mario, Patrick O'Keeffe, Alessandra Paladini, Giovanni Bertoni, and Paola Luches. Highly efficient plasmon-mediated electron injection into cerium oxide from embedded silver nanoparticles. *Nanoscale*, 11:10282–10291, 2019.

[21] Yalian Weng, Guixiong Chen, Xiongtu Zhou, Yongai Zhang, Qun Yan, and Tailiang Guo. Photoluminescence enhancement of quantum dots with different emission wavelengths using oxide shell-isolated Au nanoparticles. *Journal of Materials Science*, 57(15):7642–7652, 2022.

[22] Shijing Tan, Adam Argondizzo, Jindong Ren, Liming Liu, Jin Zhao, and Hrvoje Petek. Plasmonic coupling at a metal/semiconductor interface. *Nature Photonics*, 11(12):806–812, 2017.

[23] K. Wu, J. Chen, J. R. McBride, and T. Lian. Efficient hot-electron transfer by a plasmon-induced interfacial charge-transfer transition. *Science*, 349(6248):632–635, 2015.

[24] Nianqiang Wu. Plasmonic metal–semiconductor photocatalysts and photoelectrochemical cells: a review. *Nanoscale*, 10:2679–2696, 2018.

[25] Yuchao Zhang, Shuai He, Wenxiao Guo, Yue Hu, Jiawei Huang, Justin R. Mulcahy, and Wei David Wei. Surface-plasmon-driven hot electron photochemistry. *Chemical Reviews*, 118(6):2927–2954, 2018. PMID: 29190069.

[26] Sun Mi Kim, Hyosun Lee, Kalyan C. Goddeti, Sang Hoon Kim, and Jeong Young Park. Photon-induced hot electron effect on the catalytic activity of ceria-supported gold nanoparticles. *The Journal of Physical Chemistry C*, 119(28):16020–16025, 2015.

[27] Suljo Linic, Phillip Christopher, and David B. Ingram. Plasmonic-metal nanostructures for efficient conversion of solar to chemical energy. *Nature Materials*, 10(12):911–921, 2011.

[28] Wenbo Hou, Wei Hsuan Hung, Prathamesh Pavaskar, Alain Goeppert, Mehmet Aykol, and Stephen B. Cronin. Photocatalytic conversion of CO_2 to hydrocarbon fuels via plasmon-enhanced absorption and metallic interband transitions. *ACS Catalysis*, 1(8):929–936, 2011.

[29] Shaunak Mukherjee, Florian Libisch, Nicolas Large, Oara Neumann, Lisa V. Brown, Jin Cheng, J. Britt Lassiter, Emily A. Carter, Peter Nordlander, and Naomi J. Halas. Hot electrons do the impossible: Plasmon-induced dissociation of H_2 on Au. *Nano Letters*, 13(1):240–247, 2012.

[30] Jing Pan, Lingling Zhang, Songtao Zhang, Zhan Shi, Xiao Wang, Shuyan Song, and Hongjie Zhang. Half-encapsulated au nanorods@CeO_2 core@shell nanostructures for near-infrared plasmon-enhanced catalysis. *ACS Applied Nano Materials*, 2(3):1516–1524, 2019.

[31] Haibin Tang, Chih-Jung Chen, Zhulin Huang, Joeseph Bright, Guowen Meng, Ru-Shi Liu, and Nianqiang Wu. Plasmonic hot electrons for sensing, photodetection, and solar energy applications: A perspective. *The Journal of Chemical Physics*, 152(22):220901, 2020.

[32] Daniele Catone, Lorenzo Di Mario, Faustino Martelli, Patrick O'Keeffe, Alessandra Paladini, Jacopo Stefano Pelli Cresi, Aswathi K Sivan, Lin Tian, Francesco Toschi, and Stefano Turchini. Ultrafast optical spectroscopy of semiconducting and plasmonic nanostructures and their hybrids. *Nanotechnology*, 32(2):025703, 2020.

[33] Michele Magnozzi, Remo Proietti Zaccaria, Daniele Catone, Patrick O'Keeffe, Alessandra Paladini, Francesco Toschi, Alessandro Alabastri, Maurizio Canepa, and Francesco Bisio. Interband transitions are more efficient than plasmonic excitation in the ultrafast melting of electromagnetically coupled au nanoparticles. *The Journal of Physical Chemistry C*, 123(27):16943–16950, June 2019.

[34] Gregory V. Hartland. Optical studies of dynamics in noble metal nanostructures. *Chemical Reviews*, 111(6):3858–3887, 2011.

[35] Yi Pan, Niklas Nilius, Hans-Joachim Freund, Joachim Paier, Christopher Penschke, and Joachim Sauer. Titration of Ce^{3+} ions in the ceo$_2$(111) surface by au adatoms. *Phys. Rev. Lett.*, 111:206101, 2013.

[36] M. Baron, O. Bondarchuk, D. Stacchiola, S. Shaikhutdinov, and H.-J. Freund. Interaction of gold with cerium oxide supports: CeO_2(111) thin films vs CeO_x nanoparticles. *The Journal of Physical Chemistry C*, 113(15):6042–6049, 2009.

[37] María Marta Branda, Norge C. Hernández, Javier Fdez. Sanz, and Francesc Illas. Density functional theory study of the interaction of cu, ag, and au atoms with the regular CeO_2 (111) surface. *The Journal of Physical Chemistry C*, 114(4):1934–1941, 2010.

[38] Charles T. Campbell. Ultrathin metal films and particles on oxide surfaces: structural, electronic and chemisorptive properties. *Surface Science Reports*, 27(1):1–111, 1997.

[39] Benxia Li, Ting Gu, Tian Ming, Junxin Wang, Peng Wang, Jianfang Wang, and Jimmy C. Yu. (gold core)@(ceria shell) nanostructures for plasmon-enhanced catalytic reactions under visible light. *ACS Nano*, 8(8):8152–8162, 2014.

[40] V Grosse, R Bechstein, F Schmidl, and P Seidel. Conductivity and dielectric properties of thin amorphous cerium dioxide films. *Journal of Physics D: Applied Physics*, 40(4):1146–1149, 2007.

[41] Jacopo Stefano Pelli Cresi, Emiliano Principi, Eleonora Spurio, Daniele Catone, Patrick O'Keeffe, Stefano Turchini, Stefania Benedetti, Avinash Vikatakavi, Sergio D'Addato, Riccardo Mincigrucci, Laura Foglia, Gabor Kurdi, Ivaylo P. Nikolov, Giovanni De Ninno, Claudio Masciovecchio, Stefano Nannarone, Jagadesh Kopula Kesavan, Federico Boscherini, and Paola Luches. Ultrafast dynamics of plasmon-mediated charge transfer in $Ag@CeO_2$ studied by free electron laser time-resolved x-ray absorption spectroscopy. *Nano Letters*, 21(4):1729–1734, 2021. PMID: 33570965.

[42] Luchao Du, Akihiro Furube, Kohjiro Hara, Ryuzi Katoh, and Masanori Tachiya. Ultrafast plasmon induced electron injection mechanism in gold-TiO_2 nanoparticle system. *Journal of Photochemistry and Photobiology C: Photochemistry Reviews*, 15:21–30, 2013.

[43] Jacopo Stefano Pelli Cresi, Eleonora Spurio, Lorenzo Di Mario, Patrick O'Keeffe, Stefano Turchini, Stefania Benedetti, Gian Marco Pierantozzi, Alessandro De Vita, Riccardo Cucini, Daniele Catone, and Paola Luches. Lifetime of photogenerated positive charges in hybrid cerium oxide-based materials from space and mirror charge effects in time-resolved photoemission spectroscopy. *The Journal of Physical Chemistry C*, 126(27):11174–11181, 2022.

Part II

Copper and Cuprous Oxide

Chapter 6

Cu nanoparticles

In this chapter, I will describe the study of the optical and morphological properties of Cu NPs, either embedded in a CeO_2 thin film or directly deposited on a substrate, grown using two different physical deposition methods. In the first section, I will describe systems composed by Cu NPs grown via MBE either bare or surrounded by ceria layers, similar to the samples described in the previous chapter. The bare NPs were grown in different oxygen partial pressures and substrate temperatures and with different post-processing conditions. Finally, the last part of this chapter will focus on Cu NPs grown via magnetron sputtering, without any capping or protected by a MgO shell. The final aim is to analyze the effects of the different growth conditions on the plasmonic properties of the Cu NPs and on their stability over time.

6.1   Cu NPs in ceria

As already mentioned in the first chapter, Cu NPs are promising candidates for the sensitization of ceria to visible radiation. Cu is an abundant and cheap material compared to other noble metals, with LSPRs excited by visible radiation [1, 2, 3] and a high hot electron generation rate after LSPR de-excitation in the NPs [4]. In this section, I will present the investigation of the optical and morphological properties of Cu NPs embedded in matrices of CeO_2. For this study, the procedure used is similar as the one used for Au NPs in chapter 5.1: we have measured the static optical absorbance of Cu NPs surrounded by ceria layers of different thicknesses, then compared to the theoretical expectations obtained by performing numerical simulations of polarizability based upon the Maxwell-Garnett model for optical absorption [5]. Since Cu has a very strong tendency to oxidation, the stability of optical properties over time has also been studied, in order to understand whether the ceria capping layer is sufficient to preserve the plasmonic properties, related to the metallic nature of the NPs.

6.1.1   Experimental

The samples used in this chapter were grown in RAGNO-1, using the same strategy as for the samples described in 5.1. Also in this case, the samples used for the optical characterization were grown onto a quartz substrate and the sample for SEM imaging was grown on a Si substrate with thermal oxide. The samples for optical measurements consisted of a layer of Cu NPs of 2 nm nominal thickness, embedded between ceria layers of either 4 or 8 nm, while the sample for SEM measurements
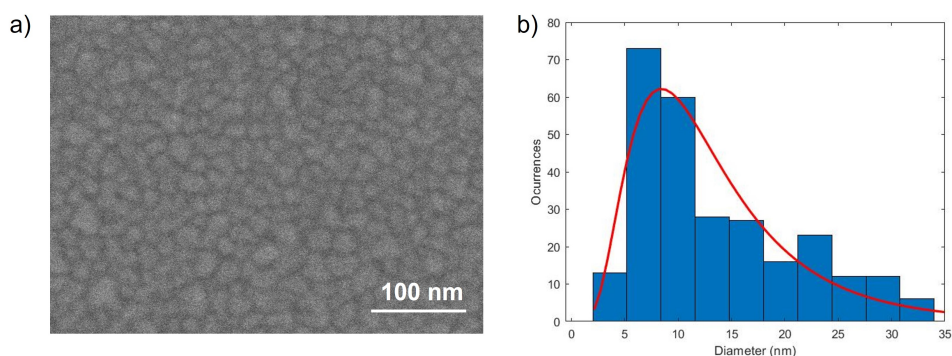
Figure 6.1: *a) SEM image of a 2 nm CeO$_2$+ 2 nm Au sample and b) the size distribution extracted from the SEM images.*

was composed of 2 nm CeO$_2$ + 2 nm of Cu on top. The procedures for cleaning the substrates and evaporation of ceria films and NPs are the same as explained in chapter 5.1.1. Also in this case, all samples were characterized by in-situ XPS using Al K_α photons from a double anode X-Ray source. The Cu 2p XPS measurements have also been repeated after 3 months to investigate the variations in the chemical state of the surface Cu of the NPs.

6.1.2   Results and discussion

Morphology

Figure 6.1a reports a representative SEM image, acquired from a sample composed of 2 nm CeO$_2$ + 2 nm Cu. Cu NPs appear small and characterized by irregular and different shapes, partially interconnected with each other. The NPs are uniformly distributed on the CeO$_2$ substrate, with an average coverage of $\sim 47\%$. The diameter distribution of Cu NPs, evaluated from the SEM images using the GMS3 GATAN software by DigitalMicrograph, is reported in figure 6.1b. The distribution was fitted using a lognormal distribution (red line in figure 6.1b), obtaining an average diameter ~ 8.5 nm with a FWHM ~ 11 nm.

In analogy with the procedure followed for Au NPs, we calculated an average AR of ~ 2.2, and the aspect ratio (AR) of each Cu NPs has been evaluated to be between 1.5 and 3. The AR is defined as the ratio between the *in-plane* and the *out-of-plane* dimensions: the first term has been deduced from the diameter distribution, while the *out-of-plane* dimension has been approximated as the fraction between the nominal thickness of the deposited Cu layer (2 nm) and the estimated coverage of the NPs, i.e. the fraction between the total area scanned by the SEM and the sum of the areas of the NPs.

Optical properties

The optical absorbance of Cu NPs surrounded by ceria layers of 4 nm or 8 nm thickness has been then measured, with the impinging beam forming an angle $\Theta = 22°$ with respect to the sample normal. The study of bare Cu NPs has not been included in this section because they are much more likely than Au NPs to react with oxygen in the atmosphere and direct exposure to air might compromise the plasmonic nature of the NPs. The direct analysis of the effects of air onto bare Cu NPs grown under different conditions has been performed separately, and it will be presented in the next section. As already done with Au NPs, the experimental
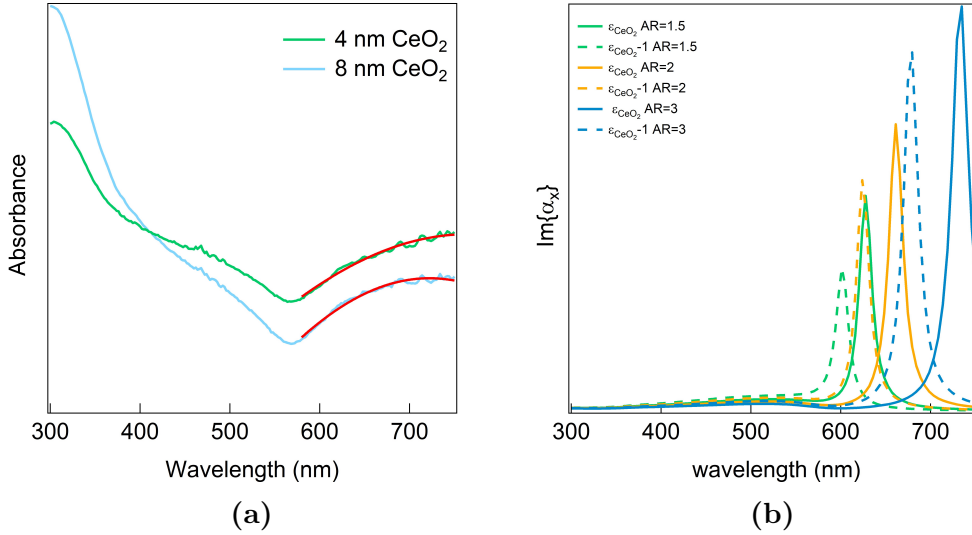
Figure 6.2: *(a) Experimentally measured UV-Vis absorbance spectra of Cu NPs embedded within CeO$_2$ films of different thickness and imaginary part of simulated in-plane component of polarizability of ellipsoidal Cu NPs with AR = 1.5 (green lines), AR=2 (orange lines) and AR=3 (blue lines) embedded within ceria with different dielectric function.*

results have been compared with theoretical simulations, performed assuming two different dielectric constants for CeO$_2$ (i.e. ϵ_{CeO_2} and $\epsilon_{CeO_2}-1$) and different ARs for the NPs. For the calculations, we followed the same procedure explained in chapter 5.1.2. The dielectric function used for Cu NPs was extracted from [6]. To account for the two different thicknesses of ceria, the thickest layer has been assumed to have the bulk dielectric function ϵ_{CeO_2} and the thinnest one $\epsilon_{CeO_2} - 1$.

Figure 6.2a shows the optical absorbance spectrum of a layer of 2 nm nominal thickness of Cu NPs surrounded by ceria layers of different thicknesses (4 nm and 8 nm), deposited onto a quartz substrate and acquired using s polarized radiation. Figure 6.2b reports the imaginary part of the *in-plane* component of the polarizability of Cu NPs with AR = 1.5, AR=2 and AR=3 immersed in different dielectric environments. The absorbance of the system composed by CeO$_2$ and Cu NPs shows an intense absorbance peak in the UV range, in correspondence with the band gap excitation of ceria, and a broad absorbance peak in the visible range, ascribed to the LSPR excitation in the NPs [7, 8, 9]. The broad and faint peak around 450 nm is ascribed to interband transitions, caused by transitions from the d-band to the unoccupied conduction s-band states [10].

If we focus on the LSPR peak position of NPs with different ARs, we can note that, in accordance with the previous results on Au NPs and with the behavior of Ag NPs described in [11], the peak position blue-shifts when the NPs AR decreases, while the increase in the value of the dielectric function causes a red-shift of the LSPR absorbance. Also in this case, the LSPR peaks obtained experimentally, reported in figure 6.2a, is broader than in the ideal case of the simulations, because of the a wide distribution of ARs. It is evident that a slight variation in the AR also causes a non-negligible shift of the polarizability peak. Small differences in NPs morphology can lead to differences in the optical absorbance. From the Gaussian fit performed to the spectra in figure 6.2a, it was possible to extract the peak position of the plasmonic resonance of Cu NPs in 4 and 8 nm ceria layers to be respectively $\lambda_4 = 766$ nm and $\lambda_8 = 722$ nm. According to the simulations shown in figure 6.2b, one would
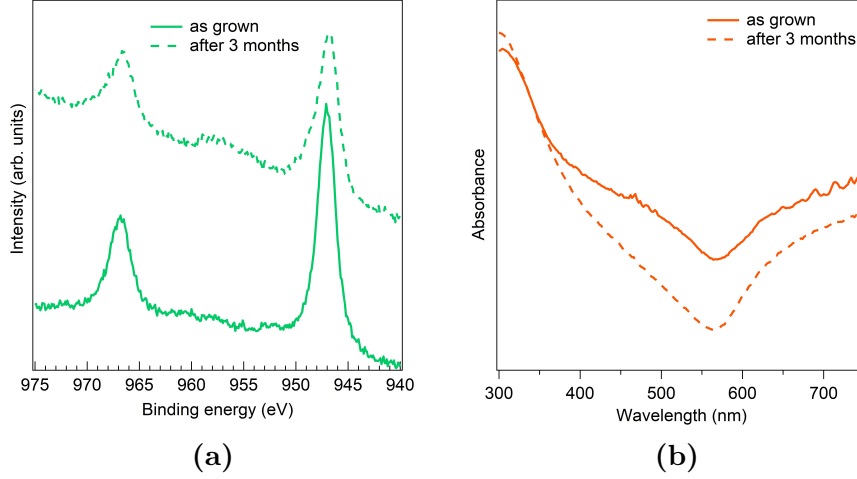
Figure 6.3: *Measurement of (a) Cu 2p XPS lines and (b) optical absorbance of the sample composed by Cu NPs in 4 nm of CeO_2 after the growth and after 3 months in controlled N_2 atmosphere.*

expected a red-shift as the ceria thickness increases, while the experimental spectra exhibit a slight blue-shift. As already observed for Au NPs in chapter 5.1, this result means that the dielectric functions of the two samples can not be strongly different with each other, otherwise one would have noticed a red-shift in the 8 nm film with respect to the 4 nm one. Since this shift is not observed, moreover, the signal from the thinnest ceria sample is slightly blue-shifted, it is possible to conclude that the two films have a similar dielectric function, that can be approximated with the bulk ceria ϵ_{CeO_2}. Since, as highlighted by the simulations presented in figure 6.2b, the plasmonic peak position is strongly affected also by the NP ARs, the blue-shift of the 4 nm absorbance signal can be justified by a possible slightly different average NP AR in the two samples. The absorbance bands of the samples in figure 6.2a ($600nm < \lambda_{peak} \leq 750nm$) are coherent with the sum of the contributions of NPs with AR ranging between 1.5 and 3 and immersed in a dielectric environment with dielectric function ϵ_{CeO_2}

Stability over time

Since Cu NPs have a strong tendency to oxidize under ambient conditions, the stability of the plasmonic properties of Cu NPs in ceria layers have been studied by repeating the optical measurements after 3 months from the deposition of the sample (kept in a controlled atmosphere of N_2), as shown in figure 6.3b. To study the modifications of the surface of the NPs, we have also measured the XPS of the Cu 2p region after growth and after 3 months: the results are shown in figure 6.3a.

The Cu 2p spectrum in figure 6.3a provides information on the chemical state of the NP surface. The sample measured as-grown, i.e. before taking the sample in air, exhibits the Cu 2p lines typical of metallic Cu, with the well separated peaks corresponding to the Cu 2p$_{1/2}$ and Cu 2p$_{3/2}$ lines [12]. This suggests an almost negligible oxidation of the Cu atoms after the growth of the sample. The Cu 2p lines measured after 3 months from the growth present a slight increase in the oxide concentration, evidenced by the shake-up satellite peaks between the Cu 2p$_{1/2}$ and Cu 2p$_{3/2}$ lines, typical of the Cu^{2+} species [13, 14, 15]. The optical absorbance spectrum in figure 6.3b shows an increase in absorbance in the UV range and a small decrease in the visible region, suggesting that the plasmonic behavior of the NPs

is preserved even after long times from the deposition, despite the slight oxidation of the NPs. This is in agreement with the partial oxidation of the NPs surface, observed by XPS, possibly caused by an inhomogeneous coverage of the NPs by the uppermost ceria layer. On the other hand, the presence of the plasmonic band even after 3 months implies that the NPs still have a plasmonic behavior and that there is only a small oxidation of the NPs, limited to the surface.

6.2 Bare Cu NPs

In this section, I will present the characterization of bare Cu NPs grown under different conditions, to study how the electronic and optical properties depend on the parameters used during Cu evaporation, in particular on the oxygen partial pressure and the substrate temperature. To have a deeper look on the self-assembled NPs, we have also performed morphology measurements using Scanning Transmission Electron Microscopy (STEM) and using Electron Energy Loss Spectroscopy (EELS) combined with STEM to obtain STEM-EELS maps.

As discussed in chapter 1.2.4, Nilius et al. have highlighted the effects of temperature and pressure on the oxidation of Cu films, demonstrating that the preparation of well controlled stoichiometric Cu_2O films requires specific temperature and O_2 pressure conditions. Indeed, when NPs are considered, as in the present case, the procedures may be different and dependent on the specific morphology of the system investigated.

6.2.1 Experimental Methods

In the present work, we have studied Cu NPs grown by MBE on transparent quartz substrates for optical characterization with UV-Vis and on SiN grids for STEM measurements. The samples were all grown in RAGNO-1 (see chapter 2.1), under different O_2 pressure conditions and using different temperatures during the growth. The quartz substrates were cleaned with a 5-minute bath in acetone at 423 K and two subsequent ultrasonic baths in acetone and in isopropanol at 353 K for 3 minutes each, and before starting the deposition, they were heated in UHV at 773 K for 15 minutes. The SiN substrate used for STEM was heated at 773 K for 15 minutes before starting the deposition. Cu atoms were evaporated from a Knudsen cell [16]. Table 6.1 summarizes the growth conditions used for each sample grown on the quartz substrate.

Sample	Oxygen pressure (mbar)	Substrate temperature (K)	Post-processing
Cu1	$1 \times \times 10^{-10}$ (UHV)	RT	-
Cu2	1×10^{-10} (UHV)	RT	annealing at 923 K in $P_{O_2} = 1 \times 10^{-7}$ mbar for 60 minutes.
Cu3	1×10^{-7}	523	-
Cu4	1×10^{-6}	523	-
Cu5	1×10^{-6}	RT	-
Cu6	1×10^{-10} (UHV)	RT	annealing 723 K in $P_{O_2} = 1 \times 10^{-7}$ for 30 minutes
Cu7	1×10^{-10} (UHV)	RT	annealing 723 K in UHV for 30 minutes

Table 6.1: *Different evaporation conditions of Cu NPs on the quartz substrate and different post-processing conditions.*
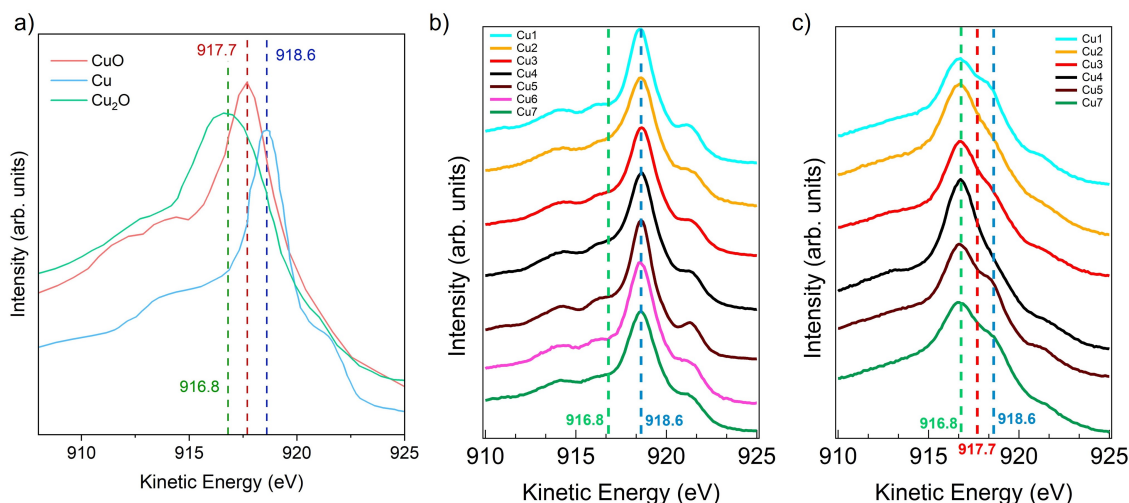
Figure 6.4: *(a) AES reference spectra of metallic Cu (blue line), Cu_2O(green line) and CuO (red line) (data taken from [22]) (b) and (c) experimental Cu L_3MM Auger lines for the different NPs listed in 6.1, before and after the exposure to air. The lines of the main Cu^0- and Cu+-related peaks are reported as a reference (in c, also the Cu^{2+}-related peak is drawn).*

6.2.2 Results and discussion

Analysis of Cu NPs surface via AES

Early works demonstrated that Auger Electron Spectroscopy (AES) is particularly suitable to detect the oxidation state of Cu atoms [17, 18, 19, 20, 21]. In fact, Cu L_3MM Auger lines are very sensitive to Cu oxidation state, as evident from the spectra lines in figure 6.4a: the AES spectral line-shapes and positions vary with species oxidation state and ligand variety [21].

Figure 6.4a shows the reference spectra for the different oxidation state of Cu: the blu line, characterized by a main peak at 918.6 eV, correspond to the AES spectrum of metallic Cu, the red line to the AES signal of CuO, with a main peak at 917.7 eV, and the green line to the Cu_2O spectrum, peaked at 916.8 eV. Figure 6.4b shows the experimental AES spectra of the different Cu samples. **Cu1**, i.e. the sample grown in UHV without any exposure to oxygen after growth, distinctively shows the characteristic AES shape of pure metallic Cu, with the main peak at 918.6 eV and other three clearly distinguishable peaks. The shape of the spectra appears slightly broadened for the other samples, even though the characteristic peaks related to Cu^0 ions give the main contribution to the spectra, suggesting only a small amount of Cu oxides is formed during oxygen exposure.

The AES spectra shown in figure 6.4b were fitted to have qualitative information about the various Cu species composing the NPs. The Auger spectral fitting parameters for all species analyzed have been taken from [21], reported for bulk materials. The peak positions and each peak FWHM have been constrained, leaving the area of each peak component as free parameter. As suggested in the reference, we used 6 Cu^0-related peaks (the intensity of the 7th peak in the reference was below the detection limit and that peak was neglected), and 4 and 3 peaks for respectively the Cu^+- and Cu^{2+}-related components. We do not expect to find a very accurate value for a quantitative description the concentration of the different copper ions, because of the wide size distribution of the NPs, evident from figure 6.1. In fact, Auger spectra are complex and the position and shape of Auger lines is strongly
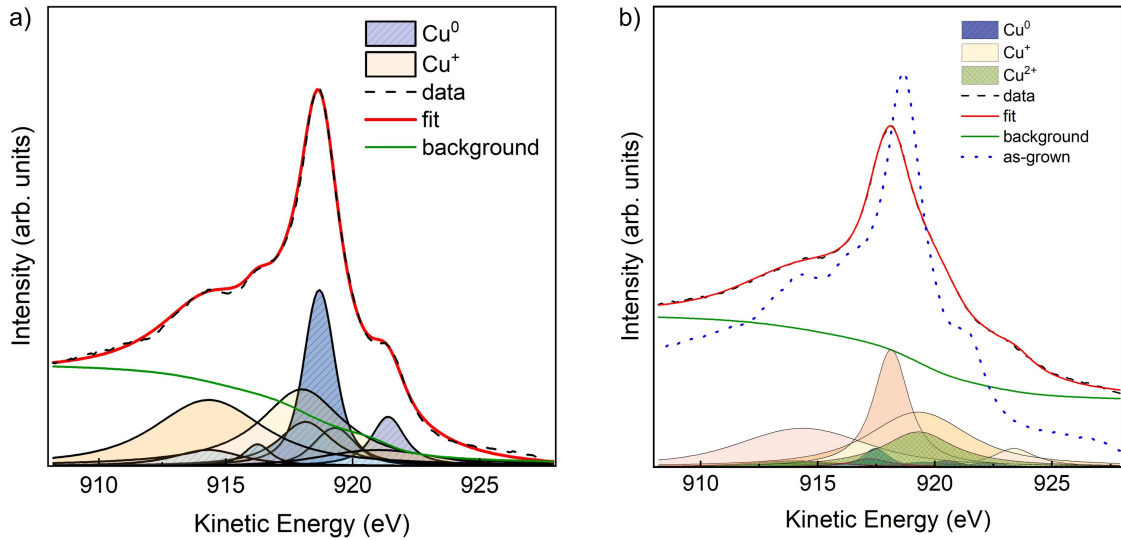
Figure 6.5: *Cu-$L_3 M_{4,5} M_{4,5}$ Auger lines of **Cu4** (dashed black line) and the fits (red continuous line) (a) before and (b) after the exposure to air. In blue the components related to Cu^0, in orange the components related to Cu^+ and in green the components related to Cu^{2+} [21]. In b the Auger line of the sample before air exposure is also reported as a reference.*

influenced by multiple factors, including the size of copper NPs and the nature of support [18, 23, 24]. Moreover, the presence of some residual gas within the chamber cannot be excluded, which can produce a slight oxidation of the NP surface. Despite this complexity, it is possible to compare the concentration of Cu^+ ions obtained by the fitting procedure to extract information on the effects of the growth conditions and post-processing on the NPs.

From the data fitting, we could extract a non-negligible concentration of Cu^+ ions, depending on the growth conditions. For **Cu1**, a Cu^+/Cu concentration of $\sim 35\%$ was measured. One would expect **Cu1** NPs, grown in UHV and never exposed to air, to be metallic, with a negligible concentration of Cu_2O on the surface, but, as already mentioned, we can not aim to a quantitative description of the samples because of the complexity of the spectra. However, as expected, among all samples, **Cu1** contains the lowest concentration of Cu^+ ions, because it has never been exposed to oxygen during or after growth. In the other samples, the extracted Cu^+ concentration is slightly higher: for the three samples grown in oxygen (i.e. **Cu3, Cu4, Cu5**), independently on the substrate temperature, the intensity of Cu^+ ions is between 0.1 and 0.15 times higher than in the **Cu1** sample. The samples that have been grown in UHV and post-processed in oxygen show a slightly higher concentration of Cu^+ ions, approximately 15%-20% higher than in **Cu1**. For all samples, the concentration of Cu^{2+} ions is below the detection limit. This result is in agreement with the theory of Cabrera–Mott, that predicts that Cu atoms, exposed at pressures below 100 Torr at temperatures up to 1273 K, form only Cu_2O and no CuO [25]. This result has been revisited by many following papers (as for example [26, 27, 28, 29]), which however confirmed the absence of the CuO phase under the pressure and temperature conditions used in the present work. The same result was also confirmed by works studying the optical properties of Cu NPs, as [1, 3].

Figure 6.5a shows as an example the AES spectrum of **Cu4** (acquired *in-situ* after the growth), together with the Cu^0-related components (in blue) and the Cu^+-

related components (in orange). The application of the fitting procedure taken from [21] on this sample gave a Cu^0 and a Cu^+ concentration of $\sim 50\%$ each.

To see the variations of the NP surface, the AES measurements have been repeated after investigation of optical properties, i.e. after exposing the sample to air for one day. The spectra are shown in figure 6.4c (the spectrum of **Cu6** has not been acquired because of a damage of the sample): the spectral shape is clearly different from the as-grown samples, with a strong decrease of the peak correspondent to metallic Cu and a sharp increase of the Cu^+-related peak. The differences between the spectra of different samples are more pronounced than in the as-grown samples, suggesting a different oxidation in air conditions. Some of the spectra present a more evident peak related to Cu^{2+} (main peak at 917.7 eV, red dashed line in fiugre 6.4c), as for example **Cu1** and **Cu5**, while it is very faint for other samples, as **Cu2** or **Cu4**. In **Cu2** and **Cu7** it is also evident the peak related to the Cu^0 component at 918.6 eV (blue dashed line in figure 6.4c). The fitting results confirm the qualitative evidences: all samples reported a strong decrease of surface Cu^0 concentration when exposed to air of more than 40%, with a final concentration of this species below 10% for all samples. The highest Cu^0 concentration is found for the samples post-processed in oxygen (**Cu2** and **Cu7**). Simultaneously, a small increase in CuO concentration is observed (about 20% for **Cu1** and **Cu5**, below 15% for **Cu3** and **Cu4** and about 10% for **Cu1** and **Cu7**) while the Cu^+ concentration is between 80% and 90% for all samples.

Figure 6.5b reports the fitting of **Cu4** after the exposure to air: we derived a low Cu^0 concentration ($\sim 5\%$), a $\sim 13\%$ of Cu^{2+} and a high concentration ($\sim 80\%$) of Cu^+ ions. However, since AES is a very surface sensitive technique, the strong oxidation of the surface does not imply a uniform oxidation of the bulk, which was investigated using other techniques, namely, optical spectroscopy and STEM in EELS mode.

Optical properties

Figure 6.6a shows the UV-Vis static optical absorbance of the Cu NPs samples listed in table 6.1. We clearly see a strong dependence of the optical properties on the growth and post-processing conditions. Samples **Cu3**, **Cu4** and **Cu5**, grown under similar conditions and without any further process after growth, present a similar optical absorbance, with a very broad absorbance band peaked around 1 μm and a pronounced and narrow absorbance peak at 350 nm. **Cu2**, grown in UHV with the substrate kept at RT and oxidized after growth, also shows a broad absorbance band, but narrower than **Cu3**, **Cu4** and **Cu5** and shifted toward lower wavelengths ($\lambda_{peak} \sim 750$ nm). The peak becomes narrower and shifted towards progressively lower wavelengths for samples **Cu6**, **Cu7**, and **Cu1**. Previous works on Cu NPs on glass or quartz substrates [1, 3] demonstrated that the formation of an oxide shell around a Cu metallic core leads to the broadening and red-shift of the LSPR absorbance band. For oxidation at relatively low temperatures (below ~ 900 K) and low pressures, it was demonstrated that the oxide shell is predominantly formed by Cu_2O, coherently with our observations made on the basics of AES fitting (figure 6.5a) and of STEM-EELS maps discussed in the next section (figure 6.8).

We repeated the absorbance measurements one month after the NPs deposition, after keeping the samples in controlled N_2 atmosphere. No significant changes were observed in the optical spectra (we reported as an example the spectra of **Cu1** and **Cu2** in 6.6b), but a small decrease in absorbance, combined with a slight red-shift
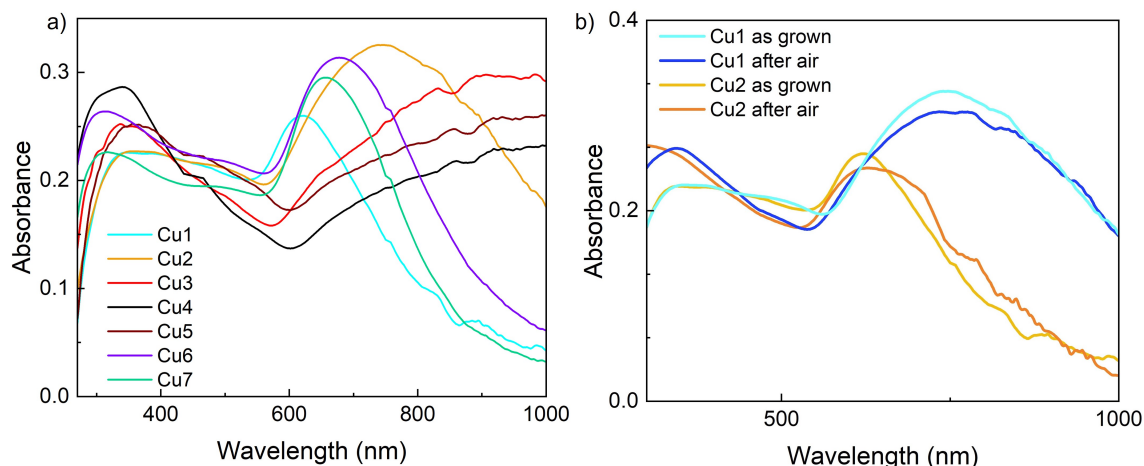
Figure 6.6: *Optical absorbance spectra of the different NPs (a) as-grown and (b) after 1 month.*
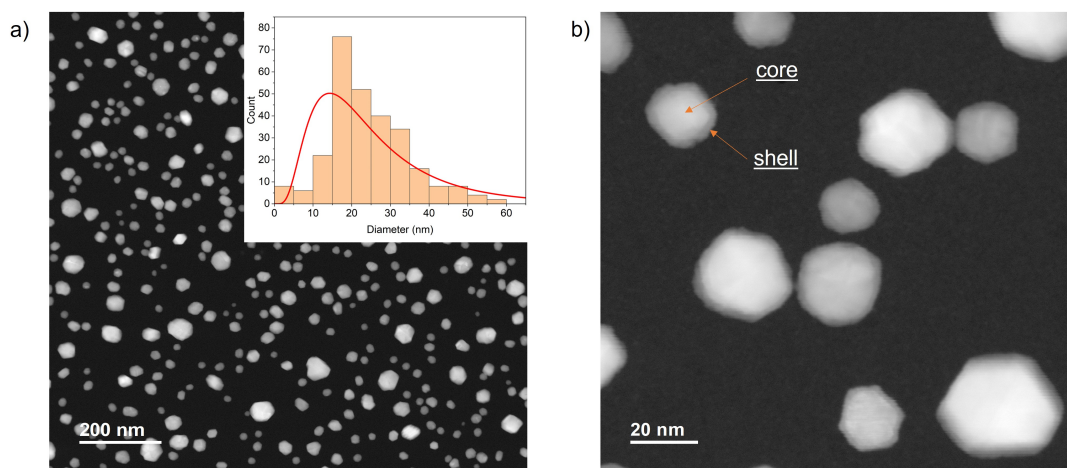

Figure 6.7: *(a) ADF-STEM image of Cu NPs grown under the same conditions as **Cu2**. The inset shows the NPs diameter distribution. (b) Image of the same the NPs at a higher magnification. From the contrast in the NPs, it can probably distinguished two different phases of the Cu NPs, forming a core-shell structure, as is further confirmed by AES (figure 6.5a) and STEM-EELS maps (figure 6.8).*

and peak broadening, compatible with a slightly higher degree of oxidation of the NPs, similar to the variations observed for the optical spectra of the NPs surrounded by CeO_2.

Morphology

Figure 6.7 shows the image acquired using annular dark-field (ADF) scanning transmission electron microscopy (STEM) of Cu NPs grown on a thin Si_3N_4 TEM grid. The NPs were grown under the same conditions as **Cu2**: the substrate was first heated to 923 K, the Cu NPs were evaporated on the substrate kept at RT and then annealed in oxygen at 923 K for 100 minutes. Figure 6.7 shows representative ADF-STEM images at two different magnifications. In these dark-field images, the NPs look bright on a dark background. The inset in figure 6.7a shows the diameter distribution of the NPs, obtained using the ImageJ software. The distribution was fitted using a lognormal distribution, from which we extracted an average diameter of 24 nm, with a full width at half maximum (FWHM) of 10 nm. Qualitatively,
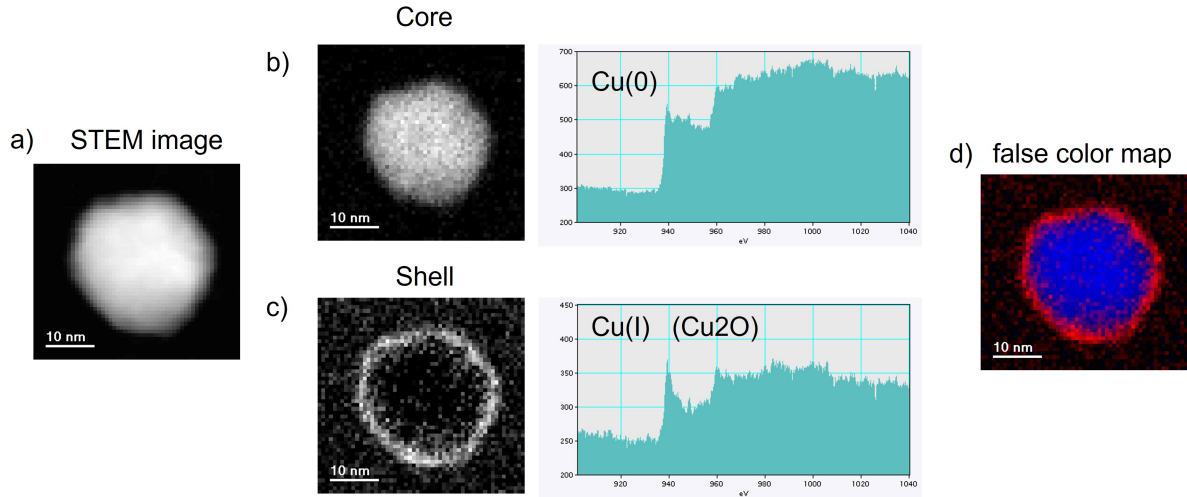
Figure 6.8: *(a) STEM image of a single self-assembled Cu NP, (b) and (c) STEM-EELS images of the Cu^0 core and Cu^+ shell and (d) EELS false-color map of the investigated NP. Blue represents Cu^0, red Cu^+ ions.*

the NPs tend to be clearly separated from each other, and they assume a hexagonal *in-plane* shape, coherently with the fact that Cu(111) represents the most stable face.

Cu NPs shown in figure 6.7 appear larger and more monodisperse compared to figure 6.1. This is probably related to the weak interaction between Cu and the support [30] and to the heating of the NPs after the growth that facilitates diffusion. Figure 6.7b is a magnification of 6.7a, and it allows to distinguish a thin shell, with darker contrast, surrounding the Cu NPs core. To verify the presence of different chemical compositions in the NP structure, we acquired the Cu-$L_{2,3}$ edges (at ~940 eV) with electron energy-loss spectroscopy (EELS) from individual NPs. We used STEM-EELS, in which a spectrum is acquired at every beam position in the scan, obtaining a spectral dataset (x, y, E). Similar datasets are suited for noise reduction and features extraction using multivariate statistical methods, such has the principal component analysis (PCA) [31]. The result of PCA on a STEM-EELS acquisition from an individual NP is shown in figure 6.8. It is indeed possible to distinguish two different phases that compose the Cu NP from the spectral features in the two extracted components: a metallic Cu^0 core, surrounded by an oxide shell of Cu^+ (i.e., Cu_2O). This analysis confirms the results obtained by fitting the AES spectra (following the example shown in figure 6.5b), from which we obtained a high Cu_2O concentration on the NPs surface, and are coherent with the observations of references [1] and [3].

6.3 Morphology and Optical Properties of Gas-Phase-Synthesized Plasmonic Nanoparticles: Cu and Cu/MgO

The optical and morphological properties of Cu and Cu/MgO NPs, prepared with gas-phase synthesis, i.e. a different technique with respect to the ones described above, are also investigated, in order to compare the two techniques and to study the effect of a different dielectric environment in which the NPs are immersed on their optical properties and on their stability.

6.3.1 Experimental methods

The samples investigated in this work are all grown in the chamber RAGNO-2 in the SESAMo lab (see chapter 2.1). Different characteristics of the samples were investigated with different techniques. The morphology of the NPs was studied *ex-situ* with SEM, atomic force microscopy (AFM), and TEM, to obtain information on the size and shape of the NPs and the formation of MgO shells, also verified with energy dispersion X-Ray (EDX) maps. The chemical state of the different samples was investigated using *in-situ* XPS, while the optical properties were analyzed using UV–Vis spectrophotometry and compared with simluations of the polarizability.

The deposition is based on a magnetron-assisted gas aggregation source (GAS), and the charged nanocluster beam was focused by means of the ion optics of a quadrupole mass filter (QMF) on the different substrates under HV conditions. The substrates used during the experiments were Si with its native oxide (Si/SiO_x) wafers and freshly exfoliated highly oriented pyrolytic graphite (HOPG) crystals for SEM measurements, quartz slabs for AFM and optical experiments, and C-coated Ni grids for TEM analysis. The quartz and the Si/SiO_x substrates were cleaned with the procedure explained in the previous section. We have studied Cu NPs grown under different conditions, with and without MgO capping, in order to study the differences in morphological and optical properties. We investigated samples characterized by different Cu nominal thicknesses, as-grown either in HV or in oxygen pressure, post-oxidized or coated by a MgO matrix.

During the sputtering of the Cu target, the GAS discharge was kept fixed at $V = 200$ V, $I = 0.21$ A, with an Ar gas flow $f = 60$ sccm. The measured deposition rate r^1 on the substrates was measured using a quartz microbalance, and varied between 0.1 and 0.4 nm/min, depending on the Cu target conditions. For NP oxidation experiments, two procedures were used: flowing oxygen gas in the aggregation region of the NP source with a flow $f = 5$ sccm as in [32] or flowing oxygen ($P_{O_2} = 2 \times 10^{-7}$ mbar for 20 minutes) in the deposition chamber after the Cu NP film was formed on the substrate (post-oxi samples). Deposition or co-deposition of MgO on the sample was obtained by thermally evaporating Mg in an oxygen partial pressure $P_{O_2} = 2 \times 10^{-6}$ mbar, with a Mg deposition rate varying between r = 0.4 and r = 0.6 nm/min.

6.3.2 Morphology

We have characterized the morphology of samples with two different Cu coverage and on different substrates (Si/SiO_x, HOPG and quartz), with and without MgO capping, in order to investigate the agglomeration and diffusion tendency under different conditions. The different samples were analyzed using SEM, TEM, and AFM. We have started our analysis by acquiring SEM images of Cu NPs grown onto Si/SiO_x substrates, shown in figure 6.9. Figure 6.9a shows the morphology of a sample obtained with a low Cu coverage $C \sim 5\%$, obtained by depositing a Cu layer with a nominal thickness t = 0.5 nm, as measured by the thickness monitor. In this sample, the NPs have almost circular shapes, and they are well separated, but in some cases they form a small number of dimers and trimers (shown by red closed lines in figure 6.9a). The diameter distribution of the NPs was calculated in the low coverage case by individuating the NPs in the SEM image using imageJ software, and the coverage was calculated as the fraction between the total area

---

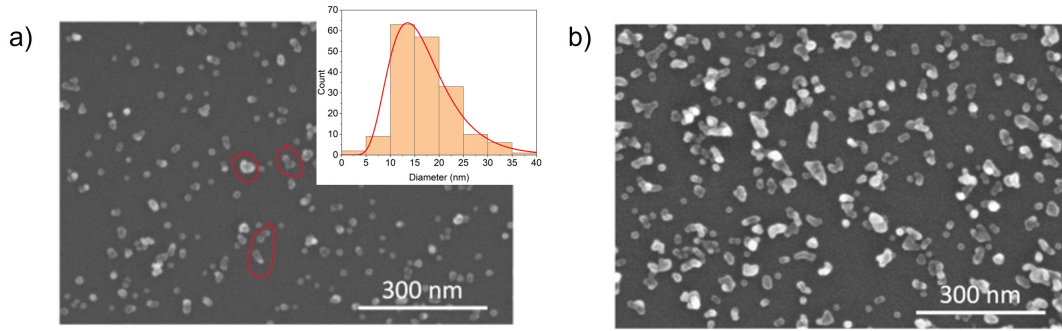[1]thickness of a Cu solid film deposited on a unit area per unit time.

Figure 6.9: *SEM images of Cu NPs deposited on Si/SiO_x substrate, (a) with nominal thickness t = 0.5 nm and low coverage $C \sim 5\%$ and (b) with nominal thickness t = 2.4 nm and high coverage $C \sim 15\%$. The red circles in (a) highlight the formation of dimers and trimers, while the inset represents the diameter distribution of Cu NPs with low coverage.*
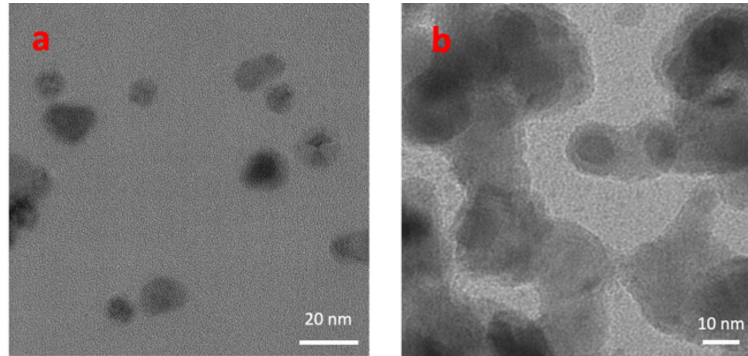

Figure 6.10: *TEM images of Cu NPs deposited on C-coated Ni grids (a) with nominal thickness t = 0.2 nm and low coverage $C \sim 2\%$ and (b) with nominal thickness t = 6.7 nm. In the latter image, the coverage fraction is not a meaningful parameter, since NPs agglomerate also in the direction normal to the surface.*

scanned by the SEM and the sum of the areas of the NPs. In figure 6.9a, the NPs have an average diameter $< d > \sim$ 16 nm with FWHM $\Delta d \sim$ 6 nm. With increasing coverage, the number of agglomerates increases, as can be seen in figure 6.9b. In this case, the nominal thickness of Cu is t = 2.4 nm, with coverage $C \sim 15\%$, and the NPs tend to coalesce, similar to what was previously observed for Ag NPs [33].

The tendency of Cu NPs to coalesce as the nominal thickness of Cu increases is confirmed by the TEM analysis performed on Cu NPs on C-coated Ni grids, shown in figure 6.10. Figures 6.10a and 6.10b, respectively, show a bright-field image of low- and high-coverage Cu NP films. The formation of agglomerates in the second case is evident even if the Cu NPs start to coalesce also at low coverage. This tendency to form bigger agglomerates, even with lower coverage, with respect to the previously investigated samples on Si/SiO_x can be ascribed to higher mobility of the NPs on the C film of the TEM sample support when compared with Si/SiO_x substrates used in the SEM analysis [30, 34, 35].

To analyze the differences in the diffusion of Cu NPs on the two different substrates, a low-coverage film of Cu NPs was also deposited on HOPG and investigated using SEM. From the SEM image, shown in figure 6.11, we can see that Cu NPs decorate the steps, in a similar way to what occurs to adatoms on crystalline sur-
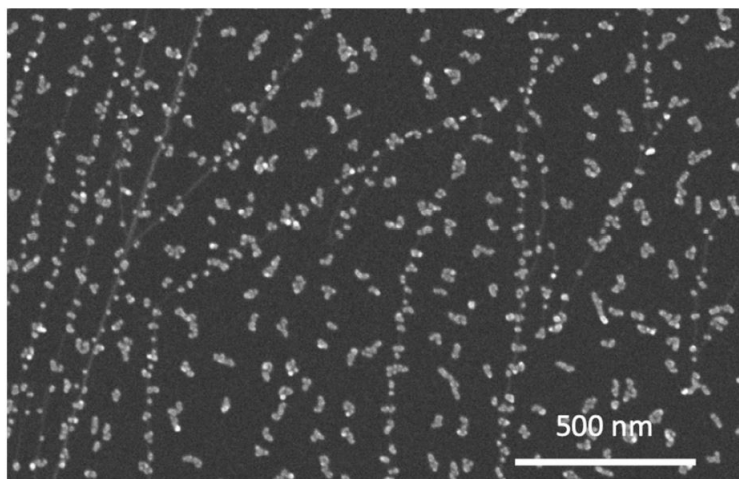
Figure 6.11: *SEM image of Cu NP deposited on HOPG, t = 0.2 nm, C = 4%*

faces, forming elongated structures, resulting from diffusion after landing. Direct measurement of the diffusion coefficient D is not possible in the case of the deposition of pre-formed NPs. In a previous study, D'Addato et al. demonstrated the mobility of large clusters of atoms (up to tens of thousands atoms) by acquiring a series of TEM images during the movement of two Ag NPs (grown with the same technique as the investigated Cu NPs) that eventually coalesced [33]. The diffusion coefficient D was estimated following [34]:

$$D = \Big(\frac{0.41}{N_{agg}}\Big)^{\frac{1}{\chi}} \frac{F\pi d^4}{16} \tag{6.1}$$

where N_{agg} is the average number of NP aggregates[2], F is the number of incident NPs on a unit surface area, d is the average particle diameter and $\chi = 0.336$. Using the average diameter of the NPs $< d >= 16$ nm calculated from figure 6.9a, $N_{agg} \sim 3\%$, and F = 0.1 NP/s cm^2, we obtained a diffusion coefficient $D = 1 \times 10^{-10}$ cm^2 s^{-1}, slightly higher than the value obtained for Ni NPs [35], coherently with the weaker interaction of Cu with HOPG [36].

Figure 6.12 shows the SEM image of Cu nanoclusters and MgO co-deposited on a Si/SiO$_x$ substrate. When Mg is co-deposited with Cu in an oxygen partial pressure, the NPs tend to form islands with approximately square or rectangular shapes and an average lateral size ranging from 20 to 50 nm, much larger than the average diameter of the bare Cu NPs of 16 nm calculated from 6.9a. The formation of these rectangularly shaped islands is ascribed to the formation of MgO shells embedding the Cu NPs, similar to what was observed in the Ag/MgO system [33], obtained using the same apparatus and synthesis method. Based on previous results [33, 37], it can be inferred that this peculiar arrangement is essentially due to two main reasons: (1) a higher reactivity of Mg to O species, resulting in preferential oxidation of Mg compared to Cu clusters during codeposition, and (2) a higher sticking coefficient of MgO to metal NPs than to the inert substrates, such as Si/SiO$_x$ and carbon films used in TEM experiments [38, 39]. The deposition might result either in the formation of metal-core/MgO-shell NP structures or in metal NPs embedded in a MgO matrix, depending on the NPs and Mg atoms flux during co-deposition.

---

[2]Obtained by counting the number of agglomerates composed of two or more NPs and normalizing them to the number of possible sites of nucleation in the same image, assumed to be the maximum number of particles of diameter d that can be arranged in close-packed surface geometry
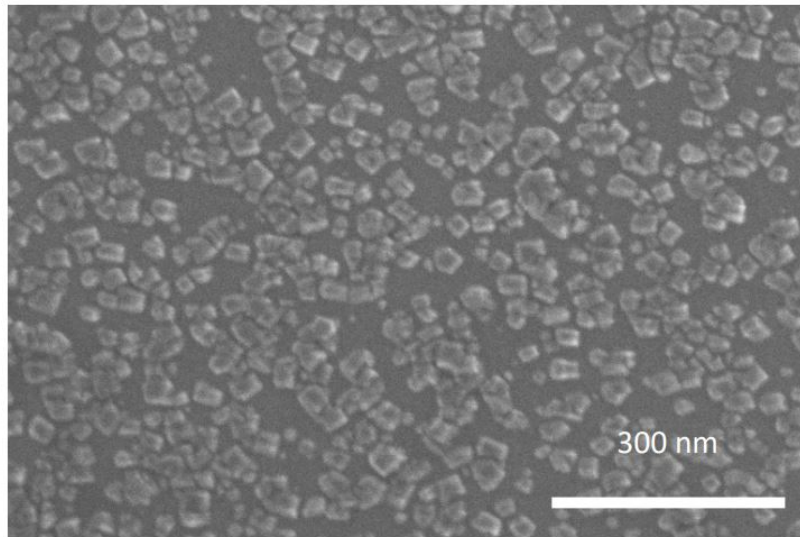
Figure 6.12: *SEM image of Cu NP co-deposited with Mg in O atmosphere. The nominal thickness for Cu NP and MgO are $t_{Cu} = 0.4$ nm, $t_{MgO} = 1$ nm.*

To better understand the morphology of the investigated Cu/MgO structures, bright field TEM and EDX mapping experiments were performed. On the TEM image in figure 6.13a, it is possible to recognize Cu clusters (darker areas) partially agglomerated, with MgO embedding them (lighter areas). To better resolve the different species, EDX maps were also acquired, as shown in figures 6.13b, c and d. The three images respectively show Cu, Mg, and Cu/Mg maps in false colors: the Mg signal is rather diffuse, but its intensity is higher in the regions around Cu NPs, confirming the formation of a core-shell structure.
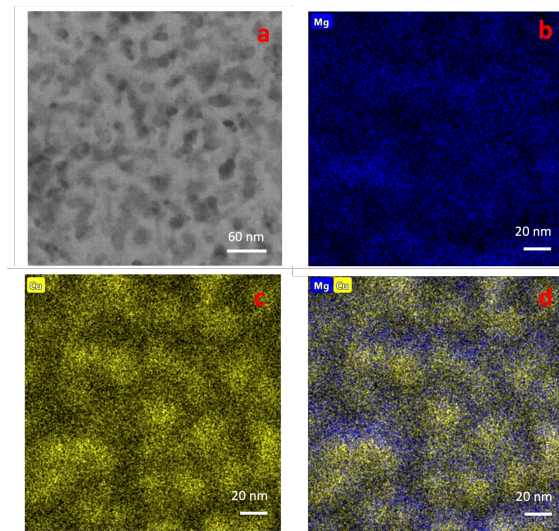
Figure 6.13: *(a) Bright-field TEM image of Cu/MgO NP film obtained with co-deposition (b) EDX map obtained by measuring the intensity of the Mg EDX signal (c) EDX map of Cu signal (d) combination of maps (b) and (c).*

Since one of the main aims of this work is to obtain plasmonic systems with well-controlled and stable resonances, it is crucial to understand the optical properties of the investigated systems, taking into account all variables that can influence them. Since the plasmonic properties of the NPs and thus their optical absorbance are strongly affected by the shape of the NPs when they are deposited on a support [11,

40], we have acquired AFM images to obtain information on the vertical height of the deposited Cu NPs, on the same quartz substrate used for optical measurements. A representative AFM image is shown in figure 6.14a. The vertical height distribution obtained by a detailed grain analysis of the AFM in figure 6.14a is plotted in figure 6.14b. By fitting the main peak of the distribution with a Gaussian profile, we obtained an average height $< h >= 7.5$ nm, with an FWHM value equal to $\Delta h = 2.2$ nm. Dividing the diameter found in figure 6.9 by the calculated height, an aspect ratio $AR = < d > / < h >= 2.13$ is obtained. An $AR > 1$, caused by the 'flattening' of the NPs, was expected from previous observations of similar samples [41, 42, 43]. Here, the deformation of the NPs has been attributed to the agglomeration and coalescence of NPs and their interaction with the support. This deformation affects the optical properties, as will be discussed in the next section.
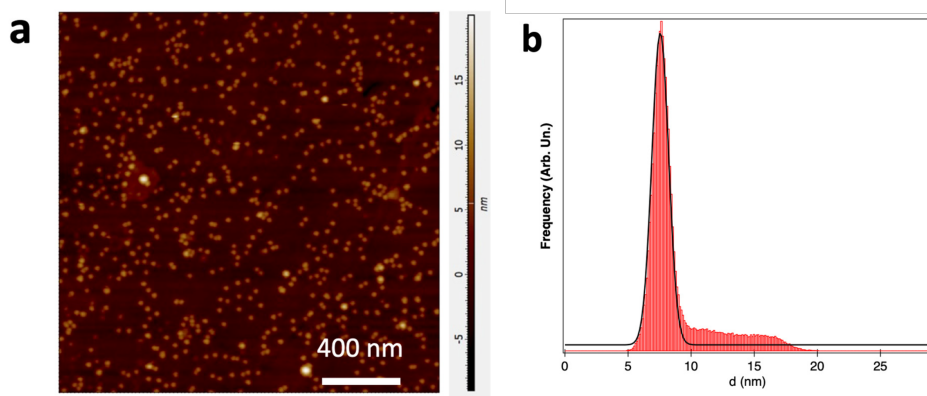

Figure 6.14: *AFM topography image of Cu NPs deposited on quartz, with nominal thickness t = 0.36 nm (b) vertical height distribution of Cu NPs obtained via a grain analysis of image a (red histogram) and fitting curve (black line).*

6.3.3 Electron and optical properties

After morphological investigation, we studied the optical properties of Cu NPs and Cu/MgO NPs grown on quartz substrates under different conditions. Before the optical experiments, carried out in air as described in chapter 1.2.3, we performed an *in-situ* XPS analysis of the samples to extract information on the chemical state of Cu NPs in the investigated samples. Figure 6.15 shows the Cu 2p and Cu L_3VV line shapes taken with the Al K_α emission line from three different samples: as-deposited Cu NPs, Cu NPs co-deposited with MgO, and Cu NPs grown in UHV and exposed to oxygen ($P_{O_2} = 2 \times 10^{-7}$ mbar) for 30 minutes. Due to the poor electrical conductivity of the quartz substrate, the samples were electrically charged during the XPS experiment and the binding energy (BE) positions were realigned by calibrating them with the Si 2p signal in SiO_2 (BE = 103.3 eV). The XPS lines of both as-grown Cu NPs and Cu/MgO NPs have the typical line shape of metallic Cu [44], while both photoemission and Auger spectra are modified when bare Cu NPs are exposed to oxygen. The appearance of the characteristic features of copper oxides in the Cu 2p and Cu L_3VV lines [21] only when the bare Cu NPs are exposed to oxygen suggests that the NPs retained their metallic state if oxygen is codeposited with Mg, resulting in the formation of an MgO shell or matrix protecting the Cu core.

The optical properties of bare Cu and Cu/MgO NPs were also investigated with UV–Vis spectroscopy. UV–Vis absorbance spectra taken using p polarized light
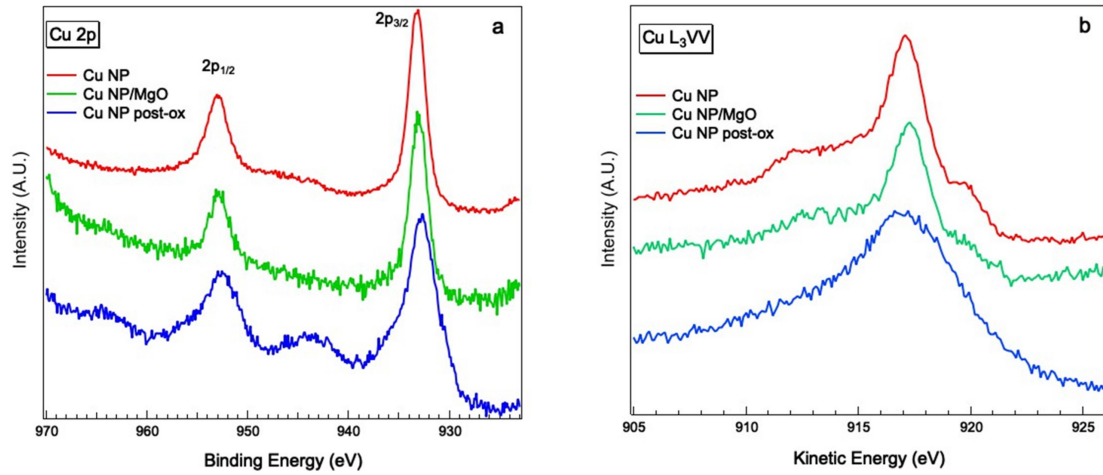
Figure 6.15: *(a) Cu 2p XPS spectra obtained from Cu NPs (red line), Cu/MgO NPs (green line), and Cu NPs after exposure to oxygen in the deposition chamber (blue line) (b) Auger Cu L₃VV from the same samples shown in (a).*

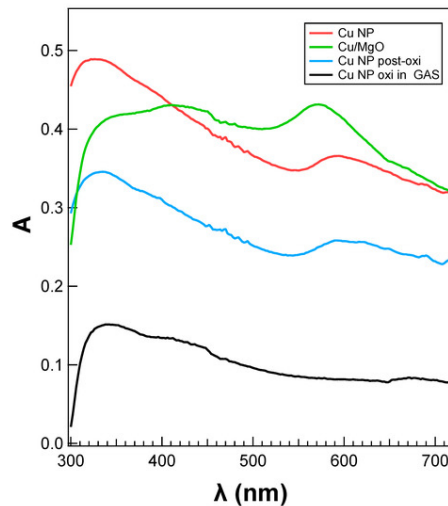**Figure 6.16:** *UV–Vis absorbance spectra from Cu/MgO NPs, bare Cu NPs, Cu NPs post-oxidized, and Cu NPs completely oxidized by flowing O_2 in the GAS.*

with an incidence angle of $\Theta = 22°$ are plotted in figure 6.16. The spectra show the optical absorbance, calculated from the measured reflectance and transmittance of the samples, of four different samples: as-grown bare Cu NPs (labeled Cu NPs), Cu/MgO, and Cu after exposure to oxygen (labeled post-oxi) in the deposition chamber, and oxidized Cu NPs obtained by flowing oxygen in the aggregation region of the nanocluster source during the deposition. Cu NPs and Cu NPs post-oxi show the same broad absorbance band in the visible range, peaked around 600 nm, attributed to LSPR excitation in Cu NPs [45, 46], while the plasmon-related feature disappears when the deposition of Cu NPs occurs at an oxygen pressure (Cu NPs oxi in GAS), suggesting complete oxidation of the NPs. The plasmonic peak is also present in the Cu/MgO sample, but in this case it is more intense and narrow with respect to the absorbance band of the two samples previously described, and the peak position results slightly blue-shifted. The shape and position of the LSPR peak are consistent with the formation of an oxide shell protecting the metallic Cu core [1, 3, 45].

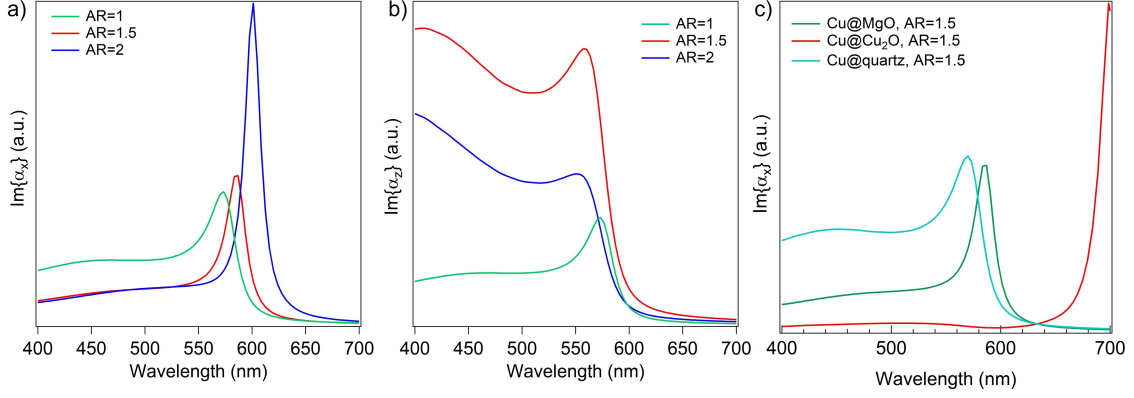To compare the experimental results with theoretical predictions, we calculated

Figure 6.17: *(a) in-plane and (b) out-of-plane component of the calculated imaginary part of the optical polarizability $Im(\alpha)$ from the Maxwell–Garnett model of Cu NP embedded in MgO with AR=1, 1.5 and 2; (c) Comparison between the simulated $Im(\alpha)_x$ of Cu NPs with AR=1.5 embedded in Cu_2O (red line) and in MgO (green line), in quartz (blue line).*

Sample - λ_{exp}	AR	$Im(\alpha_x) = Im(\alpha_y)$	$Im(\alpha_z)$
Cu/MgO - 572 nm	1	557 nm	557 nm
	1.5	583 nm	557 nm
	2	601 nm	554 nm
Cu - 586 nm	1	551 nm	551 nm
	1.5	563 nm	545 nm
Cu post-oxi - 592 nm	1	551 nm	551 nm
	1.5	563 nm	545 nm

Table 6.2: *Experimental and theoretical wavelength positions of the LSPR maximum for Cu, Cu post-oxi and Cu/MgO NPs.*

the imaginary part of the optical polarizability α for bare Cu and for Cu NPs embedded in MgO by assuming a spherical and an oblate ellipsoidal geometry, with different values for the AR calculated on the basis of the morphology of the sample. The calculations were based upon the Mawell-Garnett model. We calculated the imaginary part of the polarizability $Im(\alpha)$ using equation 2.3d for three different values of AR (AR=1, AR=1.5 and AR=2). As already done for bare Au NPs, in the simulations we assumed the NPs to be immersed in quartz. This is obviously an approximation, since a complete simulation would have required to consider an inhomogeneous medium formed by air and quartz, but this goes beyond our aim. Figure 6.17c reports the calculated *in-plane* polarizability for NPs with AR=1.5 in different dielectric environments (quartz, MgO and CuO). The Cu, MgO and CuO dielectric functions used for the calculations are taken respectively from [47], [48] and [49], while we calculated the real part of the complex refractive index for quartz from the Sellmeier equation [50] applied to fused SiO_2 at room temperature [51]. Figures 6.17a and 6.17b show the calculated imaginary part of respectively the *in-plane* and *out-of-plane* optical polarizability at different ARs for the NPs surrounded by MgO. All simulated polarizability spectra shows a dominant absorbance feature in the visible range related to LSPR of Cu, and both $Im(\alpha)_x$ when AR=1 and $Im(\alpha)_z$ present a tail at a shorter wavelengths related to interband transitions [10].

Table 6.2 reports the experimental and theoretical positions of the LSPR maxima for bare Cu NPs, Cu NPs post oxidized, and Cu NPs embedded in a MgO matrix. When Cu/MgO NPs are considered, the best agreement between calculated and

experimental value for the LSPR position is obtained for AR=1.5. It should be kept in mind that, in the adopted experimental geometry (p-polarization with an incidence angle of $\Theta = 22°$), the spectrum is the result of a combination of the two components of the polarizability. It is reasonable to assume that the combination of the two components of the imaginary part of polarizability for AR = 1.5 would give a position for the LSPR at intermediate values between $\lambda = 584$ nm and $\lambda = 564$ nm, which is the wavelength range under which the experimental position of the LSPR fell ($\lambda_{exp} = 572$ nm), so an oblate Cu ellipsoid with AR = 1.5 and embedded in MgO is a reasonably accurate model to describe the optical properties of this system.

In the case of bare NPs, as-grown or post oxidized, the position of the LSPR in the experimental data is slightly red-shifted with respect to the case of Cu/MgO. Comparing the experimental data with the calculated ones, it is possible to notice a moderate discrepancy between the experimental position of the LSPR and the theoretical one for bare metallic Cu NPs, even though *in-situ* XPS analysis showed that the bare Cu samples were in a clean metallic state after deposition. On the other hand, the LSPR feature in the data taken from post-oxi Cu NPs fell at a similar wavelength as the one in the bare Cu NPs. Since the optical measurements were performed in the air after a few hours, this behavior can be probably explained by partial oxidation of the bare Cu NPs when exposed to air, and the optical data were found to be similar to the data of the NPs that were intentionally oxidized. The formation of an oxide shell around the metallic Cu NP core probably gave rise to the red-shifted LSPR compared with the (theoretical) Cu and Cu/MgO systems. To further investigate this hypothesis, the *in-plane* simulated polarizability of Cu NPs with AR=1.5 surrounded by MgO (Cu@MgO) and by CuO (Cu@Cu$_2$O) have been compared in figure 6.17c. The LSPR band of Cu NPs in Cu$_2$O peaks around 700 nm, i.e. it is more than 100 nm red shifted with respect to the peak position of Cu NPs in MgO. Comparing the spectra in figure 6.16 with figure 6.17c, we notice a discrepancy between the peak position obtained from the simulations for the Cu@Cu$_2$O system ($\lambda_{peak} \sim 700$ nm) and the experimental results ($\lambda_{peak} \sim 600$ nm). This discrepancy can be explained by the fact that for numerical simulations we are assuming the NPs to be immersed in a bulk film of Cu$_2$O, while in the real scenario they are only surrounded by a thin shell. The LSPR peak position of the NPs is strongly influenced by the thickness of the shell, as highlited for Au NPs in the previous chapter and by many previous works [11, 52, 53, 54]. In particular, [54] studied systems composed by Au NPs surrounded by Cu$_2$O shells, observing a progressive red shift of the SPR peak up to ~ 150 nm as the shell thickness is increased from 2 nm to 40 nm.

6.3.4 Conclusions

We analyzed the optical, electron and morphological properties of Cu NPs in different dielectric environment and grown with different physical deposition techniques. First, we analyzed Cu NPs evaporated by MBE on a cerium oxide layer and capped with a second CeO$_2$ film. From the SEM analysis, we can individuate a uniform distribution of small Cu NPs (with an average diameter of 8 nm) and a wide size distribution. To investigate the optical properties of the NPs in ceria, we measured the UV-Vis absorbance of Cu NPs in CeO$_2$ layers of 4 and 8 nm: in both cases, the absorbance spectra exhibit a broad plasmonic band, peaked around 700 nm. The experimental results were compared with numerical simulations performed using the

Maxwell-Garret model: the observed optical absorbance is compatible with Cu NPs with ARs ranging from 1.5 to 2 immersed in a ceria layer with dielectric function similar to the one of bulk CeO_2. The stability over time of the plasmonic properties of the system was also evaluated: the optical absorbance spectrum acquired after 3 months from the growth shows an increase in absorbance in the UV range and a small decrease in the visible region, suggesting that the plasmonic behavior of the NPs is preserved even after long times from the deposition.

Afterwards, we compared the optical properties of bare Cu NPs, evaporated by MBE and grown under different conditions and which underwent different post processing procedures, to evaluate the effects of oxygen and of the substrate temperature in the different stages of the NPs growth. We have also acquired STEM images to obtain morphological information, and STEM-EELS maps for elemental analysis of the system. The investigated NPs showed similar surface chemical composition, but significantly different optical absorbance properties. In particular, the NPs grown in an oxygen partial pressure showed a broad absorbance band in the Vis range, peaked around 1000 nm, while the NPs that have been exposed to oxygen after the growth, under different conditions, presented a narrower peak at 700 nm, if exposed to atmosphere only when removed from the UHV for optical measurements, or a slightly higher wavelengths, if oxidized in the UHV chamber filled with oxygen partial pressure $P_{O_2} = 10^{-6}$ or $P_{O_2} = 10^{-7}$ mbar. The TEM images and the STEM-EELS maps acquired for the post-oxidized samples suggest the formation of hexagonally shaped NPs, surrounded by a thin shell of Cu_2O.

Finally, we investigated bare Cu and core-shell Cu/MgO NPs grown using gas-phase-synthesis. From morphological data we extracted an aspect ratio of 1.5 for Cu NPs, also confirmed by comparing the optical experimental data with numerical calculations. The aspect ratio greater than 1 is caused by the deformation of the NPs due to their interaction with the substrate and by the presence of small agglomerates formed during deposition. As the coverage increased, the formation of agglomerates became more evident. When Cu NPs were deposited on freshly exfoliated HOPG, diffusion and aggregation with the formation of islands occurred, and this was also evident in the preferential adsorption at surface step edges. When MgO is co-deposited with Cu NPs on Si/SiO_x, SEM images showed approximately square or rectangular islands, due to the growth of MgO around the metal NPs. TEM images and EDX maps confirmed that the co-evaporation of MgO during the deposition of Cu NPs favors the formation of a protective and transparent oxide shell around the NPs. This shell preserves the metallic nature of the copper core, as indicated by the results of *in-situ* XPS results of Cu 2p and Auger LVV. Moreover, UV–Vis optical absorbance spectra showed the presence of a distinct feature that was ascribed to the Cu LSPR, which was confirmed by calculations of the polarizability using the Maxwell–Garnett model for an oblate ellipsoid embedded in MgO. This result is compatible with previous observations made on Ag/MgO and Ag/CaF_2 NPs grown with the same method [33, 37]. These results demonstrate the efficacy of the co-deposition method of Cu NPs with MgO in preventing the contamination of the metallic NP, preserving the presence of the LSPR, and opening a pathway for the use of this nanomaterial in devices such as sensors and photovoltaic cells.

Bibliography

[1] George H. Chan, Jing Zhao, Erin M. Hicks, George C. Schatz, and Richard P. Van Duyne. Plasmonic properties of copper nanoparticles fabricated by nanosphere lithography. *Nano Letters*, 7(7):1947–1952, 2007.

[2] Sunari Peiris, John McMurtrie, and Huai-Yong Zhu. Metal nanoparticle photocatalysts: emerging processes for green organic synthesis. *Catal. Sci. Technol.*, 6:320–338, 2016.

[3] Mariano D. Susman, Yishai Feldman, Tatyana A. Bendikov, Alexander Vaskevich, and Israel Rubinstein. Real-time plasmon spectroscopy study of the solid-state oxidation and Kirkendall void formation in copper nanoparticles. *Nanoscale*, 9:12573–12589, 2017.

[4] Tianji Liu, Lucas V. Besteiro, Zhiming Wang, and Alexander O. Govorov. Generation of hot electrons in nanostructures incorporating conventional and unconventional plasmonic materials. *Faraday Discuss.*, 214:199–213, 2019.

[5] C. G. Granqvist and O. Hunderi. Optical properties of ultrafine gold particles. *Phys. Rev. B*, 16:3513–3534, 1977.

[6] Kevin M. McPeak, Sriharsha V. Jayanti, Stephan J. P. Kress, Stefan Meyer, Stelio Iotti, Aurelio Rossinelli, and David J. Norris. Plasmonic films can easily be better: Rules and recipes. *ACS Photonics*, 2(3):326–333, 2015. PMID: 25950012.

[7] Ellen J. Zeman and George C. Schatz. An accurate electromagnetic theory study of surface enhancement factors for silver, gold, copper, lithium, sodium, aluminum, gallium, indium, zinc, and cadmium. *The Journal of Physical Chemistry*, 91(3):634–643, 1987.

[8] C.F. Bohren and D.R. Huffman. *Absorption and Scattering of Light by Small Particles*. Wiley, 2008.

[9] Jagmeet Singh Sekhon and S S Verma. Refractive index sensitivity analysis of Ag, Au, and Cu nanoparticles. *Plasmonics*, 6(2):311–317, 2011.

[10] Changhwan Lee, Yujin Park, and Jeong Young Park. Hot electrons generated by intraband and interband transition detected using a plasmonic Cu/TiO$_2$ nanodiode. *RSC Advances*, 9(32):18371–18376, 2019.

[11] Jacopo Stefano Pelli Cresi, Enrico Silvagni, Giovanni Bertoni, Maria Chiara Spadaro, Stefania Benedetti, Sergio Valeri, Sergio D'Addato, and Paola Luches. Optical and electronic properties of silver nanoparticles embedded in cerium oxide. *The Journal of Chemical Physics*, 152(11):114704, 2020.

[12] John F Moulder, William F Stickle, and Peter E Sobol. *Handbook of X-ray photoelectron spectroscopy.* Perkin-Elmer, Physical Electronics Division, 1992.

[13] N. Pauly, S. Tougaard, and F. Yubero. Determination of the Cu 2p primary excitation spectra for Cu, Cu_2O and CuO. *Surface Science*, 620:17–22, 2014.

[14] Gunnar Schön. ESCA studies of Cu, Cu_2O and CuO. *Surface Science*, 35:96–108, 1973.

[15] V. Hayez, A. Franquet, A. Hubin, and H. Terryn. XPS study of the atmospheric corrosion of copper alloys of archaeological interest. *Surface and Interface Analysis*, 36(8):876–879, 2004.

[16] Charles T. Campbell. Ultrathin metal films and particles on oxide surfaces: structural, electronic and chemisorptive properties. *Surface Science Reports*, 27(1):1–111, 1997.

[17] Alexander Gloystein and Niklas Nilius. High-pressure oxidation of copper on Au(111)—a route toward bulk-like Cuprous oxide films. *The Journal of Physical Chemistry C*, 124(52):28605–28613, 2020.

[18] Svetlana Saikova, Sergey Vorobyev, Maxim Likhatski, Alexander Romanchenko, Simon Erenburg, Svetlana Trubina, and Yuri Mikhlin. X-ray photoelectron, Cu L3MM Auger and X-ray absorption spectroscopic studies of Cu nanoparticles produced in aqueous solutions: The effect of sample preparation techniques. *Applied Surface Science*, 258(20):8214–8221, 2012.

[19] S. Poulston, P. M. Parlett, P. Stone, and M. Bowker. Surface oxidation and reduction of CuO and cu2o studied using XPS and XAES. *Surface and Interface Analysis*, 24(12):811–820, 1996.

[20] G. Deroubaix and P. Marcus. X-ray photoelectron spectroscopy analysis of copper and zinc oxides and sulphides. *Surface and Interface Analysis*, 18(1):39–46, 1992.

[21] Mark C. Biesinger. Advanced analysis of copper X-ray photoelectron spectra. *Surface and Interface Analysis*, 49(13):1325–1334, 2017.

[22] https://www.thermofisher.com/it/en/home/materials-science/learning-center/periodic-table/transition-metal/copper.html.

[23] J. Morales, J. P. Espinos, A. Caballero, A. R. Gonzalez-Elipe, and Jose Antonio Mejias. XPS study of interface and ligand effects in supported Cu_2O and CuO nanometric particles. *The Journal of Physical Chemistry B*, 109(16):7758–7765, 2005.

[24] J. P. Espinós, J. Morales, A. Barranco, A. Caballero, J. P. Holgado, and A. R. González-Elipe. Interface effects for Cu, CuO, and Cu_2O deposited on SiO_2 and ZrO_2. XPS determination of the valence state of copper in cu/SiO_2 and cu/ZrO_2 catalysts. *The Journal of Physical Chemistry B*, 106(27):6921–6929, 2002.

[25] N Cabrera and N F Mott. Theory of the oxidation of metals. *Reports on Progress in Physics*, 12(1):163–184, 1949.

[26] Vladimir N Popok, Sergey M Novikov, Yurij Yu Lebedinskij, Andrey M Markeev, Aleksandr A Andreev, Igor N Trunkin, Aleksey V Arsenin, and Valentyn S Volkov. Gas-aggregated copper nanoparticles with long-term plasmon resonance stability. *Plasmonics*, 16(2):333–340.

[27] Jung Hyeun Kim, Sheryl H Ehrman, and Thomas A Germer. Influence of particle oxide coating on light scattering by submicron metal particles on silicon wafers. *Appl. Phys. Lett.*, 84(8):1278–1280.

[28] J C Yang, B Kolasa, J M Gibson, and M Yeadon. Self-limiting oxidation of copper. *Appl. Phys. Lett.*, 73(19):2841–2843.

[29] J C Yang, D Evan, and L Tropia. From nucleation to coalescence of Cu2O islands during in situ oxidation of Cu(001). *Appl. Phys. Lett.*, 81(2):241–243.

[30] Vladimir Zubkov, Joseph Han, Grace Sun, Charles Musgrave, and Sheldon Aronowitz. Modeling copper diffusion in silicon oxide, nitride, and carbide. *MRS Proceedings*, 716, 2002.

[31] Rasmus Bro and Age K. Smilde. Principal component analysis. *Anal. Methods*, 6(9):2812–2831, 2014.

[32] Maria Chiara Spadaro, Sergio D'Addato, Gabriele Gasperi, Francesco Benedetti, Paola Luches, Vincenzo Grillo, Giovanni Bertoni, and Sergio Valeri. Morphology, structural properties and reducibility of size-selected CeO_{2-x} nanoparticle films. *Beilstein Journal of Nanotechnology*, 6:60–67, 2015.

[33] Sergio D'Addato, Daniele Pinotti, Maria Chiara Spadaro, Guido Paolicelli, Vincenzo Grillo, Sergio Valeri, Luca Pasquali, Luca Bergamini, and Stefano Corni. Influence of size, shape and core–shell interface on surface plasmon resonance in Ag and Ag@MgO nanoparticle films deposited on Si/SiO_x. *Beilstein Journal of Nanotechnology*, 6:404–413, 2015.

[34] Laurent Bardotti, Pablo Jensen, Alain Hoareau, Michel Treilleux, and Bernard Cabaud. Experimental observation of fast diffusion of large antimony clusters on graphite surfaces. *Phys. Rev. Lett.*, 74:4694–4697, 1995.

[35] Sergio D'Addato, Federica Perricone, and Guido Paolicelli. Adhesion, mobility and aggregation of nanoclusters at surfaces: Ni and Ag on Si, HOPG and graphene. *SN Applied Sciences*, 4(2), 2022.

[36] David Appy, Huaping Lei, Cai-Zhuang Wang, Michael C. Tringides, Da-Jiang Liu, James W. Evans, and Patricia A. Thiel. Transition metals on the (0 0 0 1) surface of graphite: Fundamental aspects of adsorption, diffusion, and morphology. *Progress in Surface Science*, 89(3-4):219–238, 2014.

[37] Sergio DÁddato, Avinash Vikatakavi, Maria Chiara Spadaro, Sergio Valeri, and Luca Pasquali. Physical synthesis and study of $Ag@CaF_2$ core@shell nanoparticles: Morphology and tuning of optical properties. *physica status solidi (b)*, 256(7):1800507, 2019.

[38] Alexander Wolfram, Quratulain Tariq, Cynthia C. Fernández, Maximilian Muth, Martin Gurrath, Daniel Wechsler, Matthias Franke, Federico J.

Williams, Hans-Peter Steinrück, Bernd Meyer, and Ole Lytken. Adsorption energies of porphyrins on MgO(100): An experimental benchmark for dispersion-corrected density-functional theory. *Surface Science*, 717:121979, 2022.

[39] Martin Amft, Sébastien Lebègue, Olle Eriksson, and Natalia V Skorodumova. Adsorption of Cu, Ag, and Au atoms on graphene including Van der Waals interactions. *Journal of Physics: Condensed Matter*, 23(39):395001, 2011.

[40] Uwe Kreibig and Michael Vollmer. *Optical properties of metal clusters*. Springer Series in Materials Science. Springer, 1995 edition.

[41] M. Getzlaff, J. Bansmann, F. Bulut, R.K. Gebhardt, A. Kleibert, and K.H. Meiwes-Broer. Structure, composition and magnetic properties of size-selected FeCo alloy clusters on surfaces. *Applied Physics A*, 82(1):95–101, 2005.

[42] A Kleibert, F Bulut, R K Gebhardt, W Rosellen, D Sudfeld, J Passig, J Bansmann, K H Meiwes-Broer, and M Getzlaff. Correlation of shape and magnetic anisotropy of supported mass-filtered Fe and FeCo alloy nanoparticles on W(110). *Journal of Physics: Condensed Matter*, 20(44):445005, 2008.

[43] S. D'Addato, L. Gragnaniello, S. Valeri, A. Rota, A. di Bona, F. Spizzo, T. Panozaqi, and S. F. Schifano. Morphology and magnetic properties of size-selected Ni nanoparticle films. *Journal of Applied Physics*, 107(10):104318, 2010.

[44] L. Martínez, K. Lauwaet, G. Santoro, J. M. Sobrado, R. J. Peláez, V. J. Herrero, I. Tanarro, G. J. Ellis, J. Cernicharo, C. Joblin, Y. Huttel, and J. A. Martín-Gago. Precisely controlled fabrication, manipulation and in-situ analysis of Cu based nanoparticles. *Scientific Reports*, 8(1), 2018.

[45] Hongbu Yin, Yan Zhao, Xibin Xu, Jie Chen, Xuemin Wang, Jian Yu, Jin Wang, and Weidong Wu. Realization of tunable localized surface plasmon resonance of Cu@Cu$_2$O core-shell nanoparticles by the pulse laser deposition method. *ACS Omega*, 4(11):14404–14410, 2019.

[46] Vladimir N. Popok, Sergey M. Novikov, Yurij Yu. Lebedinskij, Andrey M. Markeev, Aleksandr A. Andreev, Igor N. Trunkin, Aleksey V. Arsenin, and Valentyn S. Volkov. Gas-aggregated copper nanoparticles with long-term plasmon resonance stability. *Plasmonics*, 16(2):333–340, 2020.

[47] P. B. Johnson and R. W. Christy. Optical constants of the noble metals. *Phys. Rev. B*, 6:4370–4379, 1972.

[48] Robert E Stephens and Irving H Malitson. Index of refraction of magnesium oxide. *Journal of Research of the National Bureau of Standards*, 49(4):249–252, 1952.

[49] Harold Wieder and A. W. Czanderna. Optical properties of copper oxide films. *Journal of Applied Physics*, 37(1):184–187, 1966.

[50] Gorachand Ghosh. Sellmeier coefficients and dispersion of thermo-optic coefficients for some optical glasses. *Appl. Opt.*, 36(7):1540–1546, 1997.

[51] G. Ghosh, M. Endo, and T. Iwasaki. Temperature-dependent sellmeier coefficients and chromatic dispersions for some optical fiber glasses. *Journal of Lightwave Technology*, 12(8):1338–1342, 1994.

[52] Leandro Pascua, Fernando Stavale, Niklas Nilius, and Hans-Joachim Freund. Ag/ZnO hybrid systems studied with scanning tunnelling microscopy-based luminescence spectroscopy. *Journal of Applied Physics*, 119(9):095310, 2016.

[53] Xiaotong Liu, Dabing Li, Xiaojuan Sun, Zhiming Li, Hang Song, Hong Jiang, and Yiren Chen. Tunable dipole surface plasmon resonances of silver nanoparticles by cladding dielectric layers. *Scientific Reports*, 5(1), 2015.

[54] Shilei Zhu, Dan Deng, Mai Thanh Nguyen, Yuen ting Rachel Chau, Cheng-Yen Wen, and Tetsu Yonezawa. Synthesis of Au@Cu$_2$O Core-Shell nanoparticles with tunable shell thickness and their degradation mechanism in aqueous solutions. *Langmuir*, 36(13):3386–3392, 2020.

Chapter 7

Photoluminescence Spectroscopy from Metal-Supported Cu$_2$O Films: Excitonic versus Plasmonic Excitations

Cuprous oxide (Cu$_2$O) is one of most relevant p-type semiconducting oxides in the field of photocatalysis, because of its band gap in the visible range together with its abundance, sustainability and non-toxicity. Moreover, different techniques for thin-film deposition have been developed that facilitate low-cost and large-scale production [1]. Investigations on the band structure and on the separation of photo-generated charge carriers are a key point with a view of employing Cu$_2$O as an active photocatalyst. A precise optical characterization of Cu$_2$O films is then crucial to determine the excitons behaviour in the material and the role played by the defects. For this purpose, photoluminescence can be used for the detection of defects and impurities within dielectric solids, even at very low concentration [2, 3]. In this chapter, we investigated a bulk Cu$_2$O crystal and thin films of 10 to 65 nm thickness by means of electron diffraction, scanning tunneling microscopy (STM) and photoluminescence (PL) spectroscopy in a wide temperature range from 100 to 300 K. Although the chemical composition of the samples is the same, and the surface morphology is very similar, large differences are found in the optical response.

7.1 Introduction and theoretical background

Photoluminescence (PL) is a very sensitive detector of even smallest impurities and imperfections in dielectric solids [2, 3]. Whereas photoelectron spectroscopy is limited to defect concentrations of 1% in the near-surface region, PL can safely detect bulk imperfections in the $10^{-5} - 10^{-7}$ concentration range, high optical activity provided. Moreover, well resolved PL spectra acquired at low temperature contain information on the chemical nature of the imperfections, their charge state and the composition of their immediate environment. Phonon replica next to the PL peaks give further insights into electron-vibrational coupling for a given optical transition. A fundamental problem of PL spectroscopy is the intrinsic difficulty to connect a given luminescence peak to a specific defect configuration, as a direct view onto the atomic environment is typically unavailable [4]. A powerful pathway of assignment is the comparison of experimental emission data with the results of theoretical simulations performed for potential defect candidates [5]. Respective calculations

are however demanding as they require a reliable computation of excited electronic states, of the dynamics of structural relaxations and of the role of many-particle effects to mimic exciton and trion formation [6]. Not surprisingly, correlating low-temperature PL spectra to underlying atomic-scale defects remains challenging and has not unambiguously achieved even for prototype dielectrics, such as ZnO or GaN [4, 7, 8].

In the present work, we have investigated the unique optical response of Cu_2O by means of PL spectroscopy. As already mentioned in the first chapter, Cu_2O is one the most attractive p-type semiconductors for a large variety of applications, such as electronics, spintronics and solar water splitting. In particular, its band gap (~ 2.15 eV) is nearly in the center of the visible spectrum, making this material a promising candidate for photovoltaic and photochemical applications. Even band-gap gradients from 2.15 to 1.35 eV can be reproducibly fabricated by introducing a gradual composition shift from Cu_2O to CuO [9]. To optimize the photovoltaic and photo-catalytic response of the oxide, it is crucial to precisely control the Cu_2O stoichiometry and defect landscape [10, 11, 12]. The overall optical properties of Cu_2O are governed by the interplay of various excitons and their trapping behavior at lattice defects [1, 13]. Both the singlet para- and triplet ortho-excitons are hereby characterized by extremely long lifetimes, as involved electrons and holes occupy Cu 4s conduction and Cu 3d valence states, respectively, which makes a direct optical decay parity forbidden. Radiative recombination of ortho-excitons becomes possible, however, via phonon involvement and gives rise to a complex exciton PL at 620 nm, comprising several phonon-replica and higher-order peaks [14, 15, 16]. Moreover, Cu_2O excitons can be trapped at various point defects in the oxide lattice, whereby Cu (V_{Cu^-}) and O vacancies ($V_{O^{2+}}$ and V_{O^+}) produce the strongest in-gap peaks at 730, 840 and 920 nm, respectively [13]. Reported PL spectra of Cu_2O single crystals and, even more, thin films and powder samples exhibit a rather high variability, which complicates their analysis. High-quality floating-zone crystals, for example, exhibit dominant V_{Cu^-} luminescence, reflecting the high Cu-defect concentration expected for a p-type material [13, 17]. Natural crystals, on the other hand, do not show V_{Cu^-} emission, although p-type conductivity has been reported also for those samples [13, 18]. More surprisingly, the PL spectra of powder materials often comprise both, strong V_O and V_{Cu} peaks, suggesting insufficient annihilation of majority and minority defects in the lattice [14, 19, 20, 21]. The free-exciton PL, on the other hand, is hardly detected because of the disruptive interplay between long exciton lifetime and low crystallinity in the granular samples. In general, it is impossible to infer the Cu_2O stoichiometry only on the basis of the PL intensity ratio of Cu versus O defects, as the involved emission channels follow different excitation and recombination schemes and have a different time and temperature dependence [13, 17, 18]. To obtain reliable insights into composition and defect structure of Cu_2O, the PL data thus needs to be complemented with other microscopic and spectroscopic techniques that provide further information on the electronic structure and conductance behavior [22]. To have a deeper understanding of the stoichiometry and on defects, we have compared the distinct PL emission of a Cu_2O bulk crystal with the one of Cu_2O thin films grown on Au(111) and Pt(111) supports. The PL measurements have also been correlated with low-energy electron diffraction (LEED), X-Ray photoelectron spectroscopy (XPS) and scanning tunneling microscopy (STM) analysis, which suggested comparable structural, electronic and chemical properties of the examined samples [23, 24]. However, a markedly different PL signature indicates a rather specific defect landscape in the three oxide lattices. The present study aims
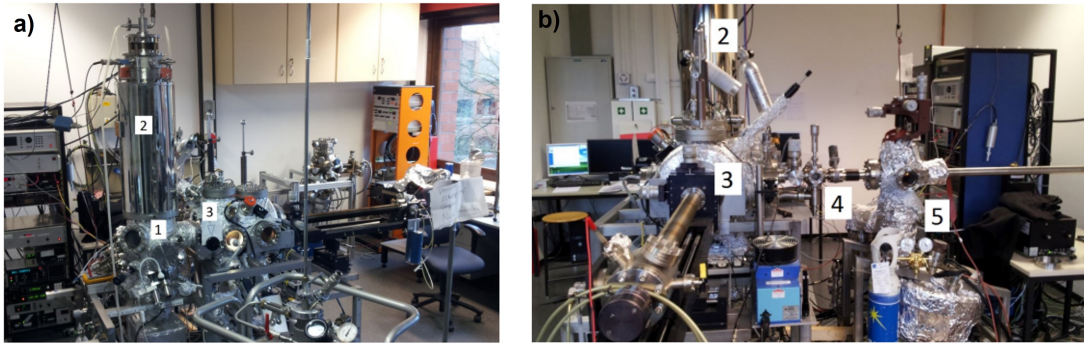
Figure 7.1: *Pictures of the UHV-Setup. 1: STM chamber, 2: bath cryostat, 3: preparation chamber, 4: high pressure chamber, 5: XPS chamber [28].*

at comparing the specific PL response of bulk and thin-film samples. Moreover, we investigated whether the strong V_O luminescence observed in thin films is compatible with a p-type conductance behavior that naturally relies on an abundance of Cu-defects [25], or if n-type Cu_2O can be synthesized in poor-oxygen atmosphere [21, 26]. Finally, we address why interface plasmons localized at the metal/oxide boundary do not contribute to the thin-film emission response, although plasmonic light dominates the STM luminescence behavior of 5 nm-thick Cu_2O film grown on Au(111) [27].

7.2 Experimental

7.2.1 Experimental setup

The samples described in this chapter were all grown and characterized in the apparatus shown in figure 7.1, composed by four UHV chambers: the STM, Preparation, XPS and high pressure chamber. The preparation chamber (3 in figure 7.1) is mainly dedicated to surface preparation and sample deposition. It is kept at a pressure $P \sim 2 \times 10^{-10}$ mbar and it is equipped with tools for sample cleaning (ion sputtering and a heating stage), thin-film growth (molecular evaporators and a gas line that allows to modify the composition of the deposition atmosphere) and surface analysis through low energy electron diffraction (LEED). XPS measurements are performed in a second UHV chamber (5), connected to the preparation chamber with a transfer arm. The chamber is equipped with a hemispherical electron analyzer (ESCALAB 200) combined with non-chromatized Mg K_α and Al K_α twin sources. Between the preparation chamber and the XPS chambers, there is the high pressure chamber (4), which allows sample oxidation in an oxygen partial pressures adjustable between 10^{-4} and 200 mbar, and temperatures ranging between 300 and 700 K. Finally, the preparation chamber is connected to a beetle-type STM operated at liquid-nitrogen temperature (1). A schematics of the LN_2-cooled STM is reported in figure 7.2. During the scans, the sample is placed on three piezo tubes, electrically isolated from the samples by small sapphire parts. The small steel balls on top of the sapphire connect the tunnel bias voltage to the sample holder and reduce mechanical friction during sample movement. The tip is mounted on a fourth piezo in the middle of the setup which is used for the scan movement [29].

An attached optical setup enables *in-situ* PL and white-light reflectivity measurements performed with a NdYag laser (20 mW power) and a halogen lamp, respectively. In this setup, the measurements can be done in a temperature range
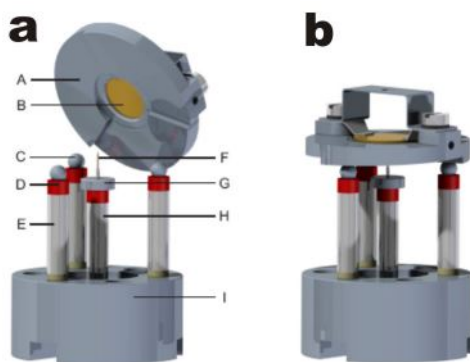
Figure 7.2: *Drawing of the scan head setup [29]. A: ramp with different sectors, B: sample, C: support ball, D: sapphire, E: support-piezo, F: tip, G: tip-holder, H: scan-piezo, I: base.*

between 100 and 300 K, by cooling down the manipulator using liquid nitrogen. PL data at temperatures down to 10 K could be acquired in an external He-cooled apparatus. As the supported Cu_2O films revealed irreversible changes of their interface and surface morphology during air transfer, reliable low-temperature data could only be taken for the bulk crystal. In both experiments, the optical response was detected with a LN_2-cooled, single-line CCD detector attached to a grating spectrograph with 150 lines/mm.

7.2.2 Sample preparation

Cuprous oxide films of arbitrarily thickness were grown onto Au(111) or Pt(111) single-crystal substrates. Both substrates were cleaned by repeated cycles of Ar^+ sputtering and 800 K annealing until a sharp hexagonal spot pattern was seen in LEED. The choice of the substrates derives from their (2×2) surface cells, that closely match the lattice parameter of bulk $Cu_2O(111)$, ensuring the formation of smooth metal/oxide interfaces. The $Cu_2O(111)$ bulk crystal, purchased from *Surface Preparation Laboratory*, was prepared by Ar^+ sputtering and vacuum-annealing to 800 K until a sharp LEED pattern was detectable [24]. The Cu_2O thin-films were prepared in the three-step procedure developed in [23].

1. Physical vapor deposition of 10 nm metallic Cu (purity 99.9%) on Au(111) and Pt(111) surfaces cleaned by sputtering and annealing cycles before;

2. Oxidation in the high-pressure cell at 50 mbar O_2 and 450 K;

3. Low-pressure annealing in front of a pin-hole doser ($P_{O_2} = 10^{-4}$ mbar) at 600 K to stimulate film crystallization.

7.3 Results and discussion

7.3.1 Thickness determination

The precise thickness determination of the supported films is fundamental to correlate defect landscape and PL signature of the Cu_2O thin films. The deposition chamber is not equipped with a microbalance, and XPS can not be used for this purpose, as the substrate peaks become invisible already beyond 10 nm film thickness,

well below the range of interest in our study. We have therefore exploited thin-film interference effects to follow the thickness evolution in subsequent deposition steps, as schematized in figure 7.3a. For this purpose, the reflectivity of Cu_2O films of different thicknesses was probed with a white-light halogen lamp. The dark-blue line in figure 7.3b represents the reflectance of one of the $Cu_2O/Pt(111)$ films after normalization with the bare $Pt(111)$ reference. The spectrum exhibits a broad minimum at 665 nm, originating from destructive interference of light reflected from the Cu_2O surface and the $Cu_2O/Pt(111)$ interface. The extinction condition is given by:

$$2 \cdot d \cdot \cos\theta \sqrt{\epsilon_{Cu_2O}} = m\lambda \qquad (7.1)$$

with $\epsilon_{Cu_2O} = 6.7$ being the permittivity of the oxide layer [30], d the film thickness, $m = 1/2$ the phase factor of the 1st interference minimum and λ its wavelength. Since the measurement was performed in a geometry configuration where the incoming and outgoing beam closely follow the surface normal, $\cos\theta \sim 1$. The three curves in figure 7.3b depict similar interference data obtained for three Cu_2O films after different numbers of deposition cycles. The intensity minimum shifts toward shorter wavelengths as the film thickness decreases. Moreover, the curves became more asymmetric, as the white-light source used for the measurement lacks blue and violet intensity components and the low-wavelength region results suppressed in the spectra. To obtain an approximate minimum position, we have fitted the almost symmetric dark-blue spectrum in figure 7.3b with the Granfilm software [31], developed to simulate the optical response of particle ensembles and thin films (7.3b, dashed blue line). The high-wavelength tails of the new, blue-shifted spectra were now fitted with an identical data set, except for the film thickness that was treated as parameter. The so-obtained resonance positions yield a film thickness of 65, 57 and 50 nm for the three films. These values are in good agreement with the number of deposition cycles conducted during preparations, namely 6,7 and 8 for the cyan, light-blue and dark-blue curves, respectively. Apparently, every cycle adds 7-8 nm material to the existing film, which is comparable to 10 nm Cu deposited in each step. The discrepancy arises from Cu losses during high- and low-pressure oxidation, either as a result of evaporation or, more importantly, due to Cu alloying with the metal support. Previous works from Nilius group demonstrated that 100% of the Cu would segregate into the Pt and Au crystals in absence of chemical stabilization via oxidation [32].

The inset in figure 7.3b shows the macroscopic color variations of the sample as the thickness of the film is increased. The thin-film interference is strong enough to imprint a unique color change onto the originally metallic $Pt(111)$ surface: after depositing a ~ 40 nm thick film, the crystal adopts a pink color as only blue and red components of the incident light are reflected (central panel). The color changes to blue-green for 57 nm thick films, as now the yellow-red components are removed from the spectrum (right panel).

7.3.2   Structure, morphology and chemical composition

We investigated the lattice structure, chemical composition and surface morphology of thin (111)-oriented Cu_2O films with respect to a (111) single crystal by means of XPS and LEED. The XPS spectra of both samples revealed a dominant Cu_2O stoichiometry, as discussed in previous works [23, 24]. The comparison between the Cu 2p versus O 1s peak areas disclosed a slight O deficiency in the thin films, being close to the resolution limit of our XPS lab source. LEED measurements revealed an
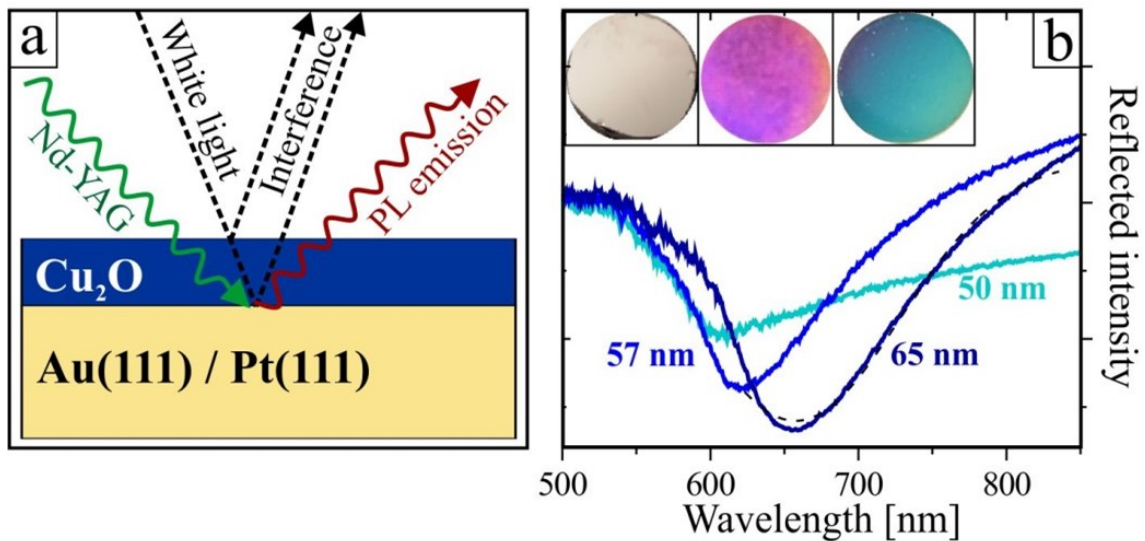
Figure 7.3: *Sketch of the approach used to deterimine the Cu_2O film thickness. Stimulating the PL by 532 nm laser photons, we could infer the thickness by measuring the wavelength position of the 1st interference minimum of the white light. (b) White-light reflectance of differently thick Cu_2O/ Pt(111) films. The inset shows photographs of pristine Pt(111) and the crystal after depositing ~ 45 (middle) and ~ 65 nm Cu_2O on top (right).*

identical crystal structure of bulk and thin-film samples (figure 7.4, insets). Both oxides exhibit hexagonal symmetry with 6.1 Å lattice parameter, in perfect agreement with the values reported for cubic Cu_2O [1]. Moreover, $\sqrt{3} \times \sqrt{3}R30°$ superstructure spots became visible on all explored surfaces, yet with higher intensity and improved sharpness on bulk than thin-film oxides. Similar superstructures were reported for (111)-oriented single crystals and thin films before [23, 33, 34], while the atomic nature of the reconstruction was unraveled in a recent DFT study by Gloystein et al. [35]. In the model, every third Cu-O six ring of the regular (111) surface gets occupied by a Cu_4O pyramid that saturates all oxygen dangling bonds in the surface. As a result, the surface energy is substantially reduced, which makes the nano-pyramidal reconstruction thermodynamically preferred over the stoichiometric and any other reconstruction model proposed for $Cu_2O(111)$ so far. The sharper and brighter $\sqrt{3} \times \sqrt{3}R30°$ superstructure spots suggest a superior long-range order of the nano-pyramidal reconstruction on the bulk crystal than on the oxide films.

The quality of the different Cu_2O surfaces was further explored by high-resolution STM measurements (figure 7.4). On all three oxide systems, wide and atomically flat terraces are revealed, indicating the perfect crystallinity of the underlying lattices. The terraces are homogenously covered with a hexagonal ad-pattern with 10.5 Å periodicity that represents the nano-pyramidal reconstruction (figure 7.4, insets). Each maximum hereby reflects one Cu_4O nano-pyramid that can even be resolved into a distinct shamrock shape at higher resolution [23]. As already suggested by LEED measurements, the $\sqrt{3} \times \sqrt{3}R30°$ reconstruction is better ordered in the bulk crystal, but it can be clearly identified for both Au(111)- and Pt(111)-supported Cu_2O films as well. At this point, we have no indication that the slightly lower quality of the surface pattern on the thin films is responsible for the markedly different PL response with respect to bulk samples, as detailed later in the text.

To get information on the valence electronic structure of thin-film versus bulk Cu_2O samples, we used STM conductance spectroscopy (figure 7.5). All three sam-
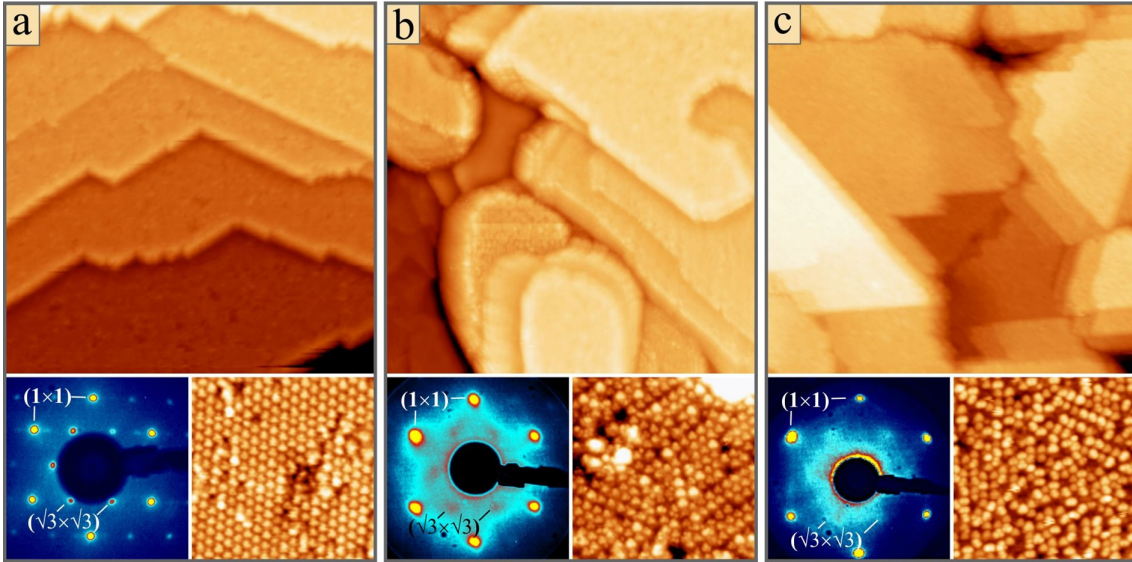
Figure 7.4: *Overview and high-resolution STM topographic images of the $Cu_2O(111)$ surface of (a) a single crystal (b) a 10 nm thick film grown on Au(111) and (c) a 25 nm thick film on Pt(111) (150×150 nm^2, $U_B = 3.5$ V, $I = 0.1$ nA). All oxide surfaces are homogeneously covered with Cu_4O nano-pyramids (20×20 nm^2, $U_B = -1.7$ V, $I = 0.1$ nA) that give rise to the $\sqrt{3} \times \sqrt{3}R30°$ reconstruction seen in LEED ($E_{kin} = 37$ eV, insets).*

ples exhibit similar spectra, characterized by a broad region of negligible dI/dV intensity, representing the oxide band gap, enclosed by the valence (VB) and conduction band (CB) onsets at 0 and +2.0 V, respectively. The corresponding gap size of ~ 2.0 eV is identical for bulk and thin-film samples, and also in line with respective values found in the literature [1]. Moreover, pinning of the VB top to the Fermi level provides a clear manifestation of the p-type character of the oxide and points to an abundance of acceptor-type V_{Cu} defects in the oxide matrix [25, 26]. The in-gap dI/dV peak at 0.3-0.5 V, clearly seen in logarithmic representation, originates from tunneling into an empty-state pocket at the VB top. It arises from upward bending of the surface bands due to the non-stoichiometric, i.e., Cu-deficient nature of the pyramidal reconstruction, and is detected for all three samples [36].

7.3.3 Luminescence spectroscopy

Figure 7.6 represents the PL signature of bulk $Cu_2O(111)$, stimulated with 532 nm photons of a NdYag laser and recorded for 20 s with a CCD detector. The PL spectrum is characterized by three bands at 620, 730 and 920 nm. The 920 nm peak hereby dominates the emission, while the low-wavelength intensity needs to be multiplied by twenty to be depicted at the same scale. The intensity evolution as a function of temperature was derived by Gaussian fitting and is displayed for all three bands in figure 7.6. The high-wavelength peak at 920 nm exhibits a steady intensity rise, whereas the 730 nm emission sets in only at 230 K and the 620 nm peak runs through a broad maximum at 120 K and decreases again at lower temperature. Figure 7.7a and b represent normalized PL spectra of supported Cu_2O films on Au(111) and Pt(111) measured at similar conditions as the bulk crystal. While the Cu_2O/Au(111) film has a thickness of ~ 10 nm, the Pt(111)-supported film is ~ 65 nm thick. The mean emission yield, calculated per nanometer, is however comparable in both cases and amounts to ~ 100 photons/s/nm at the peak
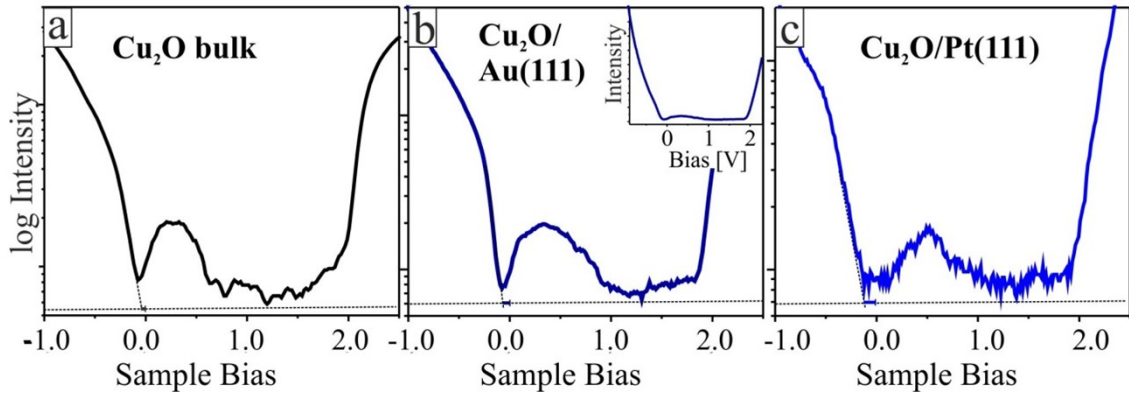
Figure 7.5: *STM conductance spectra of (a) bulk Cu_2O, (b) 10 nm $Cu_2O/Au(111)$ and (c) 25 nm $Cu_2O/Pt(111)$ shown on a logarithmic scale. The spectra were acquired at 2.5 V setpoint bias and a starting current of 0.1 nA (a) and 1 nA (b,c). The inset in (b) shows the same spectrum on a linear scale, demonstrating the negligible weight of the in-gap conductance with respect to direct tunneling into the oxide bands. The dotted lines are guides to the eye to approximate the VB onset with respect to the Fermi level.*
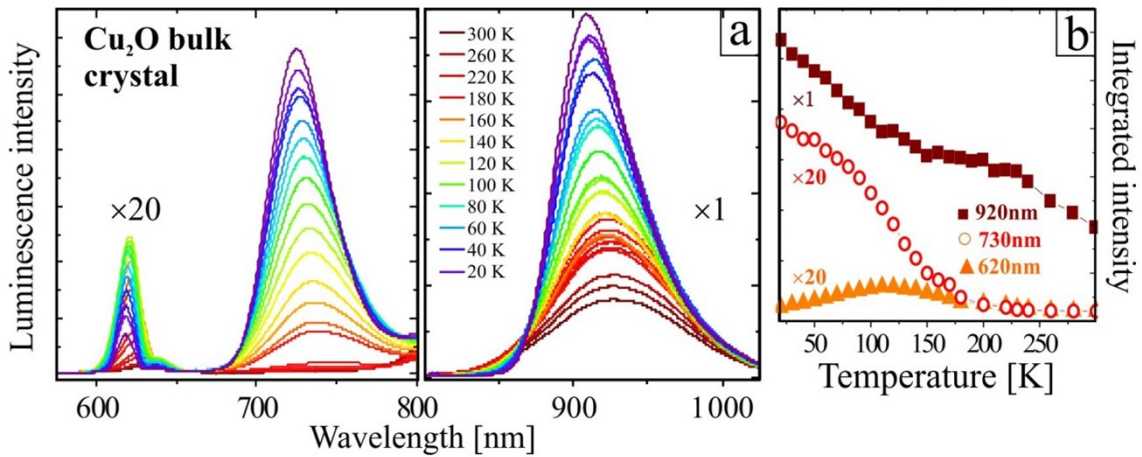

Figure 7.6: *PL spectra of a Cu_2O bulk crystal. Given the dominance of the 920 nm peak the spectrum is divided into two wavelength sections with different y-axis. (b) Temperature dependence of the three PL bands. Given the low intensity of the 620 and 730 nm band, their temperature curves have been multiplied by a factor of 20.*
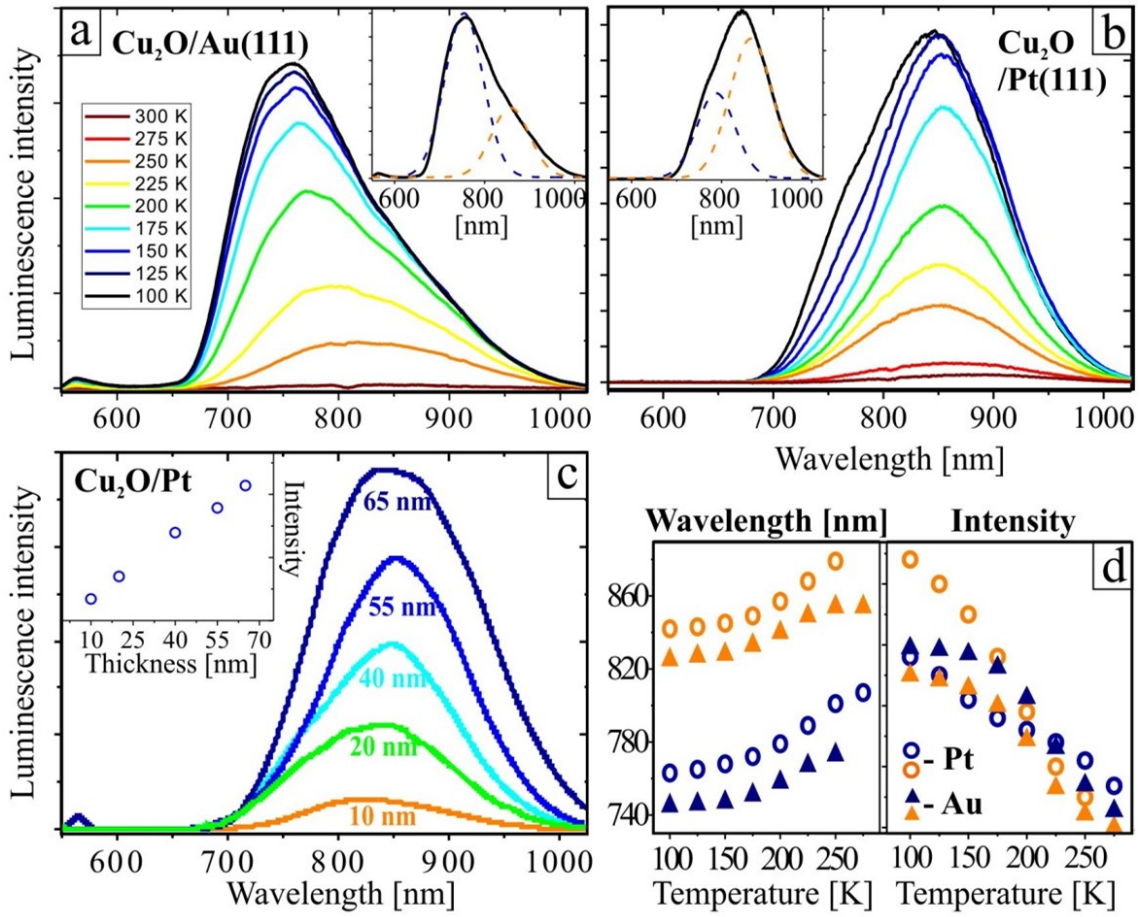
Figure 7.7: *Normalized PL spectra of (a) 10 nm Cu₂O/Au(111) and (b) 65 nm Cu₂O/Pt(111) films at different temperatures. (c) Thickness-dependent data of the Cu₂O/Pt(111) film at 100 K. Inset: evolution of the integral emission intensity. (d) Central wavelength and peak intensity of the two emission contributions used to fit the thin-film PL spectra (insets in a and b. Blue and orange symbols are for the short- and long-wavelength component, open and closed symbols for the Pt and Au support, respectively*

maximum. The PL spectra of the thin films are substantially different from that of the bulk crystal shown in figure 7.6. The PL data of Au-supported films have an asymmetric shape and are characterized by a sharp onset at 670 nm, a broad maximum at 775 nm and a slow decay at higher wavelengths. The $Cu_2O/Pt(111)$ luminescence spectrum is red-shifted, with onset and peak position at 700 and 850 nm, respectively. Both PL spectra can be deconvoluted into two Gaussians of similar position and width (figure 7.7a, b, inset). While the low-wavelength peak at ~ 750 nm (FWHM 80 nm) is the most intense in the Au(111)-derived spectra, the high-wavelength peak at ~ 830 nm (FWHM 100 nm) becomes dominant for Pt(111)-supported oxide film. The two contributions are both characterized by a gradual blue-shift of the peak wavelength and a steady intensity rise upon cooling down to 100 K (figure 7.7d). Panel 7.7c finally represents the evolution of the $Cu_2O/Pt(111)$ luminescence as a function of film thickness: the emitted intensity monotonously rises when thickening the film from 10 to 65 nm, as compiled in the inset. The origin of the surprisingly different PL response of thin-film versus bulk Cu_2O samples is addressed in the next section.

7.3.4 Nature of thin-film versus bulk Cu_2O luminescence

The luminescence behaviour observed for the bulk $Cu_2O(111)$ crystal is the one expected from literature [1, 13, 16]. The three maxima in the PL spectrum in figure 7.6 are assigned to the radiative decay of free and bound excitons. The free excitation emission is governed by the phonon-assisted decay of ortho-excitons, resulting in several sharp peaks centered at 620 nm [14]. At the spectral resolution of our experiment, the individual phonon replicas are not resolved and overlap to a single, asymmetric emission band. Its blue-shift with decreasing temperature, due to renormalization of the Cu_2O band gap, is however discerned [37]. Also, the detected temperature evolution of the free-exciton peak agrees well with the reported behavior (figure 7.6b, orange symbols) [13]. With decreasing temperature, the probability of radiative exciton decay increases, as the probability for thermal exciton separation into unbound electrons and holes decreases. This trend reverses at ~ 125 K, when ortho-excitons switch to non-radiative para-excitons that are more stable by 12 meV [38].

The peaks at 730 and 920 nm, on the other hand, are assigned to Cu_2O excitons trapped at $V_{O^{2+}}$ and V_{Cu^-} vacancies, respectively [13, 39]. The point defects introduce distinct gap states localized below the CB edge (initial state in the $V_{O^{2+}}$ decay) and above the VB top (final state in the V_{Cu^-} decay), explaining the red-shift of the respective exciton modes. The dominance of the V_{Cu^-} with respect to $V_{O^{2+}}$ emission is in line with the p-type nature of Cu_2O and reflects the thermodynamic preference to insert acceptor-type Cu vacancies into the lattice [25]. The observed temperature dependence of the 730 and 920 peaks (light- and dark-red lines in figure 7.6b) additionally strengthens our assignment. While the $V_{O^{2+}}$ related channels only opens below 230 K, as electrons are back-promoted from the defect state to the CB at higher temperature, the final state in the V_{Cu^-} transition is blocked by thermal electrons from the VB at elevated temperature [13, 39]. Finally, the coexistence of Cu and O vacancies in the lattice indicates incomplete equilibrium of these two fundamental defect types in the bulk crystal [40].

At first glance, the luminescence of $Cu_2O(111)$ thin films seems incompatible with an exciton-mediated scheme, as neither the 620 nm peak related to free excitons nor the 930 nm peak arising from exciton-trapping at V_{Cu^-} sites is observed. Moreover, the appearance of a PL band around 800 nm depends on the nature of the substrate, and a clear red-shift of the emission is revealed when switching from Au(111) to Pt(111) supports (figure 7.7). A first possible explanation for this behavior would be stimulation and radiative decay of surface plasmon polaritons (SPPs) at the metal/oxide interface [41, 42]. To test this assumption, we have evaluated the plasmon dispersion relation at the Cu_2O/Au(111) interface (figure 7.8a) that follows:

$$k^2 = \left(\frac{\omega}{c}\right)^2 \cdot \frac{\epsilon_{Cu2O} \cdot \epsilon_{Au}}{\epsilon_{Cu2O} + \epsilon_{Au}} \tag{7.2}$$

where ϵ_{Cu_2O} and ϵ_{Au} are the complex dielectric functions of Cu_2O and Au, k and ω are plasmon wavevector and frequency respectively, and c is the speed of light [43]. At the detected PL maximum of Cu_2O/Au(111) (775 nm, figure 7.7a), we found a value for the plasmon wavevector $k_{SPP} = 0.7 \times 10^8$ m^{-1}, which compares to a corresponding free-photon wavevector of $k_{Ph} = 0.22 \times 10^8$ m^{-1}. This well-known wavevector mismatch of $\Delta k = 0.48 \times 10^8$ m^{-1} prohibits excitation and radiative decay of metal/oxide interface plasmons, unless it gets compensated by an auxiliary wavevector provided by an optical grating or interface roughness [44]. However, neither the periodicity ($\frac{2\pi}{\Delta k} \sim 130$ nm) nor the height corrugation (70 nm or 10% of
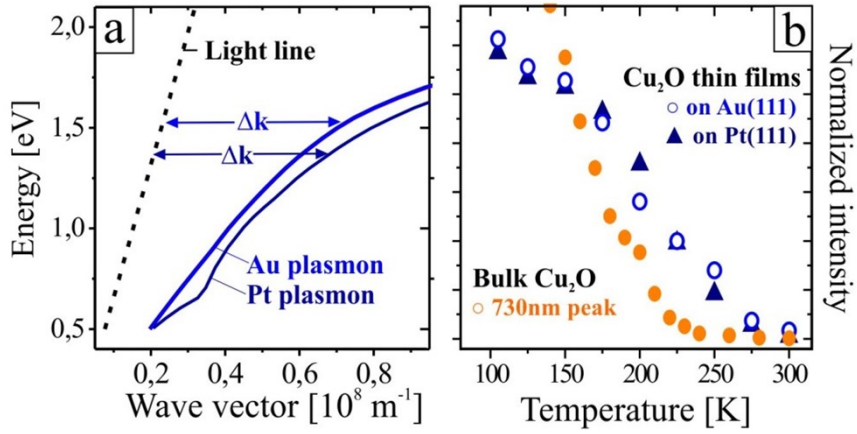
Figure 7.8: *(a) Dispersion relation of the $Cu_2O/Au(111)$ (blue curve) and the $Cu_2O/Pt(111)$ (dark-blue curve) interface plasmon in addition to the light line. The significative wavevector mismatch needs to be balanced by interface roughness, in clear conflict with the rather flat film morphologies depicted in figure 7.4. (b) Temperature dependence of the 730 nm peak intensity from bulk Cu_2O and the integrated PL intensity from the thin films.*

the photon wavelength) of the required grating would be compatible with the rather flat film morphologies shown from the STM images of the metal-supported Cu_2O films shown in figure 7.4. Moreover, the revealed temperature dependence of the thin-film PL cannot be reconciled with a plasmon-mediated emission mechanism. We can therefore exclude that metal/oxide interface plasmons activated by surface roughness are responsible for the observed PL signature of our Cu_2O thin films.

In contrast, PL bands in the range between $700 - 800$ nm have been frequently observed before for Cu_2O films, powders and nanostructures [19, 45]. Moreover, Cu_2O layers synthesized by magnetron sputtering revealed a distinct PL doublet at around 800 nm, again with little intensity in the wavelength region of the oxide excitons [46]. A correlation between the 800 nm emission and the presence of O defects in the Cu_2O lattice was first proposed by Zouaghi [18] and supported by several control-experiments thereafter. For example, while Cu_2O single crystals grown in a floating-zone scheme in air feature a strong 920 nm PL peak due to V_{Cu} defects, this changes to a maximum of 730 nm after crystal growth in an argon environment [13]. Similarly, the V_{Cu^-} PL gets replaced by a strong $V_{O^{2+}}$ peak in nitrogen doped cuprous oxide, as the insertion of substitutional N_O gets accompanied by the formation of oxygen vacancies [20]. Theoretically, the $V_{O^{2+}}$ emission from Cu_2O has been connected to an empty-state resonance at 1.53 eV above the VB onset, being localized at the four Cu atoms adjacent to the O defect [47]. The resonance downshifts to 1.45 eV if one electron remains in the defect and a V_{O^+} complex is formed. According to HSE calculations, the $V_{O^{2+}}$ defect becomes particularly stable if the Fermi level of Cu_2O locates directly at the VB top, while any EF shift into the band gap promotes generation of singly charged V_{O^+} defects. On this basis, we assign the distinct emission doublet from Cu_2O thin films to the PL fingerprint of O vacancies, whereby low- and high-wavelength components are attributed to double ($V_{O^{2+}}$) and single charged (V_{O^+}) defects in the lattice, respectively.

145

7.3.5 Origin of the V_O luminescence in thin films

The detection of two strong V_O-related PL peaks comes not unexpected in our experiments, as the Cu_2O preparation scheme is designed to be compatible with an UHV environment. Although an O_2 pressure as high as 50 mbar is used for initial Cu oxidation, the subsequent post-annealing step is carried out in 10^{-4} mbar O_2 at 600 K, thus at reduced oxygen chemical potential (μ_{O_2}). Previous studies have already shown that μ_{O_2} is the most sensitive parameter for oxide formation and insufficient oxygen availability triggers Cu alloying with the support rather than oxidation to Cu_2O [32].

A first hint on the stoichiometry deviations between bulk and thin-film Cu_2O may be derived directly from the ratio of V_{Cu^-} versus V_{O^+}-mediated luminescence peaks. Although no Cu-vacancy emission was detected for Au(111)- and Pt(111)-supported films, the STM conductance data presented in figure 7.5 unambiguously reveal a Fermi energy position at the VB top and the development of an empty-state VB pocket, both providing clear evidence for a p-type electronic characteristic. The reason for the absence of V_{Cu}-related emission can not be taken as a signature of an n-type oxide nature, because the PL response is a poor indicator of the defect landscape of the investigated material. Three main reasons can be found to justify the latter statement [17, 48]: (i) The defect luminescence in Cu_2O follows entirely different recombination pathways. The V_O emission is triggered by hot electrons generated upon optical stimulation. Given the short carrier lifetimes in the material, the decay process occurs on very short time scales (4 ps at low temperature) and is therefore insensitive against competing non-radiative decay channels [17]. The V_{Cu} emission, on the other hand, gets initiated by the trapping of free excitons at Cu defects. The associated decay times are at least one order of magnitude longer than those of the V_O luminescence, reflecting the long lifetime of dipole-forbidden Cu_2O excitons. Because of this excitation asymmetry, the thin-film luminescence is primarily governed by O defects that provide a fast and effective decay channel after optical stimulation. In contrast, the V_{Cu} emission relies on the long-lived Cu_2O excitons, and is consequently highly susceptible to structural disorder and non-radiative decay channels in the thin films. (ii) The defect emission channels have different temperature dependence, which favors V_{Cu} emission at high temperatures, but V_O emission at low temperatures. (iii) Especially the V_{Cu} luminescence is the result of pronounced multi-phonon emission, as reflected in large Huang-Rhys factors, which reduced the emission probability. All three factors prohibit any quantitative insights into the V_{Cu} versus V_O concentration alone from the intensity ratio of the respective PL peaks.

To obtain more precise information on the defect characteristics of the different sample lattices, we analyzed the XPS spectra of $Cu_2O/Au(111)$, $Cu_2O/Pt(111)$ and of the bulk crystal (shown in figure 7.9). To estimate the corresponding oxide stoichiometry, we have divided the peak areas of Cu $2p_{3/2}$ (935 eV) and O 1s (530.5 eV) core levels after correcting them for their atomic sensitivity factors. In contrast with our expectations, we obtained a generally higher Cu deficiency in the oxide films as compared to the bulk crystal. However, the charge transfer between support and interfacial O atoms and small CuO inclusions also contribute to the detected Cu deficiency: the observations made on the basis of XPS do not automatically imply a lower concentration of O vacancies in the films. Among the two films, the Au(111)-supported layers exhibit a lower Cu content than its Pt counterparts, which will be of relevance when discussing details of the PL spectra later in this chapter. The observed Cu deficiency of both, thin-film and bulk Cu_2O emphasizes the robust p-type
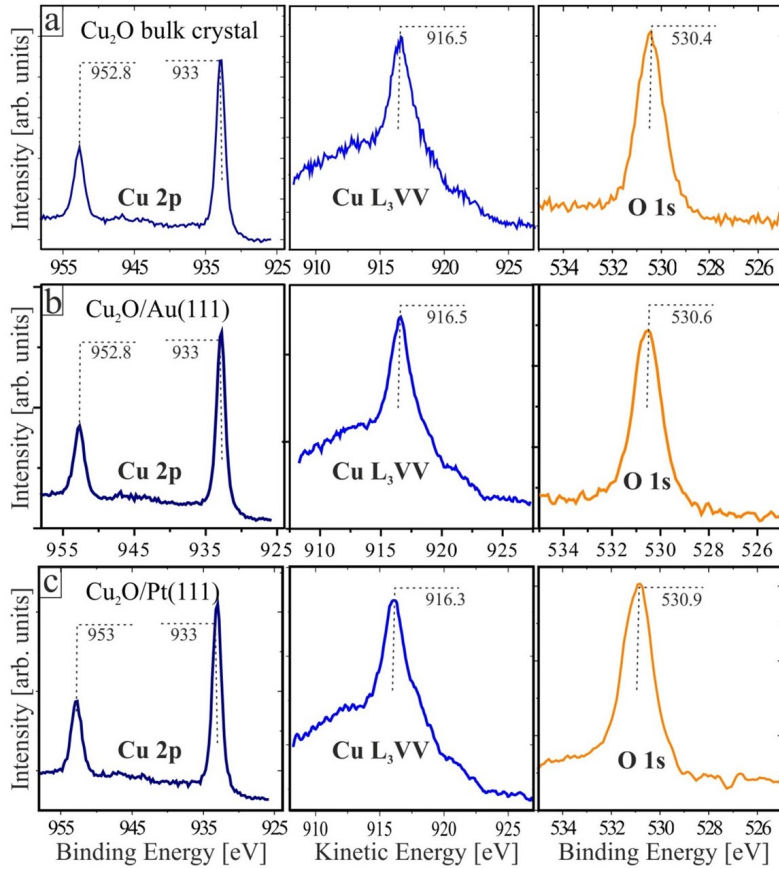
Figure 7.9: *XP spectra of (a) bulk Cu_2O, (b) 10 nm thick $Cu_2O/Au(111)$ and (c) 25 nm thick $Cu_2O/Pt(111)$ films measured in the energy window of the Cu2p peaks (left), the Cu Auger lines (middle) and the O1s peak (right).*

nature of Cu_2O. It is also in line with the STM conductance data presented in figure 7.4, where the position of the Fermi level at the VB top and the development of an empty-state VB pocket provide clear evidence for the p-type electronic characteristic of all three samples. Consequently, a strong V_O luminescence in combination with missing V_{Cu} emission cannot be taken as indication for an n-type nature of the thin films, although similar conclusions have been drawn from earlier experiments [21]. In fact, a dominant V_O signal only points to a different balance between defect-mediated and non-radiative decay channels in our supported films compared to a bulk Cu_2O crystal that is of much higher structural quality. We note that the suppression of free-exciton and V_{Cu} luminescence is a common observation for Cu_2O powders and thin films and frequently reported in the literature [19, 21, 30, 45].

Particularly interesting in our work is the dominance of the 830 nm with respect to the 750 nm PL peak for Pt(111)-supported Cu_2O films, whereas the intensity ratio reverses on an Au(111) support. As discussed before, the two maxima arise from radiative electron decay via single (V_{O+}) and double-charged (V_{O2+}) oxygen vacancies that develop different defect states within the oxide band gap [20]. However, their charge state is controlled by a low-lying state that is in resonance with the oxide VB. While in the V_{O2+} defects, the two electrons initially left behind by a neutral desorbing O atom are annihilated by two holes from the p-type oxide, one electron remains trapped in the V_{O2+} complex. The thermodynamic stability of V_{O2+} with respect to V_{O+} complexes is therefore governed by the hole concentration in the oxide, or analogously by the oxide Fermi level. For E_F positions directly at the VB top (high hole density), formation of V_{O+} defects is thermodynamically

unfavorable with respect to $V_{O^{2+}}$ complexes, while more V_{O^+} defects develop for an E_F position inside the band gap.

With this information, the different defect landscapes of Au(111) and Pt(111)-supported Cu_2O films can be rationalized. Oxide growth on Au(111) intrinsically results in highly Cu-deficient films. The reason is the strong incentive of copper-gold alloy formation, driven by the similar structural, electronic and chemical properties of both metals [49]. The Au(111) surface thus acts as sink for the deposited Cu atoms, making interfacial mixing and oxide formation two highly competitive channels. Conversely, Pt shows a lower tendency for alloy formation and some unreacted Cu always accumulates at the Pt(111)-Cu_2O interface, serving as Cu source during film growth [32]. As a consequence, the Au(111)-supported films typically show higher Cu deficiency, yet better p-type conductivity and lower E_F position than their Pt(111) counterparts. This gets reflected in a stronger $V_{O^{2+}}$ than V_{O^+} emission from Cu_2O/Au(111) films, while the ratio inverts for Cu_2O/Pt(111), in good agreement with our data. Being aware of intrinsic uncertainties of STM conductance spectroscopy, this conclusion is also supported with the dI/dV spectra presented in figure 7.5. While the energy separation between VB top and E_F is ~ 0.1 eV for Cu_2O/Au(111), it increases to 0.2 eV for Cu_2O/Pt(111), making the latter system less Cu-deficient, hence more susceptible to the formation of V_{O^+} complexes.

Finally, we studied the temperature evolution of the V_O peak intensities in bulk and in thin-film Cu_2O (figure 7.8b). Although the two curves follow a similar behavior, they do not coincide. While the onset temperature for emission is 230 K for the bulk crystal, it up-shifts to almost 270 K for the thin films. Although we can not exclude a systematic error here due to the lower thermal conductivity of bulk oxides with respect to metallic samples, a part of the effect might be of physical origin. The temperature dependence of PL is generally governed by the competition between radiative and non-radiative decay channels, with phonon or thermal electron excitations being examples for the latter. It now appears plausible that this interplay is different for bulk dielectrics and thin films. Possible deviations concern a phonon softening in metal-supported oxide layers, as observed for MgO [50] and CaO [51] or a weakening of dipole selections rules due to strain in the Cu_2O films. Although a detailed analysis of this phenomenon is beyond the scope of the paper, it certainly warrants closer inspection.

7.4 Conclusions

PL measurements have been performed on bulk and thin-film Cu_2O samples over a wide temperature rang. While the luminescence of bulk Cu_2O is governed by the radiative decay of free excitons and excitons trapped at Cu and O vacancies, only the V_O-mediated emission channel prevails in Cu_2O films. The unique PL signatures of bulk and thin-film oxides have been connected with their different defect landscapes. While Cu defects are abundant in both systems, as concluded from their robust p-type conduction behavior found through STM spectroscopy, the oxigen vacancy concentration is substantially larger in the oxide films. This has been ascribed to the vacuum-compatible preparation scheme of Cu_2O thin films that includes a final annealing step at 10^{-4} mbar O_2. In addition, the V_O-mediated emission channel is less sensitive to structural disorder, favoring this recombination pathway in thin films. Also, the metal substrate used for oxide growth affects the defect landscape and Au(111)-supported films have a higher Cu deficiency (more $V_{O^{2+}}$ complexes) than their Pt(111)-grown counterparts (more V_{O^+} complexes). Future experiments

shall clarify, whether the distinct V_O emission can be recorded also locally by STM luminescence spectroscopy [26]. This would open a pathway to probe individual O defects, hence the local O deficiency of Cu_2O samples directly in a spatially resolved experiment.

Bibliography

[1] B. K. Meyer, A. Polity, D. Reppin, M. Becker, P. Hering, P. J. Klar, Th. Sander, C. Reindl, J. Benz, M. Eickhoff, C. Heiliger, M. Heinemann, J. Bläsing, A. Krost, S. Shokovets, C. Müller, and C. Ronning. Binary copper oxide semiconductors: From materials towards devices. *Physica Status Solidi (b)*, 249(8):1487–1509, 2012.

[2] B. Henderson and G. F. Imbusch. Optical spectroscopy of inorganic solids. *Journal of Modern Optics*, 37(10):1688–1688, 1990.

[3] Chris D Geddes, editor. *Reviews in fluorescence 2017*. Reviews in Fluorescence. Springer International Publishing, 1 edition.

[4] Andres Galdámez-Martinez, Guillermo Santana, Frank Güell, Paulina R. Martínez-Alanis, and Ateet Dutt. Photoluminescence of ZnO nanowires: A review. *Nanomaterials*, 10(5):857, 2020.

[5] Christoph Freysoldt, Blazej Grabowski, Tilmann Hickel, Jörg Neugebauer, Georg Kresse, Anderson Janotti, and Chris G. Van de Walle. First-principles calculations for point defects in solids. *Rev. Mod. Phys.*, 86:253–305, 2014.

[6] Patrick Rinke, André Schleife, Emmanouil Kioupakis, Anderson Janotti, Claudia Rödl, Friedhelm Bechstedt, Matthias Scheffler, and Chris G. Van de Walle. First-principles optical spectra for F centers in MgO. *Phys. Rev. Lett.*, 108:126404, 2012.

[7] Claus Klingshirn, J. Fallert, H. Zhou, J. Sartor, C. Thiele, F. Maier-Flaig, D. Schneider, and H. Kalt. 65 years of ZnO research - old and very recent results. *Physica Status Solidi (b)*, 247(6):1424–1447, 2010.

[8] Michael A. Reshchikov and Hadis Morkoç. Luminescence properties of defects in GaN. *Journal of Applied Physics*, 97(6):061301, 2005.

[9] Meral Balık, Veysel Bulut, and Ibrahim Y. Erdogan. Optical, structural and phase transition properties of Cu_2O, CuO and Cu_2O/CuO: Their photoelectrochemical sensor applications. *International Journal of Hydrogen Energy*, 44(34):18744–18755, 2019.

[10] A.O Musa, T Akomolafe, and M.J Carter. Production of cuprous oxide, a solar cell material, by thermal oxidation and a study of its physical and electrical properties. *Solar Energy Materials and Solar Cells*, 51(3-4):305–316, 1998.

[11] Mandeep Singh, Deshetti Jampaiah, Ahmad E. Kandjani, Ylias M. Sabri, Enrico Della Gaspera, Philipp Reineck, Martyna Judd, Julien Langley, Nicholas

Cox, Joel van Embden, Edwin L. H. Mayes, Brant C. Gibson, Suresh K. Bhargava, Rajesh Ramanathan, and Vipul Bansal. Oxygen-deficient photostable cu$_2$o for enhanced visible light photocatalytic activity. *Nanoscale*, 10(13):6039–6050, 2018.

[12] Md. Ghulam Saber and Rakibul Hasan Sagor. Analysis of cuprous oxide-based ultra-compact nanoplasmonic coupler. *Applied Nanoscience*, 5(2):217–221, 2014.

[13] Takayuki Ito and Taizo Masumi. Detailed examination of relaxation processes of excitons in photoluminescence spectra of Cu$_2$O. *Journal of the Physical Society of Japan*, 66(7):2185–2193, 1997.

[14] J. I. Jang, Y. Sun, B. Watkins, and J. B. Ketterson. Bound excitons in Cu$_2$O: Efficient internal free exciton detector. *Phys. Rev. B*, 74:235204, 2006.

[15] T. Kazimierczuk, D. Fröhlich, S. Scheel, H. Stolz, and M. Bayer. Giant rydberg excitons in the copper oxide cu2o. *Nature*, 514(7522):343–347, 2014.

[16] J. Thewes, J. Heckötter, T. Kazimierczuk, M. Aßmann, D. Fröhlich, M. Bayer, M. A. Semina, and M. M. Glazov. Observation of high angular momentum excitons in cuprous oxide. *Phys. Rev. Lett.*, 115:027402, 2015.

[17] Laszlo Frazer, Richard D. Schaller, Kelvin B. Chang, Aleksandr Chernatynskiy, and Kenneth R. Poeppelmeier. Seeing the invisible plasma with transient phonons in cuprous oxide. *Physical Chemistry Chemical Physics*, 19(2):1151–1157, 2017.

[18] M. Zouaghi, B. Prevot, C. Carabatos, and M. Sieskind. Near infrared optical and photoelectric properties of cu2o. III. interpretation of experimental results. *Physica Status Solidi (a)*, 11(2):449–460, 1972.

[19] H. Solache-Carranco, G. Juárez-Díaz, A. Esparza-García, M. Briseño-García, M. Galván-Arellano, J. Martínez-Juárez, G. Romero-Paredes, and R. Peña-Sierra. Photoluminescence and x-ray diffraction studies on Cu$_2$O. *Journal of Luminescence*, 129(12):1483–1487, 2009.

[20] Junqiang Li, Zengxia Mei, Lishu Liu, Huili Liang, Alexander Azarov, Andrej Kuznetsov, Yaoping Liu, Ailing Ji, Qingbo Meng, and Xiaolong Du. Probing defects in nitrogen-doped Cu$_2$O. *Scientific Reports*, 4(1), 2014.

[21] Rohana Garuthara and Withana Siripala. Photoluminescence characterization of polycrystalline n-type cu2o films. *Journal of Luminescence*, 121(1):173–178, 2006.

[22] M. Nyborg, Ilia Kolevatov, G. C. Vásquez, K. Bergum, and E. Monakhov. Dominant defects and carrier transport in single crystalline cuprous oxide: A new attribution of optical transitions. *Journal of Applied Physics*, 130(17):175701, 2021.

[23] Alexander Gloystein and Niklas Nilius. High-pressure oxidation of copper on au(111): A route toward bulk-like cuprous oxide films. *The Journal of Physical Chemistry C*, 124(52):28605–28613, 2020.

[24] Alexander Gloystein, Jack Anthony Creed, and Niklas Nilius. Atomic view on the (111) surface of a Cu_2O single crystal: Reconstruction, electronic properties, and band-bending effects. *The Journal of Physical Chemistry C*, 126(39):16834–16840, 2022.

[25] Hannes Raebiger, Stephan Lany, and Alex Zunger. Origins of the p-type nature and cation deficiency in Cu_2O and related materials. *Phys. Rev. B*, 76:045209, 2007.

[26] David O. Scanlon and Graeme W. Watson. Undoped n-type Cu_2O: Fact or fiction? *The Journal of Physical Chemistry Letters*, 1(17):2582–2585, 2010.

[27] Alexander Gloystein and Niklas Nilius. Copper oxide phases probed via plasmonic light emission in the STM. *New Journal of Physics*, 23(9):093021, 2021.

[28] Hanna Fedderwitz. *Reparation and characterization of cuprous oxide thin films using low-temperature scanning tunneling microscopy*. PhD thesis, 2017.

[29] Stefan Ulrich. Design and construction of a low-temperature scanning tunneling microscope for spectroscopic applications on model catalysts, 2013.

[30] Jun-Woo Park, Hyungkeun Jang, Sung Kim, Suk-Ho Choi, Hosun Lee, Joongoo Kang, and Su-Huai Wei. Microstructure, optical property, and electronic band structure of cuprous oxide thin films. *Journal of Applied Physics*, 110(10):103503, 2011.

[31] Rémi Lazzari and Ingve Simonsen. GranFilm: a software for calculating thin-layer dielectric properties and fresnel coefficients. *Thin Solid Films*, 419(1-2):124–136, November 2002.

[32] Alexander Gloystein and Niklas Nilius. Copper oxidation on Pt(111) - More than a surface oxide? *The Journal of Physical Chemistry C*, 123(44):26939–26946, 2019.

[33] Kirk H. Schulz and David F. Cox. Photoemission and low-energy-electron-diffraction study of clean and oxygen-dosed $Cu_2O(111)$ and (100) surfaces. *Phys. Rev. B*, 43:1610–1621, 1991.

[34] Anneli Önsten, Mats Göthelid, and Ulf O Karlsson. Atomic structure of $Cu_2O(111)$. *Surf. Sci.*, 603(2):257–264.

[35] A Gloystein, N Nilius, J Goniakowski, and C Noguera. Nanopyramidal reconstruction of $cu_2O(111)$: A long-standing surface puzzle solved by STM and DFT. *J. Phys. Chem. C Nanomater. Interfaces*, 124(49):26937–26943.

[36] Alexander Gloystein and Niklas Nilius. Empty valence-band pocket in p-type $cu_2o(111)$ probed with scanning tunneling spectroscopy. *physica status solidi (b)*, 258(11):2100337, 2021.

[37] D. W. Snoke, A. J. Shields, and M. Cardona. Phonon-absorption recombination luminescence of room-temperature excitons in Cu_2O. *Phys. Rev. B*, 45:11693–11697, 1992.

[38] J. T. Warren, K. E. O'Hara, and J. P. Wolfe. Two-body decay of thermalized excitons in Cu_2O. *Phys. Rev. B*, 61:8215–8223, 2000.

[39] N Harukawa, S Murakami, S Tamon, S Ijuin, A Ohmori, K Abe, and T Shigenari. Temperature dependence of luminescence lifetime in Cu_2O. *Journal of Luminescence*, 87-89:1231–1233, 2000.

[40] G. P. Pollack and Dan Trivich. Photoelectric properties of cuprous oxide. *Journal of Applied Physics*, 46(1):163–172, 1975.

[41] Satoshi Kawata, editor. *Near-Field Optics and Surface Plasmon Polaritons.* Springer Berlin Heidelberg, 2001.

[42] J M Pitarke, V M Silkin, E V Chulkov, and P M Echenique. Theory of surface plasmons and surface-plasmon polaritons. *Reports on Progress in Physics*, 70(1):1–87, 2006.

[43] Edward D Palik. *Handbook of optical constants of solids.* Academic Press.

[44] Heinz Raether. *Surface Plasmons on Smooth and Rough Surfaces and on Gratings.* Springer Berlin Heidelberg, 1988.

[45] Paul R. Markworth, R. P. H. Chang, Y. Sun, G. K. Wong, and J. B. Ketterson. Epitaxial stabilization of orthorhombic cuprous oxide films on MgO(110). *Journal of Materials Research*, 16(4):914–921, 2001.

[46] Jun-Woo Park, Hyungkeun Jang, Sung Kim, Suk-Ho Choi, Hosun Lee, Joongoo Kang, and Su-Huai Wei. Microstructure, optical property, and electronic band structure of cuprous oxide thin films. *Journal of Applied Physics*, 110(10):103503, 2011.

[47] Chiara Ricca, Lisa Grad, Matthias Hengsberger, Jürg Osterwalder, and Ulrich Aschauer. Importance of surface oxygen vacancies for ultrafast hot carrier relaxation and transport in Cu_2O. *Phys. Rev. Research*, 3:043219, 2021.

[48] Laszlo Frazer, Erik J. Lenferink, Kelvin B. Chang, Kenneth R. Poeppelmeier, Nathaniel P. Stern, and John B. Ketterson. Evaluation of defects in cuprous oxide through exciton luminescence imaging. *Journal of Luminescence*, 159:294–302, 2015.

[49] F Grillo, H Früchtl, S M Francis, and N V Richardson. Site selectivity in the growth of copper islands on Au(111). *New Journal of Physics*, 13(1):013044, 2011.

[50] L. Savio, E. Celasco, L. Vattuone, M. Rocca, and P. Senet. MgO/Ag(100): Confined vibrational modes in the limit of ultrathin films. *Phys. Rev. B*, 67:075420, 2003.

[51] Yi Cui, Sergio Tosoni, Wolf-Dieter Schneider, Gianfranco Pacchioni, Niklas Nilius, and Hans-Joachim Freund. Phonon-mediated electron transport through CaO thin films. *Physical Review Letters*, 114(1), 2015.

Conclusions

This thesis reports the investigations of the properties of systems at the nanoscale, that are promising candidates for visible light photocatalysis. In particular, I have focused on samples composed by cerium oxide combined with plasmonic nanoparticles (NPs), on copper NPs either bare or in different dielectric environments and on films of cuprous oxide. The different samples have been grown using different physical deposition methods, and characterized using different techniques, including XPS and UPS for the electronic properties, SEM, TEM, AFM and STM for the morphology, and ultrafast spctroscopies such as FTAS, trPES and trXAS to study the dynamic evolution of the excited samples on time scales that range from hundreds of fs to 300 ps. In particular, the use of time-resolved techniques to study ultrafast carrier transport in metal/oxide systems is crucial to properly describe the light-induced excitation in a photocatalytic system, to have a deep understanding of its functionalities. This knowledge would permit to elucidate the functioning of the investigated material, the velocity of its response, the duration and the modification of the excited states after the interaction with photons of different energies, in order to tune and optimize its photocatalytic properties.

In the first part of the present thesis, I have described the growth and the characterization of samples composed by CeO_2 combined with Ag and Au NPs with the aim of extracting information on their optical properties, with a specific focus on the ultrafast dynamics of the excitations. First, we have studied samples composed by Ag NPs grown by MBE and embedded in thin films of CeO_2, grown by evaporating Ce in an O_2 partial pressure. After a first characterization by *in-situ* XPS and by UV-Vis absorbance, we have characterized the dynamic evolution - and in particular the reneutralization characteristic time - of positive charges generated by photoexcitation in ceria films with and without the NPs. From the analysis of the time-resolved photoemission spectra, we could observe that after the interaction with radiation above the ceria band gap, a large fraction of positive carriers with a lifetime that exceeds 100 ps are generated, independently on the presence of the NPs. The sub-band-gap excitation of bare ceria films induces instead the formation of a significantly smaller fraction of charges with lifetimes of tens of picoseconds, ascribed to the excitation of defect sites or to multiphoton absorption. When the oxide is combined with Ag NPs, the sub-band-gap excitation of localized surface plasmon resonances leads to reneutralization times longer than 300 ps. This was interpreted by considering the electronic unbalance at the surface of the NPs generated by the injection of electrons in CeO_2 as a consequence of the LSPR relaxation in the NPs. In this study we found a way to exploit the space charge effect in gaining access to the surface carrier dynamics in CeO_2 within the picosecond range of time, which is fundamental to describe the photocatalytic processes.

Secondly, we also investigated a sample composed by Ag NPs surrounded by ceria, but in this case the NPs have been coevaporated with Ce in oxygen partial pressure, and they have been deposited using a magnetron sputtering source coupled

with an Ar-filled aggregation region. The dynamic of the system has been investigated by means of free electron laser time resolved XAS, a chemically sensitive technique that permitted us to investigate the electron transfer process from the Ag NPs to the CeO_2 film generated by the NPs plasmonic resonance photoexcitation. The observed ultrafast changes (< 200 fs) of the Ce $N_{4,5}$ absorption edge allows to conclude that the excited Ag NPs transfer electrons to the Ce atoms of the CeO_2 film through a highly efficient mechanism.

In the third part, we focused on samples composed by Au NPs either bare or immersed in ceria layers. In this case both the NPs and the ceria films were deposited by MBE. Because of the strong dependence of plasmonic properties of NPs on the characteristics of the dielectric properties of the surroundings, we have investigated the interplay between the morphology, the electronic properties and the static optical absorbance of Au NPs. We demonstrated that the plasmonic absorption band can be tuned by modifying the dielectric environment in which the NPs are immersed, accompanying the experimental observations with numerical calculations based upon the Mie theory. The almost unmodified XPS and optical measurements repeated after 3 months from the samples deposition lead us to the conclusion that the plasmonic properties of Au NPs are stable in air conditions. Afterwards, we investigated the ultrafast dynamics of excited states induced by ultra-violet and visible light excitation in Au NPs combined with CeO_2, aimed at understanding the excitation pathways. The data, obtained by FTAS, showed that the excitation of LSPR in the Au NPs leads to an ultrafast injection of electrons into the empty 4f states of the surrounding CeO_2. Within the first few ps the injected electrons couple with the lattice distortion forming a polaronic excited state, with similar properties to the one which is formed after direct band-gap excitation in the oxide. At sub-ps delay times we observed relevant differences in the energetics and the time dynamics as compared to the case of band-gap excitation. Using different pump energies across the LSPR-related absorption band, the efficiency of the electron injection from the NPs into the oxide was found to be rather high, with a maximum above 30%. The injection efficiency has a different trend in energy as compared to the LSPR-related static optical absorbance, showing a significant decrease at low energies. This behavior is explained considering different de-excitation pathways with variable weight across the LSPR band. The result obtained suggests that improving the matching of the plasmonic response to the low energy part of the solar spectrum would not improve the overall solar catalytic efficiency of the material.

The last part of the thesis is focused on Cu NPs and Cu_2O thin films. Cu NPs, grown either by magnetron sputtering or by MBE, have been investigated in different environments: bare, surrounded by CeO_2 and surrounded by MgO. Cu NPs in CeO_2 exhibit a good stability of plasmonic properties, that remained almost unchanged after 3 months from the sample deposition. The electronic and especially the plasmonic properties of bare Cu NPs deposited via MBE showed a strong dependence on the growth and post-processing conditions. NPs exposed to oxygen during the growth showed a red-shifted plasmonic absorbance band broader than NPs grown in UHV or exposed to oxygen after the deposition. TEM images and the STEM-EELS maps acquired for the post-oxidized samples suggest the formation of hexagonally shaped NPs, surrounded by a thin shell of Cu_2O. Bare Cu and core-shell Cu/MgO NPs grown using gas phase-synthesis are bigger than the ones deposited via MBE. The embedding of Cu NPs in MgO was confirmed by TEM and EDX maps. UV-Vis absorbance revealed the presence of an intense LSPR for Cu/MgO, while the signal obtained for bare NPs, weaker and red-shifted, suggested the formation of a oxide

layer surrounding the NPs. These results confirmed the role of MgO as a protective transparent medium for Cu.

Finally, the work presented in the last chapter, conducted in the laboratories of the University of Oldenburg, deals with thin films of Cu_2O deposited via MBE. In this work, Cu_2O films of 10-65 nm thickness are investigated by LEED, STM and PL spectroscopy in a temperature range from 100 to 300 K. Their PL response have been then compared with the response of a bulk Cu_2O crystal. Although the chemical composition and surface morphology of both systems are identical, large differences have been found in the optical response. While bulk Cu_2O shows pronounced PL peaks at 620, 730 and 920 nm, compatible with the radiative decay of free and bound excitons, broad and asymmetric PL bands are detected at 775 and 850 nm for Cu_2O films grown on Au(111) and Pt(111) substrates, respectively, suggesting a substrate-dependent concentration of O^{2+} and O^{+} defects. Since STM conductance spectroscopy clearly shows p-type conductivity, indicating an abundance of Cu defects in the lattice, the fact that oxygen defects govern the thin-film PL is explained by a faster and more efficient recombination via the V_O than V_{Cu} emission channel, as the latter requires assembly and trapping of Cu_2O excitons first.

The results obtained in this work mean to provide new information on functional oxide-based materials, also in combination with plasmonic nanoparticles, suitable for solar light photocatalysis. The final aim is to obtain materials with increased visible light harvesting efficiency, with an optimized density of long-living excited states and with a good stability over time, which can be used, for example, for green-hydrogen production from solar water splitting or for other photocatalytic applications.

Acknowledgments

I really want to thank every person in the SESAMo group. A special thank goes to my supervisor, Dr. Paola Luches for her precious guide and for always being ready to support me. I really want to also thank Prof. Sergio D'Addato, for his wise advises, Dr. Stefania Benedetti, for her help every time I needed it, and Samuele Pelatti, with whom I shared part of the experimental activities in the SESAMo laboratory. I also want to acknowledge Giovanni Bertoni for his valuable contribution for the TEM and the people of SUPERMAN laboratory.

During these years, I had the good fortune of working with very prepared and available people. In particular, I want to express my gratitude to Stefano Pelli Cresi, a precious help and support through every part of this work. A special thank also to all "i romani", and in particular to Daniele, Patrick and Stefano. I am grateful to all people I have been working with at the ELETTRA Synchrotron, the groups of people at the SPRINT, ALOISA and EIS-TIMEX beamlines.

Last but certainly not least, the last chapter of this thesis would not have been possible without Dr. Prof. Niklas Nilius, of the Oldenburg University, and his collaborators. I really want to thank Niklas, who warmly welcomed me in Oldenburg: he has been a unique guide not only in the scientific field, but also for exploring the city and the surroundings. A special thank also to Alexander Gloystein and to Mina Soltanmohammadi.

Appendix A

Activity report

1. Conferences and Schools

   (a) **29/08/2022 – 02/09/2022** **ECOSS35** Luxembourg Oral Contribution: *Ultrafast dynamics of charge transfer from Au nanoparticles to cerium oxide*

   (b) **04/07/2022 – 08/07/2022** **ZCAM-ASEVA METAL-OXIDE ULTRATHIN FILMS AND NANOSTRUCTURES** Zaragoza Oral Contribution:*Dynamic charge transfer processes from Au NPs to CeO$_2$ layers*

   (c) **3/09/2021 – 17/09/2021** **107° Congresso Nazionale SIF Italia** Online Oral Contribution:*Dynamics of charge transfer from plasmonic nanoparticles to cerium oxide*

   (d) **21/06/2021 – 23/06/2021** **SILS meeting 2021** Online Poster Contribution:*Dynamics of charge transfer from plasmonic nanoparticles to cerium oxide*

   (e) **01/03/2021** **DPG spring meeting** Online Poster Contribution: *Dynamics of charge transfer processes at nanoparticle/oxide interface studied by free electron laser*

   (f) **13/09/2021 – 17/09/2021** **School on Synchrotron Radiation "Gilberto Vlaic": Fundamentals, Methods and Applications** Online Online summer school about synchrotron radiation, organized by the Italian Society of Synchrotron Radiation (SILS) in collaboration with ELETTRA-Sincrotrone Trieste SCpA

2. Teaching Activities

   (a) **2019 – 2020** **University teaching assistant** Universitá di Modena e Reggio Emilia 40 hours for the General Physics class of the Bachelor degree in Mechanical Engineering

   (b) **2020 – 2021** **University teaching assistant** Universitá di Modena e Reggio Emilia 40 hours for the General Physics class of the Bachelor degree in Mechanical Engineering

   (c) **2021 – 2022** **University teaching assistant** Universitá di Modena e Reggio Emilia 20 hours for the General Physics class of the Bachelor degree in Electronic Engineering

(d) **2022 – 2023 University teaching assistant** Universitá di Modena e Reggio Emilia 20 hours for the General Physics class of the Bachelor degree in Management Engineering

3. Courses and Seminars attended

   (a) Course *Physics of the single electron in the transmission electron microscope* (UNIMORE)

   (b) Course *Good practices in research* (UNIMORE)

   (c) Course *Numerical algorithms for signals and images processing* (UNIMORE)

   (d) Course *Getting Started with Python* (COURSERA, University of Michigan)

   (e) Course *Python Data Structures* (COURSERA, University of Michigan)

   (f) Course *Data Processing and Feature Engineering with MATLAB* (COURSERA, MathWorks)

   (g) Course *Basics of Synchrotron Radiation* (UNIMORE)

   (h) Course *Ultrafast spectroscopies applied to functional materials* (UNIMORE)

   (i) Course *Ultrafast optical spectroscopy* (MUSIQ, POLIMI)

   (j) Course *The transmission electron microscope-basics* (UNIMORE)

   (k) Course *Introduzione al linguaggio Python* (UNIMORE)

   (l) Seminar *Fuel cell day* (LIFC-Laboratorio Interdipartimentale Fuel Cell - UNIMORE)

   (m) Seminar *Italy @ EuXFEL Workshop*

   (n) Seminar *Gas-phase synthesis of nanoparticles and their interaction with gases* Prof Lidia Martínez (UNIMORE)

4. Experience in other Laboratories

   (a) **25/11/2019 - 29/11/2019 FTAS - EuroFEL Support Laboratory (ISM)** Online

   (b) **15/01/2020 - 31/01/2020 Beamtime@NFFA-Trieste (Elettra)** Proposal Title: *Plasmon-mediated electron injection into cerium oxide from embedded silver nanoparticles*

   (c) **14/09/2020 - 21/09/2020 Beamtime@ALOISA at ANCHOR-SUNDYN endstation at the HASPES branchline (Elettra)** Proposal Title: *Charge transfer processes in plasmonic nanoparticle - reducible oxide systems*

   (d) **06/01/2022 - 27/05/2022 Scientific stage activity in the group of Prof. Dr. Niklas Nilius "Scanning Probe Spectroscopy" in the Department of Physics at Oldenburg University, Germany**

Appendix B

List of publications

1. Jacopo Stefano Pelli Cresi, Emiliano Principi, Eleonora Spurio, Daniele Catone, Patrick O'Keeffe, Stefano Turchini, Stefania Benedetti, Avinash Vikatakavi, Sergio D'Addato, Riccardo Mincigrucci, Laura Foglia, Gabor Kurdi, Ivaylo P. Nikolov, Giovanni De Ninno, Claudio Masciovecchio, Stefano Nannarone, Jagadesh Kopula Kesavan, Federico Boscherini, and Paola Luches. **Ultrafast Dynamics of Plasmon-Mediated Charge Transfer in Ag@CeO$_2$ Studied by Free Electron Laser Time-Resolved X-ray Absorption Spectroscopy**, Nano Letters 2021 21 (4), 1729-1734 10.1021/acs.nanolett.0c04547

   Abstract: *Expanding the activity of wide bandgap semiconductors from the UV into the visible range has become a central goal for their application in green solar photocatalysis. The hybrid plasmonic/semiconductor system, based on silver nanoparticles (Ag NPs) embedded in a film of CeO$_2$, is an example of a functional material developed with this aim. In this work, we take advantage of the chemical sensitivity of free electron laser (FEL) time-resolved soft X-ray absorption spectroscopy (TRXAS) to investigate the electron transfer process from the Ag NPs to the CeO2 film generated by the NPs plasmonic resonance photoexcitation. Ultrafast changes (< 200 fs) of the Ce $N_{4,5}$ absorption edge allowed us to conclude that the excited Ag NPs transfer electrons to the Ce atoms of the CeO$_2$ film through a highly efficient electron-based mechanism. These results demonstrate the potential of FEL-based TRXAS measurements for the characterization of energy transfer in novel hybrid plasmonic/semiconductor materials.*

2. Jacopo Stefano Pelli Cresi, Eleonora Spurio, Lorenzo Di Mario, Patrick O'Keeffe, Stefano Turchini, Stefania Benedetti, Gian Marco Pierantozzi, Alessandro De Vita, Riccardo Cucini, Daniele Catone, Paola Luches. **Lifetime of Photogenerated Positive Charges in Hybrid Cerium Oxide-Based Materials from Space and Mirror Charge Effects in Time-Resolved Photoemission Spectroscopy**, The Journal of Physical Chemistry C 2022 126 (27), 11174-11181 10.1021/acs.jpcc.2c02148

   Abstract: *Space and mirror charge effects in time-resolved photoemission spectroscopy can be modeled to obtain relevant information on the recombination dynamics of charge carriers. We successfully extracted from these phenomena the reneutralization characteristic time of positive charges generated by photoexcitation in CeO$_2$-based films. For the above-band-gap excitation, a large fraction of positive carriers with a lifetime that exceeds 100 ps are generated.*

Otherwise, the sub-band-gap excitation induces the formation of a significantly smaller fraction of charges with lifetimes of tens of picoseconds, ascribed to the excitation of defect sites or to multiphoton absorption. When the oxide is combined with Ag nanoparticles, the sub-band-gap excitation of localized surface plasmon resonances leads to reneutralization times longer than 300 ps. This was interpreted by considering the electronic unbalance at the surface of the nanoparticles generated by the injection of electrons, via localized surface plasmon resonance (LSPR) decay, into CeO_2. This study represents an example of how to exploit the space charge effect in gaining access to the surface carrier dynamics in CeO_2 within the picosecond range of time, which is fundamental to describe the photocatalytic processes.

3. Sergio D'Addato, Matteo Lanza, Anthea Boiani, Eleonora Spurio, Samuele Pelatti, Guido Paolicelli and Paola Luches. **Morphology and Optical Properties of Gas-Phase-Synthesized Plasmonic Nanoparticles: Cu and Cu/MgO**, Materials 2022 15 (13), 4429 https://doi.org/10.3390/ma15134429

Abstract: *In this paper, an investigation of the properties of Cu and Cu/MgO nanoparticles (NPs) is presented. The NPs were obtained with gas-phase synthesis, and the MgO shells or matrices were formed via the co-deposition method on inert substrates. SEM and AFM were used to investigate the NP morphology on Si/SiO_x, quartz, and HOPG. The Cu NPs revealed flattening of their shape, and when they were deposited on HOPG, diffusion and formation of small chains were observed. The embedding of Cu NPs in MgO was confirmed by TEM and EDX maps. XPS showed that Cu was in its metallic state, regardless of the presence of the surrounding MgO. UV–Vis revealed the presence of an intense localized surface plasmon resonance (LSPR) for Cu/MgO and for "bare" NPs. These results confirmed the role of MgO as a protective transparent medium for Cu, and the wavelength position of the LSPR in the Cu/MgO system was consistent with calculations. The wavelength position of the LSPR observed for "bare" and post-oxidized Cu NPs was probably affected by the formation of copper oxide shells after exposure to air. This study paves the way for the use of Cu/MgO NPs as plasmonic nanomaterials in applications such as photovoltaics and sensor technology.*

4. Eleonora Spurio **Dynamics of charge transfer from plasmonic nanoparticles to cerium oxide**, . Il nuovo cimento C 2021 45 (6) 1-4 10.1393/ncc/i2022-22181-9

Abstract: *The combination of semiconducting oxide-based materials with plasmonic nanoparticles (NPs) aims to efficiently convert solar light into chemical or electric energy, exploiting the excitation of localized surface plasmon resonance (LSPR) in the NPs that leads to a significant energy/charge transfer to the oxide. By performing UV-Visible spectrophotometry measurements on systems composed of Cu/Au NPs embedded in a matrix of CeO_2, we observed a wide absorption band in the visible range, ascribed to the LSPR excitation in the NPs. Femtosecond transient absorption spectroscopy at different pump energies across the LSPR band of the NPs unveiled a persistent charge transfer from the NPs to CeO_2. Efficiency up to 35% for systems with Au NPs has been estimated.*

5. Mina Soltanmohammadi, Eleonora Spurio, Alexander Gloystein, Paola Luches,

Niklas Nilius **Photoluminescence Spectroscopy of Cuprous Oxide: Bulk Crystal versus Crystalline Films** Accepted by physica status solidi (a)

6. Eleonora Spurio, Giuseppe Ammirati, Jacopo Stefano Pelli Cresi, Samuele Pelatti, Alessandra Paladini, Sergio D'Addato, Stefano Turchini, Patrick O'Keeffe, Daniele Catone, Paola Luches Tentative title: **Ultrafast dynamics of photoexcited states in CeO$_2$ coupled with Au NPs** In pre-submission